2015

Mineral Deposits and Tectonic Evolution of the Qinling Orogenic Belt, Central China

Jessica MJ Walsh

Mineral Deposits and Tectonic Evolution of the Qinling Orogenic Belt, Central China

Abstract

Synthesizing the tectonic evolution of collisional orogens provides an important framework with which to place spatial and temporal constraints on the formation of various ore deposits in complexly deformed rocks. The Qinling Orogenic Belt (QOB), central China represents a composite orogen that has experienced four main episodes of accretion, subduction and subsequent collision between discrete continental blocks. Multiple tectonic events, from rifting to arc collisions to continental collisions since the Proterozoic have formed an orogen with

an abundant and diverse suite of mineral deposits. Although there are several metallogenic epochs throughout the geological evolution of the QOB and the adjacent areas including the North China Block and South China Block, the most pervasive, voluminous and abundant is the large-scale granite-related (Mo, Cu) event that occurred during final continental collision in the Mesozoic. This event saw the widespread emplacement of porphyry Mo-(Cu ± Au) deposits which were directly influenced by a post-collisional extensional regime, and subsequent influx of large-scale granitoid intrusives. Two mineralised aplite samples collected from the Nantai porphyry-skarn

Mo-(Cu) deposit were dated via SHRIMP zircon U-Pb methods at ANU and revealed an age of

151 – 148 Ma. The granites display geochemical patterns consistent with A-type granites but transitional towards S-type. Folded and faulted Devonian sedimentary sequences are host to high- grade Carlin-type and orogenic gold deposits, which are spatially and temporally associated with the Mesozoic granitoids (158 – 100 Ma). The Longtougou and Liujiaxia orogenic Au deposits are representative of this suite of gold deposits and mineralisation is thought to be coincident with the main post-Devonian deformation event responsible for folding and faulting of the Devonian units, possibly related to continental collision and voluminous magmatism in the Triassic. Other unusual deposit types include REE-hosting carbonatites within the South Qinling Belt. These are thought

to be Permo-Triassic in age and related to the voluminous alkali basaltic dyke swarms that intrude much of the Qinling Orogen. Petrographic and geochemical analysis of these rocks suggests they may have formed via the interaction of highly fractionated, alkalic silica-poor magmas which may have interacted with the abundant limestone country rocks to produce the carbonatite magmas and associated REE mineralisation. The formation and deformation of the QOB has been intensely debated from the onset of the earliest evolutionary histories and tectonic frameworks. This investigation provides the first multi-deposit approach to supplement the knowledge and broader literature on the development of the region.

Degree Type

Thesis

Degree Name

BSc Hons

Department

School of Earth & Environmental Science

Advisor(s)

Solomon Buckman

Keywords
Tectonometallogenesis, ore genesis, Asia, tectonics, metallogeny

MINERAL DEPOSITS AND TECTONIC EVOLUTION OF THE QINLING OROGENIC BELT, CENTRAL CHINA

Jessica Margaret June Walsh

A thesis submitted in part fulfilment of the requirements of the Honours degree of Bachelor of Science (Geology) in the School of Earth & Environmental Sciences, Faculty of Science, Medicine and Health, University of Wollongong

2015

The information in this thesis is entirely the result of investigations conducted by the author, unless otherwise acknowledged, and has not been submitted in part, or otherwise, for any other degree or qualification

Jessica Margaret June Walsh
14th October 2015

ABSTRACT

Synthesizing the tectonic evolution of collisional orogens provides an important framework with which to place spatial and temporal constraints on the formation of various ore deposits in complexly deformed rocks. The Qinling Orogenic Belt (QOB), central China represents a composite orogen that has experienced four main episodes of accretion, subduction and subsequent collision between discrete continental blocks. Multiple tectonic events, from rifting to arc collisions to continental collisions since the Proterozoic have formed an orogen with an abundant and diverse suite of mineral deposits. Although there are several metallogenic epochs throughout the geological evolution of the QOB and the adjacent areas including the North China Block and South China Block, the most pervasive, voluminous and abundant is the large-scale granite-related (Mo, Cu) event that occurred during final continental collision in the Mesozoic. This event saw the widespread emplacement of porphyry Mo-(Cu ± Au) deposits which were directly influenced by a post-collisional extensional regime, and subsequent influx of large-scale granitoid intrusives. Two mineralised aplite samples collected from the Nantai porphyry-skarn Mo-(Cu) deposit were dated via SHRIMP zircon U-Pb methods at ANU and revealed an age of 151 – 148 Ma. The granites display geochemical patterns consistent with A-type granites but transitional towards S-type. Folded and faulted Devonian sedimentary sequences are host to high-grade Carlin-type and orogenic gold deposits, which are spatially and temporally associated with the Mesozoic granitoids (158 – 100 Ma). The Longtougou and Liujiaxia orogenic Au deposits are representative of this suite of gold deposits and mineralisation is thought to be coincident with the main post-Devonian deformation event responsible for folding and faulting of the Devonian units, possibly related to continental collision and voluminous magmatism in the Triassic. Other unusual deposit types include REE-hosting carbonatites within the South Qinling Belt. These are thought to be Permo-Triassic in age and related to the voluminous alkali basaltic dyke swarms that intrude much of the Qinling Orogen. Petrographic and geochemical analysis of these rocks suggests they may have formed via the interaction of highly fractionated, alkalic silica-poor magmas which may have interacted with the abundant limestone country rocks to produce the carbonatite magmas and associated REE mineralisation. The formation and deformation of the QOB has been intensely debated from the onset of the earliest evolutionary histories and tectonic frameworks. This investigation provides the first multi-deposit approach to supplement the knowledge and broader literature on the development of the region.

TABLE OF CONTENTS

LIST OF FIGURES

LIST OF TABLES

LIST OF EQUATIONS

ACKNOWLEDGEMENTS

First and foremost I would like to extend my gratitude to both supervisors Dr Solomon Buckman and Prof. Allen Nutman. Thank you for your scientific and technical guidance, your feedback on my work throughout the year, your patience with regard to my constant door-knocking, and particularly the unwavering excitement for this project and the components herein. I acknowledge the financial support that was provided for this thesis, from my supervisors' personal research grants; without this the project would not have been able to reach its full analytical potential. I sincerely want to thank you both for entrusting me with a project where I was able to travel to China - an experience I will never forget, and an opportunity I am extremely grateful for.

To Prof. Yan Zhen from the Institute of Geology and Geophysics, Chinese Academy of Science (IGGCAS) I thank you for the invitation to complete these studies in China and the financial support you provided. My thanks extend to the team of professionals and support staff that accompanied us on our geological expedition of the Qinling Orogenic Belt, central China.

My thanks go to the academic and support staff of the School of Earth & Environmental Sciences for helping me build on and expand my geological knowledge beyond measure. Particularly, I would like to thank A/Prof. Brian Jones for your assistance with the XRD component of this thesis, but more so for the guidance and time you have spent explaining the dynamics and processes of geology throughout my studies. I would like to thank José Abrantes for your assistance in sample preparation and your technical guidance in the laboratory. To Marina McGlinn (Professional Officer), thank you for assisting with the organisation and formalities of the honours program, I am particularly grateful for you constantly popping your head around the corner and checking in on myself and my peers. To Dr Mitchell Nancarrow (Professional Officer and Microscopist) thank you for your ongoing assistance with the SEM-EDS component and post-processing of data.

To my fellow honours students, particularly Wanchese Saktura - thank you for your company throughout this year. Your curiosity will make you an excellent geologist; I wish you the very best with your future endeavours. To my friends and particularly my housemates, thank you for helping me keep things in perspective and tolerating the collection of rocks I have in the house.

To my family, particularly my mum, dad and brother I owe everything I am and have achieved to you. Your support for when I was stressed and unreasonable, your unwavering enthusiasm for the degree in geology that you inadvertently took by extension of phone calls, the study snacks you sent in the mail while I was on the home-run, and the love you have provided me with is something I simply cannot express.

CHAPTER ONE – INTRODUCTION

1.1 INTRODUCTION

Central China has experienced a complex tectonic history, involving multiple collisions between numerous micro-continents, arcs and ophiolites as well as intense periods of mantle-crustal metasomatism and enrichment often associated with important mineralisation events (Dong and Santosh 2015; Dong *et al.* 2015). The Qinling Orogenic Belt (QOB) represents a composite orogen that has witnessed multiple episodes of accretion and collision between discrete continental blocks, namely the North China Block and South China Block (NCB and SCB). These multiple orogenic events have resulted in abundant mineralisation of various styles which form the focus of this study. Tectonic evolution is intimately linked to mineralisation and it is the overarching aim of this project to define better and constrain the tectonometallogenic evolution of the QOB, which is host to several world-class mineral deposits, in particular Mo-(Cu ± Au) granite-hosted systems.

The four main tectonic units of the QOB from north to south are the Southern North China Block (S-NCB), North Qinling Belt (NQB), South Qinling Belt (SQB) and the Northern South China Block (N-SCB). Five deposits, representative of different mineralisation systems are investigated in this study; the Nantai Mo-(Cu) deposit, Miaoya REE deposit, Longtougou orogenic Au deposit, Liujiaxia orogenic Au deposit and Damogou Zn-CaF_2 deposit (Figure 1.3).

1.2 AIMS AND OBJECTIVES

The aim of this project is to describe and review various mineralisation styles within the Qinling Orogen and provide zircon U-Pb geochronology for a particular granite related Mo-(Cu) deposit in order to determine the tectonometallogenic evolution of a relatively undocumented region of central China.

The outcomes of this project will provide new geochronological, petrographic and geochemical knowledge on these different mineralisation systems, providing the first multi-deposit approach to supplement knowledge regarding the formation and deformation of the Qinling Orogenic Belt, central China; the genesis of which has been intensely debated from the onset of the earliest evolutionary histories and tectonic frameworks. This project is divided into four specific objectives:

a. Date zircons from the Nantai Mo-(Cu) aplite samples using sensitive high-resolution ion microprobe (SHRIMP) U-Pb geochronology, in order to constrain better the timing and nature of this igneous event and mineralisation of the system
b. Describe the mineralised and host rock samples for the different deposit types using a multi-analytical approach incorporating standard transmitted and reflected petrographic descriptions combined with X-ray diffraction (XRD), scanning electron microscopy coupled with energy-dispersive X-ray spectroscopy (SEM-EDS) and Raman spectroscopy
c. Undertake whole-rock geochemistry using X-ray fluorescence (XRF) and inductively coupled plasma mass spectrometry (ICP-MS) to clarify and constrain the geotectonic setting of plutonic rocks from the study areas. The prime focus will be on the Nantai Mo-(Cu) deposit, with less attention paid to the other deposits
d. To propose a regional tectonometallogenic model for the QOB using the geochronological, petrographic and geochemical data from the different mineral systems investigated

1.3 BACKGROUND

1.3.1 The Eastern Asian Continent

From the Archean to the Cenozoic the Eastern Asia continent has undergone an evolutionary history marked by both long and complicated tectonic processes involving several major continental collisions (Dong and Santosh 2015). It has been well substantiated that during the Palaeozoic a number of continental blocks, namely the North China Block (NCB), Tarim Block (TB), Qaidam Block (QB), South China Block (SCB), Qiangtang/Lasa Block (Q/LB), among other smaller continental fragments occurred in a detached and free state between the much larger Gondwana and Laurasia assemblies (Scotese 2004) (Figure 1.1). The tectonic framework and evolutionary history of the Asia continent and more specifically the Eastern Asia continent has been intensely debated in the broader literature over the past decades; however common consensus has allowed for the acceptance of three major orogenic belts, which when combined attribute to the Eastern Asia continent. The eventual collision and amalgamation of these once scattered continental fragments (i.e. the aforementioned NCB, TB, QB, SCB and QTB) throughout the Palaeozoic to Early – Middle Triassic led to the development and formation of the Central Asian Orogenic Belt (CAOB), the Central China Orogenic Belt (CCOB) and the Tethys Orogenic Belt (TOB) (Figure 1.2). The almost full geological record of the Eastern Asian continent makes for an important region of interest with regard to reconstruction models and furthering understanding of the evolutionary history between the Gondwana and Laurasia super continents. A five-stage geodynamic model has been used to describe the evolution of the Eastern Asian continent within a global context, accounting for development of the earliest continental nuclei to the intercontinental development of the region (Wang *et al.* 2005, Pirajno 2012):

1. Formation of continental nuclei during the Neoarchean (2.8 – 2.7 Ga)
2. Formation of proto-platforms during the Orosirian (1.9 – 1.8 Ga)
3. Platform formation during the Cryogenian (850 – 800 Ma)
4. Amalgamation of small continental blocks (i.e. NCB, TB, QB, SCB and QTB) during the Palaeozoic to Early – Middle Triassic 540 – 240 Ma) in the assembly of the CAOB, CCOB and TOB (together make the Eastern Asian continent)
5. Intercontinental development, inclusive of tectono-thermal events from the Triassic to present (240 Ma – present)

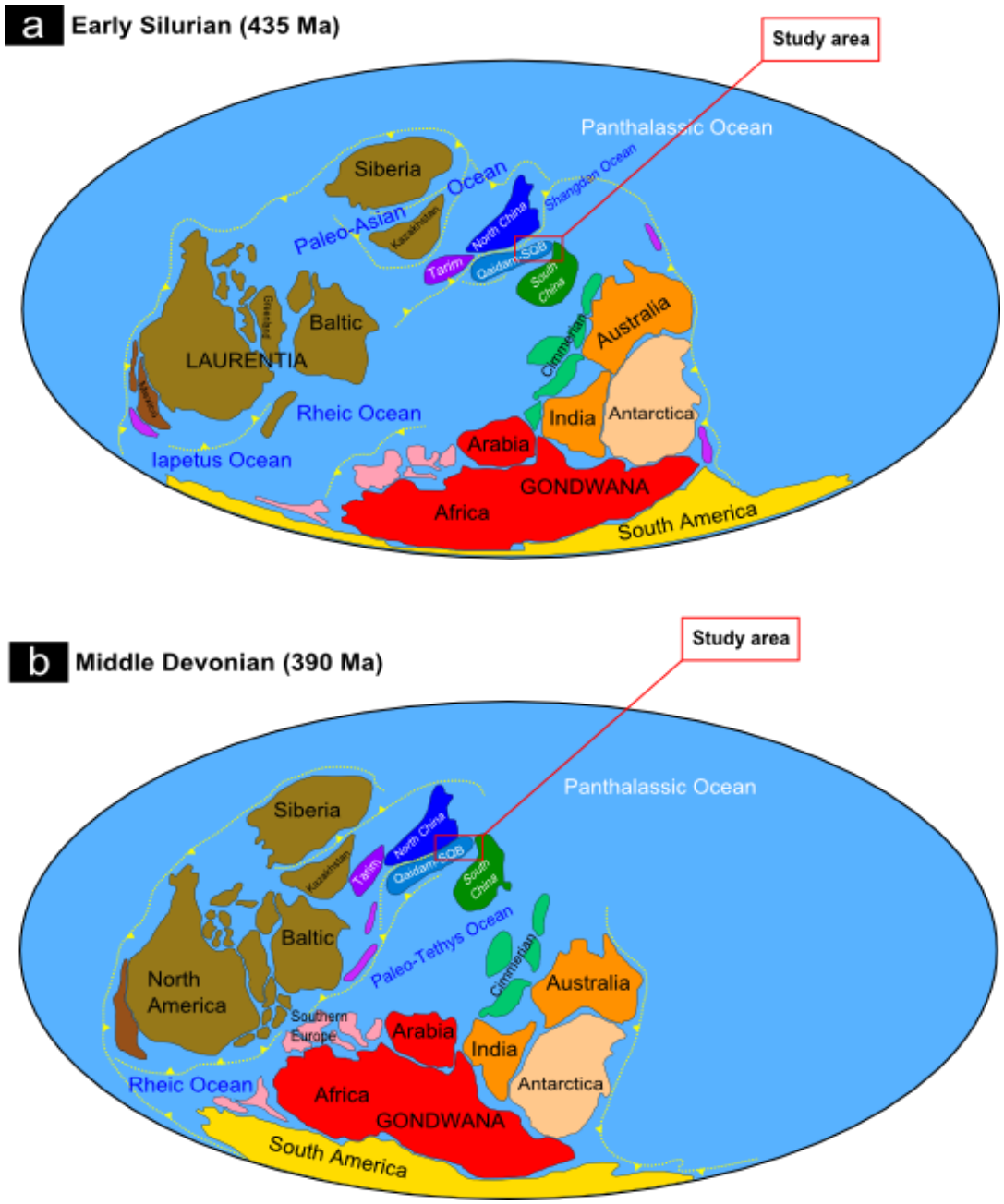

Figure 1.1 -Paleo-reconstruction model highlighting the location of the North China Block (NCB – dark blue), Qaidam/South Qinling Belt (Q/SQB – light blue) and South China Block (SCB – dark green) in Pangea during a) the Silurian (435 Ma) and b) Middle Devonian (390 Ma). The Shangdan Ocean is still apparent during the Silurian however, disappears during the Middle Devonian due to the convergence and amalgamation of the NCB with the Q/SQB. The Paleo-Tethys Ocean is apparent from the Middle Devonian. Adapted from Scotese (2004), Dong et al. (2013), Dong & Santosh (2015)

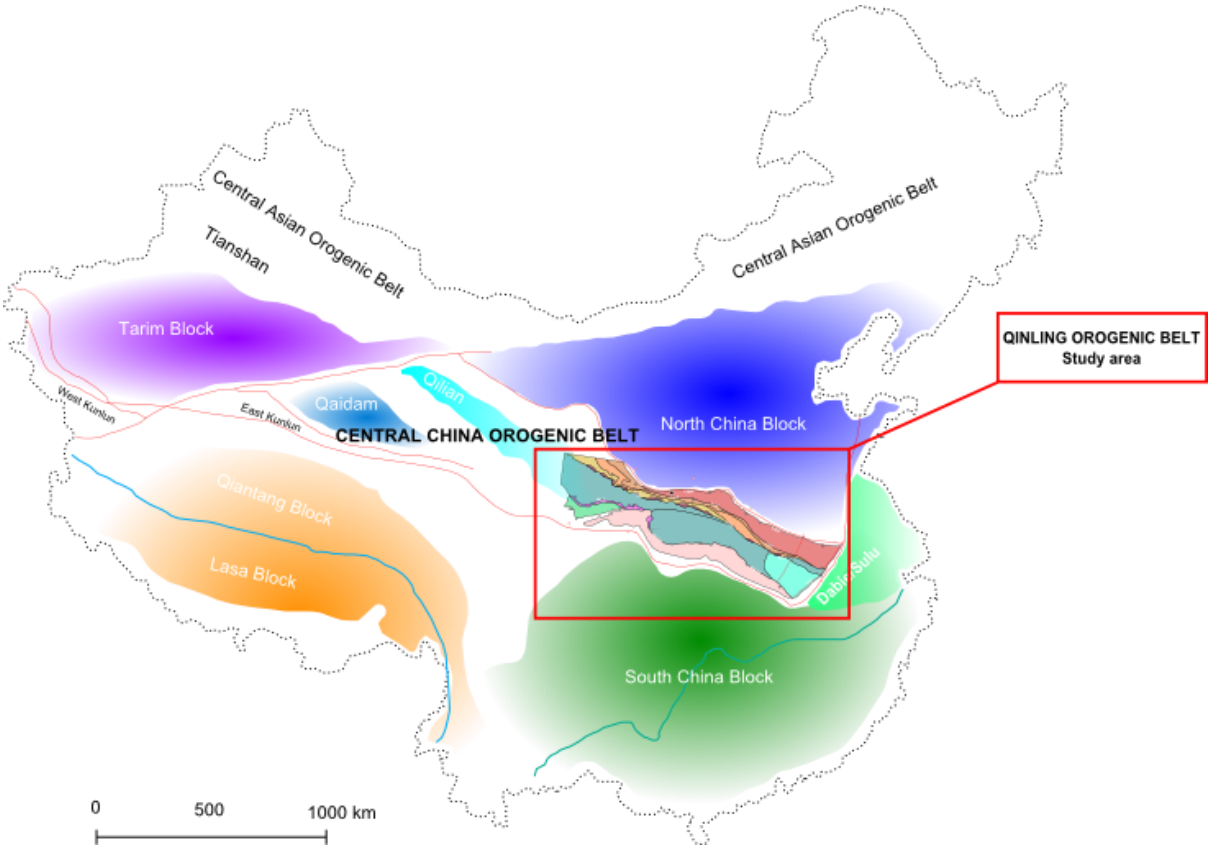

Figure 1.2- The Eastern Asia continent is a result of the collision and amalgamation of the Tarim Block (TB), the North China Block (NCB), the South China Block (SCB) and the Qiantang/Lasa Block (Q/LB). Significant to this investigation is the tectonic development of the Qinling Orogenic Belt, within the Central China Orogenic Belt (CCOB). Adapted from Dong et al. (2015)

1.3.2 The Qinling Orogenic Belt

The Central China Orogenic Belt (CCOB) is located in the central portion of the Eastern Asian continent, which consists of the Sulu, Dabie, Qinling, Qilian, Qaidam and Kunlun Orogenic belts from east to west. The significance of the CCOB is that it is representative of the collisional events between the northern blocks (North China Block and Tarim Block) and southern blocks (South China Block and Qiantang/Lasa Block). The east-west trending Qinling Orogenic Belt (QOB) links the Sulu and Dabie Orogenic Belts in the east with the Qilian and Kunlun Orogenic Belts in the west, extending for more than 1500 km across the Eastern Asian continent making it an extensive component of the CCOB. The QOB is bound in the north by the Lingbao-Lushan-Wuyang Fault (LLWF) and in the south by the Mianlue-Bashan-Xiangguang Fault (MBXF). Along both faults, the QOB was thrust outwards resulting in an extension of the orogeny onto the southern-

most periphery of the NCB and the northern-most periphery of the SCB, respectively. The LLWF formed as an intra-continental northward-thrust during the Early Cretaceous, whereas the MBXF formed as a south-directed overthurst during the Late Jurassic to Early Cretaceous, whereby the original Middle Triassic Mianlue Suture (MLS) was overlayed (Shi *et al.* 2013).

Sutures and boundary faults

Within the QOB there are three major sutures, which double as boundary defining faults. From north to south these are the Kuanping Suture (KPS), the Shangdan Suture (SDS) and the Mianlue Suture (MLS) (Figure 1.3).

Kuanping Suture (KPS)

The Kuanping Suture (KPS) occurs between the Luonan-Luanchuan fault and the Shangzhou-Nanzhao Fault (Dong *et al.* 2014). The suture consists predominantly of both clastic and carbonate rocks that have been metamorphosed and intensely deformed. Within these meta-sedimentary rocks dismembered ophiolitic remnants occur with associated volcanics (mafic and ultramafic) of which have been altered to greenschist and amphibolite facies. The assortment of meta-sedimentary rocks with randomly interspersed ophiolitic material has led to the exposure being described as a mélange that is predominantly thrust northward, along the Shangzhou-Nanzhao Fault (Dong *et al.* 2014, Dong and Santosh 2015). The dismembered ophiolite is representative of Mesoproterozoic oceanic crust from the long-lived Kuanping Ocean. This ocean boarded the S-NCB before southward subduction led to the amalgamation of the NQB and the S-NCB. The Kuanping Ocean is believed to have existed between 1.45 – 0.95 Ga (Zhang *et al.* 1994a, Zhang and Zhang 1995, Diwu *et al.* 2010b, Dong *et al.* 2014).

Shangdan Suture (SDS)

The Shangdan Suture (SDS) occurs as a disrupted exposure of mélange that extends across the QOB, and is an important component representing the major zone dividing the NCB and SCB; the exposed suture is representative of a pre-Devonian ocean between the two major blocks (Dong *et al.* 2011b). The tectonic mélange consists of volcanic and sedimentary derived rocks (530 – 470 Ma) intermixed with ophiolitic material (Sun *et al.* 1996, Zhang *et al.* 2001, Dong *et al.* 2011b). The exposure of oceanic crust with the other assemblies was known in the early literature as the Danfeng Group (Zhang *et al.* 1994b, Zhang *et al.* 1995). The Shangdan Suture zone is described as a 'tectonic' mélange because it underwent multiple episodes of thrusting, shearing and faulting during the Paleozoic, Triassic and Cretaceous, respectively (Dong *et al.* 2011a).

Mianlue Suture (MLS)

The Mianlue Suture (MLS) consists of a complicated ophiolitic complex, common to all three of the main suture zones within the QOB. Along with highly dismembered ophiolite the Mianlue Suture also contains metamorphic rocks (having been the result of high pressure and temperature regimes), arc-related volcanics and sediments (Dong *et al.* 1999, Dong *et al.* 2004, Lai 2004). The units within the complex are said to be Paleozoic to Middle Triassic in age and proposed to represent the remains of the Paleo-Tethyan Ocean on the amalgamation of SQB (i.e. the original micro-continent) and the SCB (Dong *et al.* 2011b, Dong *et al.* 2014). Recent findings have identified Neoproterozoic ophiolite material in the eastern region of the Mianlue Suture, suggesting that sections within the complex may have undergone differing tectonic evolutionary histories. The eastern region of the Mianlue Suture could be representative of oceanic material being thrust onto the continental margin; this theory is consistent as subduction was occurring along the north-western margin of the SCB during the Neoproterozoic (Lin *et al.* 2013).

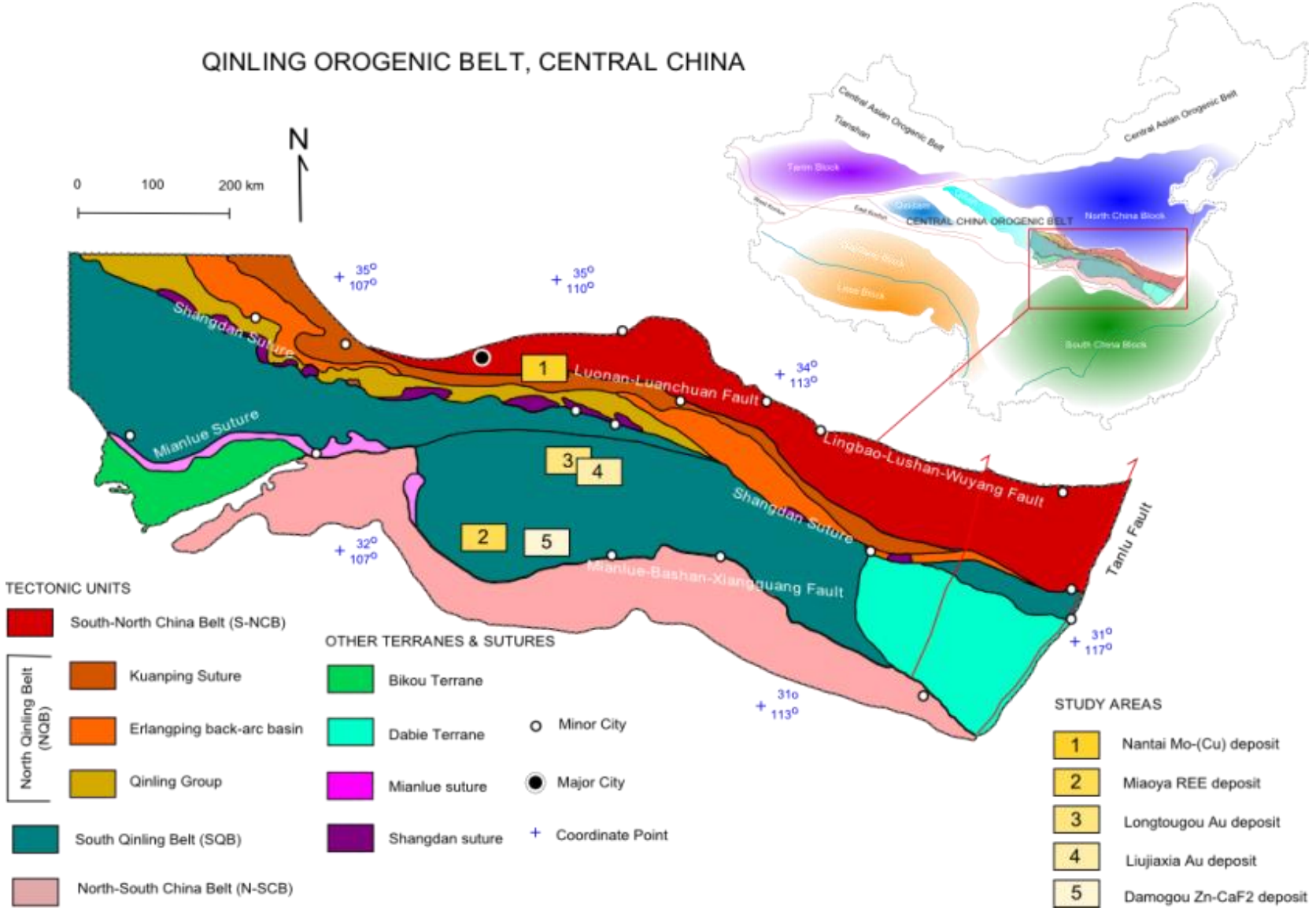
QINLING OROGENIC BELT, CENTRAL CHINA
N
0
100
200 km
35° 107°
35° 110°
34° 113°
32° 107°
31° 117°
31o 113°
Shangdan Suture
Mianlue Suture
Luonan-Luanchuan Fault
Lingbao-Lushan-Wuyang Fault
Shangdan Suture
Mianlue-Bashan-Xiangguang Fault
Tanlu Fault
1
2
3
4
5
Central Asian Orogenic Belt
Tianshan
Tarim Block
North China Block
CENTRAL CHINA OROGENIC BELT
South China Block
TECTONIC UNITS
South-North China Belt (S-NCB)
North Qinling Belt (NQB)
Kuanping Suture
Erlangping back-arc basin
Qinling Group
South Qinling Belt (SQB)
North-South China Belt (N-SCB)
OTHER TERRANES & SUTURES
Bikou Terrane
Dabie Terrane
Mianlue suture
Shangdan suture
Minor City
Major City
Coordinate Point
STUDY AREAS
1 Nantai Mo-(Cu) deposit
2 Miaoya REE deposit
3 Longtougou Au deposit
4 Liujiaxia Au deposit
5 Damogou Zn-CaF2 deposit

Figure 1.3 - (previous page) Simplified tectonic map of the QOB, central China exemplifying the division of tectonic units, the occurrence of terranes and the location of sutures within the orogen. Inset map in the upper right corner demonstrates the location of the QOB (an extensive component of the CCOB) within the larger context of the Eastern Asia Continent. The study areas, i.e. Nantai Mo-(Cu) deposit, Miaoya REE deposit, Longtougou Au deposit, Liujiaxia Au deposit and Damogou Zn-CaF_2, are represented by yellow numbered squares. Adapted from Dong and Santosh (2015), Dong et al. (2015)

Tectonic belts

The QOB can be divided into four tectonic belts separated by three major sutures; these are the Southern North China Block (S-NCB), North Qinling Belt (NQB), South Qinling Belt (SQB) and the Northern South China Block (N-SCB) from north to south. These four tectonic units are separated by major faults and differentiated as separate terranes due to their contrasting geological histories as recorded by the age and composition of sedimentary, igneous and metamorphic lithologies.

Southern North China Block (S-NCB)

The Southern North China Block (S-NCB) is the northernmost region of the QOB, and is located between the previously mentioned Lingbao-Lushan-Wuyang Fault in the north and the Luonan-Luanchuan Fault in the south. The basement of this unit (Figure 1.4) consists of Archean to Paleoproterozoic rocks that are highly deformed and have experienced amphibolite facies metamorphism (Zhang *et al.* 2000, Diwu *et al.* 2010a). The basement complex is overlain by Mesoproterozoic rift-related volcanics of lower greenschist facies metamorphic grade (Zhang *et al.* 2001, He *et al.* 2009, Tang *et al.* 2015). The volcanics are unconformably overlain by marine-derived sedimentary sequences, consisting of clastic and carbonate rocks that are Mesoproterozoic to Mesozoic in age (Zhang and Zhang 1995, Zhang *et al.* 2001). The S-NCB collided and amalgamated with the NCB during the closure of ocean basins separating several juvenile island arc systems that evolved between the converging North and South China Blocks. After collision, Mesozoic-Cenozoic deformation events saw the units thrust northward, away from the NQB toward the main continental body of the NCB. The region was also intruded by multiple and voluminous granitoid plutons during the Triassic – Cretaceous (Dong and Santosh 2015, Tang *et al.* 2015).

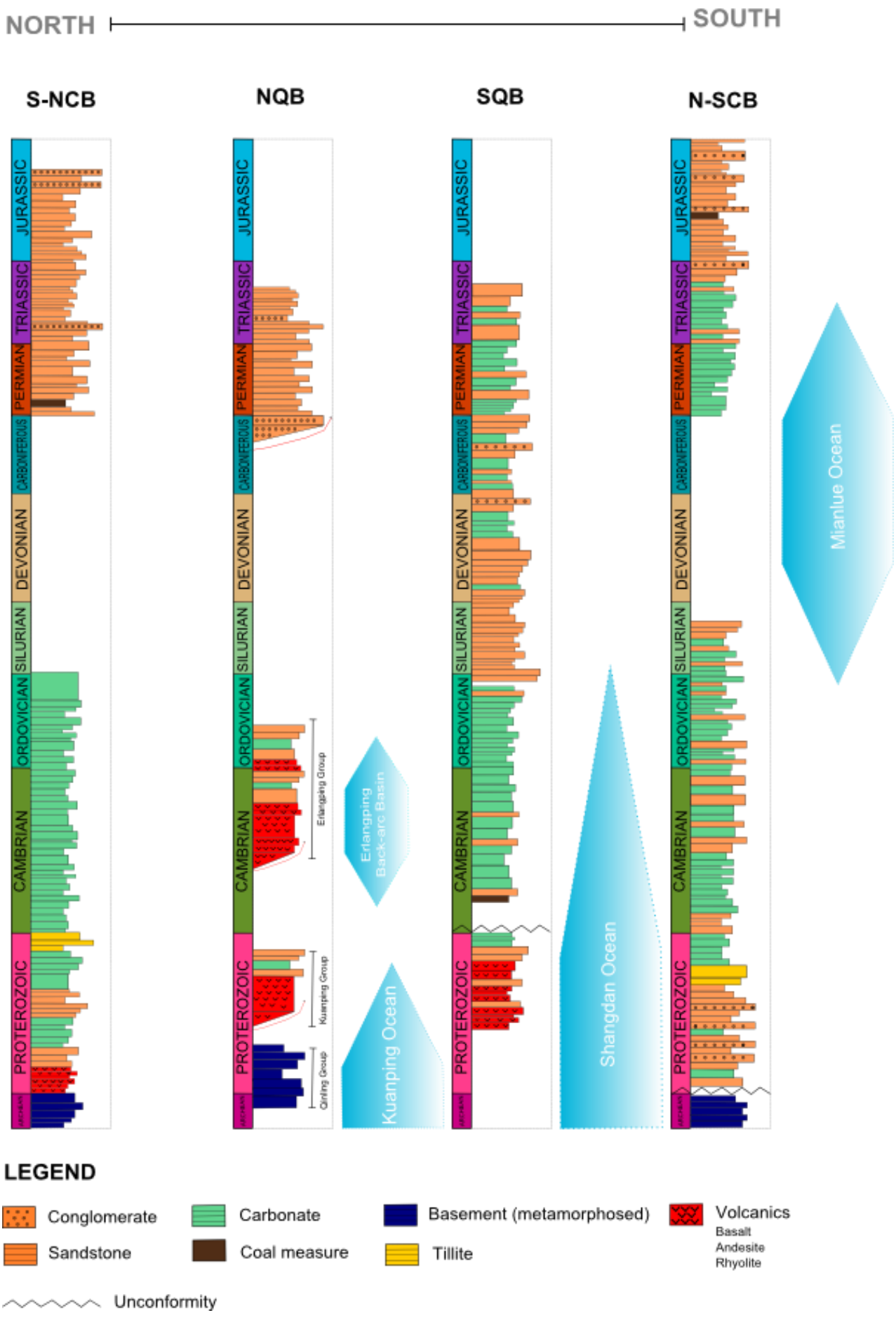
NORTH
SOUTH
S-NCB
NQB
SQB
N-SCB
JURASSIC
TRIASSIC
PERMIAN
CARBONIFEROUS
DEVONIAN
SILURIAN
ORDOVICIAN
CAMBRIAN
PROTEROZOIC
ARCHEAN
Erlangping Group
Kuanping Group
Qinling Group
Erlangping Back-arc Basin
Kuanping Ocean
Shangdan Ocean
Mianlue Ocean
LEGEND
Conglomerate
Sandstone
Carbonate
Coal measure
Basement (metamorphosed)
Tillite
Volcanics
Basalt
Andesite
Rhyolite
Unconformity

Figure 1.4 - (previous page) Stratigraphic columns of the tectonic units of the QOB, from north to south these are the Southern North China Block (S-NCB), North Qinling Belt (NQB), South Qinling Belt (SQB) and Northern South China Block (N-SCB). Also included are the oceans or basins associated with the tectonic units, compared to geological time. No vertical scale. Adapted from Dong and Santosh (2015), Dong *et al.* (2015)

North Qinling Belt (NQB)

The North Qinling Belt (NQB) is located between the S-NCB in the north, bound by the Luonan-Luanchuan Fault and the SQB in the south, bound by the Shangdan Suture. Ongoing controversy surrounding the units and their division within the NQB exists (Dong *et al.* 2014, Dong and Santosh 2015, Tang *et al.* 2015, Zhang *et al.* 2015); for this investigation the division of the belt has been made into three units. From the north to the south these are the aforementioned Kuanping Suture (commonly described as the Kuanping Group), the Erlangping back-arc basin (of which is commonly described as the Erlangping Group) and the Qinling Group. The Kuanping Suture is omitted from this description as it already features in the above section describing 'sutures and boundary faults'. Refer to Figure 1.3 for further illustration. Tectonic descriptions of the units within the NQB have been maintained rather than being assigned groups (i.e. Kuanping and Erlangping Groups) to assist in further clarifying the tectonic evolution of the broader orogenic belt (i.e. QOB).

The Erlangping back-arc basin, located between the Kuanping Suture in the north and the Qinling Group in the south, largely consisting of an ophiolitic mélange unit of early Paleozoic age that has undergone greenschist and amphibolite facies metamorphism. The next lithostratigraphic unit is predominantly clastic sedimentary sequences of middle Paleozoic age. It is proposed that the Erlangping back-arc basin is representative of the remnants of northward subduction along the Shangdan Suture during the Paleozoic (Yang *et al.* 2015).

The Qinling Group, located between the Erlangping back-arc basin in the north and the Shangdan Suture zone in the south, largely consists of a Precambrian basement that has undergone large degrees of deformation and amphibolite to granulite facies metamorphic conditions (Zhang *et al.* 2015).

An important feature throughout the broader NQB is the two-stage granitoid intrusive event; whereby Neoproterozoic granitoids intruded into the basement of the Qinling Group, followed by later stage Cretaceous granitoids, which intruded broadly into the basement units and the ophiolitic mélange of both the Kuanping Suture zone and the Erlangping back-arc basin. The last widespread granite intrusive event in the Cretaceous was followed by widespread erosion and deposition of clastic sequences (Dong *et al.* 2014, Tang *et al.* 2015).

South Qinling Belt (SQB)

The South Qinling Belt (SQB) is located between the NQB in the north bound by the Mianlue-Xiaomoling-Douling-subduction zone, which transitions into the Shangdan Suture, and the S-NCB in the south bound by the Mianlue-Bashan-Xiangguang Fault (Zhang *et al.* 2001, Dong *et al.* 2013). The geological assemblage of the SQB is characterised by multiple Precambrian units, beginning with the Neoarchean basement complex, which transitions into overlying units composed mainly of Mesoproterozoic to Neoproterozoic volcaniclastic sequences that are thought to represent a rift-related assemblage (Zhang *et al.* 1995). These rocks underwent greenschist facies metamorphism during the Paleozoic. Thick sequences of early Paleozoic to early Mesozoic carbonate and clastic sequences unconformably overlie the volcaniclastic untis (Dong *et al.* 2013). The western region of the SQB was intruded by voluminous granitoid plutons during the Triassic. In contrast, the eastern region of the SQB is largely devoid of Triassic granites, but does host swarms of Neoproterozoic mafic dykes. The sequences within the SQB are commonly described as ‘thin-skinned’ structures, with the block largely representing what was once an imbricated thrust-fold system, dominated by southward vergence of the emplaced units (Wang *et al.* 2013).

Northern South China Block (N-SCB)

The Northern South China Block (N-SCB) is the southernmost region of the QOB. It is situated south of the previously mentioned Mianlue-Xiaomoling-Douling-subduction zone (which largely overprints the Mianlue Suture), which separates it from the SQB to the north before transitioning into the main continental body of the SCB (Dong *et al.* 2012, Dong *et al.* 2014). The SCB is sub-divided into major cratonic components, including the Yangtze and the Cathaysia Blocks (Xiaoyong *et al.* 2015). With regard to

the geological assemblage of the N-SCB, the region consists of strongly metamorphosed pre-Ediacarian basement overlain by Neoproterozoic to Mesozoic sedimentary cover sequences of which are largely non-metamorphosed (Dong *et al.* 2008, Dong *et al.* 2012). The main continental body of the SCB demonstrates a similar assemblage, as would be expected from a genetically related terrane and consists of a crystalline basement that has undergone extensive deformation and metamorphism (Dong and Santosh 2015). This Neoarchean-Neoproterozoic basement is exposed at the surface, and presents itself in the western portion of the QOB known as the Bikou terrane. The basement grades into what has been deemed a 'transitional basement', dominated by green-schist facies metamorphism. Overlaying the basement and transitional basement units are unconformable sedimentary sequences, including Neoproterozoic clastic and carbonate units, limestone of Cambrian to Ordovician age and a conformably overlying sequence associated with marine deposition in the Mianlue Ocean. Permian-Triassic limestone continued to be deposited following the closure of the Mianlue Ocean (Dong *et al.* 2014). Widespread and rapid deposition of terrestrial conglomerates is associated with the development of a large foreland fold and thrust belt during the Triassic (Dong and Santosh 2015).

1.4 LOCATION

Rock samples were collected during April 2015 during a reconnaissance field trip in the Qinling Orogen at the invitation of Prof. Yan Zhen at the Institute of Geology and Geophysics, Chinese Academy of Science (IGGCAS).The locations of the deposits studied are as follows:

1. Nantai Mo-(Cu) deposit: 33°27'42" N, 109°58'54" E
2. Miaoya REE deposit: 32°49'48" N, 109°53'37" E
3. Longtougou orogenic Au deposit: 33°27'42" N, 109°58'54" E
4. Liujiaxia orogenic Au deposit: 33°25'39" N, 109°65'24" E
5. Damogou Zn-CaF_2 deposit: 32°14'51" N, 109°30'17" E

Figure 1.5 - (next page) Detailed geological maps of the study areas (deposits 1 – 5) with reference to the simplified tectonic map of the QOB. The detailed geological maps are courtesy of the Institute of Geology and Geophysics, Chinese Academy of Science (IGGCAS). Refer to Appendix A for field notes on these deposits

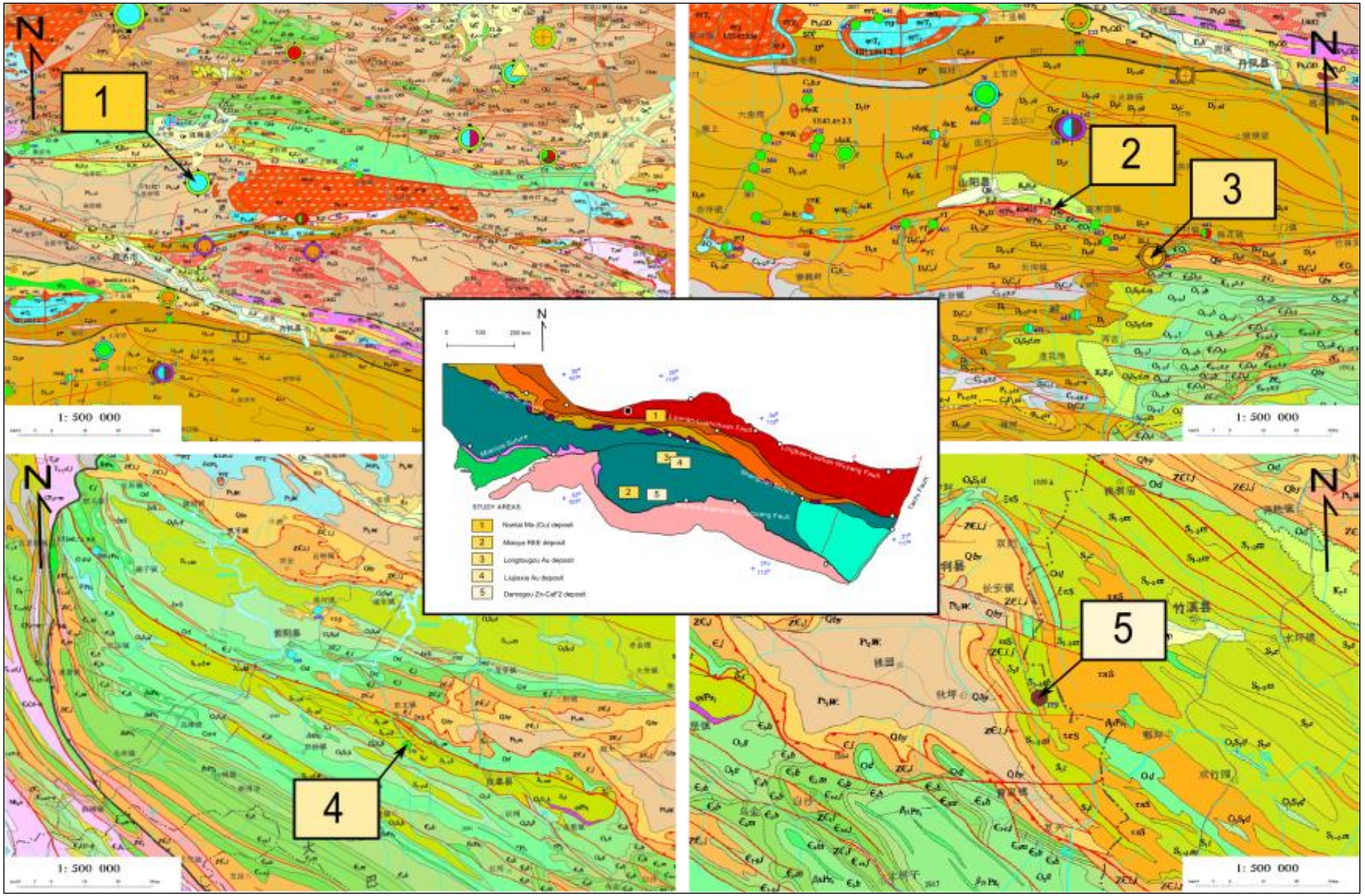
1
2
3
4
5
N
1: 500 000
STUDY AREAS
1 Nuanlai Mo (Cu) deposit
2 Maoya REE deposit
3 Longtougou Au deposit
4 Lujiaxia Au deposit
5 Damogou Zn-CaF2 deposit

CHAPTER TWO – MINERALISATION SYSTEMS

2.1 INTRODUCTION

This chapter outlines the various mineralisation styles within the Qinling Orogenic Belt (QOB) using specific examples to illustrate the diversity of mineralisation types within this orogenic system. The mineralisation classification system proposed by Downes *et al.* (2010) is used to broadly group deposits in the Qinling Orogen according to the dominant process responsible for their formation, that is, magmatic, magmatic-hydrothermal, hydrothermal, exhalative, sedimentary or surficial (Figure 2.1).

Magmatic mineralisation systems within the Qinling Orogen include important REE-bearing carbonatites and Mo-bearing granites. Magmatic hydrothermal mineralisation systems are divided into two sub-sections; i) incorporates those deposits that have a close spatial and temporal association with magmatic intrusions and, ii) incorporates mineral systems that do not necessarily have a close spatial and temporal association with magmatic intrusions, but were formed under the influence of important fluids carrying dissolved ore-forming minerals; these will be examined using porphyry-skarn systems and orogenic gold systems as examples, respectively. These will then be followed by examples within the QOB.

Figure 2.1 - (next page) Flow diagram demonstrating mineralisation systems based on dominant processes of formation. Adapted from Downes *et al.* (2010)

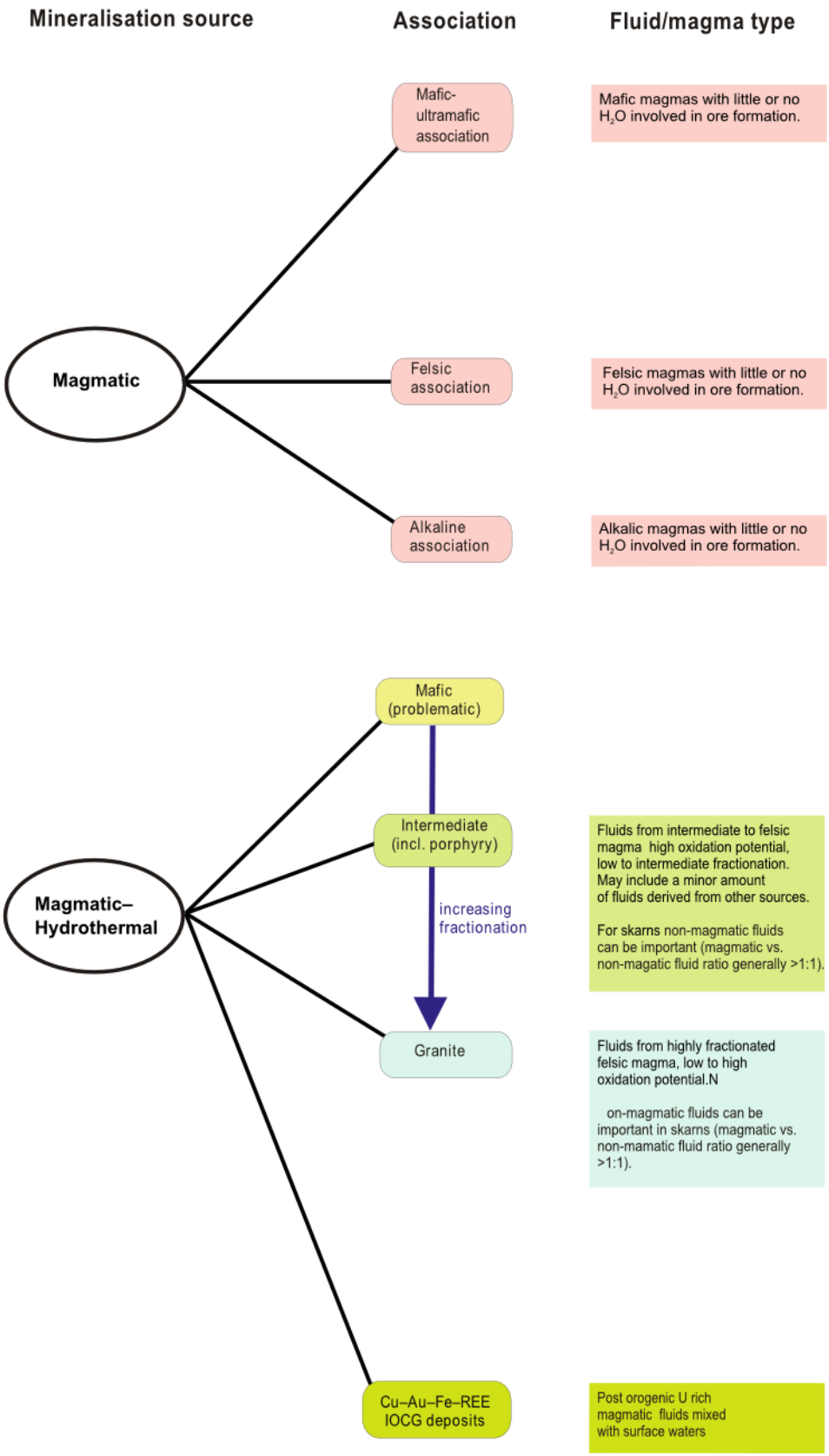
Mineralisation source
Association
Fluid/magma type
Magmatic
Mafic-ultramafic association
Mafic magmas with little or no H_2O involved in ore formation.
Felsic association
Felsic magmas with little or no H_2O involved in ore formation.
Alkaline association
Alkalic magmas with little or no H_2O involved in ore formation.
Magmatic–Hydrothermal
Mafic (problematic)
Intermediate (incl. porphyry)
increasing fractionation
Granite
Cu–Au–Fe–REE IOCG deposits
Fluids from intermediate to felsic magma high oxidation potential, low to intermediate fractionation. May include a minor amount of fluids derived from other sources.
For skarns non-magmatic fluids can be important (magmatic vs. non-magatic fluid ratio generally >1:1).
Fluids from highly fractionated felsic magma, low to high oxidation potential.N
on-magmatic fluids can be important in skarns (magmatic vs. non-mamatic fluid ratio generally >1:1).
Post orogenic U rich magmatic fluids mixed with surface waters

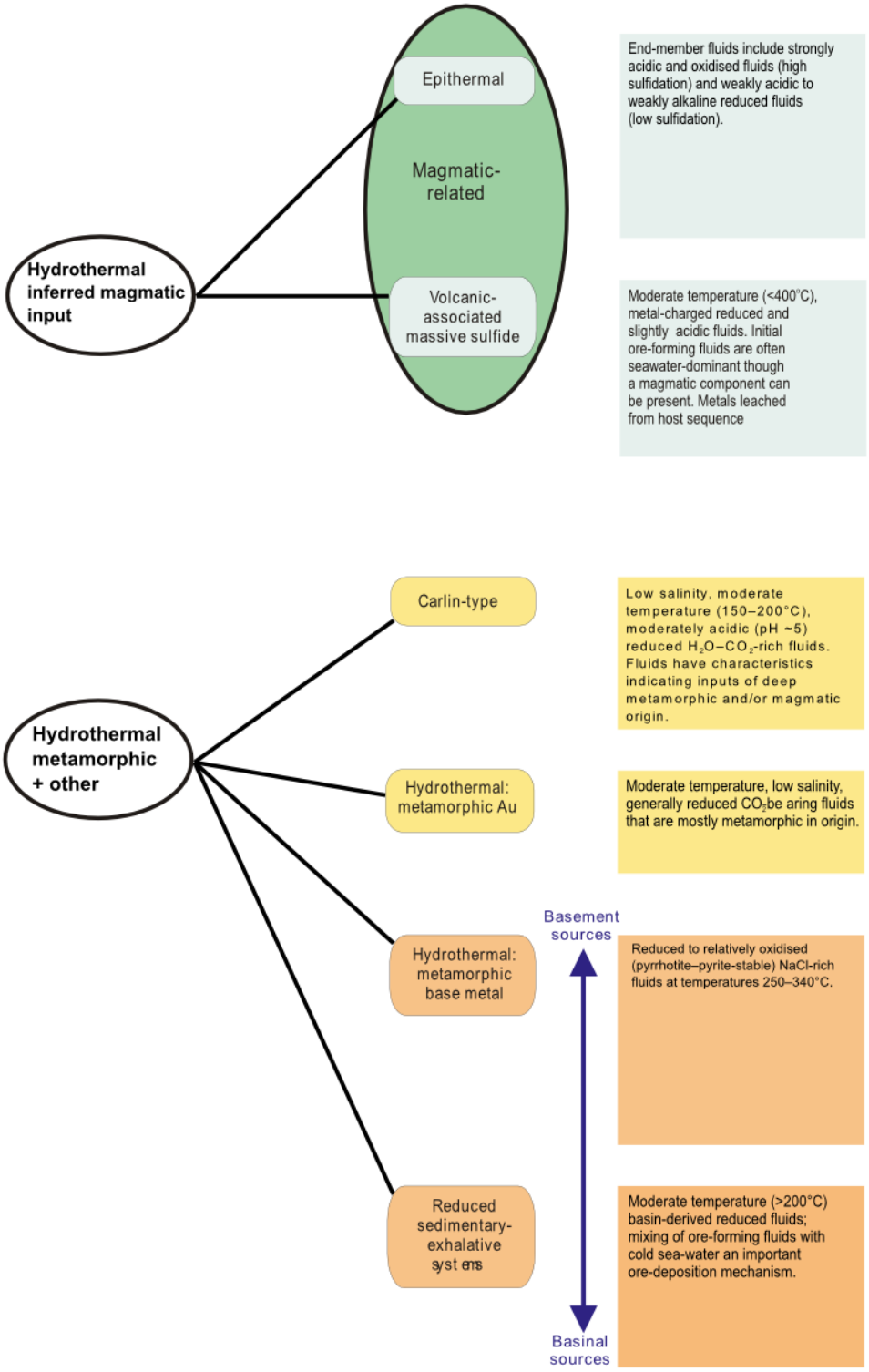
Hydrothermal inferred magmatic input
Epithermal
Magmatic-related
Volcanic-associated massive sulfide
End-member fluids include strongly acidic and oxidised fluids (high sulfidation) and weakly acidic to weakly alkaline reduced fluids (low sulfidation).
Moderate temperature (<400°C), metal-charged reduced and slightly acidic fluids. Initial ore-forming fluids are often seawater-dominant though a magmatic component can be present. Metals leached from host sequence
Hydrothermal metamorphic + other
Carlin-type
Hydrothermal: metamorphic Au
Hydrothermal: metamorphic base metal
Reduced sedimentary-exhalative systems
Low salinity, moderate temperature (150–200°C), moderately acidic (pH ~5) reduced $H_2O–CO_2$-rich fluids. Fluids have characteristics indicating inputs of deep metamorphic and/or magmatic origin.
Moderate temperature, low salinity, generally reduced CO_2-bearing fluids that are mostly metamorphic in origin.
Reduced to relatively oxidised (pyrrhotite–pyrite-stable) NaCl-rich fluids at temperatures 250–340°C.
Moderate temperature (>200°C) basin-derived reduced fluids; mixing of ore-forming fluids with cold sea-water an important ore-deposition mechanism.
Basement sources
Basinal sources

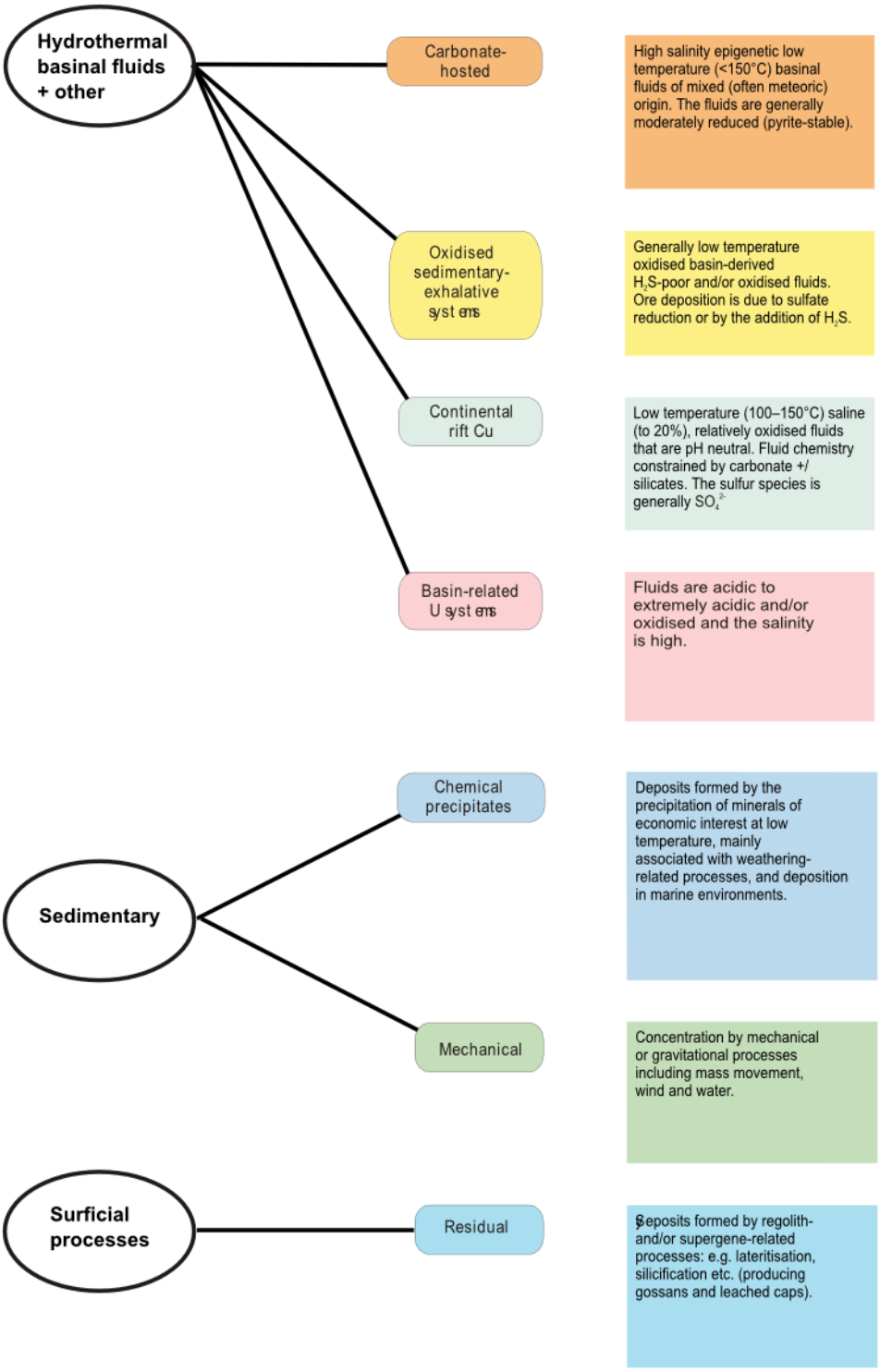
Hydrothermal basinal fluids + other
Carbonate-hosted
High salinity epigenetic low temperature (<150°C) basinal fluids of mixed (often meteoric) origin. The fluids are generally moderately reduced (pyrite-stable).
Oxidised sedimentary-exhalative systems
Generally low temperature oxidised basin-derived H_2S-poor and/or oxidised fluids. Ore deposition is due to sulfate reduction or by the addition of H_2S.
Continental rift Cu
Low temperature (100–150°C) saline (to 20%), relatively oxidised fluids that are pH neutral. Fluid chemistry constrained by carbonate +/ silicates. The sulfur species is generally SO_4^{2-}
Basin-related U systems
Fluids are acidic to extremely acidic and/or oxidised and the salinity is high.
Sedimentary
Chemical precipitates
Deposits formed by the precipitation of minerals of economic interest at low temperature, mainly associated with weathering-related processes, and deposition in marine environments.
Mechanical
Concentration by mechanical or gravitational processes including mass movement, wind and water.
Surficial processes
Residual
Deposits formed by regolith- and/or supergene-related processes: e.g. lateritisation, silicification etc. (producing gossans and leached caps).

2.2 MAGMATIC MINERALISATION SYSTEMS

Orthomagmatic mineral systems are those that include an unusually high accumulation of elements occurring either along their contacts or within igneous rocks themselves. These types of mineral systems are both genetically and intrinsically related to the melt itself, and particularly the subsequent cooling and crystallisation of the magma. Mineralisation systems formed on the basis of aqueous fluids interacting with the melt as it solidifies are known as hydrothermal systems, and although they are invariably related to a magmatic source, will be complied in Section 2.3. Mineralisation in magmatic systems is a result of precipitation of largely chalcophile and siderophile elements that have been transported in a melt phase, or otherwise have subsequently crystallised from a melt (Ridley 2013). The five processes accounting for magmatic mineral systems are:

1. Concentration of ore elements as a result of low degrees of partial melting
2. Accumulation and concentration of ore minerals in magma chambers during progressive crystallisation of magmas
3. Separation of two immiscible melts in a magma
4. Extreme fractionation during progressive crystallisation of a magma
5. Incorporation of a mineral that occurs at a specific depth in the Earth

The first four processes can be related to the sequence of steps of magma evolution from melting in the mantle to final crystallisation in the crust, as shown in Figure 2.2.

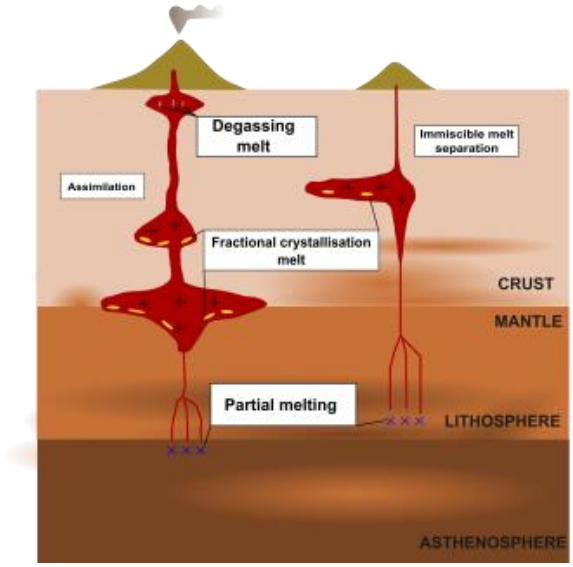

Figure 2.2 - Sites and mechanisms for the compositional evolution of magmas and the development of magmatic chemical variability within a schematic of magmatic systems extending from mantle lithosphere or asthenosphere into the upper crust. No scale. Adapted from Ridley (2013)

2.2.1 Magmatic geochemistry

A magmatic melt is dynamic, and intrinsically heterogeneous in its development and journey to solidification and crystallisation (Marsh 2006). Heterogeneity defines a magma based on the melt typically incorporating more than one phase; with phase being described as matter is a specific form, i.e. melt, crystal or gas (Ridley 2013). Throughout the evolutionary history of a melt geochemical interactions are taking place between phases, which may include multiple melts (e.g. silica-rich and carbonate-rich melts), multiple mineral phases, and even multiple gas phases due to fractionation and degassing. The distribution or partitioning of trace elements within a melt between coexisting phases, such as minerals, metals and liquids is vital for understanding the distribution of compatible and incompatible trace elements; the bearing for which has important applications for the mineralisation of magmatic systems. Assuming the trace elements are being distributed in accordance with the least amount of chemical energy required, the partitioning of these between phases can be illustrated using the Nest partition coefficients (K_i; Equation 2.1); whereby the weight fraction of a trace element c in phase a is compared to the weight fraction of a trace element in phase b to determine the ratio* of equilibrium that the trace element in question can coexist between two different phases (Aoki *et al.* 2000, Blundy and Wood 2003). NB: it is convention to use 'a' to illustrate a mineral, and 'b' to illustrate a melt. Equation 2.1 describes the coexistence of two phases; however with regard to the geochemical evolution of magmatic environments there are commonly more phases than two. Therefore the evolution of a magmatic system is better illustrated using Equation 2.2, which accounts for multiple minerals within a melt; where f^x is the weight fraction of each mineral x in the system, used to define a bulk solid vs. liquid partition coefficient for element i.

$$K_i^{a/b} = \frac{c_i^a}{c_i^b} \qquad \text{Equation 2.1}$$

$$D_i = \sum_{1 \to x} f^x K_i^x \qquad \text{Equation 2.2}$$

*The ratios of trace elements are often superior to the concentration of a single trace element, in the identification of a specific mineral

Integral to the partitioning of elements between phases in a melt is the distinction between compatible and incompatible elements. With regard to mineral-melt phases (as opposed to two minerals or two melts) compatible ($K_i > 1$) and incompatible ($K_i < 1$) elements can be distinguished by their preferential partitioning into mineral (solid) or melt (liquid) phases, respectively. Compatible elements tend to be included in rock-forming minerals due to similar ionic charge, radius and bonding behaviour. Thus, incompatible elements tend to concentrate in the residual melt, as they do not readily substitute into rock-forming minerals based on differing/juxtaposing ionic charge, radius and bonding behaviour. Incompatible elements are typically classified as being either high-field strength elements (HFSE) or large-ion lithophile elements (LILE). It is important to note that during magma evolution the compatibility status of some elements may change under the prevailing conditions; for example an evolved felsic melt will contain different crystallising minerals, comparative to a mafic melt, hence different minerals will be available for trace elements to substitute into their crystal lattice (Gill 2010, Ridley 2013).

2.2.2 Carbonatites

Carbonatites are igneous rocks that are essentially composed of carbonate material. These rocks are known to contain the highest amount of REE enrichment above any other igneous rock, and as such are host to some of Earth's most unusual mineral species (Table 2.1). The IUGS (2015) adheres to a definition that a carbonatite body must contain >50 wt.% of primary carbonate minerals (Le Maitre 2002). However, this investigation favours the definition provided by Mitchell (2005), which recognises that at depth a homogenous carbonatite melt may crystallise resulting in a range of carbonate:silica ratios, and as such applies a *senso lato* definition of an igneous body containing >30 wt.% primary carbonate minerals (calcite, dolomite, siderite, ankerite, and rare nyerereite) (Gill 2010).

With regard to the petrogenesis of carbonatites it is possible that there could be multiple types of sources, ranging from deep-seated to upper crustal levels. Some authors are fixated with attributing the parent magma of carbonatites to having originated from a mantle source, having evolved exclusively from an alkali-rich carbonatite magma through either, or a combination of (Chakhmouradian and Zaitsev 2012):

1. Liquid immiscibility, whereby an original alkali-rich silicate magma rich in carbonate components exsolves into two liquid fractions; one silicate and the other carbonate
2. Advanced fractional crystallisation

The work provided by Lentz (1999) suggests that although there is merit in mantle-related models, there is also sufficient evidence to demonstrate that there is a third process attributing to the development of a carbonatitic magma, which sees partial melting of sedimentary carbonates, due to the thermal effects of large amounts of gabbroic magma. There is a possible 'continuum' between magmatic-hydrothermal skarn systems, and the development of *some* carbonatites (Figure 2.2). Skarn-related processes and mechanisms provide an ideal platform for generating crustal carbonate melt. For example Wyllie and Tuttle (1960) described in detail the $CaCO_3 – H_2O – CO_2$ system with regard to crystal-melt volatile phase relationships, which demonstrates that limestone melts at its eutectic within the $CaO – MgO – CO_2 – H_2O$ system, between 600 – 675 °C on the interaction with fluid compositions of $CO_2/(H_2O + CO_2) = 0.05$, or 5% (Figure 2.4). These conditions mimic those found within magmatic-hydrothermal skarn-forming systems, which see the intrusion of alkalic magma into sedimentary carbonates (for example limestone adhering to consistency with the aforementioned $CaO – MgO – CO_2 – H_2O$ system). Essential to carbonate melting, obviously along with thermal effects and pressure, is the infiltration and interaction with a H_2O-rich fluid; the process of decarbonisation with the development of a skarn system produces excess CO_2, providing key components of carbonic acid (H_2CO_3). The carbonic acid, combined with H_2O-rich fluid provides a likely environment for the partial melting of sedimentary carbonates under contact metamorphic regimes (Figure 2.3). Carbonatites being mantle derived has also been based on their stable and radiogenic isotope signatures, which are not similar to those of sedimentary carbonates (e.g. limestone). However, in an intrusion-related skarn setting, the isotopic signatures of the resultant carbonatitic melt may reflect that of the silicate magma – if this alkalic melt is mantle derived then the isotopic signatures of this intrusive may dominate or overprint the original sedimentary carbonate signatures through fluid-exchange mechanisms (Lentz 1999).

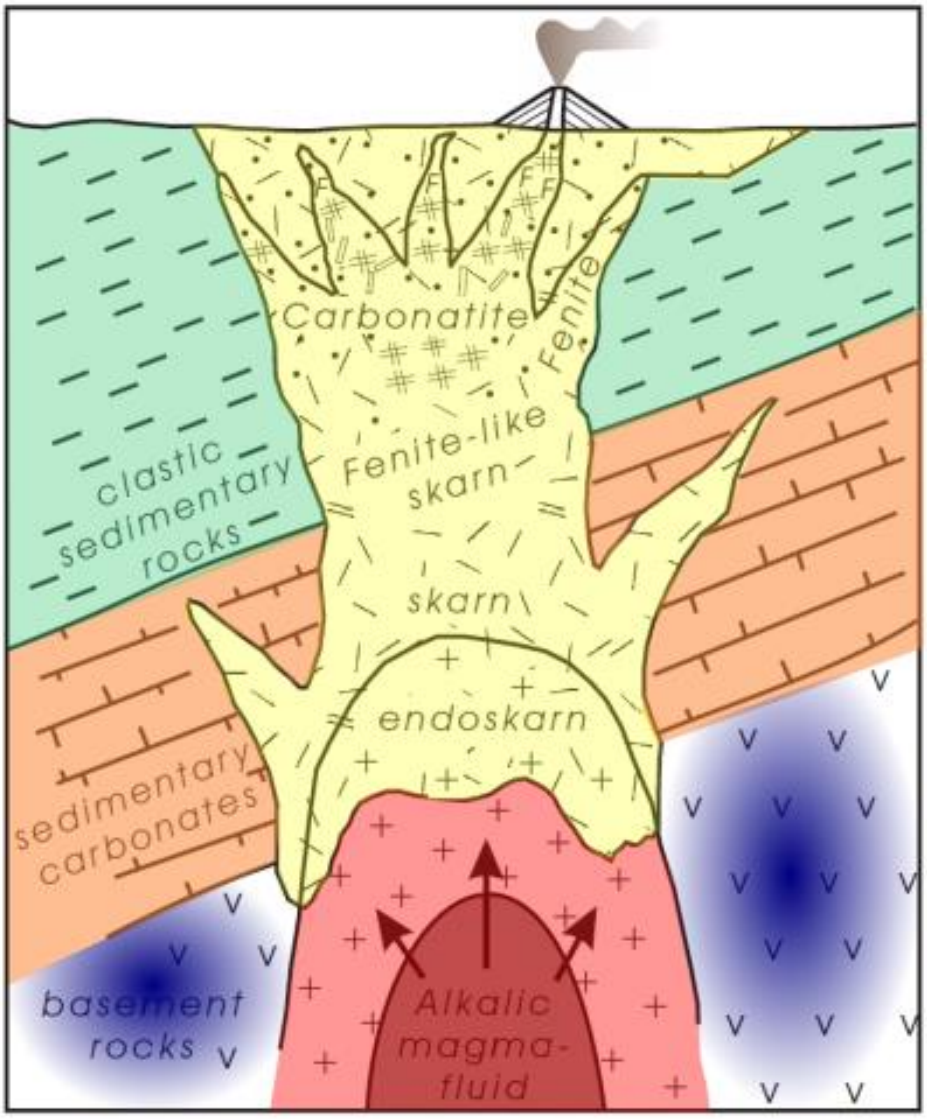

Figure 2.3 - This figure illustrates the processes involved in upper crust carbonatitc magma development through the partial melting of sedimentary carbonates, within the wider context of a skarn system. No scale; # = carbonate, // = apatite, F = fluorite. No scale. Adapted from Lentz (1999)

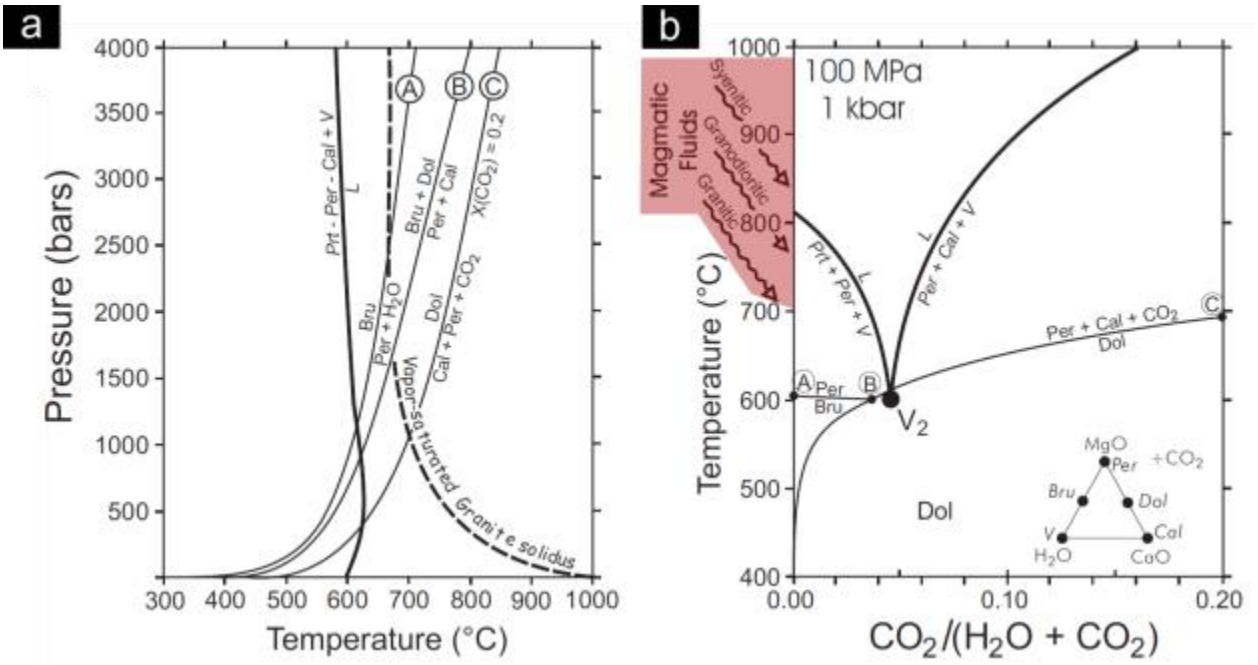

Figure 2.4 - Diagrams a) and b) demonstrate that a carbonatitic melt may be produced by the relationship between silicate-magmatic fluids (generated through contact metamorphism) and their influence on sedimentary carbonate rocks (under relevant temperature and pressure conditions, and additional solute components). Adapted from Lentz (1999)

Most carbonatitic complexes occur in interpolate settings within cratons, however there are important occurrences of carbonatitic complexes in continental rift settings (e.g. Lang-Bayan Obo rift, which is host of the world's largest REE deposit, Yang *et al.* 2011), and important to this investigation in continental collision zones (e.g. North China Block and South China Block collisional zone, i.e. QOB) (Xie *et al.* 2015). These unique magmatic rocks occur in only a small number of localities, with Ridley (2013) noting 500 carbonatite intrusions, and only 50 extrusive carbonatitic complexes. As previously mentioned, carbonatitic complexes are host to the majority of the world's REE supply, these sites of mineralisation are also important produces of Nb, P, Cu and flurorite; examples include Mountain Pass REE deposit, USA; Phalaborwa copper deposit, South Africa; Amba Dongar fluorite deposit, India; Bayan Obo REE deposit, China; Mianning-Dechang REE belt, China; Huanlongpu REE deposit, QOB, China; Huanyangchuan REE deposit, QOB, China; (Kynicky *et al.* 2012) and Miaoya REE deposit, QOB, China (this study).

China holds a monopoly on the world supply of REE's and currently accounts for >90 % of global production having been estimated to host >50 % of global reserves (Kynicky *et al.* 2012). Rare-earth elements and the minerals they are associated with have been described as 'political minerals' with the Chinese government flooding the market attempting to push other countries out; while also placing restrictions on making REE's available to the global sector. As such, the demand for some of the REE's are expected to exceed current supply. Volatility in this market has led to other REE-hosting countries (e.g. USA and Canada) attempting to create supply chains outside of China (Hatch 2012).

The QOB is host to some of China's most productive REE deposits, for example Huanglongpu Pb–Mo–REE deposit (Xu *et al.* 2010b), Huayangchuan Pb–Th–REE deposit (Mao *et al.* 2003), and Miaoya REE deposit (the third largest in China; this study). The Miaoya REE deposit, located in the South Qinling Belt (SQB) consists majorly as REE-bearing carbonatite intruding into associated syenites as stocks and dykes. Li (1980) was the first to produce geochronological constraints on the carbonatites producing a biotite K-Ar age of 278 Ma, followed by Xu *et al.* (2014) producing a monazite U-Th-Pb age of 234 Ma. Ages have also been produced for the synenite host unit; Xu *et al.* (2014) produced a zircon U-Pb age of 766 Ma. A significantly younger age for the syenites (147 Ma; zircon U-Pb) was produced by Xu *et al.* (2015) – in the same study these younger magmatic zircon grains are attributed to late-stage magmatism and/or fluid infiltration. The older Neoproterozoic zircon grains could in actuality be attributed to assimilation of the Precambrian units within the SQB (e.g. Mesoproterozoic to Neoproterozoic volcanic and clastic sequences), into the ascending syenitic melt. Xu *et al*. (2015) dismiss this hypothesis and conclude that the Miaoya carbonaties are not genetically related to the syenites; rather they were derived directly from a mantle source. Refer to Appendix A for field notes on this deposit.

Mineral name	Formula	Relevant REE	* Major deposit type	*Examples
Bastnäsite	$REECO_3(F,OH)$	53–79 wt.% ΣREO ≤2.8 wt.% ThO_2	CRB; HMD	Bastnäs, SW; Mountain Pass, USA; Maoniuping, Weishan, and Bayan Obo, CH; Karonge Gakara, Burundi
Parisite	$CaREE_2(CO_3)_3(F,OH)_2$	58–63 wt.% ΣREO ≤4.0 wt.% ThO_2	CRB; HMD	Mountain Pass, USA; Weishan and Bayan Obo, CH
Synchysite	$CaREE(CO_3)_2(F,OH)$	48–52 wt.% ΣREO ≤5.0 wt.% ThO_2	CRB; HMD associated with CRB and granites	Barra do Itapirapuã, BR; Lugiin Gol, MN; Kutessay, KR
Ba–REE fluorocarbonates	$Ba_xREE_y(CO_3)_{x+y}F_y$	22–40 wt.% ΣREO ≤0.7 wt.% ThO_2	HMD; CRB	Bayan Obo, CH
Monazite	(REE,Th,Ca,Sr)(P,Si,S)O_4 solid solution to cheralite (Ca,Th,REE)PO_4	38–71 wt.% ΣREO ≤27 wt.% ThO_2 ≤0.8 wt.% UO_2	CRB; HMD granitic pegmatites; Fe oxide–phosphate rocks; laterites; placers	Kangankunde, ML; Bayan Obo, CH; Steenkampskraal, SA; Mt. Weld, AU; Tomtor, RU; Tamil Nadu and Kerala, IN; Buena, BR; Nolans Bore and Eneabba, AU; Perak, MA
Xenotime	(REE,Zr)(P,Si)O_4	43–65 wt.% ΣREO ≤8.4 wt.% ThO_2 ≤5.8 wt.% UO_2	Granites and pegmatites; HMD associated with granites; laterites; placers; rarely CRB	Kutessay, KR; Pitinga, BR; Tomtor, RU; Mt. Weld, AU; Kinta and Selangor, MA Lofdal, Namibia
Fergusonite	$REENbO_4$	43–52 wt.% ΣREO ≤8.0 wt.% ThO_2 ≤2.4 wt.% UO_2	Granites and pegmatites; HMD associated with peralkaline rocks	Bayan Obo, CH; Nechalacho, CA
Loparite	(Na,REE,Ca)(Ti,Nb)O_3	28–38 wt.% ΣREO ≤1.6 wt.% ThO_2	Peralkaline feldspathoidal rocks	Lovozero, RU

Table 2.1 - Major rare-earth minerals. Adapted from Chakhmouradian and Wall (2012). *Abbreviations: CRB = carbonatites, HMD = hydrothermal-metasomatic deposits; AU = Australia, Br = Brazil, Ca = Canada, CH = China, IN = India, KR = Kyrgyzstan, MA = Malaysia, ML = Malawi, MN = Mongolia, RU = Russia, SA = South Africa, SW = Sweden; REO = rare-earth oxide(s)

2.3 HYDROTHERMAL MINERALISATION SYSTEMS

Hydrothermal mineral systems are those that include an unusually high accumulation of elements occurring from the transport and subsequent precipitation of important ore-forming minerals from a generally high temperature aqueous fluid. What follows is a description of; i) mineral systems that have a close spatial and temporal association with magmatic intrusions (i.e. porphyry-skarn systems), and ii) mineral systems that do not necessarily have a close spatial and temporal association with magmatic intrusions, but were formed under the influence of important fluids carrying dissolved ore-forming minerals (i.e. orogenic gold deposits). The five processes accounting for hydrothermal mineral systems are (Figure 2.5; Ridley 2013):

1. The source of the fluid and the compositional dependency and controls on said fluid
2. The source of the ore-forming minerals. It can be assumed that important elements for mineralisation are dissolved and accumulated along the path of which the fluid flows; it is also possible that there is a primary source with the majority of metals being dissolved at this site, rather than along the journey
3. The pathway for fluid migration. With regard porous rocks, fluid migration would be relative to the porosity and permeability within a unit. A crystalline rock, on the other hand would be more inclined to allow fluid migration as a function of discontinuities within the unit; for example faults and fractures are provisional to fluid migration lending to the idea of structural controls featuring in the genesis of mineral systems
4. The energy to drive fluid migration. This may be in the form of either thermal or mechanical energy
5. The chemical reaction series' necessary for mineral precipitation. The changing solubility as a function of changes in composition, temperature and pressure of the fluid

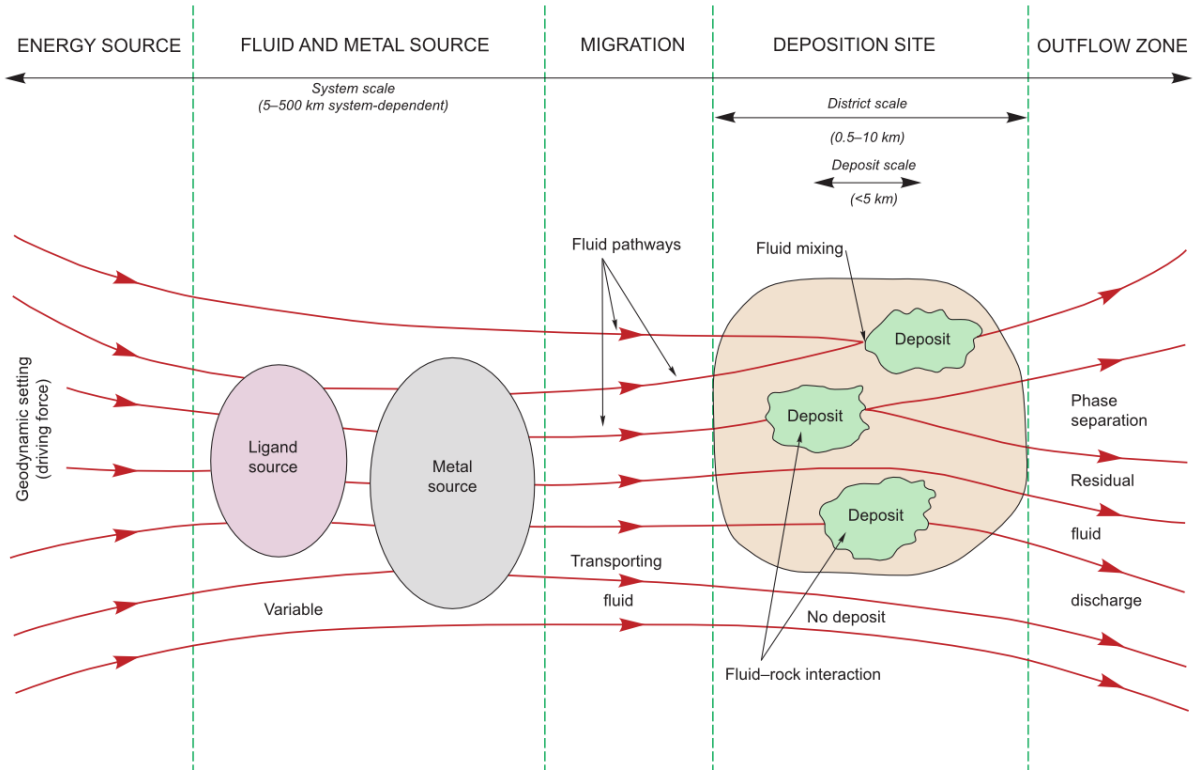

Figure 2.5 - Schematic of the potential components accounting for hydrothermal mineralisation of a system; dependant on an energy source, fluid and metal source, migration, deposition site and outflow zone. Adapted from Hagemann and Cassidy (2000)

2.3.1 Porphyry deposits

Porphyry systems are representative of large magmatic intrusions high within the crust that have undergone pervasive hydrothermal alteration resulting in high concentrations of Cu, Cu-(Au), Cu-(Mo), Mo-(Cu), Mo or Sn-Ag. The most important minerals occurring within these mineralised systems are Cu, Mo and Au, respectively. With regard to world production, porphyry deposits account for >95 % Mo and >65 % Cu, while also contributing significant amounts of Au (Ag and Re are produced as by-products). Sillitoe (2010) provides an extensive compilation of porphyry copper mineralised systems and their associated emplacement mechanisms, however this model cannot be adequately applied to a system dominated by molybendum over copper mineralisation. Molybdenum being an incompatible element in a crystallising granitic melt ($K_i < 1, where\ i = Mo$) behaves differently to its copper counterpart; on crystallisation within the system, molybdenum will preferentially reside in the melt, rather than in mineral phases. By extension, on low degrees of crystallisation prior to water saturation of the system the concentrations will not increase by significant proportions. With regard to

the genesis of molybdenum-dominated systems, it has been proposed that the original magma had an initially high water content (comparative to copper-dominate counterparts). As such these magmas, and by extension their associated porphyry systems occur at greater depths within the crust, opposed to low-hydrous melts that have a tendency to ascend higher in the crust (Robb 2007). As the melt begins to crystallise, copper will also begin to crystallise demonstrating compatibility with mineral over melt phases. The cooler marginal region of the precursor pluton is the first to begin crystallisation, which results in copper being extracted from the melt and is distributed around these margins. On saturation of the system from aqueous fluid interaction, the molybdenum is mobile within the melt and available to transition into the H_2O fluid phase due to its favourable partition coefficient. Copper is significantly depleted in the melt phase, and as such will not be significantly concentrated, whereas the molybdenum continues towards higher concentrations and enrichment due to its higher compatible nature – and by extension majorly avoiding crystal-melt sequestration (Robb 2007, Audétat 2010). Within porphyry mineralised systems there are generally distinct alteration zones, and associated mineral assemblies. These zones, namely sodic-calcic, potassic, propylitic, chlorite-sericite and argillic, are a function of the fluid and metal sources (particularly the primary composition of these), the ratio of fluid to rock available for reactions to take place, temperature and pressure (Figure 2.6). The following surmises the principal alteration zones within porphyry mineralised systems (Sillitoe 2010):

1. Sodic-calcic alteration generally occurs at deeper levels, below or adjourning the stock intrusives and commonly extends into the surrounding country rock. The alteration assemblage generally includes large concentrations of magnetite. Primary mineral constituents are typically altered with hornblende being replaced by actinolite ± biotite, and alkali feldspar being replaced by plagioclase (sodic) ± epidote
2. Potassic alteration generally occurs ubiquitously aside stock intrusives, and occurs in the main mineralised body typically in the middle to upper segment of the porphyry system. The alteration assemblage generally includes plagioclase being replaced by alkali feldspar ± biotite. Potassic alteration commonly overprints the aforementioned sodic-calcic alteration region. Importantly, it is the main ore contributor of porphyry systems

3. Propylitic alteration generally occurs in the most distal regions of the system, outboard of the porphyry stock intrusives and surrounding the lower sodic-calcic and mid-upper potasstic alteration zones. The alteration assemblage is primarily composed of albite, carbonate, chlorite and epidote. Generally, the host rock composition and geochemistry is predominantly maintained
4. Chlorite-sericite alteration generally occurs in the upper segment of the porphyry zone and generally transitions from the potassic alteration zone. The alteration assemblage generally includes majorly of chlorite, sericite (phyllic) and clays. Gradation between these minerals is commonly evident
5. Argillic alteration generally occurs above the porphyry zone, and largely constitutes the lithocap of the mineralised system. The alteration assemblage generally includes quartz, alunite and kaolinite

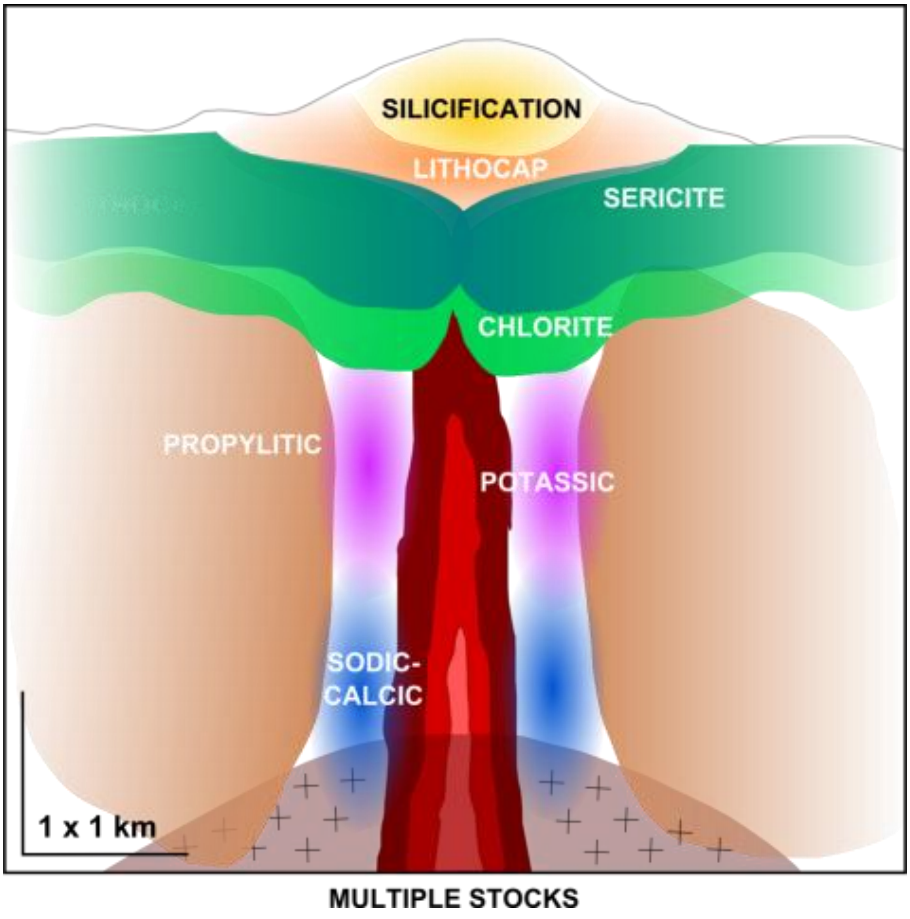

Figure 2.6 - Generalised alteration zones occurring proximal to magmatic stocks associated with the primarily percurosr pluton within a porphyry system. No scale. Adapted from Sillitoe (2010)

The QOB, in particular the eastern segment, has become one of the most important molybdenum (Mo) provinces with regard to world production; this region contains six giant Mo deposits (> 0.5 Mt Mo), and tens of large (0.1 – 0.5 Mt Mo), medium (0.01 – 0.1 Mt Mo) and small (<0.01 Mt Mo) deposits. The types of molybdenum mineralisation that occur in the eastern portion of the QOB are porphyry, skarn, porphyry-skarn, carbonatitic dyke, quartz- and fluorite-vein type (Mao *et al.* 2011). The focus of this study will be on the porphyry-skarn type of molybdenum mineralisation using the example of the Nantai porphyry-skarn Mo-(Cu) deposit. It is important to note that many of the molybdenum-dominated systems that are the result of porphyry-skarn emplacement mechanisms demonstrate specific characteristics that make them unique to the QOB. For example, the majority of the porphyry and porphyry-skarn molybdenum deposits occur north of the Luonan-Luanchuan Fault such as the Jinduicheng Mo deposit (largest producer in the QOB), the Nannihu, Shangfagggou and Shibaogou Mo deposits (Chapter 3: Zircon U-Pb Geochronology), and the Nantai Mo-(Cu) deposit (this study). The Precambrian basement (highly deformed having undergone amphibolite facies metamorphism) of the S-NCB largely controls both the distribution and number of deposits within the eastern segment of the QOB. The deposits already mentioned, along with the majority of other molybdenum-dominated mineralised systems within this region demonstrate a common age-range of emplacement spanning from the Early Cretaceous to the Late Jurassic (130 – 150 Ma). The Nantai Mo-(Cu) deposit has produced an age towards the end of this range of 151 - 147 Ma (Chapter 3: Zircon U-Pb Geochronology). Refer to Appendix A for field notes on this deposit.

Skarn-type mineral systems can be associated with relatively high crustal porphyry deposits, whereby the system has intruded into-host rocks of carbonate affinity. Examples of porphyry-skarn molybdenum-bearing deposits are common is the eastern portion of the QOB. The Nantai porphyry-skarn Mo-(Cu) deposit is an example whereby a granitic stock has intruded into dolomite; the deposit can be further typified as being magnesian as opposed to calcic, based on the host rock being dolomite over limestone. Skarn-type settings are typically associated with contact metamorphism, and metasomatism associated with granitic intrusives. Early literature (e.g. Einaudi 1981, Meinert 1992) through to more recent workings (e.g. Zhao *et al.* 2015) have illustrated that skarn mineralisation systems (regardless of different metalliferous precipitation/ore genesis e.g.

Mo, Cu, W, Sn, Fe, Pb-Zn mineralisation), have similar processes of emplacement. These main processes accounting for skarn deposits are i) contact metamorphism related to the earliest stages of granitic intrusion, and subsequent crystallisation and solidification; ii) metasomatism and alteration in association with magmatic fluid saturation and; iii) final stage influence from surface-derived meteoric fluid influx acting on the cooling pluton, effectively leading to metal precipitation.

2.3.2 Orogenic gold deposits

It is first important to note that orogenic gold deposits exemplify a hybrid type of hydrothermal mineralisation system, whereby the deposits are not necessarily spatially or temporally associated with magmatic centres (as compared to porphyry and skarn deposits) – rather, this type of mineralisation system forms during periods of regional tectonism and deformation, where the precipitation of metalliferous (in this instance gold) components from aqueous fluids results in the genesis of orogenic gold deposits. Seeing as fluid transport plays a vital role in the formation of these types of gold deposits, it has been including under the section of hydrothermal mineralisation systems.

Orogenic gold deposits were first typified by Gebre-Marium *et al.* (1995) followed by Groves *et al.* (1998), and is a term used to describe a wide variety of gold deposits that commonly form at depths of 2 – 15 km (possibly as far as 20 km, Kolb *et al.* 2015) in the crust, and hence high pressure regimes between 1.5 – 5 kbar (Groves 1993). The temperature of formation is moderate between 300 – 450 °C. The ore fluids are classified as low-salinity $H_2O – CO_2$, and exist broadly in thermal equilibrium with the surrounding wall rocks. Structurally, these deposits are generally vertically extensive having been formed in actively evolving orogenic belts under usually multiple (regional and local) deformation events (Groves and Santosh 2015).

These systems generally produce majority gold, with some deposits producing minor silver and antimony. Orogenic gold deposits are usually relatively small, hosting economically achievable amounts of ≤ 1 Mt ore material. World-class examples, which well exceed these amounts include Murantau, Uzbekistan; and the Golden Mile, Yilgarn Craton, Australia (Ridley 2013). The geological setting of orogenic gold deposits are in essence the reason behind their name; these mineralised systems are spatially associated with regionally deformed and commonly intrusive rocks that have undergone

metamorphism to generally greenschist facies regimes. Particular to these deposits types is their association with major crustal features, including structures such as anticlines; which leads to a broader tectonic influence inclusive of convergent plate margins (e.g. NCB and SCB), whereby accretionary complexes are a result of compressional deformation and subsequent formation of collisional orogenies (e.g. QOB) (Groves *et al.* 1998, Goldfarb *et al.* 2001).

Although the term 'orogenic gold' has been accepted by broader literature (e.g. Goldfarb *et al.* 2001, Bierlein *et al.* 2006), the paragenesis of these types of mineralised systems is still intensely debated. However, some distinct environments have been recognised to host such mineralised systems (the following are all contained within collisional orogenies): Cordilleran orogenic belts (or accretionary style environments), [*]Greenstone belts of Achaean to Proterozoic age, and metamorphosed slate belts. Commonly, within these three specific orogenic environments there are many orogenic gold deposits of different scales clustered together; these clustered occurrences are commonly called 'camps' and are generally spatially proximal to each other (i.e. within tens of kilometres). With regard to the tectonic processes having acted on the host-strata, orogenic gold deposits are generally post-orogenic. However, these mineralised systems are also heavily influenced by ongoing subduction and other deep-crusted activity, and in this regard can also be classified as syn-orogenic. Furthermore, the deformation and metamorphic histories of the host orogenn typically outdate the formation of the gold mineralisation (which generally forms in a relatively short period of geological time i.e. 1 – 10 Ma) (Groves and Santosh 2015).

[*]Greenstone is defined as mafic to ultramafic extrusive and intrusive rocks that have undergone deformation and greenschist facies metamorphism (Ridley 2013).

Early models of the genesis of orogenic gold deposits placed emphasis on syn-genetic (exhalative) development with metamorphic processes acting on the host-rocks. There were also suggestions made towards pure magmatic-hydrothermal regimes. These models are not acceptable due to mineralisation typically taking place long after regional deformation and metamorphism (e.g. the Jiaodong deposits formed 126 – 120 Ma, some 2 Ga after the oldest host rocks in the North China Block; Groves and Santosh 2015), and commonly orogenic gold deposits are not associated spatially or temporally with magmatic centres. The fluids carrying abundant dissolved Au (Ag ± Sb) commonly

transport these metals over long vertical distances, needing for a more robust and convincing explanation for the origins mineralised-hosting fluids (Goldfarb and Groves 2015). A metamorphic devolatisation reaction regime for the development of gold deposits is generally accepted as providing the best explanation of these mineralised systems (Figure 2.7). It is proposed that supercrustal or intrabasin (e.g. mafic or meta-marls) undergo prograde metamorphic regimes, under greenschist or amphibolite facies conditions (Liu *et al.* 2015). These metamorphic conditions promote gold to be leached into the resultant fluids. It is assumed at these depths (low in the crust), gold concentrations are similar to those of crustal averages (2 – 5 ppb) (Ridley 2013). The excess gold hosting fluids migrate to much higher levels in the crust through advection, channelled along structural pathways (e.g. faults). The concentration of sulphides (e.g. FeS_2) is particularly important to the solubility of gold; therefore the addition of sulphur-rich constituents commonly results in the precipitation of both gold and pyrite at higher crustal levels, subsequently leading to early development of orogenic gold deposits (Goldfarb and Groves 2015, Groves and Santosh 2015).

The QOB hosts numerous orogenic, Carlin-type and Carlin-like deposits, and makes for one of the largest gold producing regions of China (Chen *et al.* 2015). This study will be most concerned with orogenic gold deposits, however emphasis is still placed on the significance of Carlin-type and Carlin-like mineralisation, which account for a significance proportion of the gold deposits within the QOB (particularly in the western segment) (Chen *et al.* 2015). The majority of the orogenic gold deposits within the QOB are hosted within Devonian to Carboniferous marine derived clastic and carbonate sedimentary sequences. Mao *et al.* (2002) has further classified the orogenic gold deposits of the QOB into three sub-categories, including a brittle fault-hosted disseminated type, ductile shear-zone type and breccia-related type. Generally, the orogenic gold deposits of the QOB are controlled by WNW striking faults, parallel to the Shangdan Suture zone. This study will focus on two examples, which demonstrate the aforementioned attributes typical of orogenic gold deposits in the QOB. These are the Longtougou and Liujiaxia orogenic Au deposits. Refer to Appendix A for field notes on these deposits.

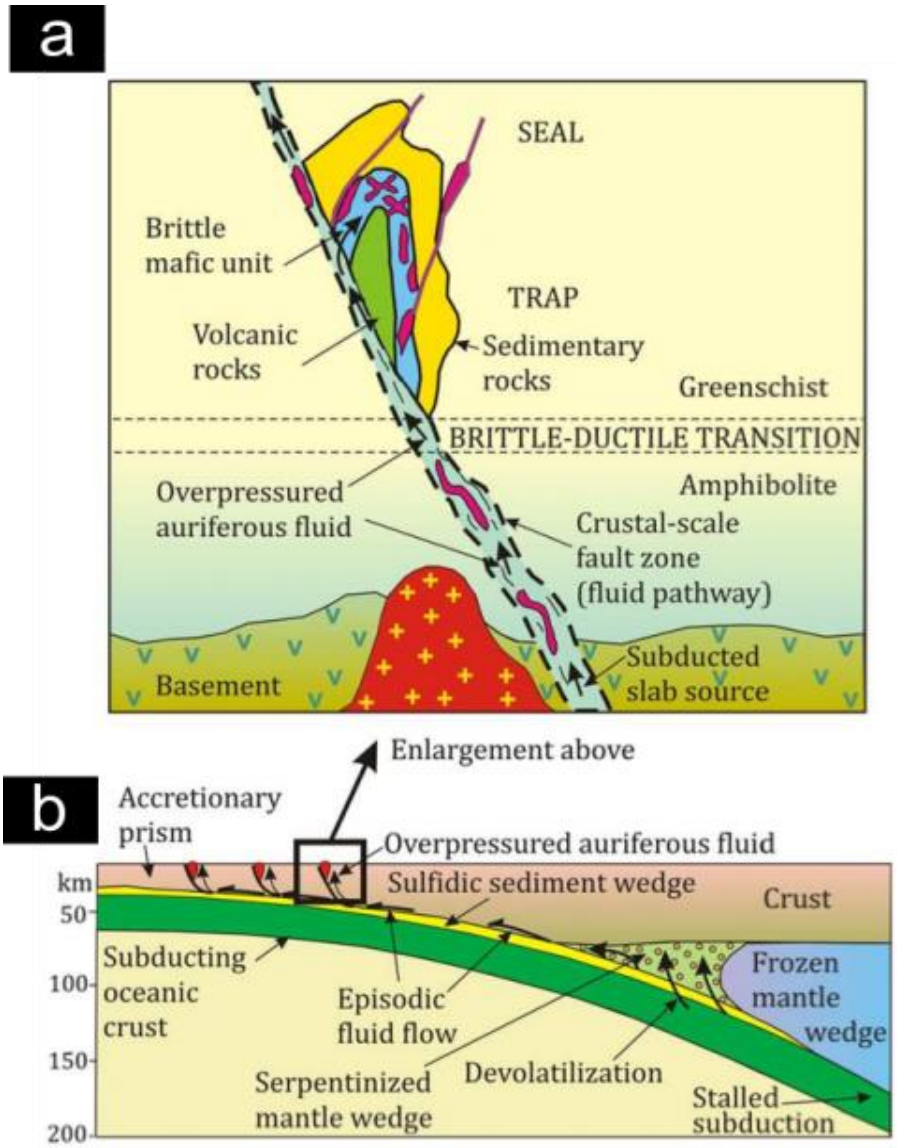

Figure 2.7 - Schematic representation of a permissive scenario for all orogenic gold deposits. No scale. Adapted from Groves and Santosh (2015)

3.1 INTRODUCTION

Sensitive high-resolution ion microprobe (SHRIMP) zircon U-Pb geochronology was employed to determine the intrusive age of the aplite dykes of the Nantai porphyry-skarn Mo-(Cu) deposit within the Qinling Orogenic Belt (QOB). Previous dating of this magmatic event (151 ± 1 Ma, Ke *et al.* 2012) has largely focused on the granitic pluton hosting the deposit. No investigation has been made into the mineralised aplite dykes, which when coupled with field relationships, will be able to constrain the timing and nature of this igneous event and mineralisation of the system in the broader context of the tectonometallogenic evolution of the QOB.

Field relationships and radiometric dating need to be integrated. Cross-cutting relationships between different units establish *relative timing* of geological units, emplacement or intrusion events, and mineralisation of systems (Schoene *et al.* 2013). Samples (15NT_01 and 15NT_03) were collected from two different aplite dykes from within the Nantai porphyry-skarn Mo-(Cu) deposit. These fine-grained, mineralised dykes cross-cut the larger granitic body, host lithology to the intrusive. Host phases are dolomitic marble and meta-quartzites.

Previous dating of the granite porphyry-skarn host of the Nantai Mo-(Cu) deposit was obtained by Ke *et al.* (2012) using the zircon U-Pb LA-ICP-MS method and yielding an age of 151 ± 1 Ma (MSWD = 0.32). Six molybdenite samples were also dated using the Re-Os dating method, producing ages ranging from 146 ± 2 Ma to 151 ± 2 Ma with a weighted average of 148.8 ± 1.7 Ma (MSWD = 0.84) (Ke *et al.* 2012). This will be further discussed in the interpretation of the results gathered for this investigation in Section 3.5.

3.1.1 Zircon preparation

Rock samples were collected during April 2015 during a reconnaissance field trip in the Qinling Orogen at the invitation of Prof. Yan Zhen at the Institute of Geology and Geophysics, Chinese Academy of Science (IGGCAS). Aplite dyke samples (15NT_01 and 15NT_03) were collected from the Nantai porphyry-skarn Mo-(Cu) deposit (33°55’15’’N, 110°03’16’’E) and sent to Langfang laboratory in China for zircon separation and whole-rock geochemistry. Zircons were separated using conventional techniques, including

crushing, sieving and magnetic and heavy liquid separation methods. More than 500 zircons were recovered from both 15NT_01 and 15NT_03. Single zircons grains were examined using a binocular microscope and handpicked for imaging and SHRIMP dating. From each separate approximately 180 zircon grains (~ 360 in total) along with 30 grains of standard were cast into one epoxy resin mount (W41). The standards, 20 grains of TEMORA II; 418.1 ± 1.6 Ma (Black *et al.* 2004) and 10 grains of OG-1; with a $^{207}Pb/^{206}Pb$ age of 3465 Ma (Stern *et al.* 2009) were distributed as several groups across the mount as a check for calibration of U-Pb isotopic ratios and data quality.

A standard 25.4 mm epoxy mount was prepared with the technical assistance of Prof. Allen Nutman. Two rows of sample and randomised groups of standard grains were placed onto double sided tape, covering approximately a 15 mm diameter area in the center of a 25.4 mm circle. A 25.4 mm cylindrical teflon mould was then positioned so as to surround the zircon grains. A 25:3 mixture of resin (12.5 g) and hardener (1.5 g) was poured over the grains into the mould, and left to cure for 48 hours at room temperature. After removing the mould by hand the mount was ground using 600 grit wet/dry sandpaper, followed by further abrasion with 1 μm diamond powder slurry on a rotary polisher to expose individual cross sections of the zircon grains. Polishing was finished using 0.3 μm alumina powder and dilute water also on a rotary polisher.

Prior to analysis transmitted and reflected light photomicrographs were taken using a petrographic microscope at the University of Wollongong (UOW), to identify sites of interest within individual grains. Observations of morphological characteristics such as size, clarity and colour were made.

3.1.2 Optical and cathodoluminescence imaging

Ahead of cathodoluminescence (CL) images, the samples were coated with approximately 10 nm of gold. Cathodoluminescence images were taken using a JEOL JSM-6610 scanning electron microscope (SEM) at the Australian National University (ANU) to reveal internal structures, including zoning, recrystallisation structures and possible pre-magmatic inheritance. The instrument has an analytically low vacuum with a high resolution of 3 nm at 30 kV allowing for clarity of fine structures. Thus, CL imaging of zircon grains reveal their internal structure, zonation patterns, U and Th content (to be

discussed) and the presence of inclusions of other minerals, which are not or rarely observed using standardised petrological techniques, i.e. transmitted and reflected light microscopy. Image acquisition of the entire zircon mount (W41) took place using a first-wave low-resolution setting. This was then followed by second-wave high-resolution imaging of individual grains of interest, determined by the previous low-resolution scan combined with prior transmitted and reflected light photomicrographs. Minerals, when bombarded by a high-energy electron beam, emit characteristic visible luminescence called cathodoluminescence (CL). This luminescence in the visible spectrum is dependent on the crystal structure and chemical composition of the mineral under examination. The process begins with the stimulation of the system (zircon grains in this instance) into an excited state through the absorption of excitation energy. The subsequent transformation and transfer of the excitation energy lends to the emission of visible light, and final relaxation of the system into an unexcited state (Pagel *et al.* 2000).

With regard to CL imaging of zircon the technique is commonly practiced in preparation for *in situ* U-Pb dating. The CL characteristics of zircon is well explored (e.g. Kempe *et al.* 2000, Poller 2000, Rubatto and Gebauer 2000 and references therein). Concentric zoning within zircon grains, a dominant feature when imaged using CL, can be attributed to the difference in abundances of trace elements uranium (U) and yttrium (Y). The identification of these different domains and subsequent dating of these within a singular zircon grain allows for an understanding to be may about the varied geological processes and potential multi-stage history the zircon grain may have undergone prior to extraction and analysis (Boggs and Krinsley 2006). As mentioned, the zones within zircon can be attributed to variation and segregation of U and Y within single zircon grains; CL images that are enriched in U and Y present dark zonation, whereas CL images that are relatively depleted in the aforementioned trace elements present bright zonation. As such, it can be correlated that other elements rather than U and Y are responsible for CL emission in zircon; U and Y cause an apparent reduction in emission intensity, acting as CL quenchers (Pagel *et al.* 2000, Boggs and Krinsley 2006).

3.2 PRINCIPLES OF ZIRCON U-Pb GEOCHRONOLOGY

3.2.1 Radioactive decay

The natural process of radioactivity is both continuous and unidirectional, making for an extremely suitable means of measuring absolute geological time. See review by Williams (1998). Uranium-Lead (U-Pb) geochronology utilises the process of radioactive decay, whereby certain unstable nuclei transform (transmute) spontaneously into other nuclei and in doing so give off particles of radiation to satisfy the laws of conservation of energy and mass (Allègre 2008). The unstable isotope, or radioisotope decays into another isotope of a different element; this process continues until finally a stable nucleus forms. Fundamental to radioactive decay is the relationship between decay and time of each element and associated isotope/s; each nucleus has a fixed rate of decay per unit of time, with these rates independent of temperature, pressure, chemical form, or other conditions of the environment. If the parent isotope's decay constant (λ) is also known (Equation 3.1) the absolute age for geological material, be it a mineral or rock, can be calculated using the age equation by determining the atomic ratio of a stable daughter isotope (D) relative to its radioactive parent isotope (P).

$$\frac{D}{P} = e^{\gamma t} - 1 \qquad \text{Equation 3.1}$$

It is of importance to note that there are many natural radioisotopes, however relatively few have suitable applications for geochronology due to inapplicable decay rates commonly expressed as a half-life (T½). To be a suitable tool for geochronological investigation, a radioisotope must have a half-life temporally comparable to the specimen being studied, that meaning there should be long enough time allowing for the parent isotope to survive, while being also short enough to allow the daughter isotope to be produced. The time taken for half of a radioisotope to decay can be expressed by Equation 3.2.

$$T½ = \frac{\ln 2}{\lambda} \qquad \text{Equation 3.2}$$

This investigation is primarily concerned with the Jurassic (~ 151 Ma) intrusive event and subsequent mineralisation within the Qinling Orogenic Belt (QOB); as such the decay of U to Pb is of interest for which there are two independent isotopic systems:

$^{235}U \rightarrow {}^{207}Pb$, where T½ = 704 Ma

$^{238}U \rightarrow {}^{206}Pb$, where T½ = 4470 Ma

One of the main advantages for the U-Pb system using $^{238}U \rightarrow {}^{206}Pb$, and $^{235}U \rightarrow {}^{207}Pb$ is the feature that both parents and both daughters are of the same chemical nature; however have very different decay constants. The system can be described as 'paired', which allows for determination of geological ages when the system is either open (affected by secondary processes), or closed (undisturbed) (Allègre 2008). Thus, as U decays, not only does radiogenic Pb accumulate, but also the isotopic composition of that Pb changes. Therefore, the ratio of $^{207}Pb/^{206}Pb$ allows for a third independent measure of elapsed time. This internal crosscheck, provided by the characteristic paired nature of the U-Pb system provides confirmation as to whether the isotopic system has remained closed or not (Williams 1998). It is easiest to graphically display U-Pb data through the means of concordia plots; the most commonly used plot is the Wetherill diagram (Wetherill 1965), however an alternative, better suited to displaying mineral U-Pb isotopic data is the Tera-Wasserburg concordia diagram and will be utilised in this investigation (Williams 1998). The Tera-Wasserburg concordia diagram plots the relation between $^{207}Pb/^{206}Pb$ and $^{238}U/^{206}Pb$, obtaining results from closed systems that plot on the concordia curve (concordant) and from open systems that plot off the curve (discordant) (Tera and Wasserburg 1972). In this way the diagram does not contain correlated errors (in most zircon analytical work ^{235}U is not measured but is calculated from ^{238}U using the modern $^{238}U/^{235}U$ ratio of ~137.8) (Williams, 1998).

3.2.2 Why zircon?

Zircon ($ZrSiO_4$) is a remarkable mineral because of its common occurrence in upper crustal rocks and its ability to incorporate U in its crystal structure but not the daughter Pb isotopes. The geochronological importance of zircon lies in the combination of chemical resilience and high concentrations of important trace elements that include two radiogenic isotope systems, those being U-Pb and Pb-Th (Hawkesworth and Kemp 2006). Any accumulation of Pb in trace amounts can be accountable to radioactive decay, whereby upon crystallisation U and Th are incorporated in the zircon crystal lattice, with Pb being disregarded (Bea 1996, Hoskin and Schaltegger 2003). Crystallisation of zircon grains typically occurs in silica-saturated magmas and at medium to high grades of metamorphism. Due to its genesis and resilience to physical and chemical attack the mineral occurs as products of primary crystallisation, detrital grains, xenocrysts, or recrystallised grains. The robustness of zircon grains enables the mineral to retain its isotopic integrity and survive long, multi-stage geological processes such as cycles of erosion, transportation, diagenesis, metamorphism and/or anatexis (Watson and Harrison 1983, Davis *et al.* 2003, Finch and Hanchar 2003). Particularly to the interests of this project, the complex growth structures or zones within zircon grains demonstrate 'encoded' isotopic and trace element information, which can be obtained through first CL-imaging to distinguish zonation boundaries, then targeted through micro-analytical techniques capable of high precision and spatial resolution.

3.3 ZIRCON U-Pb GEOCHRONOLOGY WITH SHRIMP

The sensitive high resolution ion microprobe (SHRIMP) is a double-focusing secondary ion mass spectrometer (SIMS). The development of the instrument in turn birthed modern SIMS U-Th-Pb geochronology (Compston *et al.* 1984). SIMS, developed in the early 1970s, was already recognised as an important geochemical analytical technique where a high degree of spatial accuracy is required. The advancement and subsequent foundation of the SHRIMP (SHRIMP I; ANU 1974) allowed progression into dating *in-situ* small (<100 μm) minerals and importantly multiple zones within single grains (Schoene 2014). This is because of the geometry and ion optics of SHRIMP allowed the direct measurement of U and Pb isotopes, free of interference from near isobaric species (Williams, 1998).

The SHRIMP operates by focusing a primary high-energy ion beam of O^- or O_2^- under vacuum onto a polished surface enabling ablation of small diameter spots (10 – 40 µm) with very shallow pit depths (<4 µm) (Figure 3.1). A small volume of secondary material (2 ng) is ionised through the process of sputtering, which is then accelerated into a mass spectrometer (Williams 1998, Ireland and Williams 2003). The secondary ions are propelled through a large curved chamber into a magnetic field; the behaviour of charged ions in electromagnetic fields is comparable to light passing through lenses and prisms, in that it can be deflected and split. The sheer size of the instrument and its detection capabilities allows for the distinction between atoms of very similar mass, for example $^{206}Pb^+$ (M = 205.97) and $HfSi^+$ (M = 205.92) (Ireland and Williams 2003). The production of electrical signals on reaching the detector accounts for the amount of each isotope, located at the exact spot being analysed on a zircon grain. The quantification of U and Pb atoms, based on known radioisotopic decay rates allow for the absolute age to be determined for the section within a zircon grain under examination (Williams 1998).

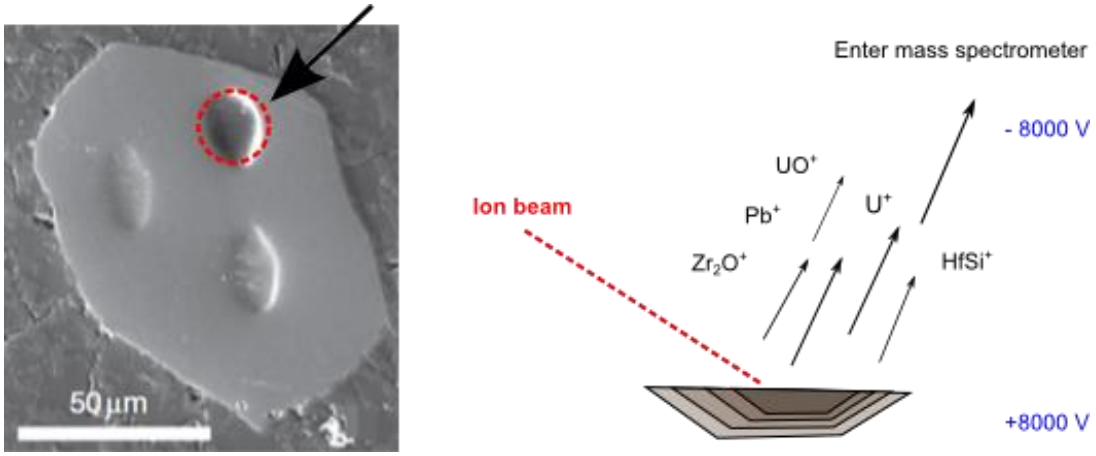

Figure 3.1 - Schematic diagram illustrating secondary ion mass spectrometry (SIMS). The method shows an image of a zircon grain that has been analysed in order to demonstrate sample size. The zircon image is that of a lunar sample analysed by Grange et al. (2011). Adapted from Schoene (2014)

Protocols of U-Pb SHRIMP geochronology follow those summarised by Williams (1998), and technical assistance and mentoring was provided by Prof. Allen Nutman. From both 15NT_01 and 15NT_03 a total of 16 zircon grains were chosen for analysis using the ANU SHRIMP II. Sites within the zircon grains were selected according to their

apparent reflectance (brightness) and polished surface (information gained from reflected light photomicrographs), along with well-formed structure (information gained from CL images). Particular note was made to avoid sampling cracked or damaged zircons, and dark zones within grains (indicative of high U content). After site selection was made, the instrument was programmed to run overnight (duration approximately 12 hours).

A total of six cycles were made at each of the detected nominal mass stations; ^{196}Zr, ^{204}Pb (background measured near $^{204.1}Pb$), Pb (^{206}Pb, ^{207}Pb, ^{208}Pb), ^{238}U, ^{248}ThO ($^{232}Th + {}^{16}O$) and ^{254}UO ($^{238}U + {}^{16}O$). Parameters particular to the analytical session include a spot size of ~20 μm, with the primary ion beam of 5 nA. The standards (TEMORA II) were analysed for U-Pb calibration and after every three analytical sites (13 times in total), and produced the same apparent age within error. The majority (10 TEMORA II grains) of the standards were analysed just once, with 3 grains being analysed twice at separate locations on the individual zircon grains.

The initial data produced from the SHRIMP II for samples 15NT_01 and 15NT_03 was processed using a combination of the ANU software programs PRAWN and L-lead. In PRAWN each analysis is scrutinised to look for outliers in analytical counts, and a set of (uncalibrated) isotopic ratios and their associated analytical errors are produced. In L-lead these ratios are calibrated using the data acquired on the TEMORA II standard in the same analytical session. Once the data had been reduced using the aforementioned programs, it was represented graphically using a combination of the Isoplot 4.15 and Microsoft Excel Data Analysis add-in.

3.4 RESULTS

Analysis sites are presented in Figure 3.2 and Figure 3.3. Reported ages are derived from $^{206}Pb/^{238}U$ ratios, as usual for Phanerozoic grains. Data for 15NT_01 (16 grains, 16 analyses) and 15NT_03 (16 grains, 16 analyses) both plot close to concordia (Figure 3.5) even before correction for common Pb, which indicates that the analysed zircon sites show little disturbance to the isotopic system. Further evidence of a closed system is the negligible presence of common lead as expressed by very low $^{207}Pb/^{206}Pb$ ratios (Table 3.2 and Table 3.3). All apparent ages are within statistical error of one another, with little to no difference between those analyses targeted at the core, middle or

rim of individual grains. The zircon grains from both 15NT_01 and 15NT_03 are interpreted to represent a single normal population as such these populations can be considered representative of being derived from the same source. A total of seven grains [(15NT_01): 3.1, 6.1, 7.1, 14.1; (15NT_03): 5.1, 13.1, 15.1] were rejected on determining the weighted mean age of the intrusives; see Table 3.1 for explanation. As such, the common Pb corrected (utilising the ^{207}Pb correction method of Compston et al. 1984) ^{206}Pb/^{238}U weighted mean age of 15NT_01 is **150.7 ± 3.8 Ma** (95% confidence, MSWD = 0.74), and **148.4 ± 3.1 Ma** (95% confidence, MSWD = 0.42) for 15NT_03.

3.4.1 Zircon characteristics

Zircon grains from the Nantai aplite average 50 – 200 μm in longest dimension, with elongation ratios averaging 3:1. The length-to-width ratio of zircon grains is believed to be a reflection of the crystallisation velocity. Corfu *et al.* (2003) describe that variable morphological characteristics of zircon grains, in terms of elongation ratios can be attributed to a relationship with relative cooling rates of geological material. Rocks that have undergone slow cooling regimes deep within the crust typically produce zircon grains that are stubby or equant, whereas rocks that have undergone rapid crystallisation, such as sub-volcanic intrusions produce grains that are needle-like and acicular. The zircons extracted from the Nantai aplite demonstrate characteristics of the latter described regime, suggesting rapid cooling. This is supportive of the development of aplitic intrusives, which are fundamentally typified by fine-grained (granitic-) constituents resulting from rapid crystallisation.

The majority of the zircon grains show well-developed prismatic habit with subhedral to euhedral face development, generally free of fracturing or fragmentation. The edges of the longest dimension or lengthwise margins of the grains are generally straight, with well-developed doubly terminated ends. It is a fair assumption that the distribution of elements (particularly trace elements) in the Nantai aplite zircon grains (and furthermore, in most igneous zircon grains) is inherently heterogeneous on account of the zonation; oscillatory zoning is a predominant texture of igneous zircon (Hoskin and Schaltegger 2003). Furthermore, the composition of the zones transitions between two end members, the first being dominated by enriched Zr and Si approaching a composition of pure zircon, and the other end member reflects a composition highly enriched in trace elements (e.g.

Hf, P, Y, the REE, U and Th) with an order of magnitude (several wt.%) of these elements (Corfu *et al.* 2003).

The grains from both 15NT_01 and 15NT_03 effectively all demonstrate growth zoning, be it weak to well-developed banding. The majority the grains selected for analysis possess well-developed, fine oscillatory zoning. The change in luminescence within individual grains is generally easily distinguishable, with contrasting bright and dark bands. The narrow growth of the bands could be related to a silica-rich primary melt from which subsequent crystallisation of zircon grains occurred (Hoskin and Schaltegger 2003). Instances of growth zoning truncation are relatively uncommon; however do occur in some instances throughout samples 15NT_01 and 15NT_03 (15NT_01: 11.1, 13.1, 15.1; 15NT_03: 10.1). These textual discontinuities are generally more homogenous and lighter in appearance than other zones identified in the zircon grains selected for analysis. These zones represent recrystallised or newly grown domains, and as such have been avoided as targets for dating. Truncation rings resulting in recrystallised areas are representative of instances where the U-Pb isotopic system has been disturbed, and as such will not be representative of the overall age of the zircon grain. Zones displaying resultant dark luminescence were generally also avoided when selecting areas for dating; U-rich areas often produce an age that is marginally older that the true weighted mean age for a particular rock unit.

Table 3.1 - **Rejected zircon grains**

15NT_01		
Grain:	[3.1]	Comments: Although this grain demonstrates U/ppm and Th/ppm values that are below the grain rejection threshold, the age (340 ± 125 Ma) produced is not consistent with the rest of the analysed zircon population, as such it is not representation of the aplite intrusive (15NT_01)
Site:	m,osc,p	
U/ppm:	346	
Th/ppm:	212	
Age (Ma):	340 ± 125	
Grain:	[6.1]	Comments: This grain demonstrates U/ppm and Th/ppm values that are above the acceptable threshold, and as such have been rejected from the data used to determine the weighted mean age of the aplite (15NT_01). On further inspection of the CL image, the grain demonstrates apparent truncation and recrystallisation, which is indicative of a disturbed system
Site:	e,osc/h,p,fr	
U/ppm:	14806	
Th/ppm:	2950	
Age (Ma):	167 ± 23	
Grain:	[7.1]	Comments: This grain demonstrates U/ppm and Th/ppm values that are above the acceptable threshold, and as such have been rejected from the data used to determine the weighted mean age of the aplite (15NT_01). On further inspection of the CL image, the grain demonstrates poorly preserved prismatic faces, with fractures radiating from the core
Site:	e,osc,p,fr	
U/ppm:	23336	
Th/ppm:	6645	
Age (Ma):	171 ± 21	
Grain:	[14.1]	Comments: This grain demonstrates U/ppm and Th/ppm values that are above the acceptable threshold, and as such have been rejected from the data used to determine the weighted mean age of the aplite (15NT_01). The grain has produced an age that is consistent with the accepted zircon analyses, however based on the elevated amount of U and Th the grain has been rejected
Site:	e,osc/h,p,fr	
U/ppm:	7696	
Th/ppm:	6514	
Age (Ma):	155 ± 6	
15NT_03		
Grain:	[5.1]	Comments: This grain demonstrates U/ppm and Th/ppm values that are above the acceptable threshold, and as such have been rejected from the data used to determine the weighted mean age of the aplite (15NT_03). On further inspection of the CL image, the grain demonstrates multiple fractures, which could be indicative of a disturbed system
Site:	m,osc/h,p	
U/ppm:	23526	
Th/ppm:	4845	
Age (Ma):	168 ± 18	
Grain:	[13.1]	Comments: This grain demonstrates U/ppm and Th/ppm values that are above the acceptable threshold, and as such have been rejected from the data used to determine the weighted mean age of the aplite (15NT_03). The grain was analysed on the dark edge (assumedly high U), rather than the bright core which could explain the threshold being crossed
Site:	e,osc,p,fr	
U/ppm:	6620	
Th/ppm:	2389	
Age (Ma):	159 ± 12	
Grain:	[15.1]	Comments: This grain demonstrates U/ppm and Th/ppm values that are above the acceptable threshold, and as such have been rejected from the data used to determine the weighted mean age of the aplite (15NT_03). On further inspection, cracks and fracturing is observed radiating from the core of the grain
Site:	e,osc,p,fr	
U/ppm:	1440	
Th/ppm:	590	
Age (Ma):	149 ± 6	

Age to the nearest Ma. Site: p = prism, fr = fragment, e = end, m = middle, osc = oscillatory zoned, h = homogenous. Abbreviations follow those of Nutman et al. (2013). Grain rejection threshold: U/ppm >1400; Th/ppm >500. Zircon grains with high U/ppm (>1400) lend to older age determinations.
On further inspection of the sites analysed the majority of the zircon grains that have been rejected were analysed on the edge of the grain; this may have contributed to the unfavourable results reflected in the above table. Refer to Appendix C for a detailed description of all the analysed zircon grains

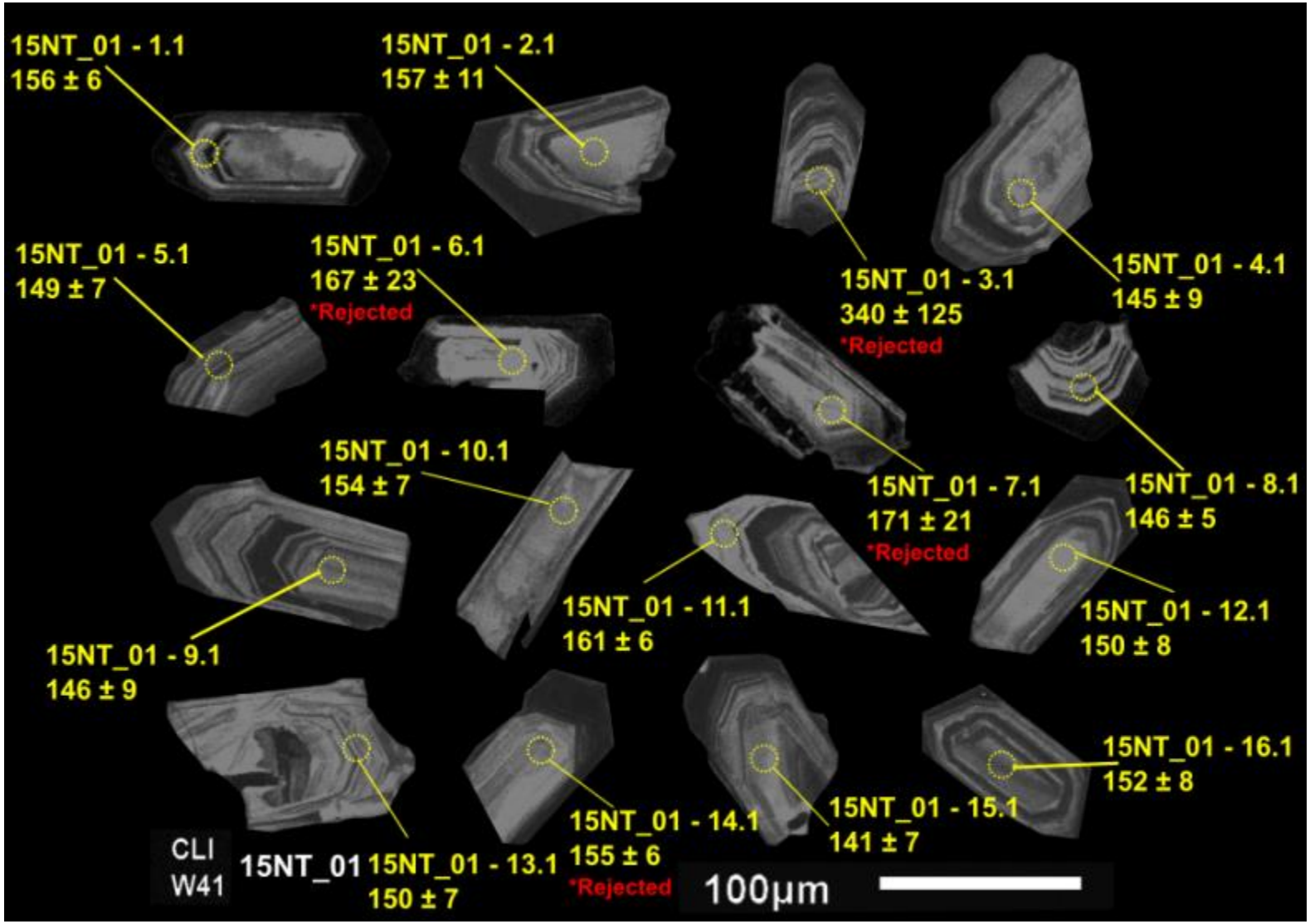

Figure 3.2 - Sample 15NT_01, Mount W41. CL images of the full suite of zircon grains analysed from the aplite dykes of the Nantai porphyry-skarn Mo-(Cu) deposit, Qinling Orogenic Belt (QOB). Zircons are labelled with $^{206}Pb/^{238}U$ ages to the nearest Ma. Those grains excluded from age calculations are explained in Table 3.1.

Mean = **151 ± 4 Ma**

95% confidence

MSWD = 0.71

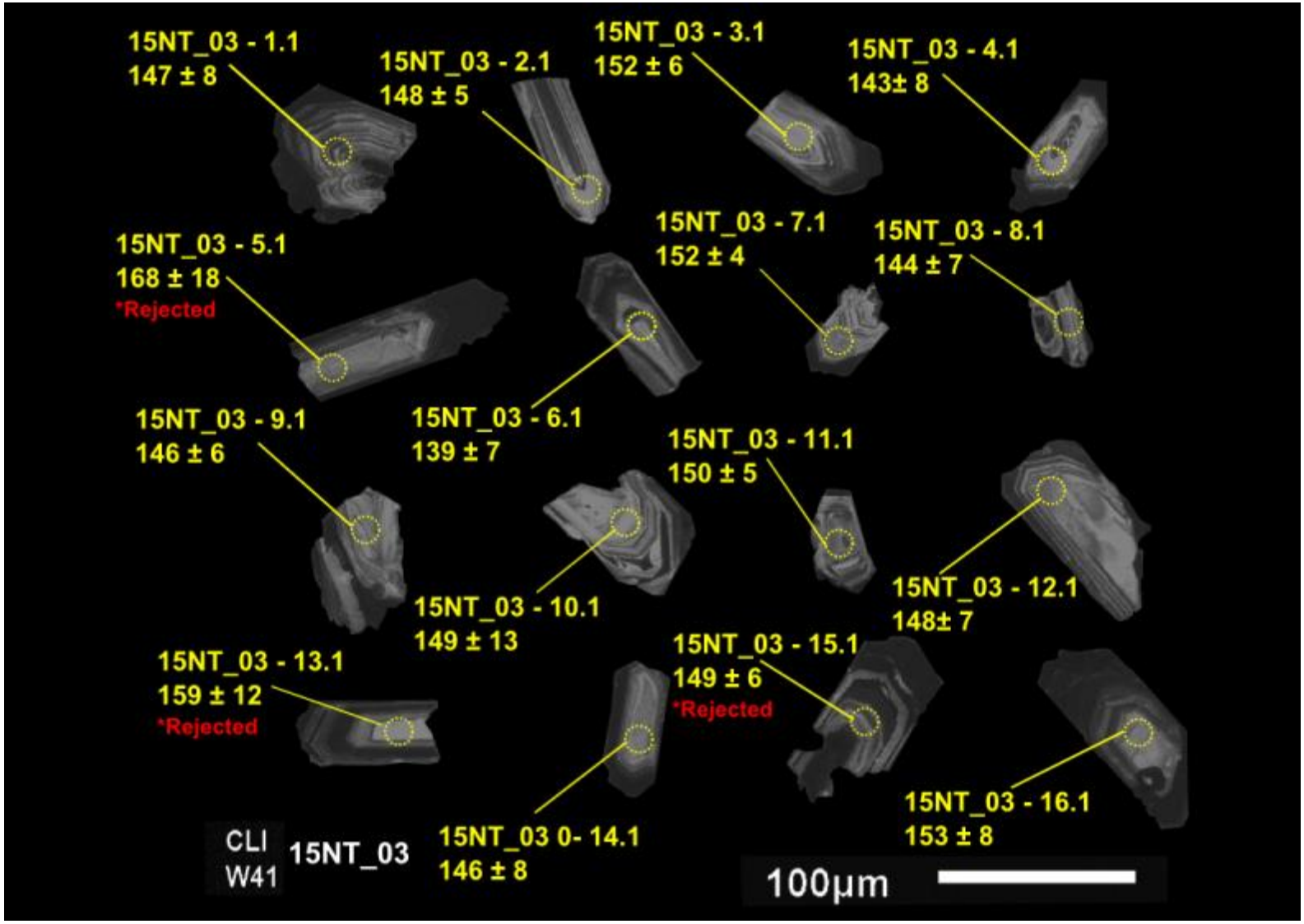

Figure 3.3 - Sample 15NT_03, Mount W41. CL images of the full suite of zircon grains analysed from the aplite dykes of the Nantai porphyry-skarn Mo-(Cu) deposit, Qinling Orogenic Belt (QOB). Zircons are labelled with $^{206}Pb/^{238}U$ ages to the nearest Ma. Those grains excluded from age calculations are explained in Table 3.1.

Mean = **148 ± 3 Ma**

95% confidence

MSWD = 0.36

Table 3.2

Zircon U-Pb SHRIMP data

Labels	Site	U/ppm	Th/ppm	Th/U	$^{204}Pb/^{206}Pb$	$^{238}U/^{206}Pb$	$^{207}Pb/^{206}Pb$	$^{206}Pb/^{238}U$ age*
15NT_01 aplite								
1.1	e,osc,p	626	342	0.55	0.00035 ± 0.00018	40.79 ± 1.76	0.0504 ± 0.0015	156 ± 6
2.1	m,osc,p,f	384	149	0.39	0.00030 ± 0.00017	40.43 ± 4.20	0.0514 ± 0.0019	157 ± 11
~~3.1~~	m,osc,p	346	212	0.61	0.00003 ± 0.00002	18.33 ± 0.45	0.0589 ± 0.0018	340 ± 125
4.1	e,osc,p,fr	391	153	0.39	0.00076 ± 0.00019	43.98 ± 3.17	0.0512 ± 0.0019	145 ± 9
5.1	m,osc,fr	639	469	0.73	0.00031 ± 0.00008	42.77 ± 2.78	0.0506 ± 0.0018	149 ± 7
~~6.1~~	e,osc/h,p,fr	14806	2950	0.20	0.00002 ± 0.00000	38.23 ± 1.37	0.0491 ± 0.0002	167 ± 23
~~7.1~~	e,osc,p,fr	23336	6645	0.28	0.00002 ± 0.00000	37.20 ± 1.68	0.0491 ± 0.0003	171 ± 21
8.1	e,osc,p,fr	558	243	0.44	0.00023 ± 0.00010	43.30 ± 1.05	0.0532 ± 0.0010	146 ± 5
9.1	m,osc,p,fr	674	414	0.61	0.00029 ± 0.00009	43.62 ± 3.68	0.0511 ± 0.0017	146 ± 9
10.1	e,osc/h,fr	510	183	0.36	0.00038 ± 0.00014	41.11 ± 2.41	0.0518 ± 0.0037	154 ± 7
11.1	e,osc,p	665	215	0.32	0.00045 ± 0.00012	39.41 ± 2.18	0.0521 ± 0.0016	161 ± 6
12.1	e,osc,p,fr	620	357	0.58	0.00019 ± 0.00008	42.46 ± 2.54	0.0517 ± 0.0012	150 ± 8
13.1	e,osc,p,fr	517	234	0.45	0.00042 ± 0.00014	42.38 ± 2.07	0.0497 ± 0.0011	150 ± 7
~~14.1~~	e,osc/h,p,fr	7696	6514	0.85	0.00034 ± 0.00003	40.82 ± 1.70	0.0541 ± 0.0005	155 ± 6
15.1	e,osc/h,p,fr	371	161	0.43	0.00104 ± 0.00021	45.03 ± 3.10	0.0540 ± 0.0027	141 ± 7
16.1	m,osc,p	832	452	0.54	0.00029 ± 0.00008	41.85 ± 2.59	0.0499 ± 0.0016	152 ± 8

Site grain type and analysis location: p = prism, fr = fragment, e = end, m = middle
Site CL imagery: osc = oscillatory zoned, h = homogenous
Abbreviations follow those of Nutman *et al.* (2013)
All analytical errors are given a 1σ
$^{238}U/^{206}Pb$ and $^{207}Pb/^{206}Pb$ ratios are uncorrected for common Pb
*Corrected for common Pb using the ^{207}Pb correction method of Compston *et al.* (1984)
~~Rejected~~ Excluded from age calculations - see Table 3.1 for explanation

Table 3.3
Zircon U-Pb SHRIMP data

Labels	Site	U/ppm	Th/ppm	Th/U	$^{204}Pb/^{206}Pb$	$^{238}U/^{206}Pb$	$^{207}Pb/^{206}Pb$	$^{206}Pb/^{238}U$ age*
15NT_03 aplite								
1.1	e,osc,p,fr	752	500	0.66	0.00048 ± 0.00010	43.25 ± 2.90	0.0511 ± 0.0009	147 ± 8
2.1	m,osc,p,fr	681	950	1.39	0.00054 ± 0.00011	42.88 ± 1.85	0.0515 ± 0.0010	148 ± 5
3.1	m,osc,p,fr	353	278	0.79	0.00083 ± 0.00029	41.55 ± 2.35	0.0535 ± 0.0015	152 ± 6
4.1	m,osc,p	406	166	0.41	0.00047 ± 0.00019	44.26 ± 3.25	0.0518 ± 0.0011	143 ± 8
~~5.1~~	m,osc/h,p	23526	4845	0.21	0.00002 ± 0.00001	38.00 ± 1.21	0.0489 ± 0.0002	168 ± 18
6.1	m,osc,p,fr	689	370	0.54	0.00064 ± 0.00022	45.66 ± 2.65	0.0501 ± 0.0017	139 ± 7
7.1	e,osc,p,fr	612	371	0.61	0.00049 ± 0.00010	41.93 ± 1.06	0.0502 ± 0.0018	152 ± 4
8.1	m,osc,fr	990	418	0.42	0.00033 ± 0.00007	44.34 ± 2.41	0.0499 ± 0.0006	144 ± 7
9.1	m,osc,fr	379	142	0.38	0.00024 ± 0.00027	43.38 ± 1.85	0.0522 ± 0.0014	146 ± 6
10.1	m,osc,p,fr	380	141	0.37	0.00015 ± 0.00014	42.73 ± 3.15	0.0516 ± 0.0018	149 ± 13
11.1	m,osc,p	704	391	0.56	0.00058 ± 0.00012	42.44 ± 1.80	0.0517 ± 0.0007	150 ± 5
12.1	e,osc,p,fr	522	221	0.42	0.00042 ± 0.00023	42.73 ± 2.61	0.0524 ± 0.0013	148 ± 7
~~13.1~~	e,osc,p,fr	6620	2389	0.36	0.00004 ± 0.00001	40.05 ± 1.49	0.0488 ± 0.0009	159 ± 12
14.1	m,osc/h,p	468	196	0.42	0.00078 ± 0.00020	43.50 ± 3.00	0.0529 ± 0.0025	146 ± 8
~~15.1~~	e,osc,p,fr	1440	590	0.41	0.00020 ± 0.00008	42.72 ± 1.85	0.0495 ± 0.0010	149 ± 6
16.1	m,osc/h,p	1084	371	0.34	0.00025 ± 0.00009	41.59 ± 2.61	0.0500 ± 0.0011	153 ± 8

Site grain type and analysis location: p = prism, fr = fragment, e = end, m = middle
Site CL imagery: osc = oscillatory zoned, h = homogenous
Abbreviations follow those of Nutman *et al.* (2013)
All analytical errors are given a 1σ
$^{238}U/^{206}Pb$ and $^{207}Pb/^{206}Pb$ ratios are uncorrected for common Pb
*Corrected for common Pb using the ^{207}Pb correction method of Compston *et al.* (1984)
~~Rejected~~ Excluded from age calculations - see Table 3.1 for explanation

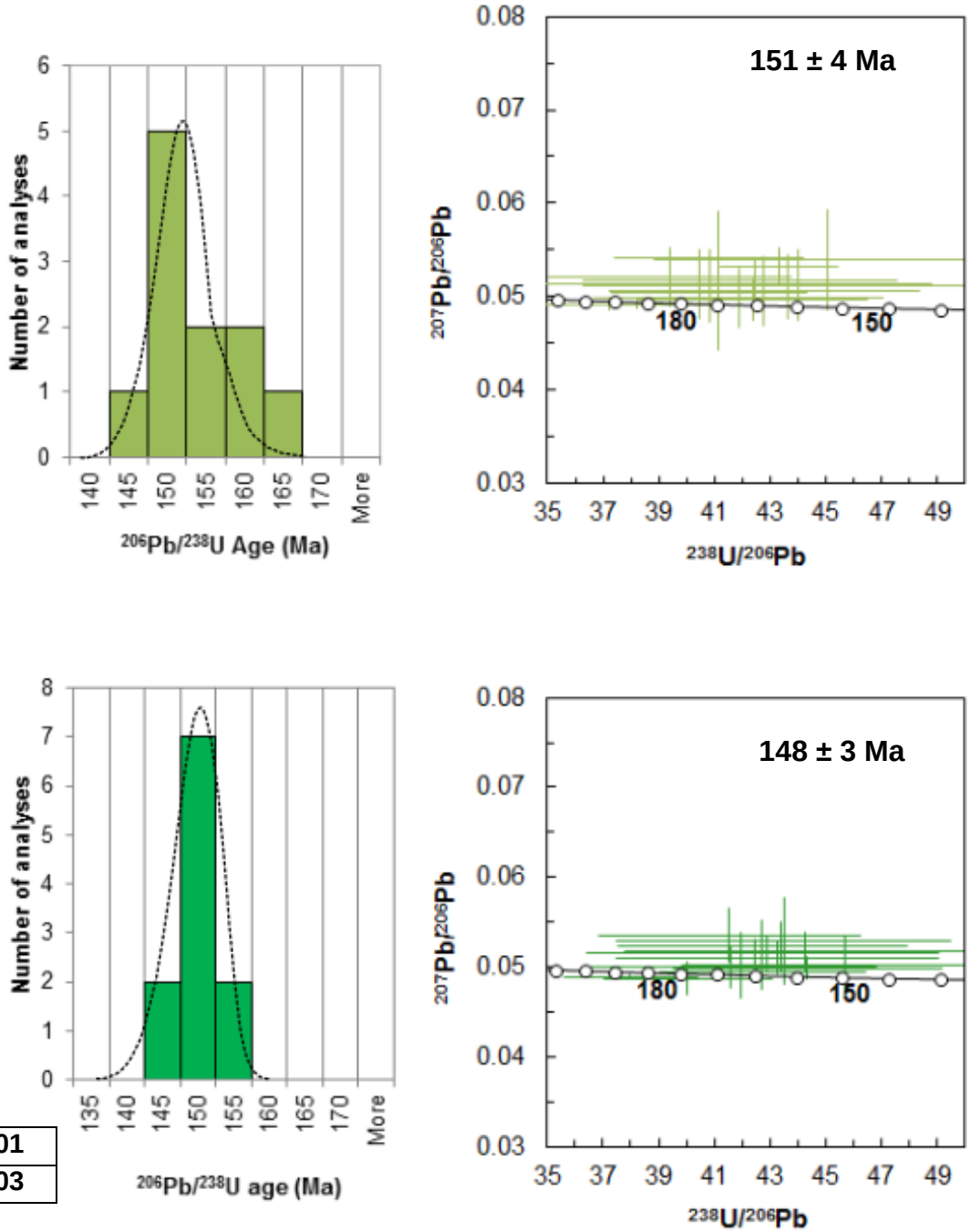

Figure 3.4 - Left side; ^{206}Pb/^{238}U cumulative frequency histograms. Using a bin size of 5 Ma, the stacked histograms were created using the Microsoft Excel Data Analysis add-in. The data used to produce the graphs was corrected for common Pb using the ^{207}Pb correction method of Compston *et al.* (1984)

Figure 3.5 - Right side; Tera-Wasserburg Concordia plots (Tera and Wasserburg 1972) of ^{238}U/^{206}Pb against ^{207}Pb/^{206}Pb created using Isoplot 4.15 (Ludwig 2008). Any rejected analyses have not been included in the diagrams; they have also been excluded from age calculations. *^{238}U/^{206}Pb and ^{207}Pb/^{206}Pb ratios are uncorrected for common Pb*

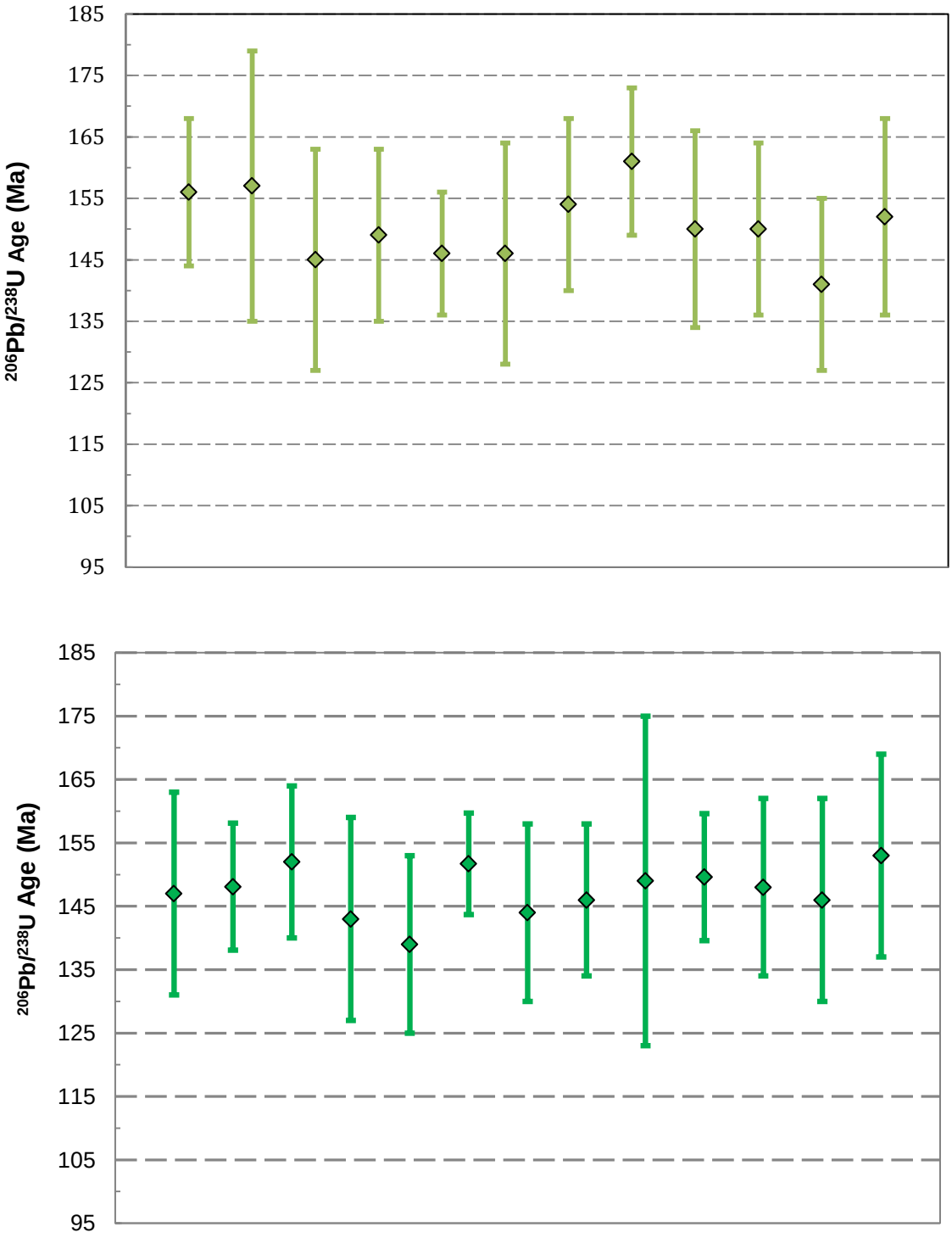

	15NT_01
	15NT_03

Figure 3.6 - (top and base) $^{206}Pb/^{238}U$ ages (Ma) of zircon grains from Sample 15NT_01 (top) and Sample 15NT_03 (base). Corrected for common Pb using the ^{207}Pb correction method of Compston *et al.* (1984)

15NT_01: Mean = **150.7 ± 3.8 Ma** [2.6%], 95% confidence, MSWD = 0.71, probability = 0.73 (error bars are 2σ)

15NT_03: Mean = **148.4 ± 3.1 Ma** [2.3%], 95% confidence, MSWD = 0.36, probability = 0.98 (error bars are 2σ)

3.4.2 Zirconium-saturation thermometry

As previously identified, there are some zircon grains that present regions of growth zone truncation, however no inherited cores were observed. Seeing as no inherited cores were identified this lends to the melt being originally hot and initially zircon under-saturated (Nutman *et al.* 2009, and references therein). This can be tested using zirconium- (Zr-) saturation thermometry. The relation between zircon saturation (also crystallisation and melt composition) was first investigated by Watson (1979) and revisited by Watson and Harrison (1983). The saturation of zircon is given in Equation 3.3 where $D_{Zr}^{zircon/melt}$ is the ratio of Zr concentration (ppm) in zircon (~476,000 ppm, Miller *et al.* 2003) to that of the saturated melt, T is the absolute temperature in kelvins (however, all temperatures referred to in this investigation have been converted to $°C$) and M is the cation ratio or a compositional factor that accounts for dependence of zircon solubility on SiO_2 and peraluminosity of the melt [(Na + K + 2·Ca)/(Al·Si)]. Equation 3.3 can be rearranged to make T the subject, yielding a geothermometer for melt demonstrated in Equation 3.4.

Section 3.2.2 '*why zircon?'* highlights the highly applicable nature of zircon as a geochronological tool for U-Pb dating; furthering on this, the behaviour of zircon during magma production and evolution is particularly significant as it acts as a host for several widely utilised trace elements. Particularly useful for this investigation is the trace element Zr; the amount of whole-rock Zr (ppm) has been used to identify the zircon saturation temperatures, which can be in turn be utilised to determine whether or not zircon was an early or late stage crystallising phase within the original melt (Hoskin and Schaltegger 2003).

$$ln\, D_{Zr}^{zircon/melt} = \{-3.8 - [0.85(M-1)]\} + 12900/T \qquad \text{Equation 3.3}$$

$$T_{Zr} = 12900/\left[2.95 + 0.85M + \ln\left(\frac{496000}{Zr_{melt}}\right)\right] \qquad \text{Equation 3.4}$$

Table 3.4 - **Results of Zr-saturation thermometry**

Nantai porphyry-skarn Mo-(Cu) (aplite dykes)				
Sample	**SiO_2 (wt.%)**	**M**	**Zr (ppm)**	**T (°C)**
15NT_01	78.6	1.3	41	682
15NT_02	76.9	1.4	49	695
15NT_03	74.9	1.5	51	688
15NT_A	80.7	0.5	31	714
15NT_B	76.7	0.4	44	748
Nannihu Mo granite porphyry				
Sample	**SiO_2 (wt.%)**	**M**	**Zr (ppm)**	**T (°C)**
14LN_1	76.1	1.2	143	791
14LN_2	74.1	1.3	123	774
14LN_3	77.0	1.1	152	802
14LN_4	73.9	1.1	136	793
Shangfanggou Mo granite porphyry				
Sample	**SiO_2 (wt.%)**	**M**	**Zr (ppm)**	**T (°C)**
14LS_06	77.1	1.2	75	740
14LS_09	79.1	1.2	69	733
Shibaogou Mo granite porphyry				
Sample	**SiO_2 (wt.%)**	**M**	**Zr (ppm)**	**T (°C)**
07_13	72.1	1.2	97	760
07_14	73.8	1.4	133	768
07_15	73.4	1.4	106	747
07_16	74.9	1.4	93	742

Results of Zr-saturation thermometry for samples from the Nantai, Nannihu, Shangfanggou and Shibaogou Mo deposits, using the methodology and equations as outlined by Watson and Harrison (1983), and Miller *et al.* (2003).

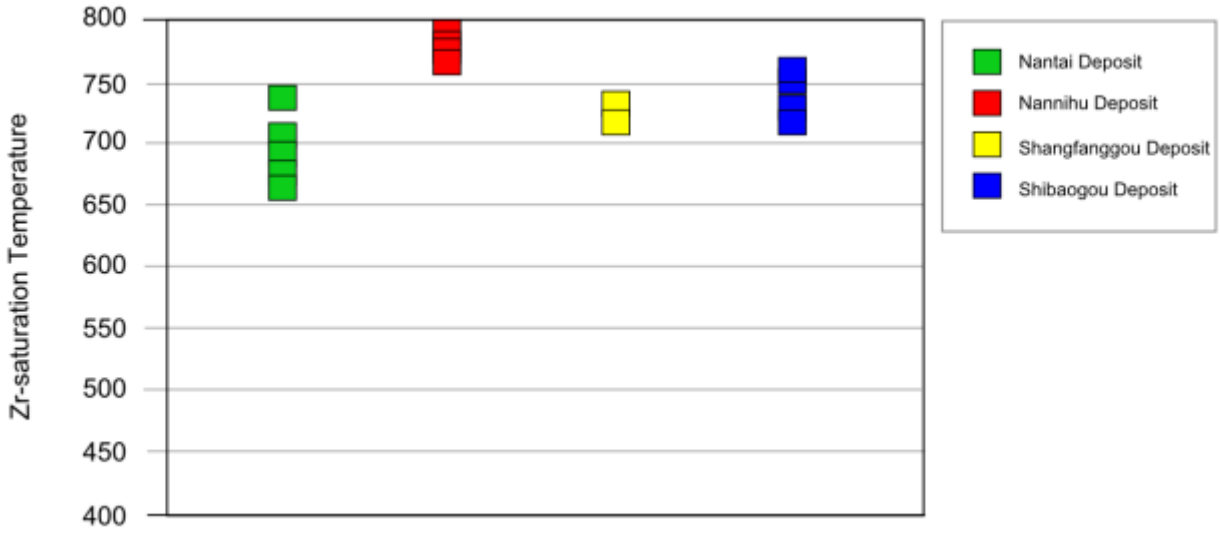

Figure 3.7 - Zr-saturation temperatures for the Nantai, Nannihu, Shangfanggou and Shibaogou Mo deposits

Geochemical data (Chapter 5) for the Nantai porphyry-skarn Mo-(Cu) deposit was used as the inputs to determine the results in Table 3.4 and displayed in Figure 3.7. Three other sites were chosen to complete a comparative study of Zr-saturation temperatures. Geochemical data for the Nannihu, Shangfanggou and Shibaogou deposits is provided by Bao *et al.* (2014). The Nantai porphyry-skarn Mo-(Cu) deposit shares similar features with these sites; attributes include genetic type (Mo-bearing granite porphyries), spatial distribution (S-NCB; Figure 3.8) and metallogenic epochs (Late Jurassic to Early Cretaceous). The temperatures calculated for the four deposits provide the upper temperature limits of zircon crystallisation within a melt. A comparative study between deposits of similar type and setting is important for further defining mineralisation in the broader system. For example, the highest temperature of zircon saturation that the Nantai deposit demonstrates is 748°C; whereas the highest temperatures that the Nannihu, Shangfanggou and Shibaogou deposits exhibit are 802°C, 740°C and 768°C, respectively. If a melt phase of which encompasses Mo and Cu is stable across a temperature range that overlaps these maximum zircon saturation temperatures (e.g. 700 - 1000°C) then it is possible for the early crystalising zircon grains within the melt to take up mineralisation phases as inclusions.

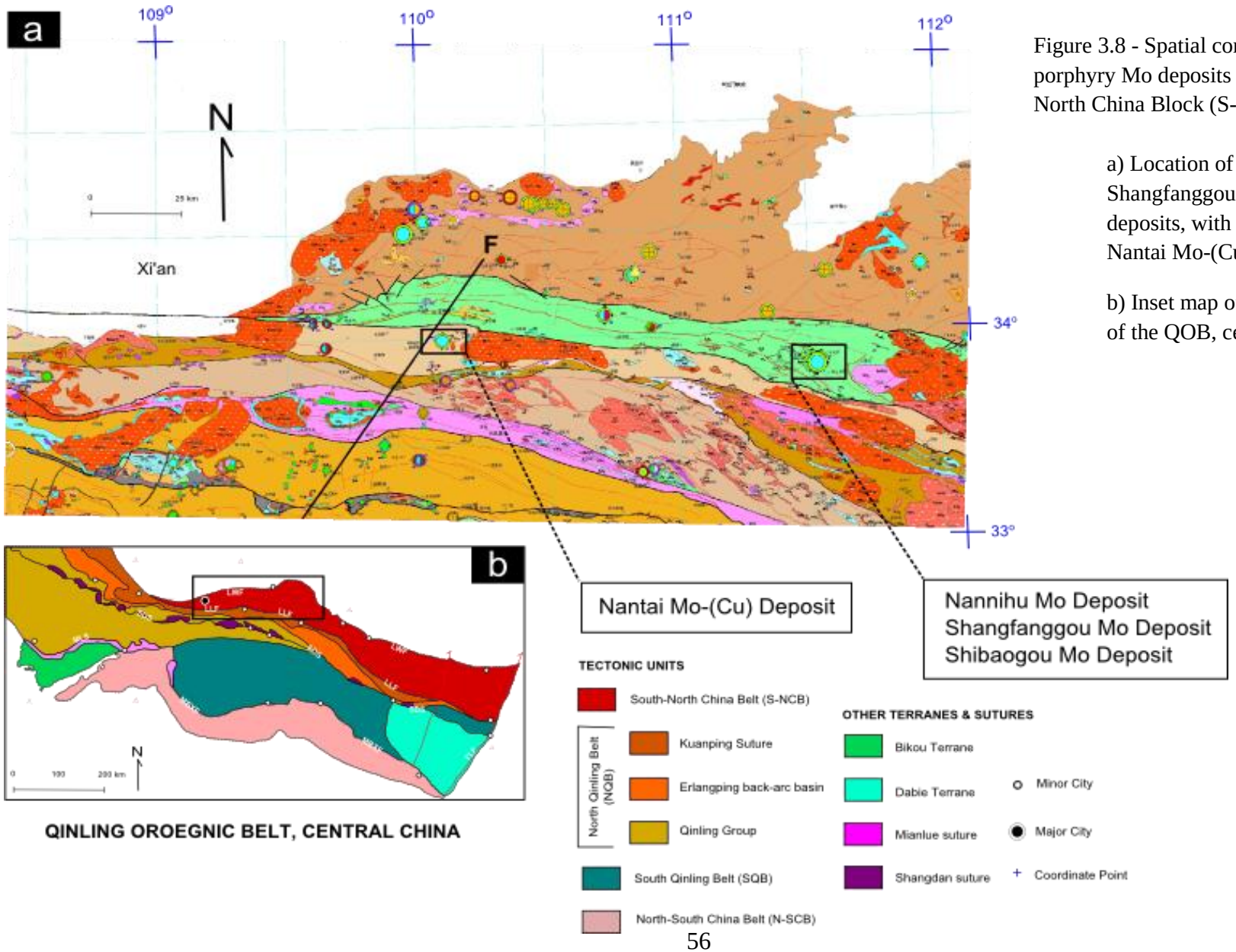

Figure 3.8 - Spatial comparison of porphyry Mo deposits within the Southern North China Block (S-NCB)

a) Location of the Nannihu, Shangfanggou and Shibaogou Mo deposits, with relation to the Nantai Mo-(Cu) Deposit

b) Inset map of the tectonic units of the QOB, central China

3.5 INTERPRETATION OF ZIRCON CRYSTALLISATION

It is evident from field-relationships, petrographic (Chapter 4) and geochemical (Chapter 5) studies that the fine-grained units cross-cutting the Nantai porphyry-skarn Mo-(Cu) deposit are aplite dykes. The presence of well-developed oscillatory zoning from the zircons grains separated from two of these aplitic intrusives (15NT_01 and 15NT_03) further complements the conclusion that the grains originated from a magmatic source rather than an environment typified by a metamorphic regime, or were alternatively produced by high temperature hydrothermal alteration (Corfu *et al.* 2003). Thus, all reporting here with regards to $^{206}Pb/^{238}U$ ages (corrected for common Pb using the ^{207}Pb correction method of Compston *et al.* 1984) of samples 15NT_01 and 15NT_03 reflect magmatic events.

The $^{206}Pb/^{238}U$ ages obtained for the zircon populations from both samples are statistically indistinguishable in age, i.e.

15NT_01 = **150.7 ± 3.8 Ma** (95% confidence, MSWD = 0.74)

15NT_03 = **148.4 ± 3.1 Ma** (95% confidence, MSWD = 0.42)

This suggests that the two intrusions were emplaced contemporaneously, or within a short time frame of each other. Therefore, they might represent a single magmatic event. As previously mentioned, the granitic pluton (host of the Nantai porphyry-skarn Mo-(Cu) deposit), has been dated yielding an age of 151 ± 1 Ma, with Mo-bearing granitoid samples also dated producing ages ranging from 146 ± 2 Ma to 151 ± 2 Ma (Ke *et al.* 2012). With the ages of these magmatic events in mind, it is a fair assumption that the pluton began its journey through the crust during the Late Jurassic, with genetically related cross-cutting aplitic dykes occurring soon after (within ~3 Ma). As evidence from the ages of the molybdenite samples, it can be inferred that mineralisation is associated with the system from the onset of the host pluton. Both the host pluton and the later-stage fine-grained dykes cross-cutting the deposit are mineralised (Mo-Cu bearing).

CHAPTER FOUR – PETROGRAPHY

4.1 INTRODUCTION

Standard transmitted and reflected petrographic descriptions were completed for all of the mineralised samples and host rocks of the five examined deposits within the Qinling Orogenic Belt (QOB), China. Petrographic descriptions are complimented by mineralogical analyses including X-ray diffraction (XRD), scanning electron microscopy coupled with energy-dispersive X-ray spectroscopy (SEM-EDS) and Raman spectroscopy (analytical details for each method are outlined in Appendix B: Sample list; Appendix D: SEM-EDS results; Appendix E: XRD results). The deposits within the QOB that have undergone petrographic analyses are:

NANTAI Mo-(Cu) DEPOSIT (aplite, lamprophyres, marl, dolomitic marble)

MIAOYA REE DEPOSIT (carbonatite)

LONGTOUGOU (orogenic) Au DEPOSIT (baryte-vein)

LIUJIAXIA (orogenic) Au DEPOSIT (siltstone)

DAMOGOU Zn-CaF_2 DEPOSIT (fluorite-vein)

Each deposit is described systematically and includes; i) a description and classification of the rock units present, ii) detailed mineralogical descriptions from thin-sections; and iii) paragenesis of the deposit according to mineralogical and textural characteristics. This study provides the first detailed petrographic study of deposits for which there is little existing English literature. An important outcome will be to provide new petrographic knowledge to help further constrain different mineralisation styles within the broader context of the tectonic evolution of the QOB.

4.2 METHODS

4.2.1 Principles of X-ray Diffraction

X-ray diffraction (XRD) is an analytical technique that can identify minerals, as well as other crystalline materials. XRD is a useful method of analysis applicable to Earth Sciences as the technique allows for information to be gained with regard to ordered atomic structures in a variety of geological materials. The ordered arrangement of atoms within crystalline materials has a direct relationship with the scatter diffraction of the incident X-rays – thereby creating patterns that can be matched/compared with known substances.

Seventeen samples were first crushed for 10 - 15 seconds into a fine powder using a TEMA chromium steel ring mill, at the University of Wollongong (UOW). The mill was rinsed with quartz between each sample. XRD analyses were carried out utilising a Spellman DF3 X-ray generator run at 35 kV and 1 kW of power, with a Phillips copper X-ray tube tower and Phillips PW1316/91 goniometer. The regions of interest were registered through scanning between 4° - 70° 2 theta (θ). The mineralogical assemblage of the samples were then determined using a combination of TRACES V4 and Siroquant V3 software. TRACES V4 software was first utilised to assign the quartz 1010 peak to 26.66° 2θ. This was then followed by sample analysis using Siroquant V3 software which contains an absorption correction that is essential for quantitative phase analysis. The potential mineralogical assemblage of the sample was determined using a library of waveforms for common rock-forming minerals.

4.2.2 Principles of SEM-EDS

A scanning electron microscope (SEM) uses a beam of electrons, carrying significant kinetic energy in order to generate a variety of different signals when focused at the surface of a thin section. The electron-sample interactions provide signal-derived information, such as chemical composition, crystalline structure and texture (Goldstein *et al.* 2003). A variety of signals are produced by electron-sample interactions, two of which play a very important role in SEM investigations; secondary and backscattered electrons are produced on the firing of electrons at an angle of incidence to the solid specimen, some of which reach the detector. The instrument scans a fine electron probe over the specimen and, using the information made available to the detector reconstructs an electron image and digital raster maps (based on elemental signatures) from the signals generated within the target sample (Goldstein *et al.* 2003). The SEM is routinely used with integrated analytical detectors, such as energy-dispersive X-ray spectroscopy (EDS). EDS when coupled with a SEM allows for elemental characterisation of a sample, whereby elements contained in a specimen are automatically detected. This is an extremely useful method to compliment standard petrographic analysis, as elemental maps can be produced and even layered to better define mineralogical phases within thin section (Goldstein *et al.* 2003).

SEM-EDS analyses were carried out at the Electron Microscope Centre, Australian Institute of Innovative Materials (AIIM), Innovation Campus (IC), UOW using a JEOL JSM-6490LA coupled to an Oxford Instruments X-max^{n} 80mm^{2} silicon drifted EDS detector. All EDS analyses were conducted at accelerating voltages between 15 – 30 kV (higher voltages used to unambiguously identify molybdenum from a sulphur rich matrix). Cathodoluminesence images (CL images) were acquired on the same instrument using a Gatan MonoCL4+ in white panchromatic (i.e. bypassing the spectrometer) mode at 5kV. Technical assistance and ongoing support was provided by Professional Officer and Microscopist Dr Mitchell Nancarrow.

4.2.3 Principles of Raman

Raman spectroscopy is a technique which utilises crystal vibrations to elucidate the molecular structure of a sample. The technique is commonly coupled with mid-infrared (IR) vibrational spectroscopic studies as a method to assist in further refining the vibrational modes of a molecule (involving vibration symmetries, and polar- and non-polar- groups) (Larkin 2011). The technique involves the study of the interaction of radiation with molecular vibrations, similar to that of IR spectroscopy. Raman differs in that the technique relies on an inelastic light-scattering event, whereby the incident photon loses a proportion of its energy with relation to vibrations (at molecular level). The result is scattered energy being dispersed, as represented by a photon with reduced frequency (Larkin 2011). This technique, unlike XRD is a non-destructive means of analysing samples which can be undertaken on both standard and polished thin sections. The importance of Raman spectroscopy for petrographic studies is that the vibrational energy levels are unique to each molecule, and as such a 'fingerprint signature' is assigned to each individual molecule in the form of spectra (Dubessy *et al.*2012). The spectral signatures are able to provide important information on the molecular structure, dynamics and environment, due to a dependency on the masses of the atoms, the durability of their chemical bonds, and their geometric arrangement (Dubessy *et al.*2012). Coupled with SEM-EDS it is particularly useful. For example SEM-EDS may identify a mineral as alumina silicate (Al_2SiO_5), whereas Raman will distinguish the three polymorphs – sillimanite, kyanite and andalusite.

The samples were observed under a petrographic microscope, with areas of interest noted for resonance studies. Raman microspectroscopy analyses were carried out at the UOW using a JY HR800 green diode solid state laser, with a spatial resolution of 0.5 – 1 µm and spectral resolution starting at 1.5 cm^{-1}. The system is equipped with optical magnification of x10, x50 and x100, allowing for multi-resolution examination of the sample. Specific to the analytical session, a wavelength of 532 cm^{-1} was utilised with the laser using a power setting of 42 mW to excite the source. A shift of 6 cm^{-1} was needed to be applied to all results to fit instrument calibration.

4.3 NANTAI Mo-(Cu) DEPOSIT - APLITE

4.3.1 Classification

In hand specimen this unit consists of a light pinkish-cream to grey white, uniformly *very* fine-grained intrusive rock with common indistinct pale-pink alkali feldspar phenocrysts (1-3 mm) and light-grey quartz (1-5 mm). Uncommon to rare pyrite is present throughout the unit. No observable relationship or coexistence between the pyrite and multiple cross-cutting quartz veins throughout the unit is distinguishable with the unaided eye; however is identified in thin section. Polished thin section, XRD and SEM-EDS analysis indicate a mineral assemblage of major minerals: quartz (40%), plagioclase (15%), alkali feldspar (10%), and micas (5%); accessory minerals: biotite, zircon, apatite (20% total); secondary minerals: sericite, pyrite, molybdenite and chalcopyrite (10%).

In thin section this unit presents as a holocrystalline, porphyritic intrusive igneous rock. With regards to granularity, the unit can be described as aphanitic whereby all minerals, other than the phenocrysts cannot be distinguished by the unaided eye. The unit can be further classified as microcrystalline (as opposed to cryptocrystalline), whereby the minerals can be identified in thin section; the fine-grained matrix has minerals large enough to demonstrate polarisation colours. Herein, this unit will be referred to as an aplite.

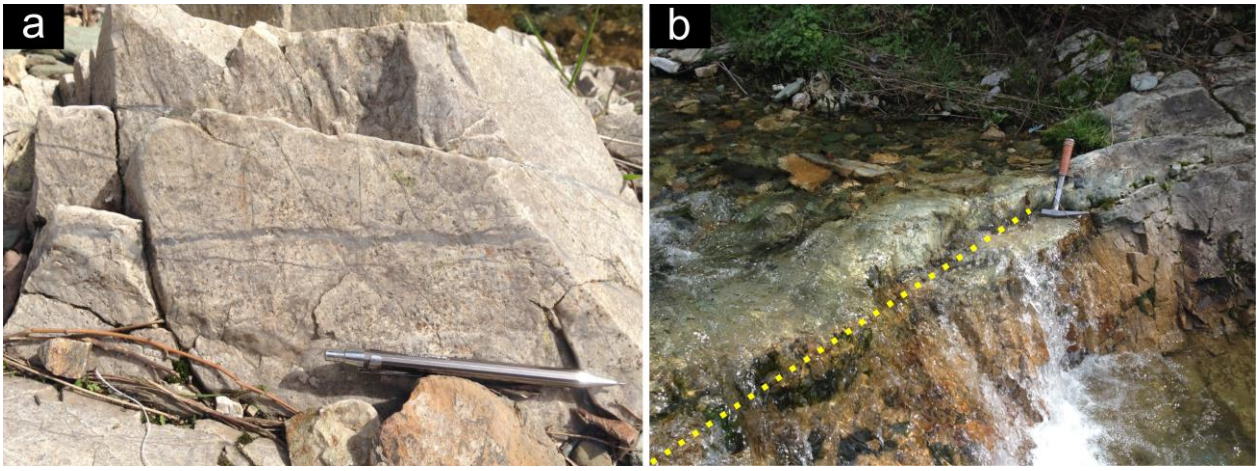

Figure 4.1 - Nantai Mo-(Cu) deposit field work photographs

a) Representative sample of the aplite unit
b) Contact between two units, i.e. aplite before and dolomitic marble after the knick-point identified by a yellow dotted line

4.3.2 Minerals

Quartz SiO_2

In this unit, the most abundant mineral is quartz (40%) occurring substantially in the matrix, and as phenocrysts. Quartz grains within the matrix of the unit are too small (1-10 μm) to distinguish features such as the development of the faces on grains, and specification as to the three-dimensional shape of individual crystals. Quartz phenocrysts average between 100 – 500 μm in size, with occasional larger 1 – 5 mm grains also occurring. Some of the randomly-dispersed grains demonstrate sub-rounded to rounded crystal shape (Figure 4.4b). This may be the result of the original euhedral quartz grains being dissolved, or resorbed as the original melt experiences influence from the injection of different magmas or upon decompression, and hence has a change in eutectic composition as the melt evolved. Another prominent feature throughout the unit is the widespread presence of non-unidirectional quartz veins that commonly cross-cut other minerals (including quartz phenocrysts), thereby indicating late-stage high-silica entry into the system. It is also common to observe two or more quartz veins intersecting one another (Figure 4.4c). Notably, in thin section a localised change in grain size of quartz crystals can also be observed. These regions of comparatively coarse-grained quartz may demonstrate fragments of slightly older aplite, which overprint the main phase of crystallisation. Mineralisation (in the form of pyrite, chalcopyrite and molybdenite) occurs through the groundmass/matrix; however occurs more commonly within quartz and quartz veinlets throughout thin section. In the quartz veins mineralisation appears to occur in pits, and to be fairly disseminated (Figure 4.7). Pyrite is often surrounded by a halo of sericitic alteration, a process of mineral alteration caused by hydrothermal fluids invading the unit (Figure 4.8).

Plagioclase $NaAlSi_3O_8 – CaAl_2Si_2O_8$

Plagioclase grains show extensive alteration, to such an extent that diagnostic features such as low relief, colourless nature (in PPL) and oscillatory zoning become difficult to identify. The prominent feature, lending to identification of the mineral as plagioclase rather than alkali feldspar is the retention of tabular or lathlike habit and residual multiple twinning (Figure 4.6m). Alteration of earlier feldspar laths resulted in the

grains appearing dusty, assumedly due to be the result of fine-grained disseminated hematite and sericite (Figure 4.6n). Noteworthy are grains with a distinct dark brown colour in PPL (Figure 4.6p). The core of some feldspars have been replaced with epidote, displaying high-order birefringence colours.

Alkali feldspar $KAlSi_3O_8 – NaAlSi_3O_8$

Myrmekitic texture is a feature commonly observed throughout the aplite (Figure 4.5) whereby there is an intimate intergrowth of quartz and feldspar. In PPL the quartz can be identified by a higher-relief comparable to the alkali feldspar (Figure 4.5i). This texture has an important application for suggesting metasomatism in the intrusive environment where contact metamorphism is involved (processes typical of a skarn setting). This texture is also indicative of low pressures and therefore emplacement at high crustal levels, and high temperature environments resulting in the exsolution of quartz and feldspar.

4.3.4 Paragenesis:

It is inferred that the sampled aplite from the Nantai Mo-(Cu) deposit has opened as a vein in a larger granitic body that was almost crystallised to a solid state. Assumedly a fracture occurred in the granitic body as it cooled and contracted. Fresh granitic magma from the source chamber below flows/intrudes into the fracture. It is inferred that the magma is a mixture of both crystals and melt, evident in the large quartz phenocrysts occurring throughout the much finer groundmass. The rapid cooling of the melt resulting in the fine-grained nature of the intrusive can be accounted to a decrease in pressure (within the newly released magma into the fracture) leading to volatiles being released/exsolved out of the magma. The release of volatiles increases the melting point and then rapidly ‘freezes’ the magma into what can now be described as aplite. The quartz veins, which are commonly observed throughout this unit, are interpreted as the conduits for the release of water and volatiles. Mineralisation occurring both within and proximal to the veinlets suggests that as the cooling aplite exsolved, the ore-forming metals and sulphides (e.g. FeS_2, CuS_2, MoS_2) were being precipitated from the associated fluids.

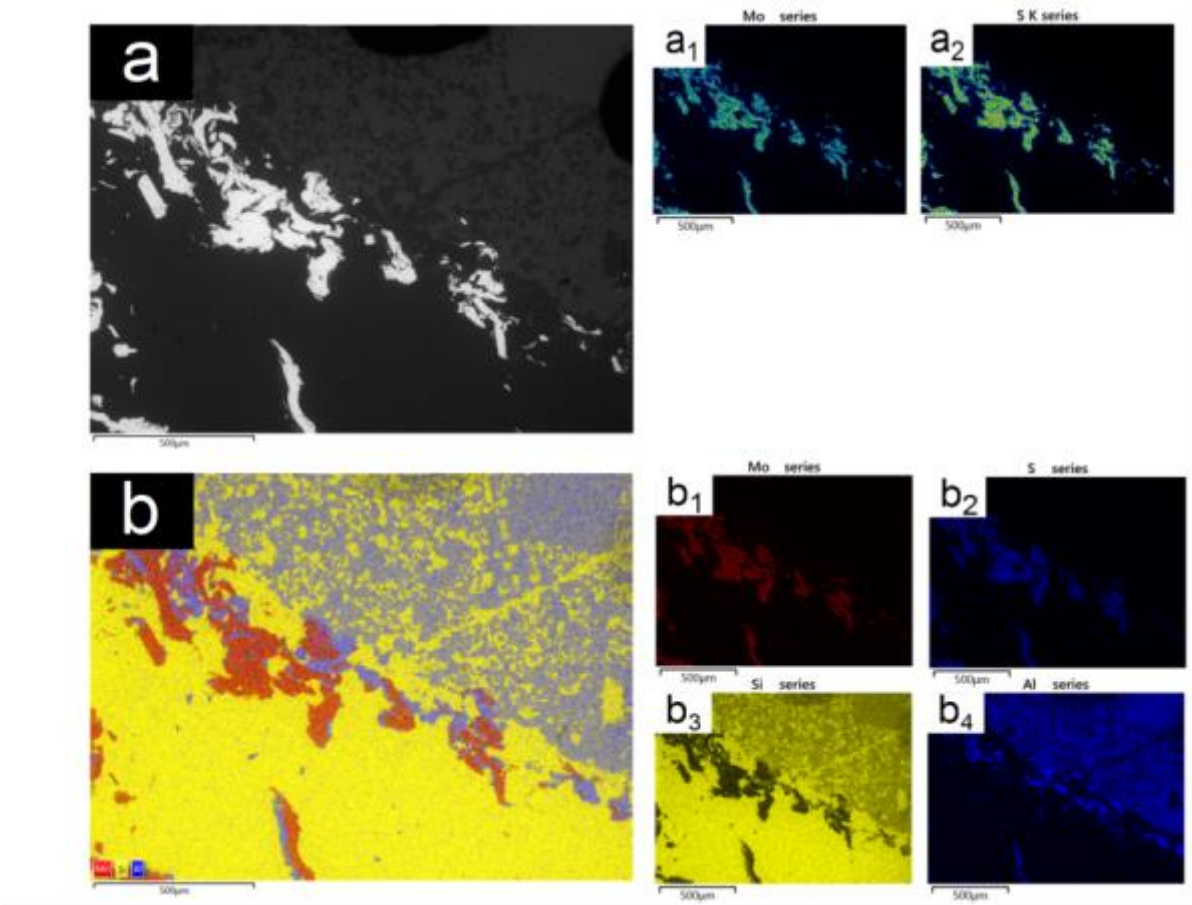

Figure 4.2 - SEM-EDS results of Nantai Mo-(Cu) deposit sample 15NT_A

a) Electron image taken of thin section 15NT_A

a_1 & a_2) Discrete colour maps displaying the occurrence of Mo and S within sample 15NT_A

b) Layered image of thin section 15NT_A

b_1) – b_4) Raster maps displaying the occurrence of Mo, S, Si, and Al within sample 15NT_A. As expected, the Mo-raster and the S-raster plot over the same areas within the region of interest indicative of molybdenite (MoS_2)

Refer to Appendix D for further SEM-EDS results of Nantai Mo-(Cu) deposit sample 15NT_A

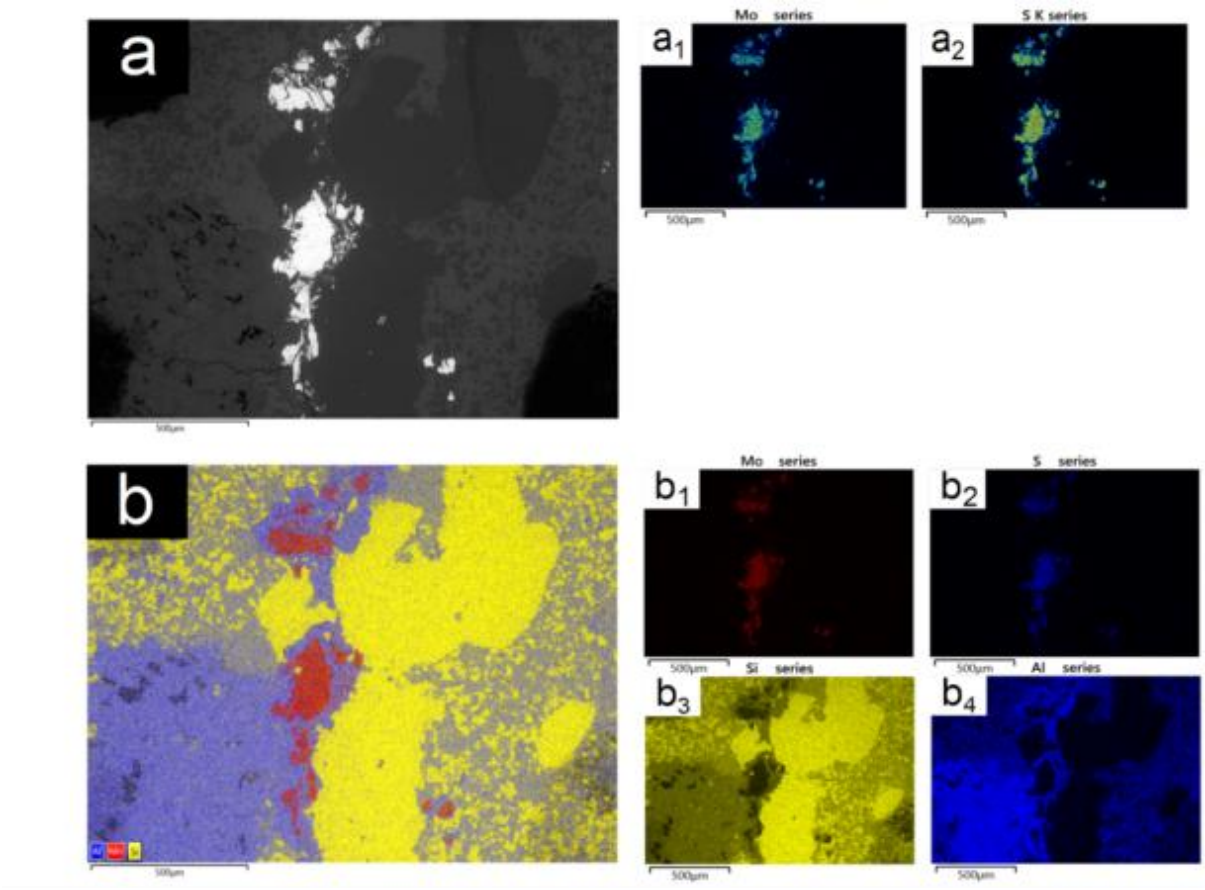

Figure 4.3 - SEM-EDS results of Nantai Mo-(Cu) deposit sample 15NT_A

a) Electron image taken of thin section 15NT_A

a_1 & a_2) Discrete colour maps displaying the occurrence of Mo and S within sample 15NT_A

b) Layered image of thin section 15NT_A

b_1) – b_4) Raster maps displaying the occurrence of Mo, S, Si, and Al within sample 15NT_A. As expected, the Mo-raster and the S-raster plot over the same areas within the region of interest indicative of molybdenite (MoS_2)

Refer to Appendix D for further SEM-EDS results of Nantai Mo-(Cu) deposit sample 15NT_A

Table 4.1 - Mineral abbreviations are in conjunction with those outlined by Whitney and Evans (2010). Apply these to all deposits

Symbol	Mineral name
Act	actinolite
Afs	alkali feldspar
Ank	ankerite
Au	gold
Ap	apatite
Bn	bornite
Brt	baryte
Bt	biotite
Cal	calcite
Ccp	chalcopyrite
Dol	dolomite
En	enstatite (ortho-)
Fa	fayalite
Fl	fluorite
Fo	forsterite
Gn	galena
Hem	hematite
Lct	leucite
Mag	magnetite
Mgs	magnesite
Mo	molybdenite
Ms	muscovite
Nph	nepheline
Phl	phlogopite
Pl	plagioclase
Po	pyrrhotite
Py	pyrite
Qtz	quartz
Rt	rutile
Sa	sanidine
Ser	sericite
Sp	sphalerite
Srp	serpentine
Tlc	talc
Ttn	titanite (sphene)
Tr	tremolite
Zrn	zircon

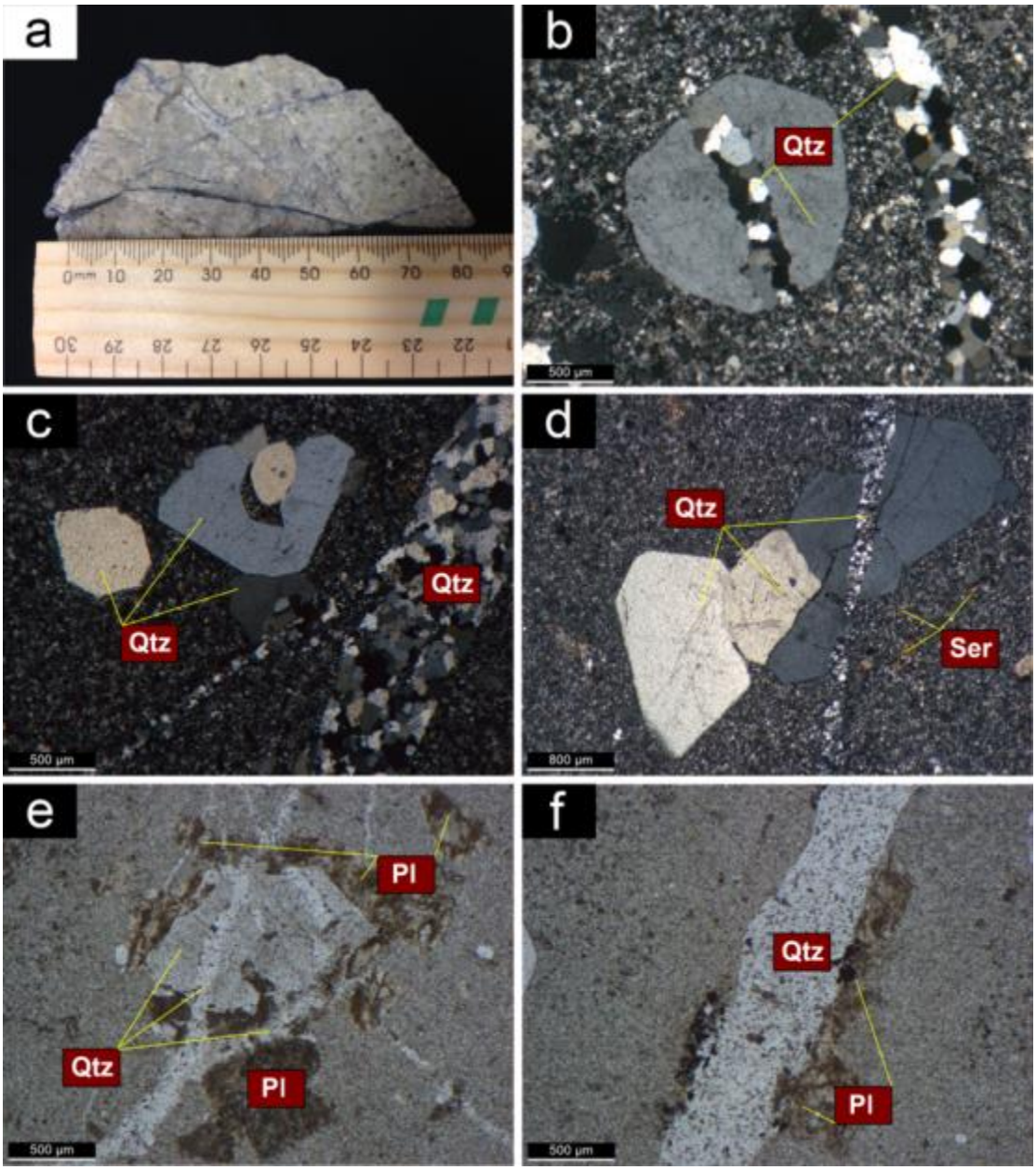

Figure 4.4 - **Nantai Mo-(Cu) Deposit – Aplite**
(a) 15NT_A, fine-grained aplite hand sample, the rapid cooling of the melt resulted in the fine-grained nature of the intrusive rock, and can be due to volatiles being released out of the magma; (**b)** 15NT_01 – XPL, cross cutting relationships common in the aplite, particularly prevalent with larger quartz phenocrysts; **(c)** 15NT_02 – XPL, two generations of quartz veinlets occurring with larger corroded quartz phenocrysts (500 – 750 µm) representing late-stage high-silica entry into the system; **(d)** 15NT_03 – XPL, sericite alteration occurs as small patches within the fine-grained groundmass; **(e)** 15NT_B – PPL, multi-phase quartz veinlets, easily distinguishable due to their high relief overprinting an earlier quartz phenocryst which has disturbed an even earlier crystalising plagioclase grain; **(f)** 15NT_B – PPL, a plagioclase grain has been split by a later stage quartz veinlet

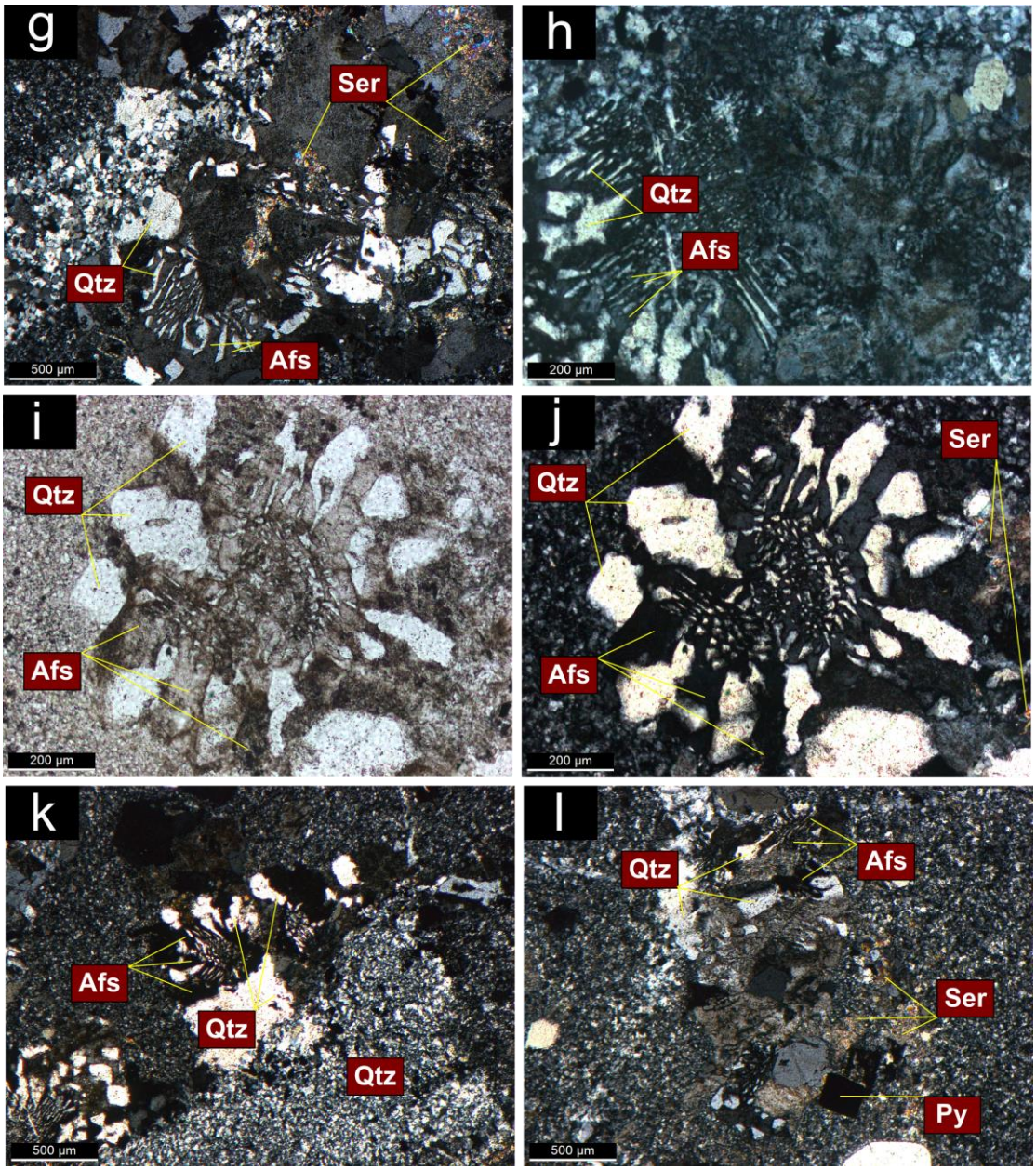

Figure 4.5 - **Nantai Mo-(Cu) Deposit – Aplite**
This plate shows the myrmekite and myrmekite-like textual growths of the Nantai Mo-(Cu) aplite, whereby commonly observed is the intergrowth of vemicular (worm-like) quartz and alkali feldspar (less commonly plagioclase). Mymekites are representative of metasomatism, and are believed to have formed from the production of excess silica (quartz) in the system which in turn replaces alkali feldspar. Important to this setting (skarn-porphyry) magnesian metasomatism can result in the replacement of alkali feldspar with myrmekite. **(g)** 15NT_A, typical myrmekitic texture and widespread sericite alteration is not restricted to certain mineral assemblages in the aplite unit; **(h)** 15NT_B, myrmekitic texture demonstrating intimate intergrowth of quartz and alkali feldspar; **(i)** 15NT_01 – PPL & **(j)** 15NT_01 - XPL, radial myrmekitic texture demonstrating intimate intergrowth of quartz and alkali feldspar; **(k)** 15NT_03 – XPL & **(l)** 15NT_02 – XPL, myrmekitic texture

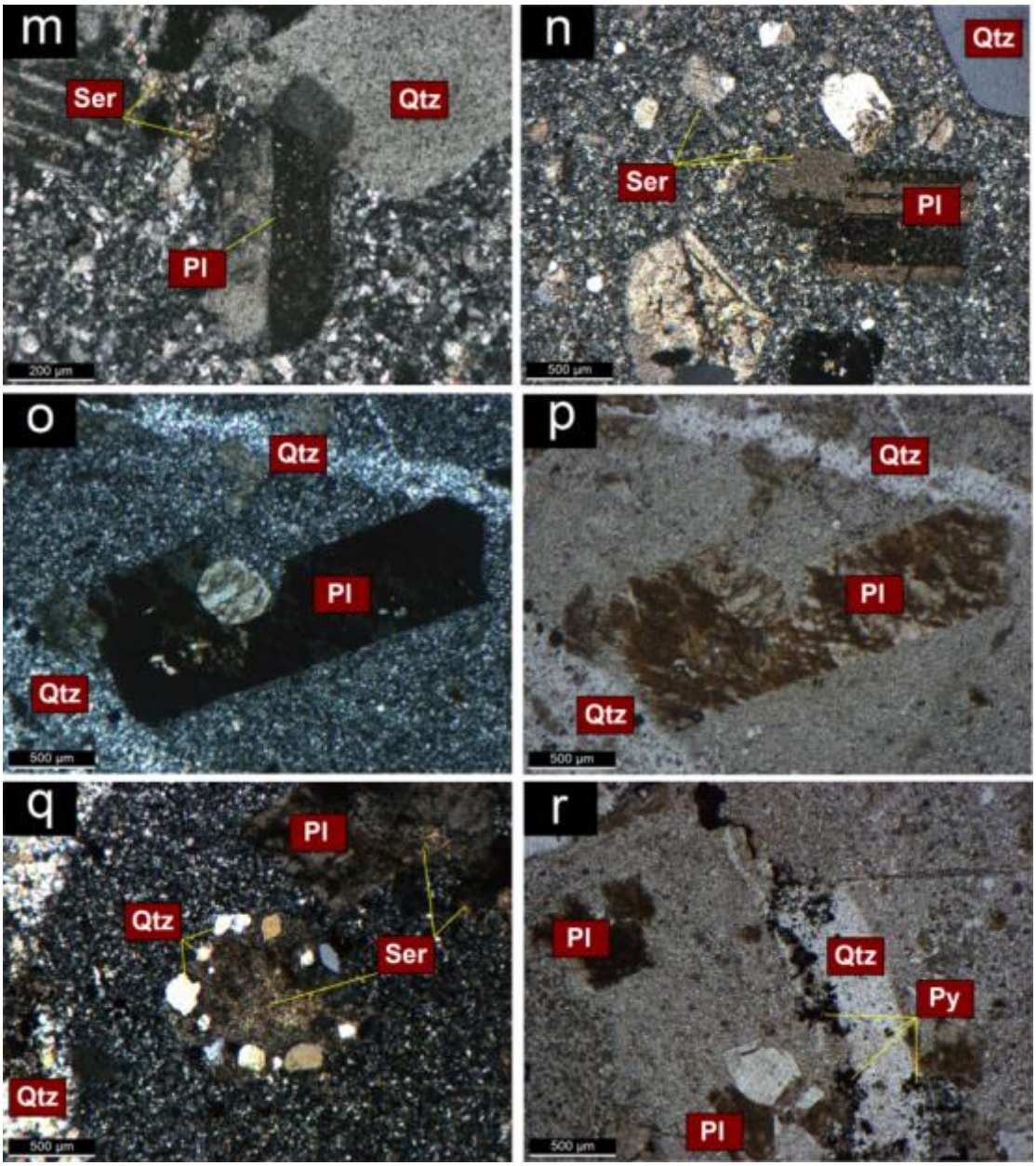

Figure 4.6 - **Nantai Mo-(Cu) Deposit – Aplite**
(m) 15NT_01 – XPL, sericite alteration is not confined to the periphery of grain boundaries, and rather is commonly observed within grains (in this instance a plagioclase grain, characteristic simple twinning) as a 'dusting' texture; (**n)** 15NT_03 – XPL, sericite alteration is not confined to particular minerals and instead occurs throughout all constituents. This indicates that in late-stage alteration most mineral grains were subject to seritisation; **(o)** 15NT_B – XPL & **(p)** 15NT_B – PPL, commonly feldspar grains demonstrate intense alteration, best evident in PPL whereby the grains demonstrate dark brown colouration. Although the grains have undergone alteration in most instances the tabular habit is maintained with clearly defined grain boundaries; **(q)** 15NT_A – XPL, quartz grains occur on the rim of an intensely sericitised alkali feldspar grain; **(r)** 15NT_A – PPL, quartz veins with mineralisation, overprinting earlier plagioclase grains

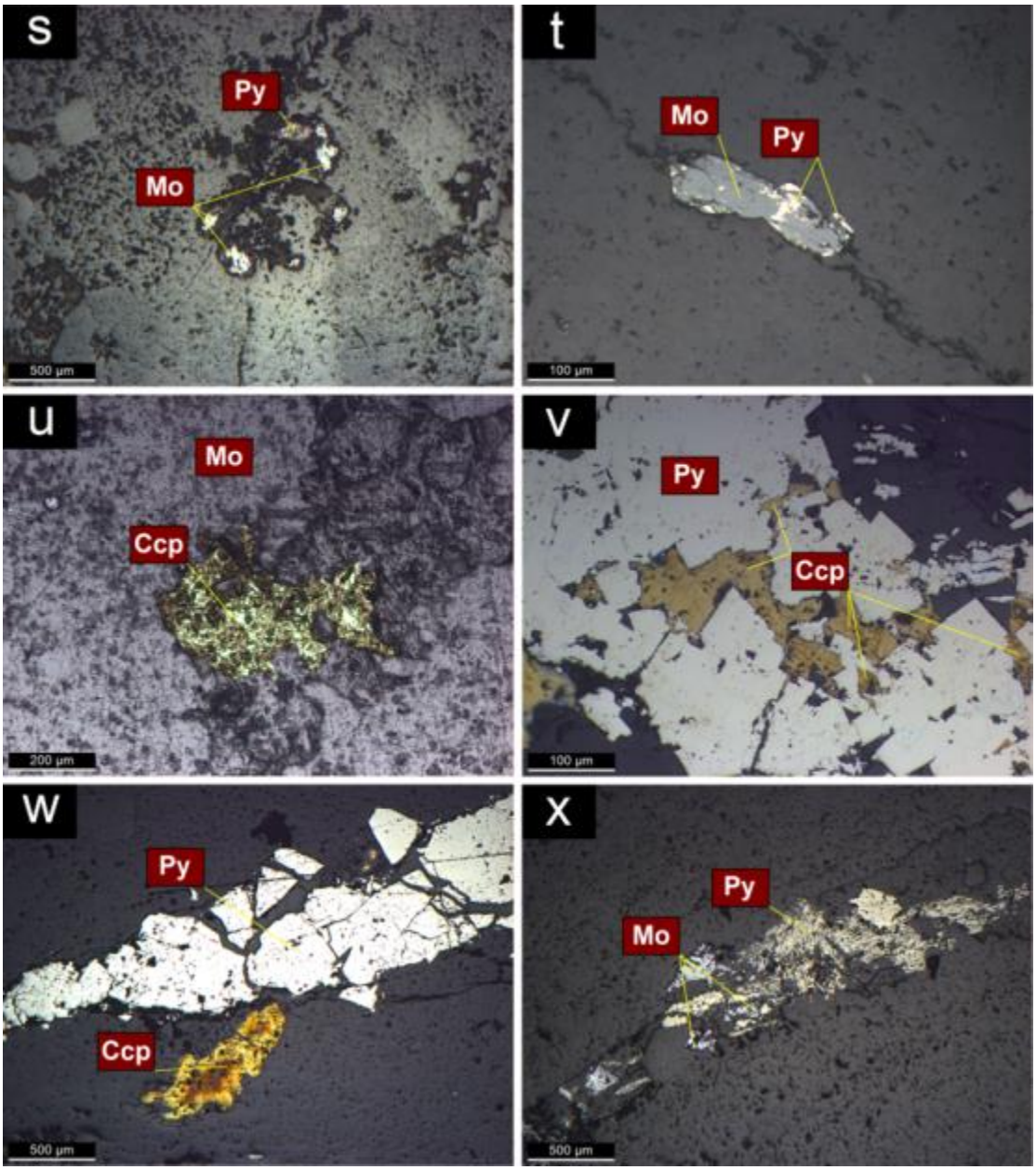

Figure 4.7 - **Nantai Mo-(Cu) Deposit – Aplite (mineralisation)**
(s) 15NT_A – PPL (reflected), finely disseminated and fracture-filling molybdenite and pyrite; **(t)** 15NT_01 – PPL (reflected), vein-type mineralisation where late fluids have recrystallised and precipitated molybdenite first followed by pyrite, which is observed as small, dispersed grains within the larger molybdenite mass; **(u)** 15NT_B – PPL (reflected), chalcopyrite occurs as a fracture fill within a larger molybdenite grain. The 'aluminium foil' texture can be accounted to late-stage sericitic alteration of the chalcopyrite; **(v)** 15NT_01 – PPL (reflected), chalcopyrite is commonly found in association with pyrite, in this instance the chalcopyrite is observed as fracture fill within a larger pyrite aggregated mass; **(w)** 15NT_01 – PPL (reflected), vein-type mineralisation (pyrite + chalcopyrite) further illustrating the importance of fluid movement through the aplite unit, and subsequent metalliferous precipitation; **(x)** 15NT_A – PPL (reflected), pervasive coarse grained quartz veins commonly demonstrate mineralisation where late fluids have recrystallised and precipitated primary pyrite, with secondary molybdenite

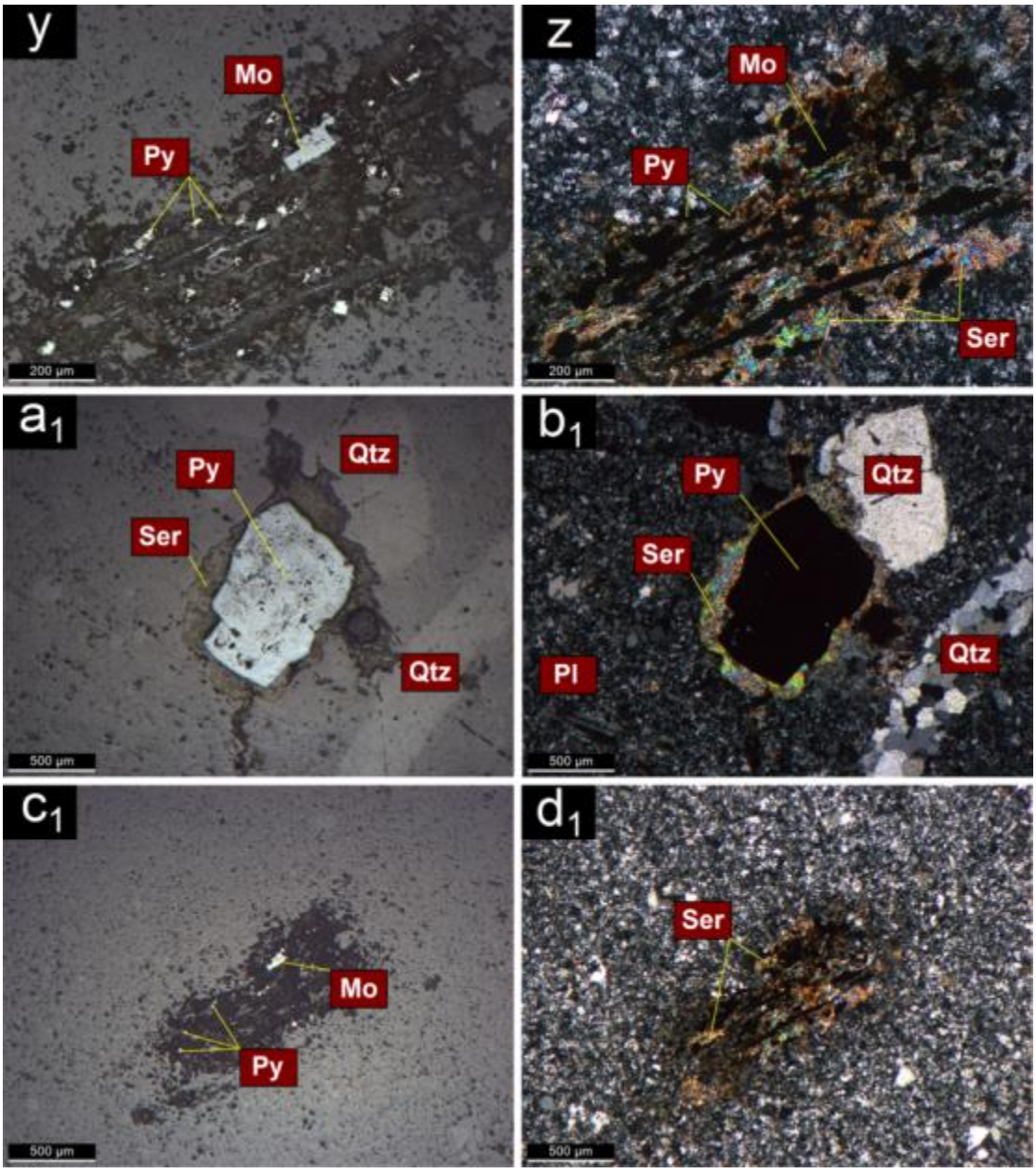

Figure 4.8 - **Nantai Mo-(Cu) Deposit – Aplite (mineralisation)**
This plate represents mineralisation associated with sericite alteration. Alteration commonly occurs as a 'halo' effect, whereby areas of high-order birefringence are observed around single grain boundaries, or around clustered/aggregated mineralised regions. Photomicrographs have been taken first in PPL (reflected) to demonstrate mineralisation, and are followed by XPL to illustrate the prevalent sericitic alteration, common to the Nantai Mo-(Cu) aplite unit. **(y)** 15NT_01 – PPL (reflected), dispersed molybdenite and pyrite grains; **(z)** 15NT_01 – XPL, sericite alteration associated with mineralisation; **(a_1)** 15NT_01 – PPL (reflected), singular pyrite grain sharing a boundary with a quartz grain (no alteration halo); **(b_1)** 15NT_01 – XPL, sericite alteration associated with mineralisation; **(c_1)** 15NT_01 – PPL (reflected), dispersed molybdenite and pyrite grains; **(d_1)** 15NT_01 – XPL, sericite alteration associated with mineralisation

4.4 NANTAI Mo-(Cu) DEPOSIT - LAMPROPHYRES

4.4.1 Classification

Dykes or sills occur as marginal facies to the intrusion associated with the Nantai Mo-(Cu) deposit. These features have been classified as lamprophyres; this is a particularly useful field term as it encompasses a diverse group of relatively rare ultra-potassic igneous rocks. Two distinct types of lamprophyres were distinguished based on grain size, and foliation. For the purposes of describing these units, the following classification will be applied:

Lamprophyre (1): unfoliated, fine- to medium-grained

This unit is a dark grey to black fine- to medium-grained ultra-potassic igneous rock. Small (~ 0.5 mm), rare sulphides occur throughout the specimen. This fine- to medium-grained porphyritic lamprophyre has a groundmass consisting of mica, amphibole and pyroxene, with phenocrysts of Fe-Ti oxides (red) occurring throughout. The specimen lacks feldspar phenocrysts, consistent with the classification of the lamprophyre ultra-potassic group (Figure 4.10a).

Lamprophyre (2): foliated, fine-grained

This unit is a dark grey to black fine-grained ultra-potassic igneous rock. The dark colour of the mafic specimen can be attributed to the abundance of ferro-magnesian silicates and paucity of feldspar (generally restricted to the groundmass, and in this specimen unobserved). Abundant xenoliths and fragments are apparent throughout the specimen, dominated by olivine (green). Modal layering is clearly observable, with the olivine demonstrating a banding texture throughout the entire rock (Figure 4.11g).

Polished thin section, XRD and SEM-EDS analysis indicate a mineral assemblage for the lamprophyre units incorporating major minerals: phlogopite (30%), nepheline (20%), olivine (10%); accessory minerals: titanite, apatite, rutile, magnesite, sanidine, leucite (30% total accessory minerals); secondary minerals: serpentine, magnetite, hematite, pyrite, chalcopyrite and molybdenite (10%).

4.4.2 Minerals

Phlogopite $K_2Mg_6[Al_2Si_6O_{20}](OH)_4$

When observed, biotite (more specifically the Mg-bearing phlogopite) is yellowish-brown relating to the Mg content, as opposed to the Fe content that would demonstrate greenish-brown colouration. The pleochroic grains occur as dismembered/disseminated flakes scattered throughout the groundmass of lamprophyre (1), whereas in lamprophyre (2) phlogopite is much more abundant, and features as prominent shearing fabrics (Figure 4.11h).

Forsterite Mg_2SiO_4

When observed, olivine has invariably undergone serpentinisation (Figure 4.10d). Commonly, the hexagonal shape of the olivines has been maintained. The secondary serpentine is characteristically green in PPL, while demonstrating blue-grey mottled/undulose extinction in XPL. Small opaque grains are secondary magnetite, which are restricted to the serpentinised olivine. The small amount of Fe-oxides associated with this indicates that the olivine is Mg-rich (forsterite). This will be discussed further in Section 4.4.3 Paragenesis.

Enstatite $MgSiO_4$

When observed, orthopyroxene (more specifically the Mg-bearing enstatite) has invariably undergone serpentinisation. Where enstatite has serpentinised, the minerals occur as laths – dissimilar to the hexagonal habit of its counterpart olivine (Figure 4.10c & Figure 4.11j). The laths are best demonstrated in reflected light by their low relief (Figure 4.13s). Observations made in thin section have demonstrated where alteration is complete the pseudomorphs display a characteristic bronze-like metallic lustre or schiller, sometimes described as a bastite (Jenner and Green 1983, Deer *et al.* 2013). Magnesium-rich enstatites, commonly associated with olivine, are important constituents for many ultramafic rocks i.e. lamprophyres (Figure 4.13w & x).

Nepheline $Na_3(Na, K)[Al_4Si_4O_{16}]$

When observed, the feldspathoid nepheline occurs largely in the groundmass as tabular grains. Seeing as lamprophyres are representative of an ultramafic system, it would be expected that feldspathoids (rather than abundant feldspars and unlikely quartz) may be present. Furthermore, the whole melt would be silica-undersaturated therefore by extension a low zircon yield would be expected. It is common to find nepheline phenocrysts together with alkali feldspar (e.g. sanidine) in the same rock (MacKenzie and Guilford 1980) however, it is difficult to distinguish between them; it could be inferred that some sanidine could be present, however none was identified with certainty. An important feature associated with nepheline is sericitic alteration (this is observed inside of the grains, rather than along the margins); and the presence of small, thin needles of apatite, which grow across the nepheline tabular grains – the apatite could represent potential late-stage crystallisation or could possibly be an alteration product (Figure 4.13).

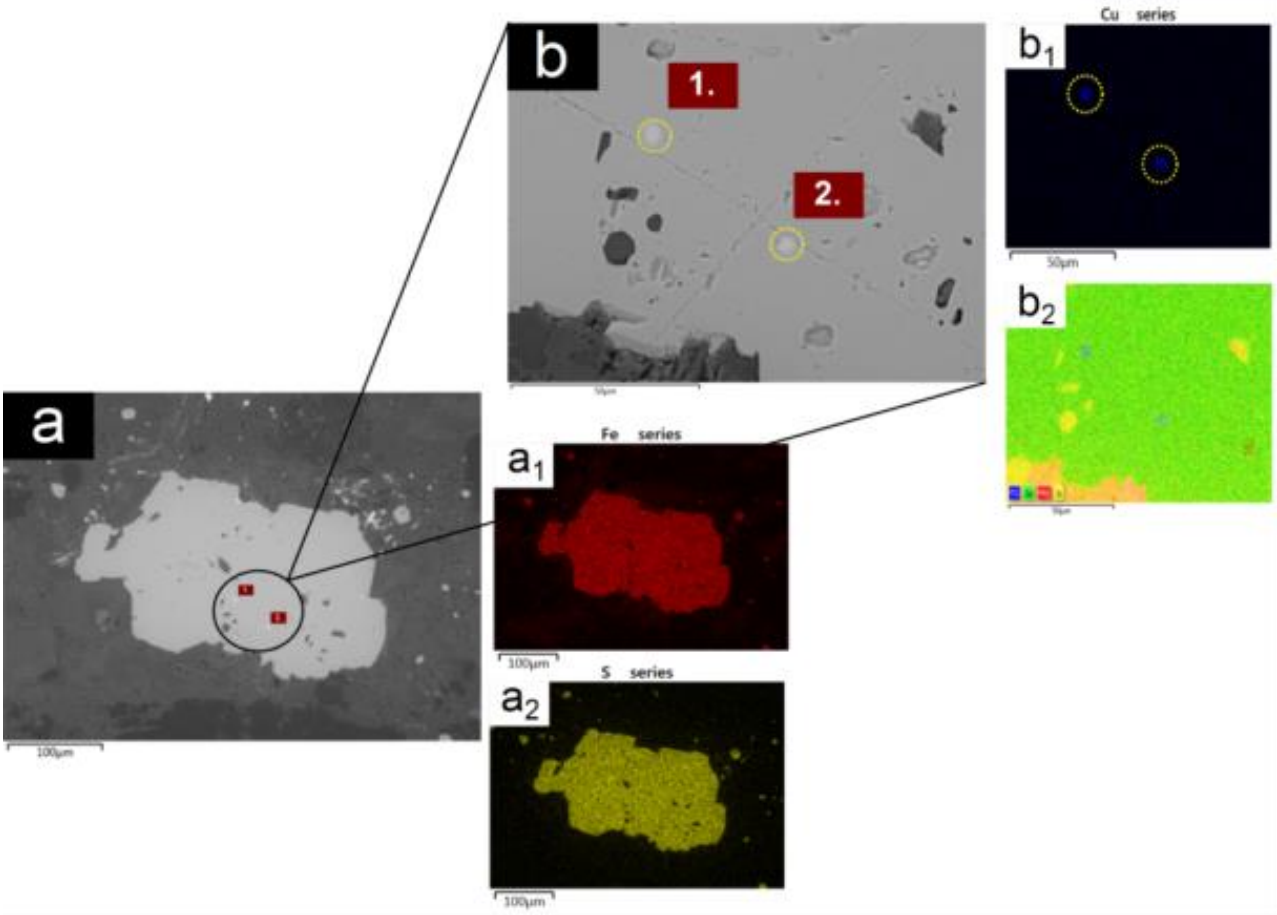

Figure 4.9 - SEM-EDS results of Nantai Mo-(Cu) deposit (lamprophyres) sample 15NT_J

a) Electron image taken of thin section 15NT_J

$a_1 – a_2$) Raster maps displaying the occurrence of Fe and S within sample 15NT_J. As expected, the Fe-raster and the S-raster plot over the same areas within the region of interest indicative of pyrite (FeS_2)

b) Increased magnification of electron image a) taken of thin section 15NT_J

b_1) Raster map displaying the occurrence of Cu blebs (chalcopyrite) within the greater pyrite mass

b_2) Layered image of thin section 15NT_J

Refer to Appendix D for further SEM-EDS results of Nantai Mo-(Cu) deposit sample 15NT_A, including elemental graphs for the spectrum points of analysis, identified by numerical maroon boxes

4.4.3 Paragenesis

Both lamprophyre (1) and lamprophyre (2) are found as hypabyssal intrusions, specifically as sills, which are spatially associated with the larger granitic pluton of the Nantai porphyry-skarn Mo-(Cu) deposit. It is evident from petrographic analysis that lamprophyre (2) has undergone a deformation event which has left it foliated, in comparison to lamprophyre (1), which shows little to no foliation. This is best demonstrated in the alignment of phlogopite. Phlogopite occurs in a great variety of geological environments; particularly phlogopite occurs mainly in ultrabasic rocks of which the original melt would have been silica-undersaturated, a feature typical of mafic to ultramafic lamprophyres (Clemens 1995, Takeda and Ross 1995). The phlogopites in the lamprophyres sampled at the Nantai Mo-(Cu) deposit are representative of a mantle-derived magma.

It is worth mentioning the behaviour of phlogopite in the context of impure limestones (e.g. marls) and dolomites, as these metamorphic rocks are the host-units being intruded. Evidence of this is the identification of carbonates made under thin section. On the basis of previous workings (Guidotti 1984) the following reactions involving phlogipite or biotite as the reactants or products includes:

$$phlogopite + calcite + quartz \rightarrow tremolite + alkali\ feldspar + CO_2 + H_2O$$

Equation 4.1

$$dolomite + muscovite \rightarrow biotite + chlorite + calcite + CO_2$$

Equation 4.2

All the products and reactants of Equation 4.1 have been observed within the other units (i.e. aplite, marl and dolomitic marble units) of the Nantai porphyry-skarn Mo-(Cu), therefore it could be assumed this reaction may have occurred.

Olivine is extremely susceptible to hydrothermal alteration, the effects of weathering if exposed to the surface, and to low-grade metamorphism (Deer *et al.* 2013). In both lamprophyre (1) and lamprophyre (2) the products of alteration of forsterite are serpentinite and lesser amounts of magnetite – making for good examples of psuedomorphs of the Mg-rich olivine. During serpentinisation (the most wide-spread form of olivine alteration), the result is a Mg-silicate that becomes hydrated. The mineral serpentine is unable to successfully incorporate iron into its crystal lattice; as such the iron precipitates out in generous amounts as magnetite within the serpentine psuedomorphs of forsterite.

Nepheline is the most common feldspathiod of SiO_2 undersaturated igneous rocks (Stebbins *et al.* 1986, Tait *et al.* 2003) and as such is important within lamprophyre (1) and lamprophyre (2). Where nepheline was observed in thin section, it was an early crystallising mineral with textural overgrowths of apatite and assumedly with but not confirmed alkali feldspar. The mineral occurs in well-formed crystals, with sericitic alteration attacking commonly (but not restricted to) the cores of the grains. Evolution of the lamprophyres can be summarised as follows:

1. Olivine (forsterite) + orthopyroxene (enstatite) are the first minerals to begin crystallising
2. With increasing fluid content of the melt due to olivine + orthopyroxene crystallisation plus decompression phlogopite ± amphibole are the next minerals to begin crystallising. This also marks the beginning of the serpentinisation process once excess water rich fluid start to exsolve from the melt
3. Late-stage sulphides (observed as pyrite) form, perhaps with influence from meteoric fluids. Note: pyrite can be found across all the mineral assemblages, whereas the magnetite is restricted to the serpentine
4. The identification of carbonates in thin section within the lamprophyre further assists in illustrating the intrusion of the lamprophyres into the dolomitic host rocks
5. Heterogeneous deformation caused the fabric development in lamprophyre (2)

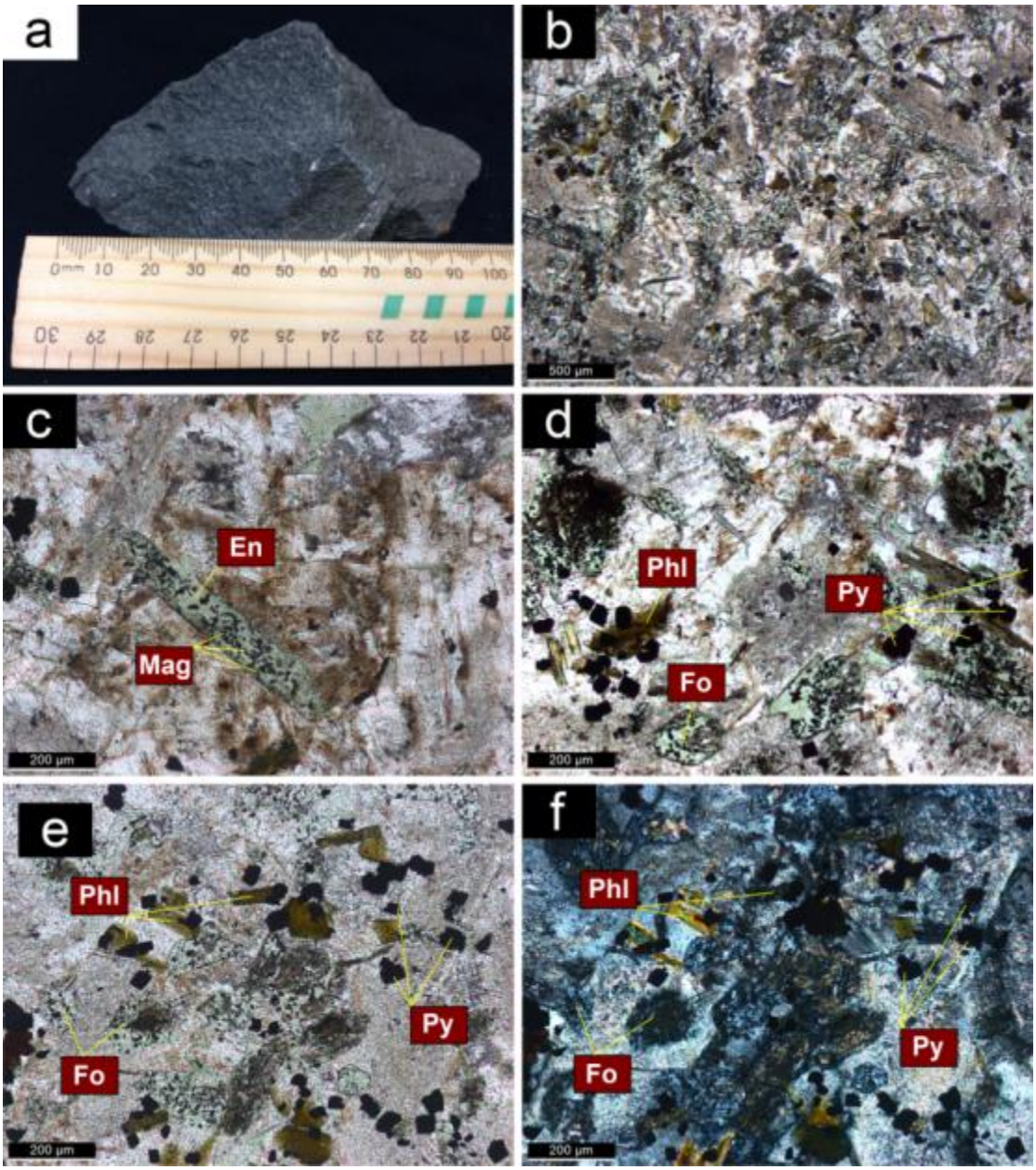

Figure 4.10 - **Nantai Mo-(Cu) Deposit – Lamprophyre (1)**
(a) 15NT_K, fine-grained non-foliated lamprophyre_1 hand sample; **(b)** 15NT_K – PPL, low magnification photomicrograph demonstrating the typical groundmass of the Nantai Mo-(Cu) lamprophyre_1; **(c)** 15NT_K – PPL, enstatite laths have invariably undergone serpentinisation, a by-product of this alteration is magnetite in the grains having been converted to serpentine; **(d)** 15NT_K – PPL, commonly, the hexagonal shape of the forsterite grains has been maintained having undergone serpentinisation; **(e)** 15NT_K – PPL, & **(f)** 15NT_K – phlogopite is yellowish-brown relating to the Mg content, as opposed to the Fe content that would demonstrate greenish-brown coloration

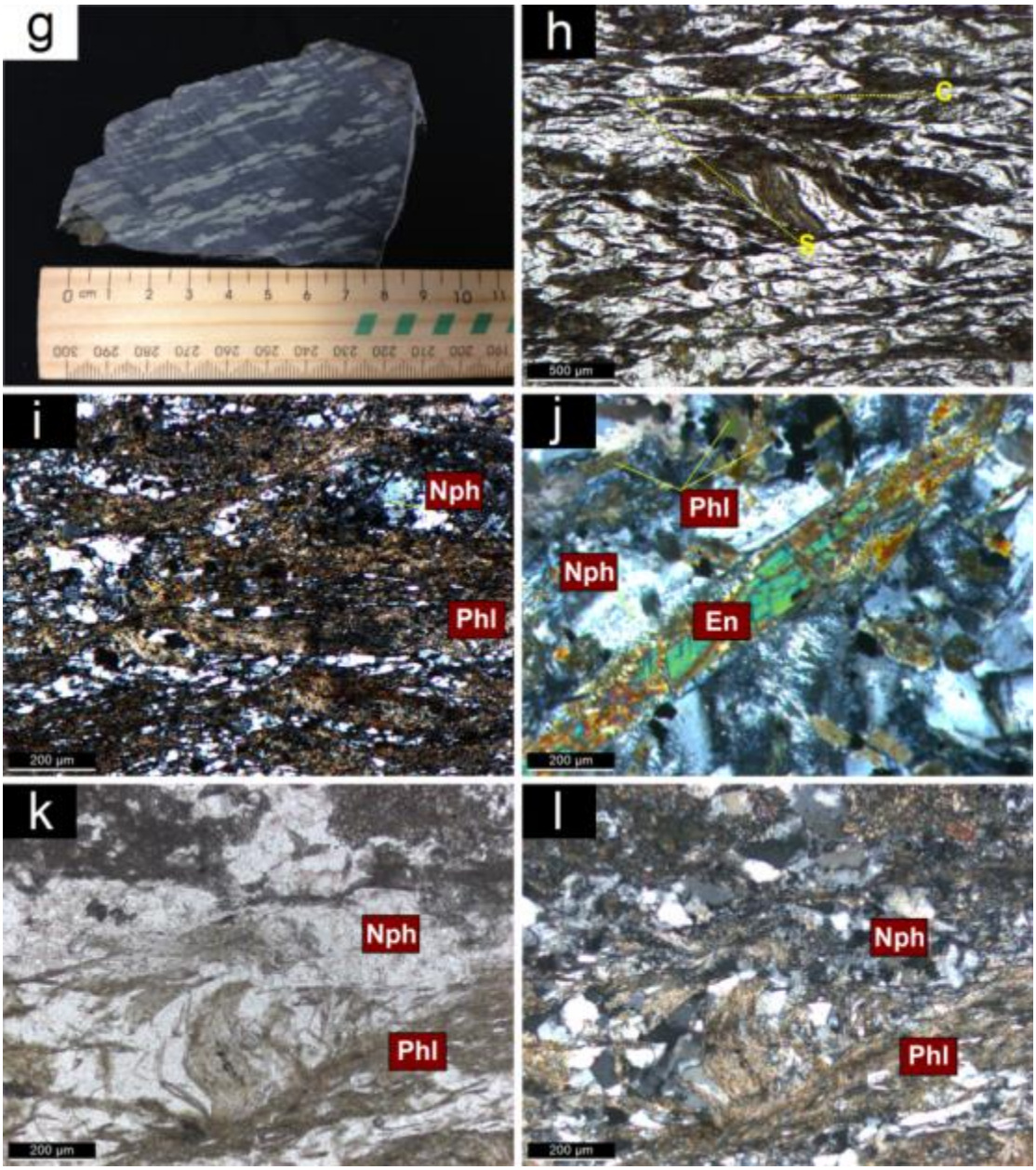

Figure 4.11 - **Nantai Mo-(Cu) Deposit – Lamprophyre (2)**
(g) 15NT_J, fine-grained foliated lamprophyre_2 hand sample; **(h)** 15NT_J – PPL, S-C fabrics (denoted in yellow text in the photomicrograph), with multiple 'mica-fish' occurring in the phlogopite; **(i)** 15NT_J – XPL, foliation is apparent at both the macroscale and mircoscale, commonly throughout lamprophyre_2; **(j)** 15NT_J – XPL, characteristic enstatite lath with surrounding nepheline and lesser phlogopite grains; observations made in thin section have demonstrated where the alteration is complete, the pseudomorphs display a characteristic bronze-like metallic lustre (particularly notably around the rim of this grain); **(k)** 15NT_J – PPL, & **(l)** 15NT_J – XPL, deformation is best illustrated in the malleable phlogopite grains

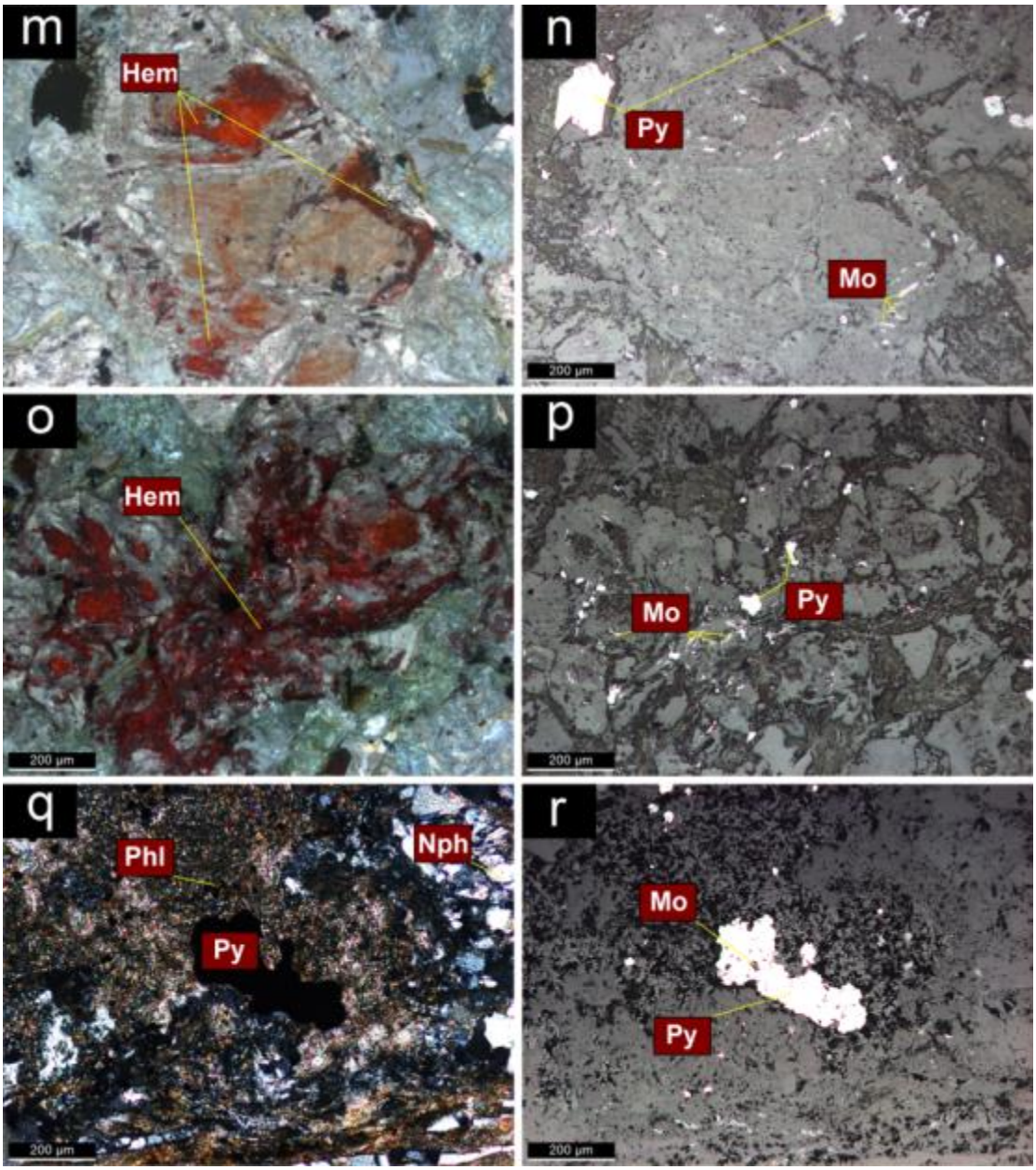

Figure 4.12 - **Nantai Mo-(Cu) Deposit – Lamprophyre 1 & 2 (mineralisation)**
This plate displays the importance of Fe within the system, which is observed as precipitated oxides [hematite (α-Fe_2O_3), magnetite (Fe_3O_4)] or sulphides [pyrite (FeS_2)] within the lamprophyre_1 and lamprophyre_2 units. **(m)** 15NT_J – XPL (reflected), & **(n)** 15NT_J – PPL (reflected), hematite occurring with pyrite and molybdenite; **(o)** 15NT_J – XPL (reflected), & **(p)** 15NT_J – PPL (reflected), hematite occurring with pyrite and molybdenite; **(q)** 15NT_K – XPL, & **(r)** 15NT_K – PPL (reflected), phlogopite surrounding pyrite with minor molybdenite in a groundmass of nepheline

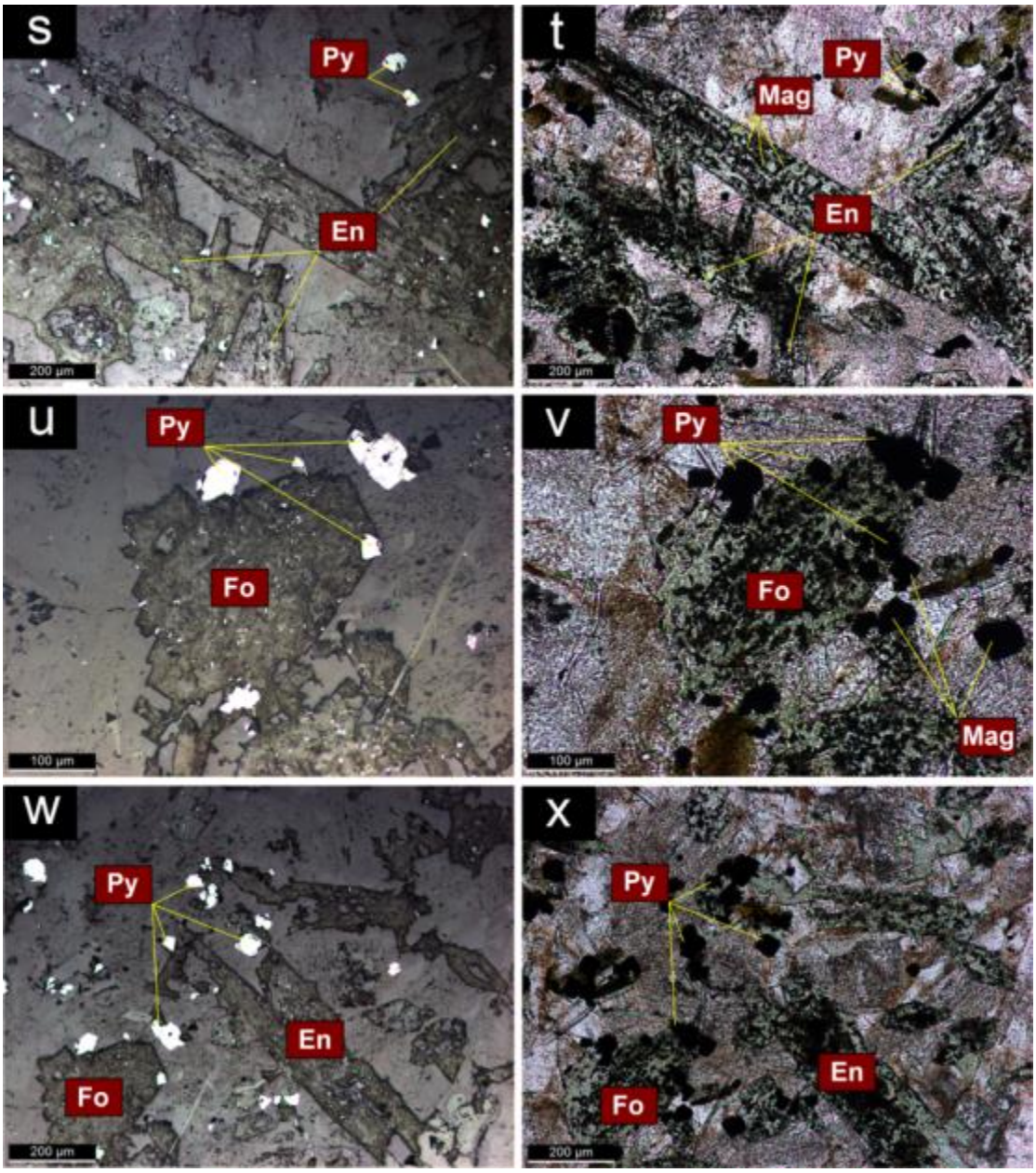

Figure 4.13 - **Nantai Mo-(Cu) Deposit – Lamprophyre 1 & 2 (mineralisation)**
This plate displays mineralisation associated with the serpentinisation process; the mineral serpentine is unable to readily take Fe into its crystal lattice, as such the Fe precipitates out as magnetite (Fe_3O_4) within the serpentine psuedomorphs of forsterite and enstatite, as observed in the above photomicrographs. Notably, magnetite is restricted to the serpentine whereas pyrite (FeS_2) occurs across all the mineral assemblage of lamprophyre_1 and lamprophyre_2. Notably, fine near-translucent laths of apatite are present within the groundmass displaying no evidence of serpentinisation. **(s)** 15NT_K – PPL (reflected), & **(t)** 15NT_K – PPL, serpentinised enstatite; **(u)** 15NT_K – PPL (reflected), & **(v)** 15NT_K – PPL, serpentinised forsterite; **(w)** 15NT_J – PPL (reflected), & **(x)** 15NT_J – PPL, serpentinised enstatite and forsterite

4.5 NANTAI Mo-(Cu) DEPOSIT – MARL AND DOLOMITIC MARBLE

4.5.1 Classification

In hand specimen this unit demonstrates deformed and contorted layering of shale and marble (Figure 4.15a). The layers have an average width of ~1 mm with the largest up to 3 mm. On comparison the marble layers seem to be the thickest; marble has a tendency of recrystallising rather than submitting to metamorphism as the shale does, which may account for the thicker bands. Sulphides are observed with the unaided eye in this unit. These are not confined to particular bands and rather occur in both the shale and marble. Polished thin section and XRD analysis indicate a mineral assemblage incorporating major minerals: tremolite (55%), dolomite (35%); accessory minerals: forsterite, talc, actinolite (totaling 10%); secondary minerals: magnetite, pyrite, chalcopyrite, molybdenite and hematite.

In thin section the deformed and contorted layering of shale and marble is apparent at the micro-scale; presumably, the banding of the unit is attributable to the original bedding of the shale, before undergoing deformation, resulting in what is now deformed and contorted layers observable in both hand specimen and thin section (Figure 4.15b & e). This unit could possibly be better typified as a ‘dirty marl’, whereby the sequence would have interbedded shales and dolomite. In this instance, fluids entering the system would preferentially replace the carbonates with sulphides, with alteration of the shale sequences into possibly mica. The classification of the unit as a marl provides more robust reasoning as to the banding not only of the shale and carbonates, but also of the mineralisation. Herein, this unit will be referred to as a marl.

4.5.2 Minerals

Tremolite $Ca_2Mg_5Si_8O_{22}(OH, F)_2$

This unit demonstrates elongated blades, with evidence of fibrous and columnar aggregates of tremolite; tremolite is the most abundant of the major minerals (over dolomite). In some instances the grains are too small to distinguish features such as the development of grain faces, and specification as to the three-dimensional shape of individual grains (Figure 4.15b). Tremolite appears as coarse blades within the carbonate, suggesting its formation with the metamorphic breakdown of carbonate (Figure 4.15c).

Dolomite $CaMg(CO_3)_2$

The second most abundant major mineral observed in thin section is dolomite. This occurs in a much lower percent compared to tremolite; seeing as tremolite forms as a result of the metamorphic reaction between dolomite and quartz in the presence of a hydrous fluid. Carbonate veinlets are a common occurrence throughout this sample, which contain mineralisation in the form of pyrite and chalcopyrite as aggregates within the veinlets. Two generations of veinlets can be observed in Figure 4.15f, with the thinner carbonate (dolomite) veinlet overprinting or cross-cutting the thicker. Noteworthy is the apparent halo-effect of tremolite on the outsides of both the veinlets – a feature best highlighted on the thinner veinlet. Two-stage mineralised veins are commonly observed throughout the banded shale/marl unit (Figure 4.17r).

Pyrite FeS_2

Pyrite occurs as a common accessory mineral in the marl unit, and furthermore is a major phase in the broader Nantai porphyry-skarn Mo-(Cu) orebody. Euhedral grains of pyrite are not uncommon, however much of the mineral occurs as massive aggregates, with some radiating and granular clusters, disseminated masses and vein-type occurrences (Figure 4.17). It is commonly observed in thin section proximally associated with chalcopyrite, magnetite and hematite. Instances of hematite forming pseudomorphs after pyrite have also been observed (Figure 4.16h & j).

Chalcopyrite $CuFeS_2$

Chalcopyrite is distinguishable from the comparatively abundant amount of pyrite in the marl unit by its pronounced yellow coloration. The mineral occurs in massive aggregates, but more commonly as intergrowths with pyrite and/or molybdenite (Figure 4.17p). Fine chalcopyrite occurs as inclusions with pyrite, with some of these submicroscopic in size.

Magnetite $Fe^{2+}Fe^{3+}{}_2O_4$

Throughout the marl unit magnetite occurs as an accessory mineral. It commonly occurs with the sulphides (i.e. pyrite and chalcopyrite), rather than dispersed throughout the matrix of the unit. The magnetite grains are commonly observed as opaque in thin section with the exception of very fine flakes. Under reflected light, the mineral appears grey with moderate reflectance. This is best demonstrated in comparison with pyrite, where the magnetite grains are grey-pink in coloration. Similar to the sulphides, magnetite grains are massive in habit, forming large accumulations of uniformly indistinguishable grains (Figure 4.16j).

Hematite α-Fe_2O_3

Throughout the marl unit, similarly to magnetite, hematite occurs as an accessory mineral. When observed the mineral is slightly transparent, with diagnostic red internal reflections noted. Throughout thin section, hematite occurs proximal to magnetite and sulphides rather than incorporated into the matrix of the unit. The blood red, opaque mineral occurs as compact splinters and blades, radiating clusters and platy dispersions (Figure 4.16h & j). In hydrothermal deposition, a platy habit of hematite is often common; this combined with possible oxidising conditions could account for the variety of different habits observed in thin section.

Dolomitic marble:

This unit may represent an extension of the aforementioned marl, and as such the paragenesis will incorporate both this unit and the marl. Rather than appearing as a dirty limestone; this sequence can be described as a dolomitic marble, and could represent a lens within the marl sequence. The mineral assemblage of this unit is very similar to that of the marl. Some features within the unit are different, and worth noting; chalcedonic quartz is observed commonly observed in veins in thin section, demonstrating characteristic undulose extinction (Figure 4.18f & Figure 4.19i). Chalcedonic quartz is representative of very low temperatures of crystallisation, which indicates an epithermal environment in a temperature range of 100 – 200°C. Assumedly, there would be very little available silica in the dolomitic marble; what is available has been recrystallised and remobilised into the veins, which can now be observed. Chalcedonic quartz observed under thin section can exemplify liquid immiscibility of two geochemically different melts, for example a silica-rich and carbonate-rich melt. This will be further explored in section 4.6 with regard to the development of the carbonate-rich igneous rocks, carbonatites.

Also notable is the much finer groundmass, in comparison to the marl unit (Figure 4.18c & d) – in the matrix of this unit, although not observed with certainty, it could be inferred that shale-incorporating minerals such as talc and pyrophyllite may occur as accessory minerals. With regards to mineralisation, there is a good example, which shows chalcopyrite with pyrrhotite in a vein, with a small bleb of hematite (Figure 4.19g & h).

4.5.3 Paragenesis

Marl and dolomitic marble

In the Nantai porphyry-skarn Mo-(Cu) deposit, magnetite occurs with the sulphides pyrite and chalcopyrite. With regard to the marl unit that occurred proximal (within ~ 500m) to the aplite dykes, magnetite can be found to occur in varying amounts in thermally metamorphosed sediments. Iron oxides are mobilised in the system (for example by hydrated ferric oxide cement or limonitic staining), which are reduced first to hematite (also observed within the dolomitic marble), and then at higher grades of metamorphism to magnetite. It can be assumed that the magnetite in the system is indicative of lower oxygen fugacity, and further illustrates (along with evident contorted banding of the unit) that the marl has undergone metamorphism to an extent that has allowed for the reduction of hematite to magnetite (Haggerty 1991, Harrison and Putnis 1996, Bowles *et al.* 2011).

The observed hematite may be the by-product of the interaction with magmatic reduced fluids with meteoric oxidised fluids. Often in this situation the interaction of the two fluid types results in the precipitation of magnetite and hematite. The occurrence of both of these minerals could be attributed to hematite forming from the oxidation of magnetite followed by regional metamorphism and later recrystallisation. For example, magnetite can be formed at high temperatures in the presence of water by the reduction of hematite and free Fe (Matthews 1976):

$$Fe + 4\,Fe_2O_3 \leftrightarrow 3\,Fe_3O_4$$
$$[free\ Fe] \qquad [hematite] \qquad [magnetite]$$

Equation 4.3

Similarly, the reduction of hematite to magnetite at elevated temperatures and pressures in the presence of water can be expressed by (Matthews 1976):

$$3\,Fe_2O_3 + H_2 \leftrightarrow 2\,Fe_3O_4 + H_2O$$
$$[hematite] \qquad [magnetite] \qquad [water]$$

Equation 4.4

Tremolite occurs in both contact and regionally metamorphosed dolomitic rocks and as such is a mineral common to skarn settings. In the Nantai porphyry-skarn Mo-(Cu) deposit contact metamorphism has occurred where the granitic pluton has intruded into a marl-dolomite making for a suitable host rock to produce tremolite, i.e. a system with abundant Ca and Mg. In thermally impure dolomites (e.g. marl), tremolite forms early by the action between dolomite and quartz, as shown in Equation 4.1 (Deer *et al.* 2013):

$$\underset{[dolomite]}{5\,CaMg(CO_3)_2} + \underset{[quartz]}{8\,SiO_2} + \underset{[water]}{H_2O} \rightarrow \underset{[tremolite]}{Ca_2Mg_5Si_8O_{22}(OH)_2} + \underset{[calcite]}{3\,CaCO_3} + 7\,CO_2$$

Equation 4.5

The temperature at which this reaction occurs is dependent on the CO_2/H_2O of the intergranular fluid phase. The presence of a more CO_2- rich fluid delays the reaction until high temperatures (Winkler 1974). If SiO_2 is still available after the reaction series expressed in Equation 4.1 with further temperature increase, tremolite reacts with calcite to form diopside. Furthermore, if there is excess dolomite relative to quartz in the system, early-forming tremolite reacts with this to produce forsterite and calcite. Seeing as no significant amounts of diopside are recognisable in this unit, it is possible that the tremolite has taken up all the excess SiO_2 and undergone metamorphism restricted to low- or medium-grade. These relationships are indicated in Figure 4.14 (after Winkler 1974).

Relevant to the marl unit, pyrite is known to occur in significant amounts in sedimentary rocks, principally in argillaceous and carbonaceous sequences (Paktunc and Dave 2002, Cody 2005, Vaughan 2006). Deer *et al.* (2013) states that pyrite is the main sulphide mineral in porphyry deposits, an accessory mineral in skarn settings and a major phase in hydrothermal deposits; in this sense pyrite is a major phase in the regional context of the Nantai porphyry-skarn Mo-(Cu) deposit. Where the chalcopyrite occurs in veinlets observed in thin section, along with other sulphides it may have exsolved from a solid solution (e.g. Cu – Fe – S) where the solution itself may be the result of sulphide/silicate liquid immiscibility in the Nantai porphyry-skarn Mo-(Cu) system. It would be assumed that the system, on crystallisation/precipitation of chalcopyrite, has not undergone significant alteration; overall the chalcopyrite is fresh, and not altered to malachite, azurite

or chrysocolla – common weathering products of chalcopyrite (Putnis and McConnell 1976, Fleet 2006).

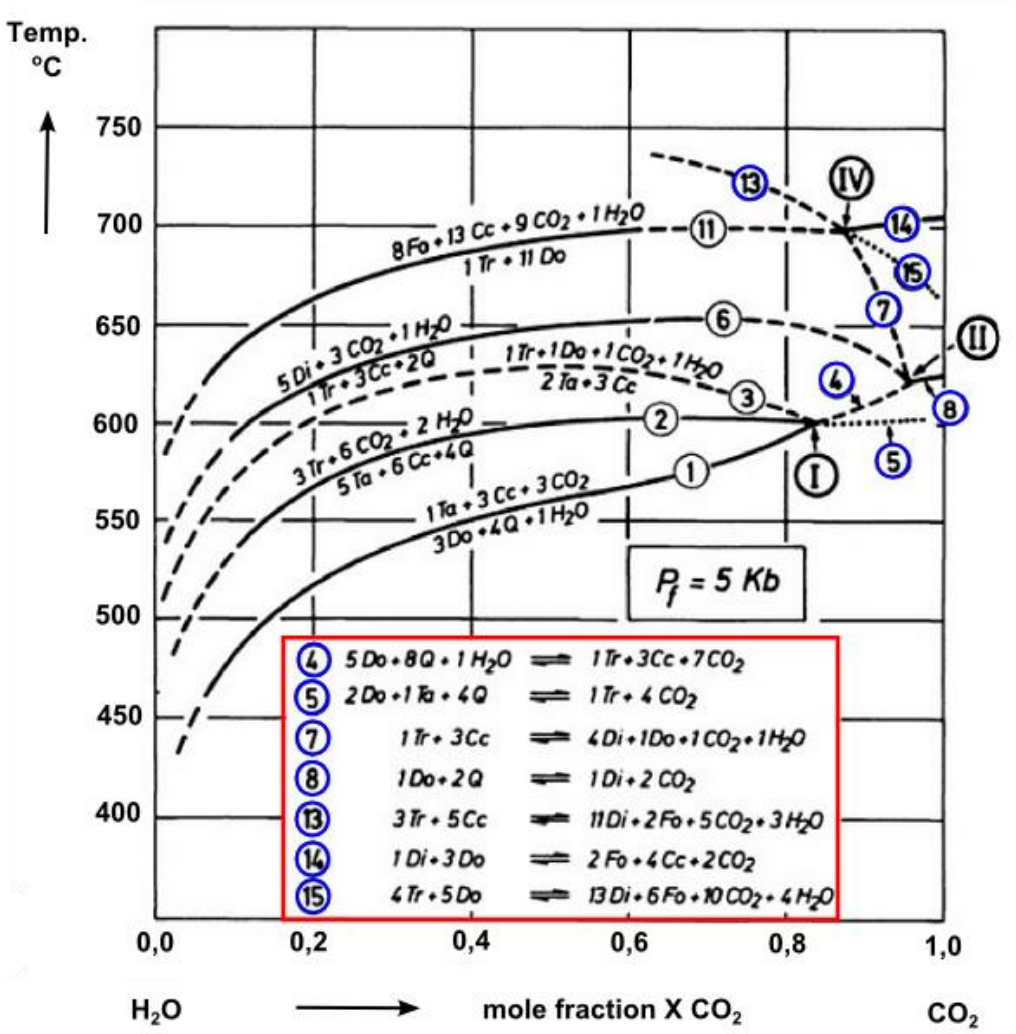

Figure 4.14 - Isobaric T-X(CO_2) diagram at P_f = 5 kb for reactions in siliceous dolomites. Adapted from Winkler (1974)

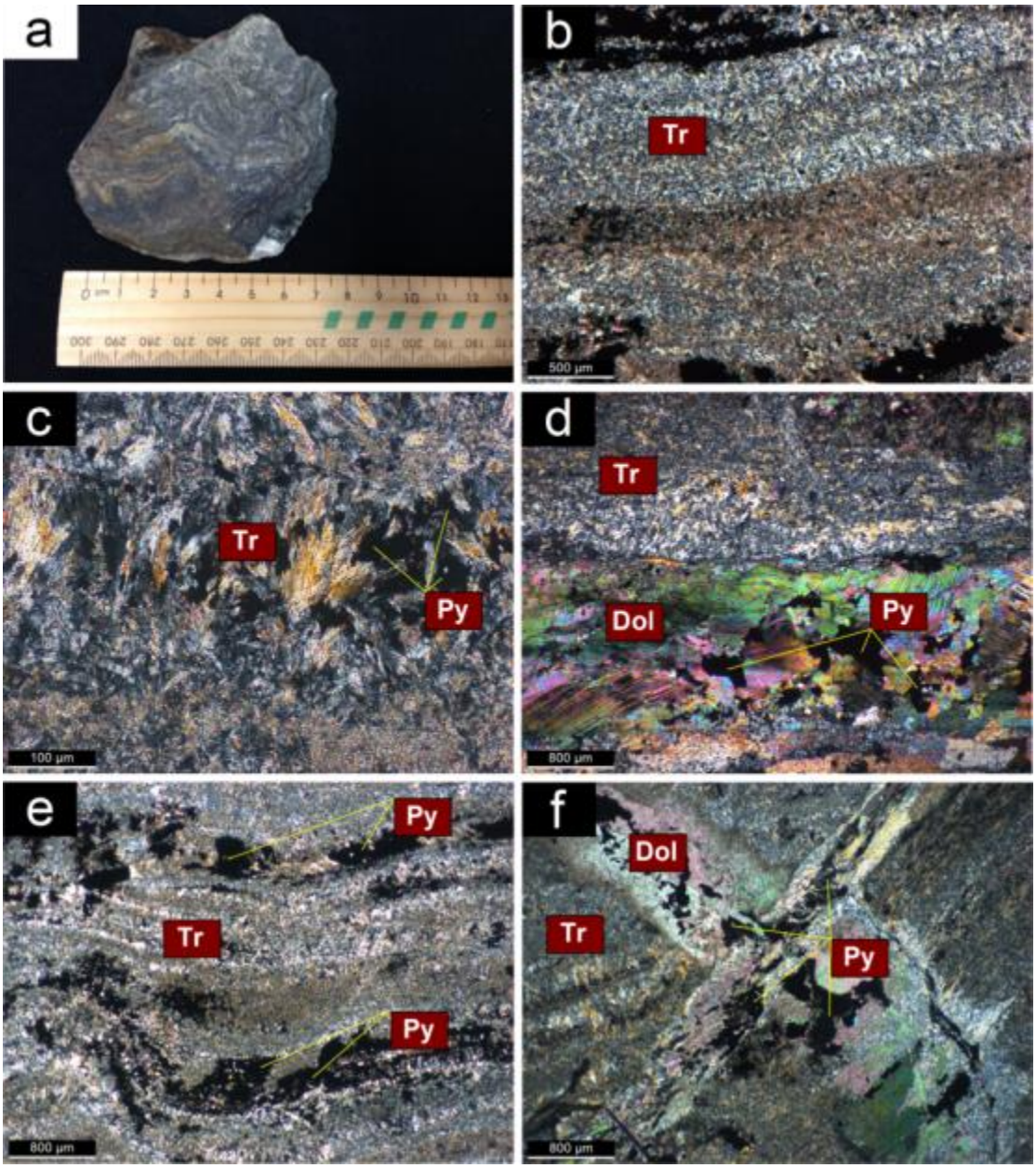

Figure 4.15 - **Nantai Mo-(Cu) deposit – Marl**
(a) 15NT_I, hand sample of the marl unit displaying deformed and contorted layers of shale and marble (metamorphosed dolomite); **(b)** 15NT_I – XPL, opaque minerals display the same banding texture as the tremolite under thin section; **(c)** 15NT_I – XPL, the marl unit of the Nantai Mo-(Cu) deposit demonstrates elongated blades of tremolite, with evidence of fibrous and columnar aggregates; **(d)** 15NT_I – XPL, contact zone between tremolite-rich groundmass and dolomitic vein material; **(e)** 15NT_I – XPL, deformation is apparent at the macroscale and microscale as evidence in this photomicrograph. Mineralisation within the marl unit commonly occurs as bands, suggesting reactivation of the system under a metamorphic regime and subsequent re-precipitation of mineralisation into bands; **(f)** 15NT_I – XPL, Two generations of veinlets can be observed with the thinner carbonate (dolomite) veinlet overprinting or cross-cutting the thicker

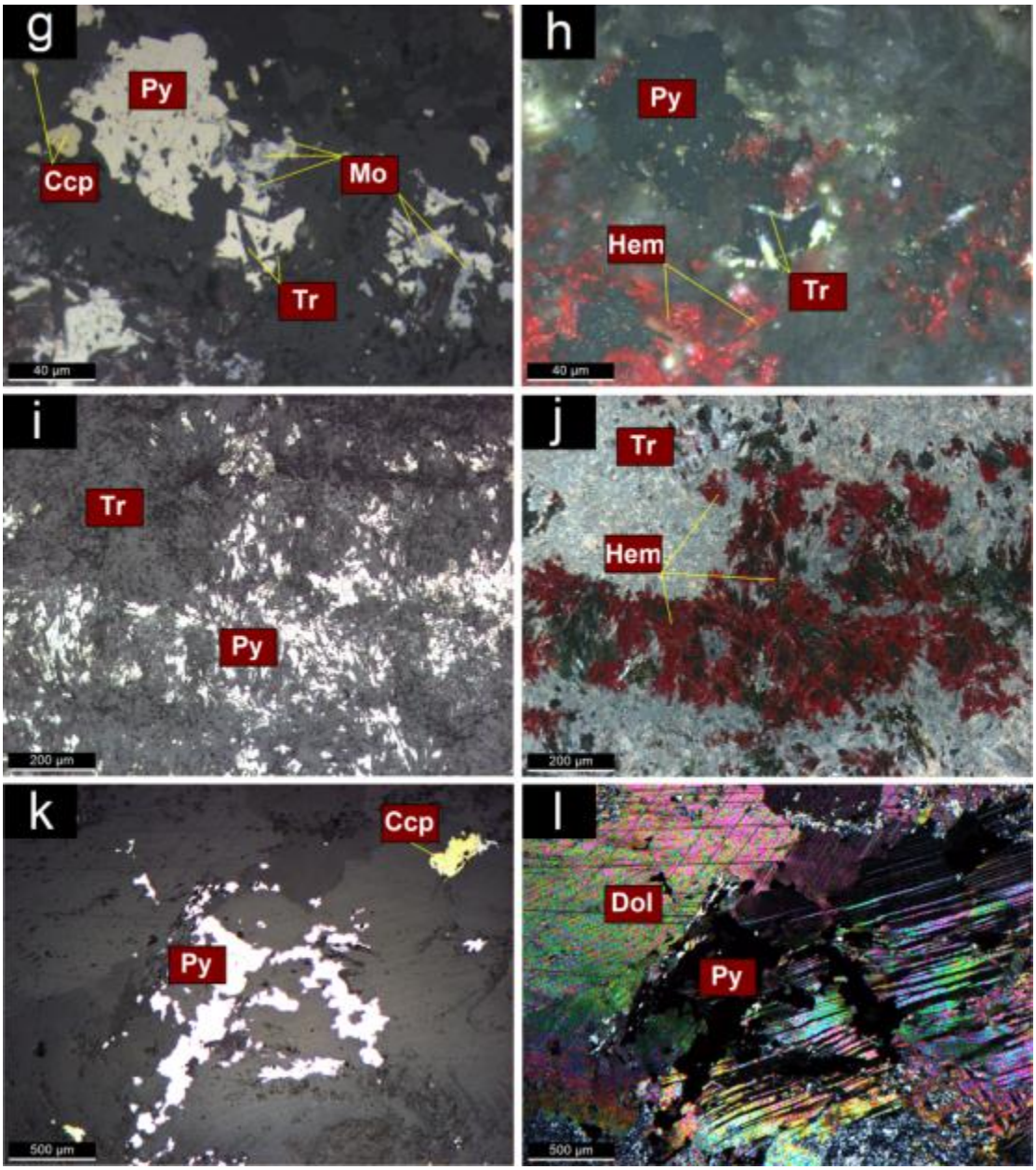

Figure 4.16 - **Nantai Mo-(Cu) deposit – Marl (mineralisation)**
This plate highlights that hematite and magnetite commonly occur in conjunction with molybdenite, chalcopyrite and pyrite. Notably, hematite may be the by-product of the interaction between magmatic reduced fluids and meteoric oxidised fluids; **(g)** 15NT_I – PPL (reflected) ,mineralisation observed includes molybdenite, chalcopyrite and pyrite with late-stage tremolite overprinting these sulphides; **(h)** 15NT_I – XPL (reflected), hematite is associated with sulphides, accounting for mineralisation of the system. Hematite is best observed in XPL (reflected) whereby characteristic blood-red internal reflections are easily distinguishable; **(i)** 15NT_I – PPL (reflected), & **(j)** 15NT_I – XPL (reflected), pyrite with associated hematite and magnetite; **(k)** 15NT_I – PPL (reflected), & **(l)** 15NT_I – XPL, mineralisation is not restricted to occurring in veins, or within the tremolite-rich groundmass. In this instance, both pyrite and chalcopyrite are observed within a dolomitic-rich groundmass

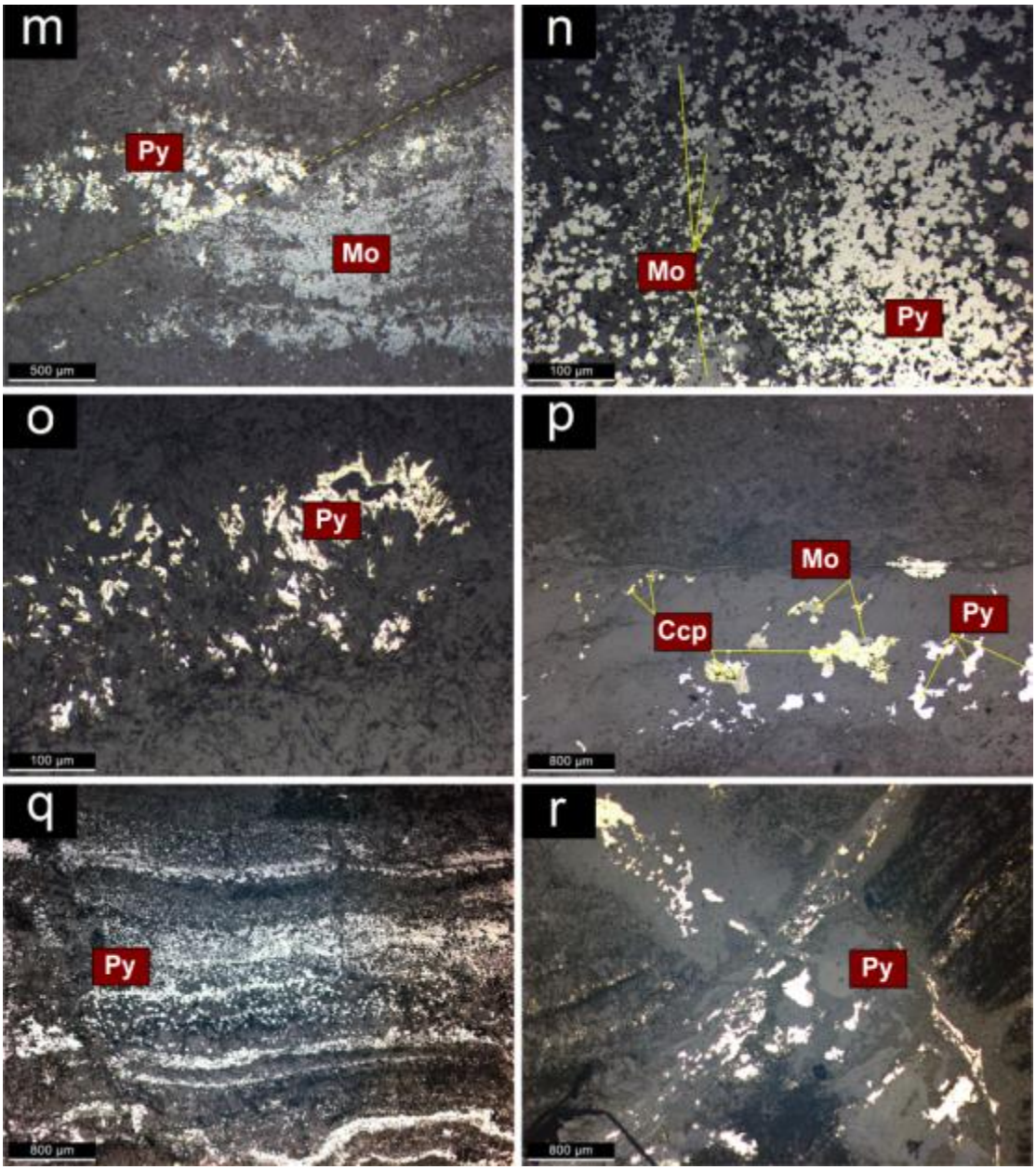

Figure 4.17 - **Nantai Mo-(Cu) deposit – Marl (mineralisation)**
This plate displays the different types of mineralisation styles within the marl unit of the Nantai Mo-(Cu) deposit. **(m)** 15NT_I – PPL (reflected), contact mineralisation with pyrite vs. molybendenite styles; **(n)** 15NT_I – PPL (reflected), massive aggregates occur mainly as pyrite with randomly interspersed molybdenite grains; **(o)** 15NT_I – PPL (reflected), mineralisation occurs as clusters over different groundmass types (i.e. tremolite-rich vs. dolomite-rich); **(p)** 15NT_I – PPL (reflected), vein-type with mineralisation occurring in the form of molybdenite, chalcopyrite and pyrite; **(q)** 15NT_I – PPL (reflected), banded mineralisation, implying reactivation of the system under metamorphic conditions; **(r)** 15NT_I – PPL (reflected), multi-generational vein-type mineralisation of primarily pyrite

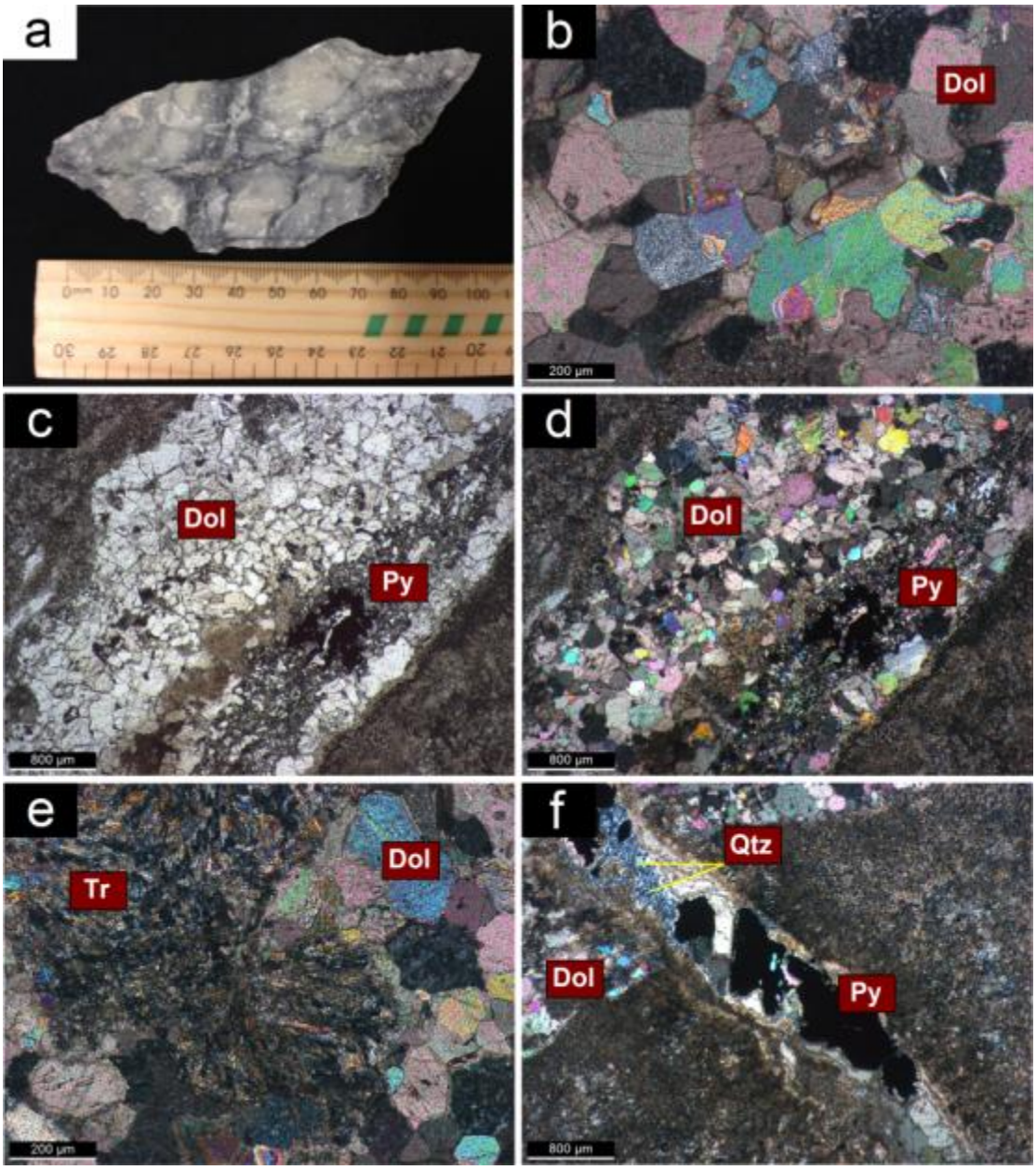

Figure 4.18 - **Nantai Mo-(Cu) deposit – Dolomitic marble**
(a) 15NT_D, dolomitic marble hand specimen with common magnetite veining throughout; **(b)** 15NT_D – XPL, representative photomicrograph of the groundmass of the dolomitic marble unit of the Nantai Mo-(Cu) deposit. Dolomite grains are generally fine- to medium grained, comparatively finer to the groundmass of the marl unit; **(c)** 15NT_D – PPL, & **(d)** 15NT_D – XPL, coarse-grained dolomitic vein with associated pyrite transecting through the finer dolomitic marble matrix; **(e)** 15NT_D – XPL, radiating fibres of tremolite occur throughout the dolomitic marble unit; **(f)** 15NT_D – XPL, chalcedonic quartz is observed in a vein, demonstrating characteristic undulose extinction. Chalcedonic quartz is representative of very low temperatures of crystallisation, further supporting an epithermal mineralising regime. The small amount of silica in the system has been recrystallised and remobilised into the veins

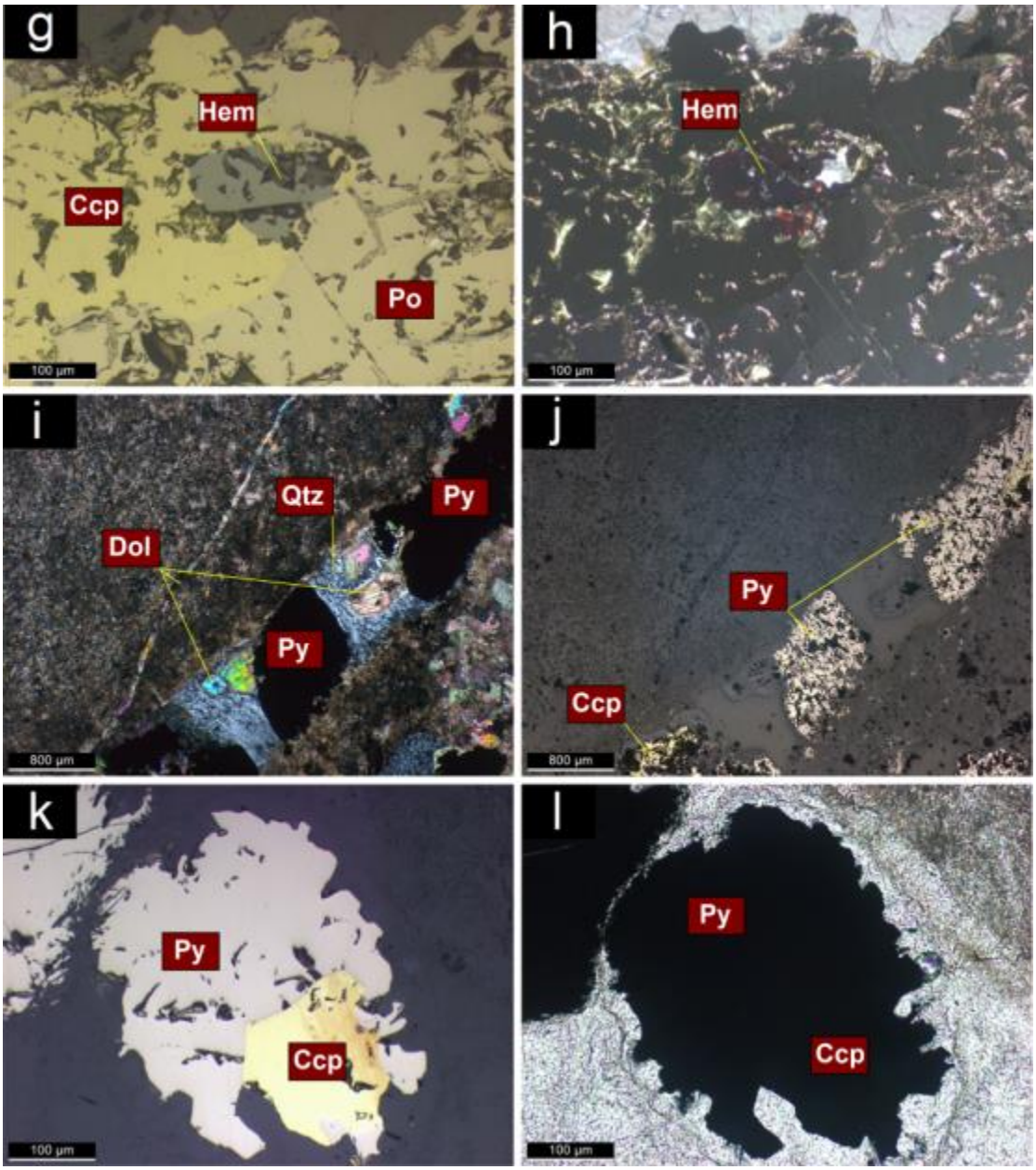

Figure 4.19 - **Nantai Mo-(Cu) deposit – Dolomitic marble (mineralisation)**
This plate displays the different types of mineralisation styles within the dolomitic marble unit of the Nantai Mo-(Cu) deposit. **(g)** 15NT_D – PPL (reflected), & **(h)** 15NT_D – XPL (reflected), vein-type mineralisation with chalcopyrite and pyrrhotite coexisting with a small bleb of hematite; **(i)** 15NT_D – XPL, & **(j)** 15NT_D – PPL (reflected), this veinlet represents the movement of fluids with many different types of mineral constituents, alternatively the vein may have occurred as a fracture that has undergone many different fluid flows resulting in the array of different minerals (i.e. chalcedonic quartz, dolomite, pyrite); **(k)** 15NT_D – PPL (reflected), & **(l)** 15NT_D – PPL, chalcopyrite (easily distinguishable due to bright yellow colouration) intruding pyrite

4.6 MIAOYA REE DEPOSIT

4.6.1 Classification

In hand specimen, this unit has a carbonate-rich groundmass, typified by cream-white colouration. The black mineral that occurs throughout the hand samples is biotite, which makes for a significant proportion of the mineralogical assembly. Polished thin section, XRD, SEM-EDS and Raman analysis indicate a mineral assemblage incorporating major mineral: calcite (70%); accessory minerals: fayalite, nepheline, biotite, muscovite, apatite, pyroxene, rutile, magnetite (20% total); secondary minerals: sericite, pyrite, chalcopyrite and serpentine (10%).

In thin section the unit is observed to be a holocrystalline, porphyritic intrusive igneous rock. With regards to granularity, the unit can be described as aphanitic whereby all minerals, other than the phenocrysts cannot be distinguished by the unaided eye. The unit can be further classified as microcrystalline (as opposed to cryptocrystalline), whereby the minerals can be identified in thin section; the fine-grained matrix has minerals large enough to demonstrate polarisation colours. Herein, this unit will be referred to as a sövite (coarse-grained calcite-rich REE-bearing carbonatite).

Figure 4.20 – Miaoya REE deposit field work photographs

a) Carbonatite (sövite) with lamellae precipitation of pyrite within the carbonate-rich matrix
b) Evidence of two-melt liquid immiscibility (carbonate-rich vs. silica-rich) in the field

4.6.2 Minerals

Calcite $CaCO_3$

In this unit, the most abundant mineral is calcite, making for the bulk of carbonate material in the Miaoya carbonatites (as opposed to dolomite, ankerite or siderite). It appears predominantly as a medium- to coarse-grained matrix comprising >70% of the samples observed under thin section. Less common fine-grained calcite is observed, which may be representative of separate pulses of magma entering the system, and crystallising at different times. The calcite grains are dominantly subhedral, demonstrating characteristic high-order birefringence colours, rhombohedral cleavage and high relief, all best observed on rotation of the specimen. Some polysynthetic twinning is observed on calcite grain faces; however simple twinning is the dominant type (Figure 4.24c, d & f).

Nepheline $Na_3(Na, K)[Al_4Si_4O_{16}]$

Nepheline occurs predominantly as stringers (Figure 4.25k) The feldspathoid also occurs as dispersed minerals, without the preservation of the crystal faces, or shape – in these instances the nepheline grains appear almost rounded (Figure 4.25j). Twinning of the grey feldspathiods is uncommon to rare, with complex twinning apparent in Figure 4.25h. Sulphides occur as opaque blebs commonly associated with nepheline throughout the carbonatite unit.

Fayalite Fe_2SiO_4

Olivine grains demonstrate fairly well-preserved hexagonal shape, with common irregular cracks with slight alteration along these (Figure 4.26q). The less altered crystals even demonstrate high birefringence on the rim, which is indicative of higher Fe content. Olivine is largely associated with the nephline, rather than the carbonate matrix (Figure 4.26o); the distinction between these minerals is relatively easy with the high birefringence of fayalite compared with the much lower relief of nepheline. Another notable feature of the Fe-rich olivine is the apparent corrosion in some of the grain margins.

Micas

Both muscovite and biotite* are abundant within the carbonatites of the Miaoya REE deposit. Biotite tends to be more prevalent, with laths of muscovite (sericite?) crystallising around the edges of the biotite. Commonly, the micas occur within the cracks and around the rim of the feldspathoids (Figure 4.26n). Another notable feature is the colloform mineralisation growing into the voids associated with the biotite (Figure 4.27u).

*Biotite possibly either:

Annite $K_2Fe^{2+}_6[Al_2Si_6O_{20}](OH)_4$

Siderophyllite $K_2Fe^{2+}_4Al_2[Al_4Si_4O_{20}](OH)_4$

Rare-earth minerals:

No rare-earth minerals were observed under thin section; however grains of apatite were observed and identified for SEM-EDS analyses. Apatite [$Ca_5(PO_4)$(F, Cl, OH)] has the capacity to host REE in its lattice making for fluroapatite, a mineral which is able to host up to 10 wt.% REE_2O_3. When subject to analysis via SEM-EDS rare earth minerals were easily distinguishable, particularly in the electron images as they fluoresced (Figure 4.21). These areas were chosen for analysis. Although only fluroapatite was identified for analysis, it could be assumed what with the abundant REE values on the elemental graphs for the spectrum points of analysis (Figure 4.21, Appendix D) that other rare earth minerals, such as the REE-bearing carbonates, bastnasite and synchysite could also be present.

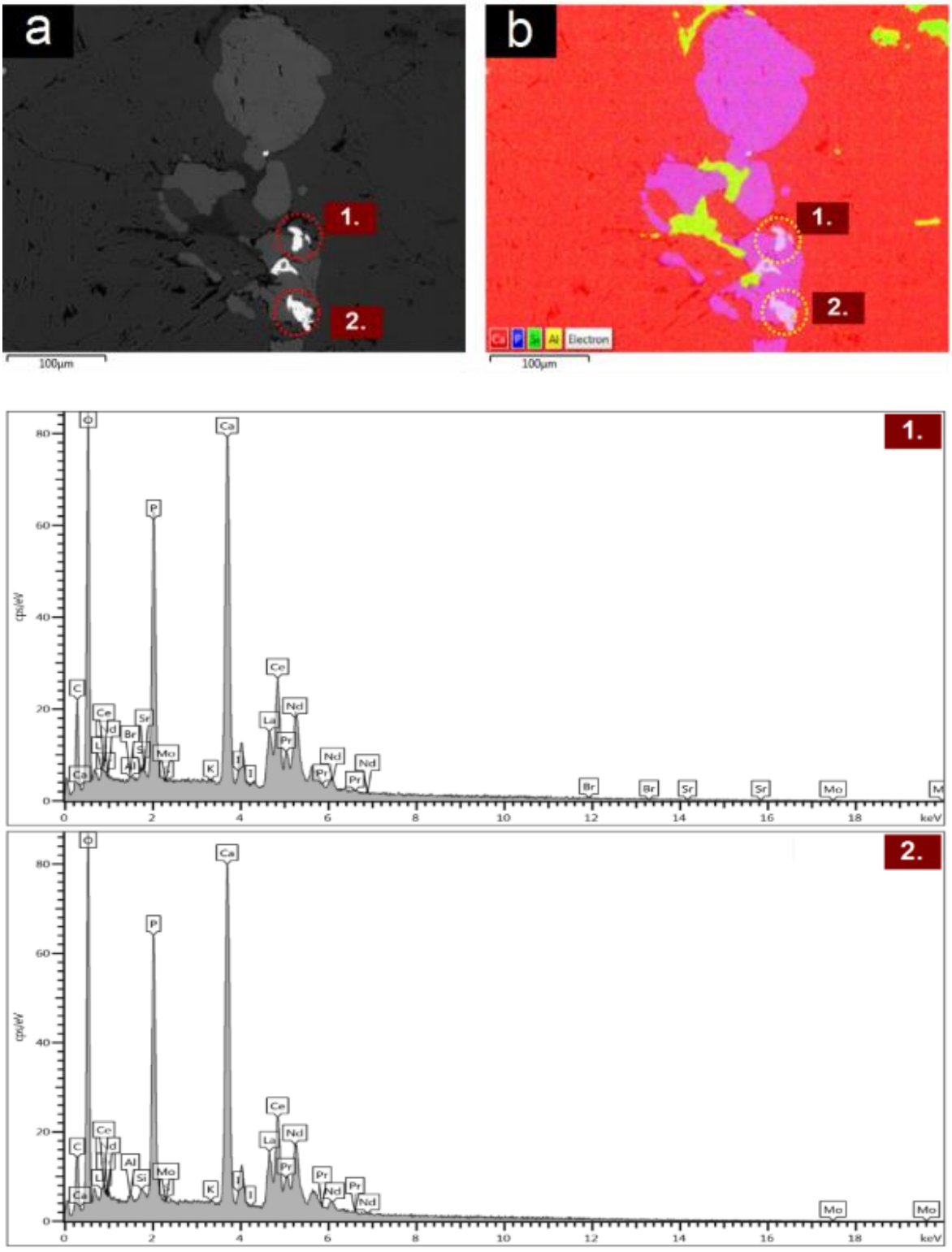

Figure 4.21 – SEM-EDS results of Miaoya REE deposit sample 15MY_A

a) Electron image taken of thin section 15MY_A
b) Layered image of thin section 15DG_A

Refer to Appendix D for further analyses of Miaoya REE deposit sample 15MY_A

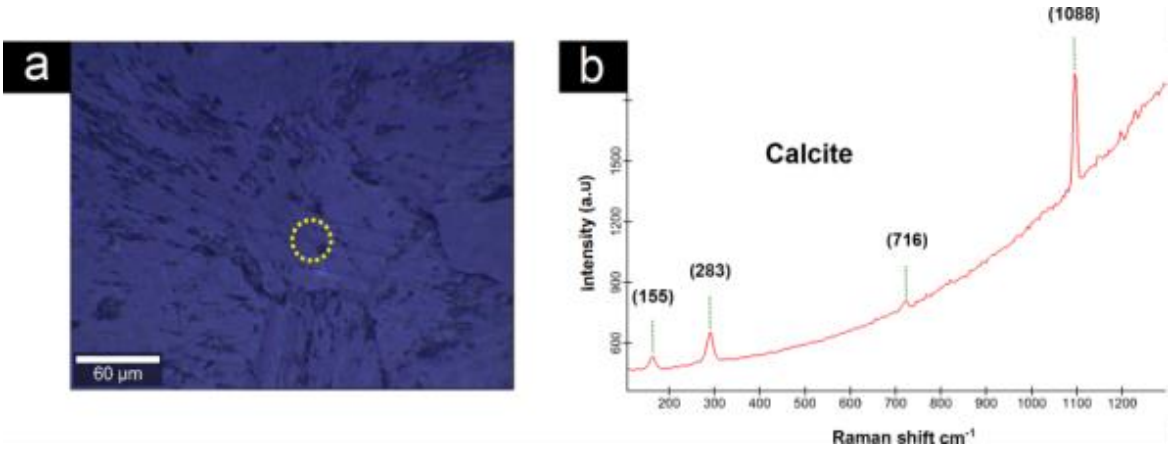

Figure 4.22 - Raman spectra of calcite ($CaCO_3$) obtained using green excitation. Raman spectroscopy has proven particularly useful as a complimentary investigation following standard petrographic analyses. This technique has allowed for identification of the dominant groundmass being calcite (rather than other carbonates such as dolomite, which are sometimes difficult to distinguish under thin section). The clarification of the carbonatite being calcite-rich has assisted in the determination of the host rock being a sövite (coarse-grained calcite-rich REE-bearing carbonatite). NB: A shift of 6 cm^{-1} was needed to be applied to all results to fit instrument calibration

a) Photomicrograph of the site analysed, indicated by a yellow circle
b) Typical calcite spectra with frequency peaks at: 155, 283, 716 and 1088 (Raman shift cm^{-1})

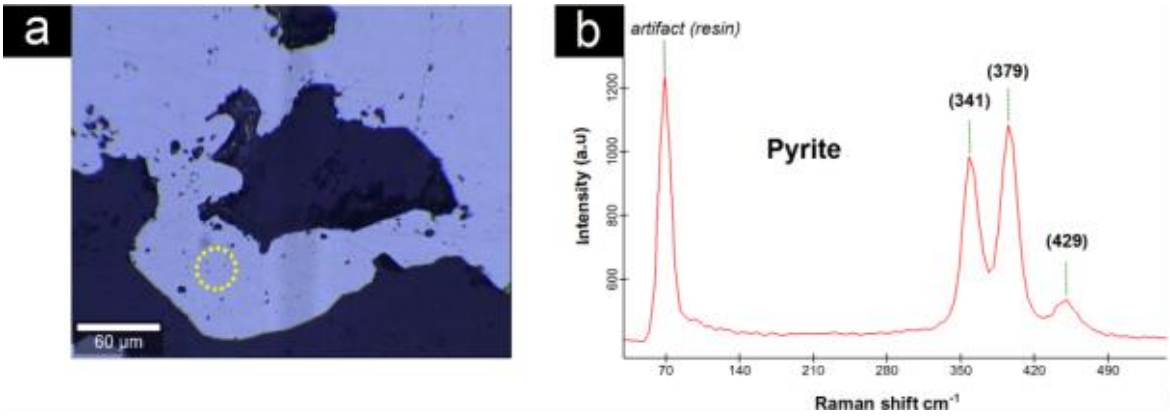

Figure 4.23 - Raman spectra of pyrite (FeS_2) obtained using green excitation

a) Photomicrograph of the site analysed, indicated by a yellow circle
b) Typical pyrite spectra with frequency peaks at: 341, 379 and 429 (Raman shift cm^{-1})

4.6.3 Paragenesis

It could be assumed that the nepheline crystallised first, followed by the carbonates, which began to attack and dissolve the comparatively silica-rich grains evident in the rounded shape and embayment of the nepheline crystals. Particularly, the embayments may be representative of the feldspathoid being dissolved into the silica-understaturated melt. The patches of silica in the abundant carbonate matrix lends to the idea of immiscible carbonate-rich and silica-rich melts interfingering. The stringer habit of the feldspathoids could be attributed to the silica-rich melt being more viscous than the carbonate-rich melt, evident in the stringer-pattern of the silica clumped together, rather than occurring as veinlets. Mineralisation (i.e. chalcopyrite) occurring alongside/proximal to the nepheline may be attributed to the sulphides being captured in the silica-rich melt, rather than the carbonate-rich melt. The Phalabowra (Palabora) carbonatite-hosted magnetite-copper deposit of South Africa may be an analogy for the observed chalcopyrite mineralisation observed within the Miaoya REE deposit. Biotite is a common occurrence throughout the carbonatites, with grains commonly mineralised (associated with pyrite and chalcopyrite). This may possibly be due to the high Fe content of the silica-rich melt (due to the sulphides being captured), with mineralised blebs being precipitated out with the biotite. Alternatively, there may have been a (third) sulphide-rich melt also immiscible with the silica melt. There is possible evidence of this in void spaces being infilled with pyrite and chalcopyrite; the void spaces associated with the crystallising biotite may act as a nucleation point for Fe – the sulphides could therefore be immiscible blebs that, as the biotite is crystallising, become caught. The excess Fe content within the silica-rich melt may have also been a contributor to the crystallisation of the Fe-rich end-member of olivine (fayalite). The Fe, with a small amount of silica is enough to produce fayalite; a mineral that occurs at lower temperatures compared to other olivine counterparts (e.g. Mg-rich end-member forsterite).

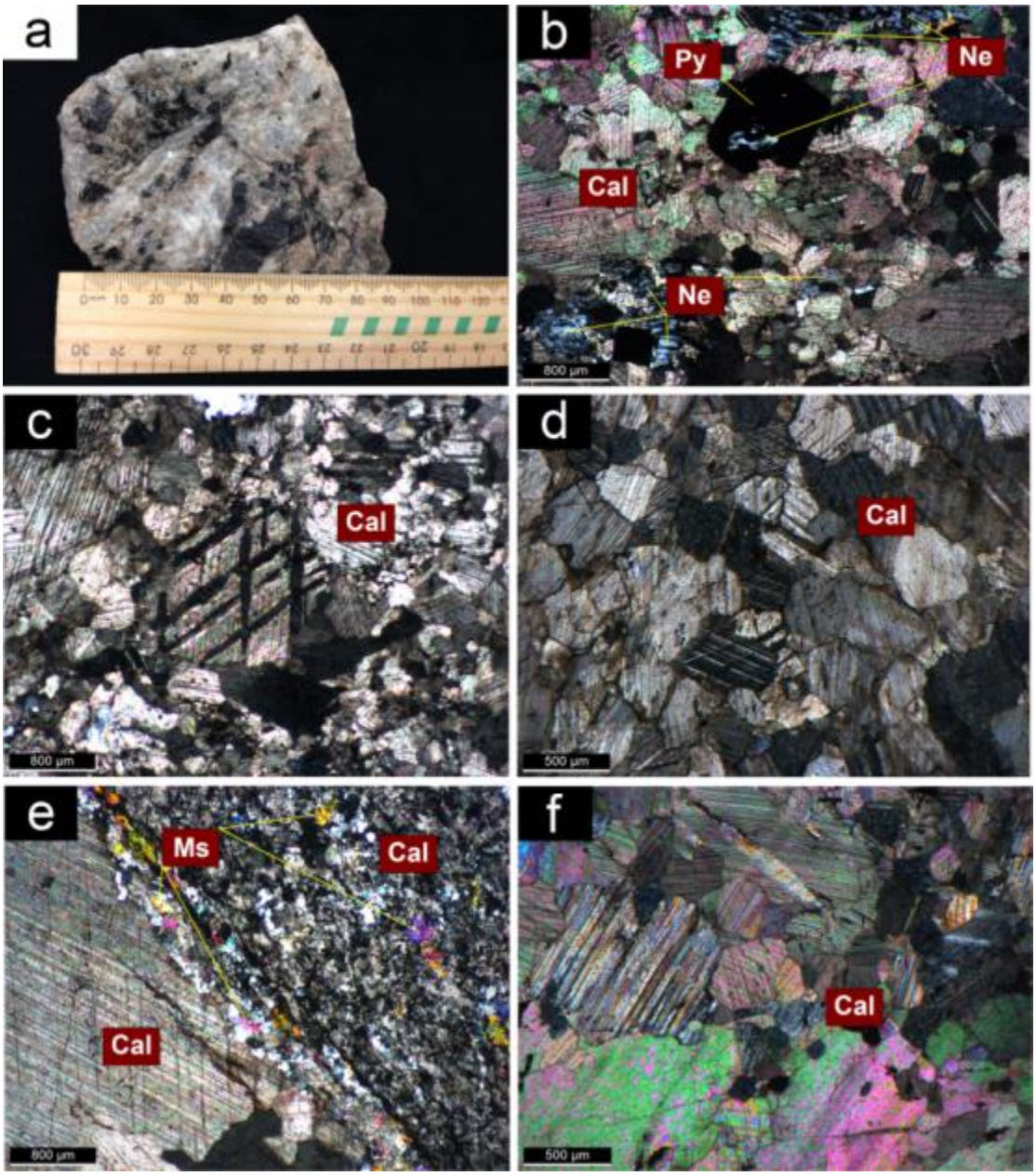

Figure 4.24 - **Miaoya REE deposit – Carbonatite/sövite**
(a) 15MY_H, carbonatite hand sample (otherwise known as a sövite - coarse-grained calcite-rich carbonatite); **(b)** 15MY_B – XPL, pyrite with nepheline inclusion, surrounded by a calcite matrix, with a larger nepheline grain in the top of the photomicrograph; **(c)** 15MY_A – XPL, characteristic high-order birefringence colours, rhombohedral cleavage and high relief of a larger (900 µm) calcite grain at the center of the photomicrograph. The 'tartan' cleavage is commonly identified throughout the Miaoya REE carbonatites (sövite); **(d)** 15MY_C – XPL, representative sample of the groundmass with the most abundant mineral being calcite; **(e)** 15MY_A – XPL, contact between coarse-grained calcite, and fine-grained calcite. Along the contact boundary and within the fine-grained calcite matrix muscovite has formed (sericite?); the hydrous mineral may have been taken up in solution and transported along grain boundaries and along contact zones, as observed in this photomicrograph; **(f)** 15MY_D – XPL, representative sample of the calcite-rich groundmass within the Miaoya REE sövite

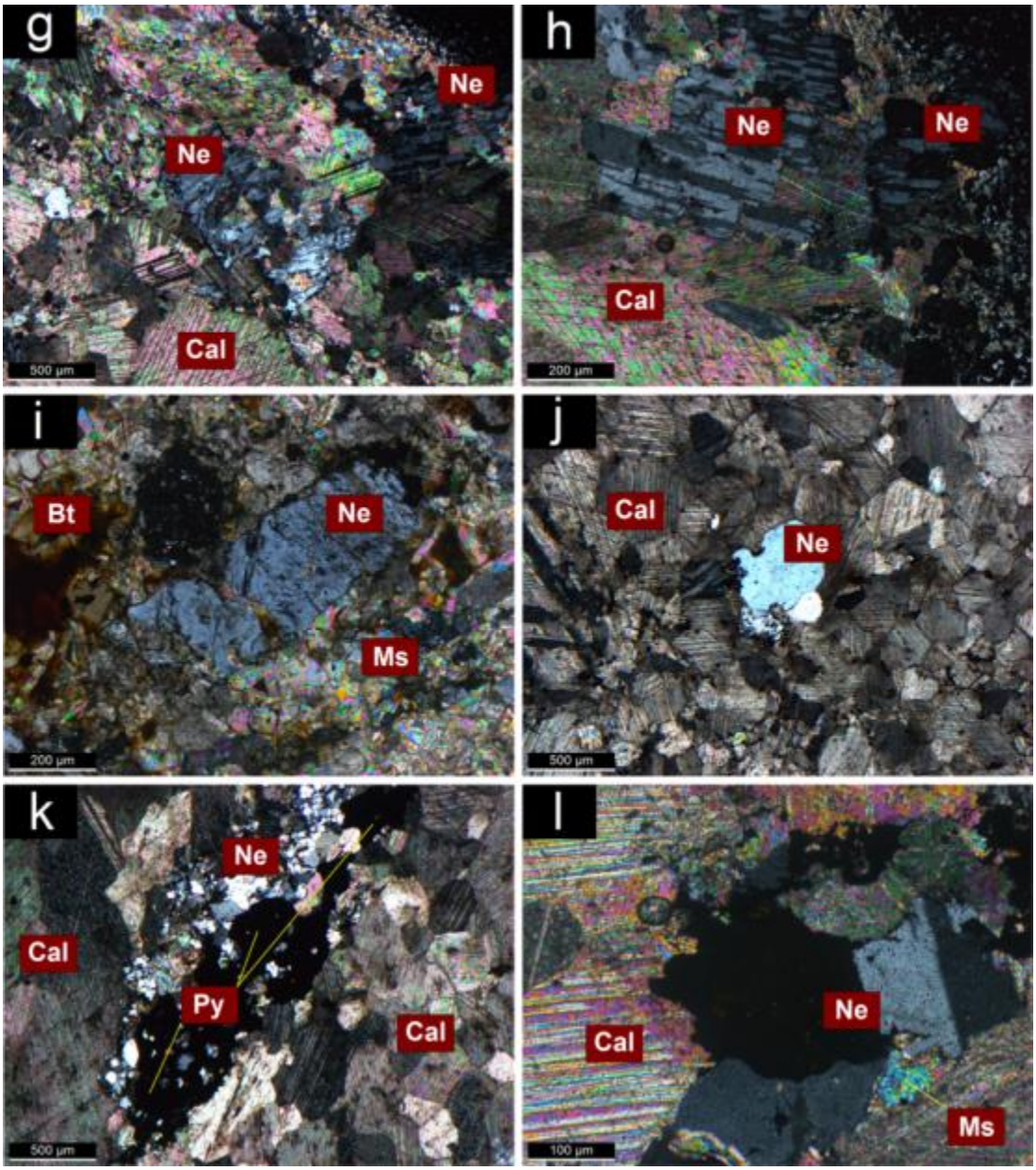

Figure 4.25 - **Miaoya REE deposit – Carbonatite/sövite**
This plate displays the importance of two-melt liquid immiscibility between a carbonate-rich melt (represented by abundant calcite) and a silica-rich melt (represented by rare to uncommon nepheline). **(g)** 15MY_E – XPL, the carbonate melt corroded the silicates as evident from the embayment of the nepheline grains; **(h)** 15NT_D – XPL, the patches of silica in the abundant carbonate matrix supports the idea of immiscible carbonate-rich and silica-rich melts interfingering; **(i)** 15MY_E – XPL, nepheline grain with associated mica (biotite and muscovite); **(j)** 15MY_A – XPL, in some cases nepheline occurs as dispersed minerals, without the preservation of the crystal faces, or shape (in these instances the nepheline grains appear almost rounded); **(k)** 15MY_B – XPL, mineralisation, occurring as small (100 µm) opaque blebs and aggregates is commonly associated with nepheline throughout the carbonatite unit; **(l)** 15MY_C – XPL, the carbonate melt attacked and dissolved the silicate grains as evident in the rounded shape of the nepheline grains

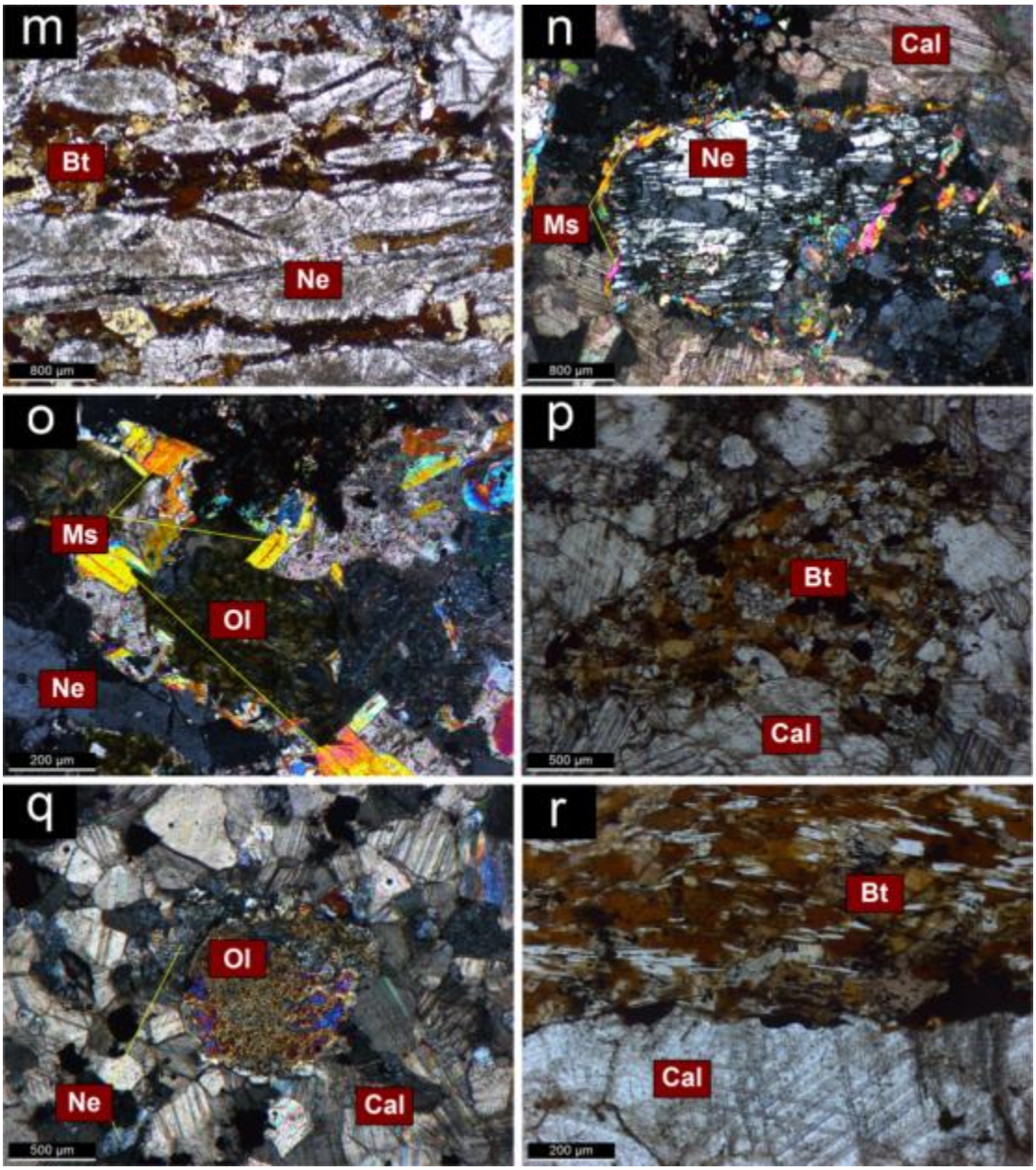

Figure 4.26 - **Miaoya REE deposit – Carbonatite/sövite**
(m) 15MY_B – PPL, biotite occurs as sheets or bands throughout the nepheline; **(n)** 15MY_B – XPL, when nepheline occurs as singular grains within the carbonate matrix muscovite occurs on the boundary between what was two immiscible melts before crystallisation. This is an important feature as it is representative of a reaction rim; **(o)** 15MY_B – XPL, reaction rim, represented by muscovite around fayalite (moderately preserved hexagonal shape) and lower relief nepheline; **(p)** 15MY_B – PPL, biotite is observed here as an aggregated mass occurring with nepheline surrounded by a carbonate matrix; **(q)** 15MY_B – XPL, olivine is largely associated with the nepheline, rather than the carbonate matrix as seen in this photomicrograph. A notable feature of this Fe-rich olivine (fayalite) grain is the apparent corrosion of its edges; **(r)** 15MY_B – PPL, contact between biotite band and calcite groundmass

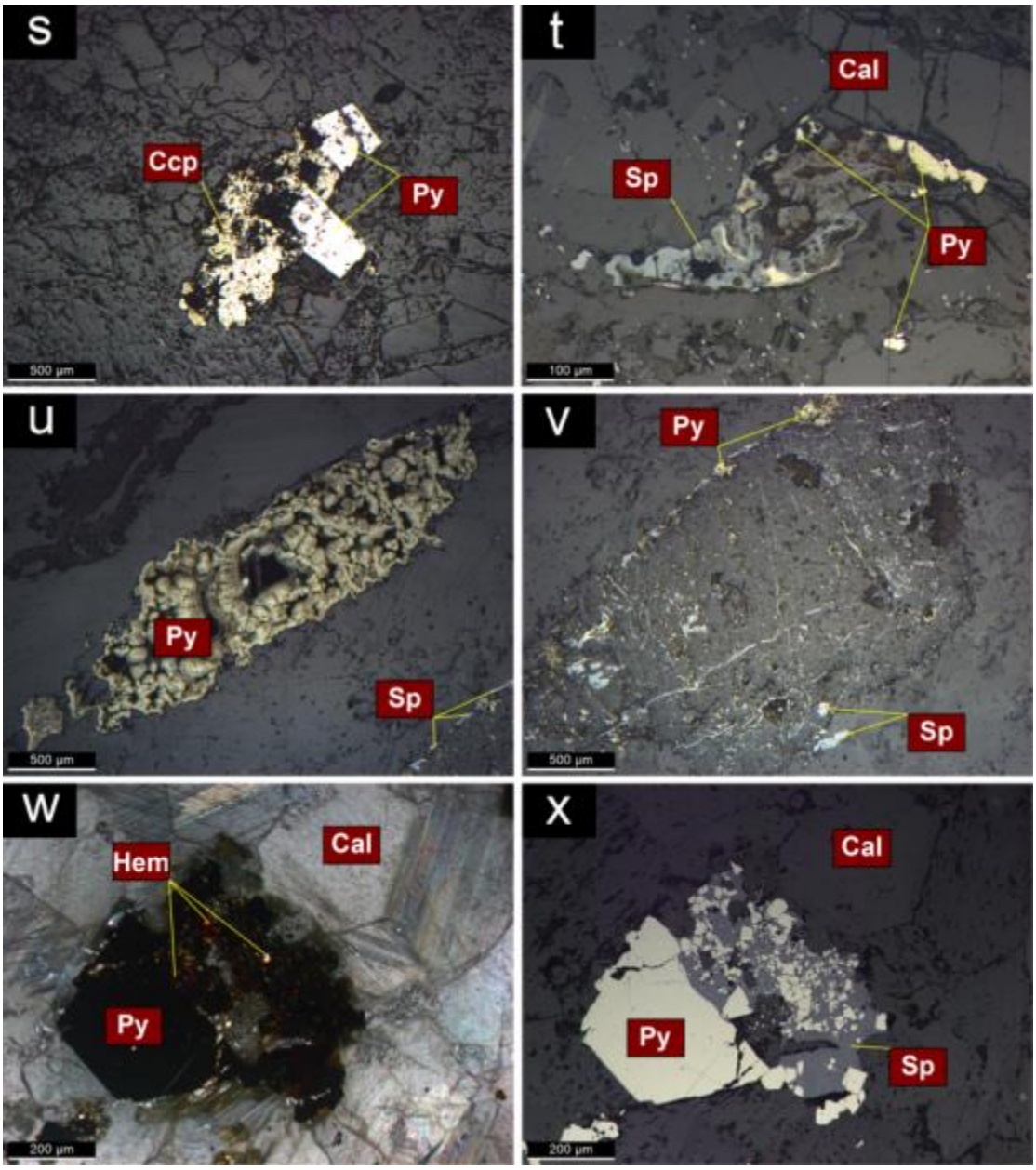

Figure 4.27 - **Miaoya REE deposit – Carbonatite/sövite (mineralisation)**
This plate displays the different types of mineralisation styles within the sövite of the Miaoya REE deposit. **(s)** 15MY_B – PPL (reflected), first stage chalcopyrite has been overgrown by later stage pyrite. The chalcopyrite is comparatively less well preserved, having undergone attack assumedly by the carbonate melt. The pyrite presents well-formed cubes that have undergone attack to a lesser extent; **(t)** 15MY_B – PPL (reflected), mineralisation is found to have precipitated into a sigmoidal void space created by mild deformation in the system; **(u)** 15MY_B – PPL (reflected), colloform pyrite is observed throughout the sövite of the Miaoya REE deposit. This has important application for the paragenesis of the unit, allowing for the assumption of at least two generations of pyrite mineralisation (i.e. cubic/disseminated and colloform); **(v)** 15MY_B – PPL (reflected), mineralisation in the form of pyrite and sphalerite have largely replaced a nepheline grain. Notable are the small mineralised veinlets occurring throughout the grain; **(w)** 15MY_B – XPL (reflected), & **(x)** 15MY_B – PPL (reflected), disseminated pyrite with larger stage associated hematite and sphalerite

4.7 LONGTOUGOU (orogenic) Au DEPOSIT

4.7.1 Classification

In hand specimen the unit is presented as largely massive bright-white baryte with grey-coloured veins cross-cutting the sample (Figure 4.28b & Figure 4.29a). The sample is particularly heavy, characteristic of barium sulphate. Figure 4.28a is the location of where the specimen was sourced. Polished thin section and XRD analysis indicate a mineral assemblage incorporating major minerals: baryte (65%), quartz (20%); accessory minerals: calcite, dolomite, ankerite (total accessory minerals 12%); and secondary minerals: hematite, pyrite, chalcopyrite, sericite, gold (3%).

In thin section the unit represents a rock that is largely dominated by baryte with minor cross-cutting quartz veinlets (these are a microscale version of the 'grey-coloured' veins observed in hand specimen). Mineralisation under thin section has very small grain size (1 – 3 μm) and is difficult to identify. Where observable, gold occurs as granules and blebs, more often in association with pyrite. This specimen is representative of vein-material, and as such the host rock material cannot be distinguished. It is known, however that the Longtougou (orogenic) Au orebody sits within an Early to Late Devonian sedimentary package of dolomites, siltstones and conglomerates, with the orogenic gold deposit located in the crest of an anticline. Herein, this unit will be described as baryte-vein material (or 'ore-vein' in the photomicrograph plates).

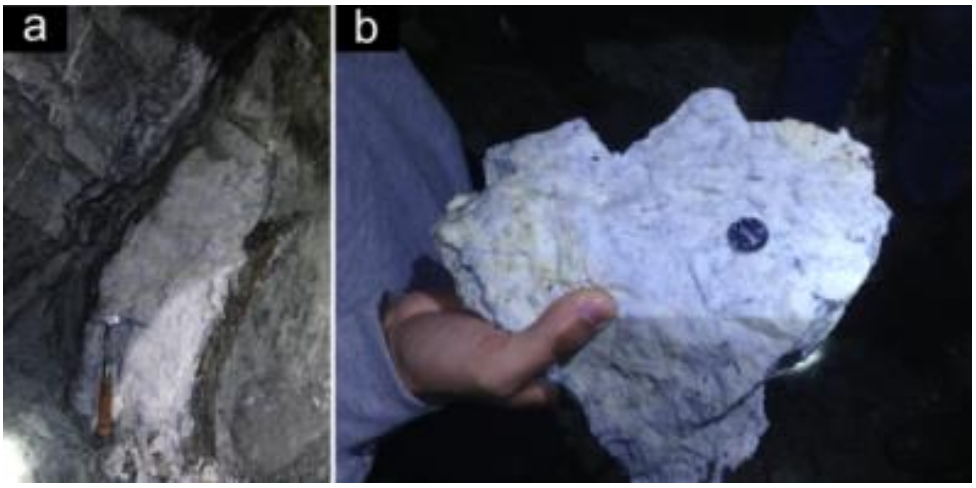

Figure 4.28 – Longtougou (orogenic) Au deposit field work photographs

a) Mineralised vein, location of where specimen was sourced
b) Baryte-vein material

4.7.2 Minerals

Baryte $BaSO_4$

Baryte occurs primarily as earthy aggregates, with some clear well-developed crystals. In some instances, the mineral is incredibly fine-grained, giving it a dusty appearance. In PPL the mineral grains are grey-brown, making them easy to distinguish between quartz (Figure 4.29c & f). In XPL the baryte grains demonstrate similarity in high order birefringence with calcite or gypsum (Figure 4.29d & e). The baryte grains demonstrate perfect cleavage, with an intersect angle of approximately 80° (Figure 4.29f).

Quartz SiO_2

Quartz often occurs as veinlets, rather than as dismembered grains throughout the sample. Brecciated hydrothermally-derived quartz is also common, displaying undulose extinction due to strain (Figure 4.29c & d). Sulphides occur most prominently on the contact, or boundary between baryte and quartz veins; this feature may be the result of fluids passing through two units (i.e. baryte and siliceous siltstone units), where the fracture planes are weakest providing ideal space and conditions for metalliferous fractions to precipitate out in the form of gold, pyrite, chalcopyrite, hematite and galena (Figure 4.30k & l).

4.7.3 Paragenesis

Baryte, being the most abundant barium mineral in Earth's crust, is also the least soluble (Blount 1977, Deer *et al.* 2013). In the Longtougou (orogenic) Au deposit the mineral commonly occurs as gangue material in metalliferous hydrothermal veins and as veins or cavity-filling concretions in limestones, sandstones, shales and clays (Dunham 1990). The Longtougou (orogenic) Au orebody sits within an Early to Late Devonian sedimentary package of dolomites, siltstones and conglomerates. Along with gold, mineralisation is present in the form of pyrite, hematite and chalcopyrite (Figure 4.30). The sedimentary-host sequences combined with metals having been precipitated out (particularly notable in vein structures) provides a suitable environment for the occurrence of baryte. The source of the baryte could potentially be sulphides in the cap rock or in other adjacent sulphur-bearing strata (whereby the precipitation of baryte can occur from the oxidation of reduced sulphur species to sulphate in solutions carrying barium or by the

mixing of barium-rich fluids in surface waters; Claypool *et al.* 1980). This could be evident in the corroded pyrite; where the pyrite is indicative of reduced conditions, followed by later-stage hematite (found within and on the edges of the pyrite), evidence of oxidising conditions (Figure 4.30j). It has also been noted that micas and feldspars within the dolomites or limestones, or clays and shales may act as an original source of barium – which provides another possibility given the tectonic setting of the Longtougou (orogenic) Au deposit.

With regard to the presence of dismembered pyrite with inclusions and dusting of hematite this may assist in further defining the setting of this deposit – to begin with, reducing fluids may have been present deeper in the crust (evident in the precipitation of pyrite) before these fluids moved upwards towards the surface. On reaching higher levels in the crust, the system begins producing hematite; it appears the pyrite is being dissolved along the edges and particularly in the middle of many grains. Hematite is a secondary Fe-oxide phase, overprinting and attacking the primary pyrite (Figure 4.30j).

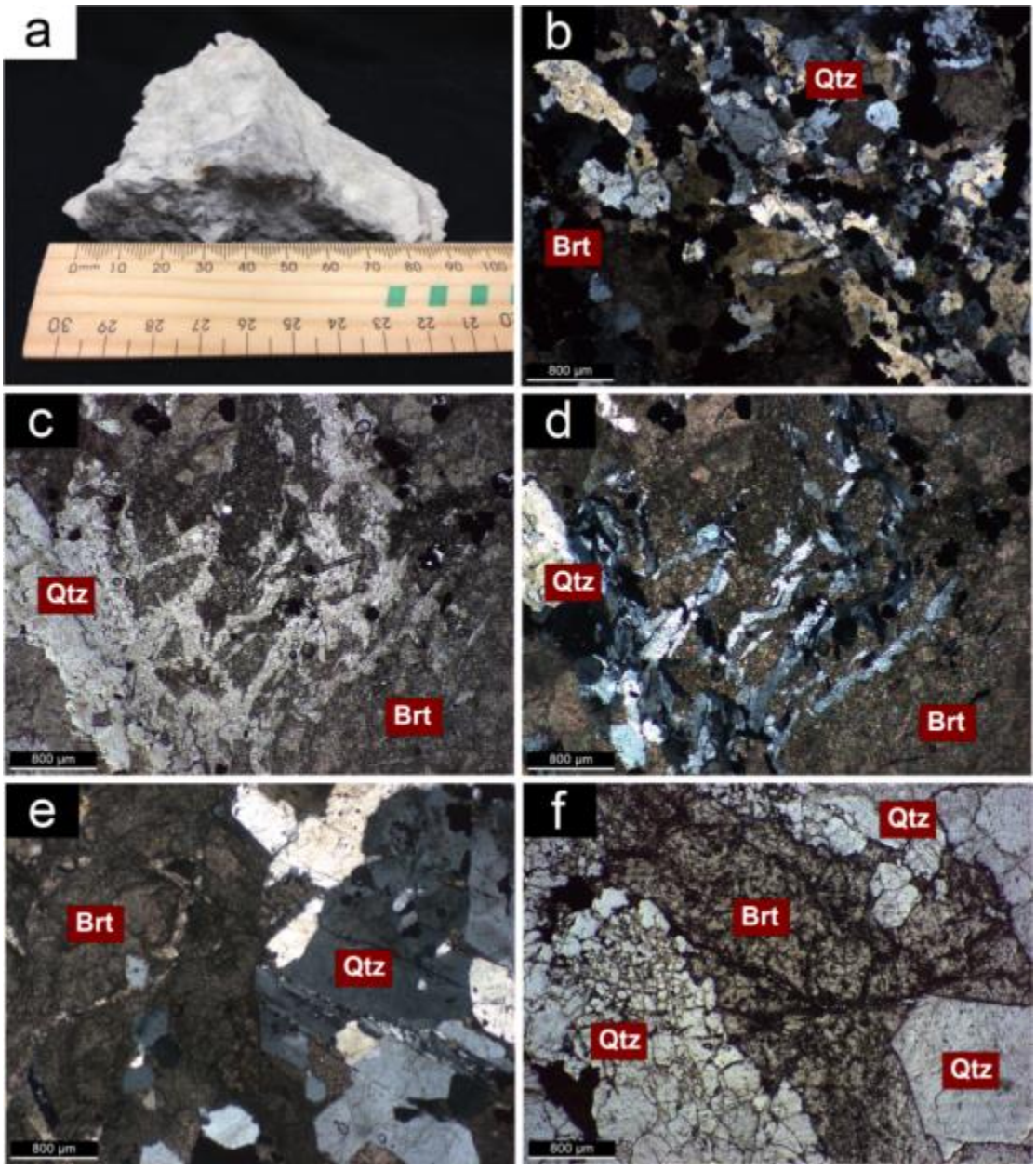

Figure 4.29 - **Longtougou (orogenic) Au deposit – ore vein**
(a) 15LT_A, fine-grained baryte, note: this is a vein rather than a host rock sample; **(b)** 15LT_A - XPL, representative sample of the groundmass, with main constituents quartz and baryte, this sample may be indicative of a siliceous siltstone protolith; **(c)** 15LT_A - PPL, & **(d)** 15LT_A - XPL, splay of quartz veinlets within a fine-grained baryte matrix. This could be representative of an explosive episode of volatile release within the unit; **(e)** 15LT_A - XPL, contact between baryte and quartz. The bartye grains occur as earthy aggregates, with some clear well-developed crystals. In this instance however, the mineral is very fine-grained, giving it a dusty appearance. The quartz often occurs as veinlets, rather than dispersed grains throughout the sample; **(f)** 15LT_A - PPL, when preserved the baryte grains demonstrate perfect cleavage, with an intersection angle of approximately 80°. This is best demonstrated in PPL

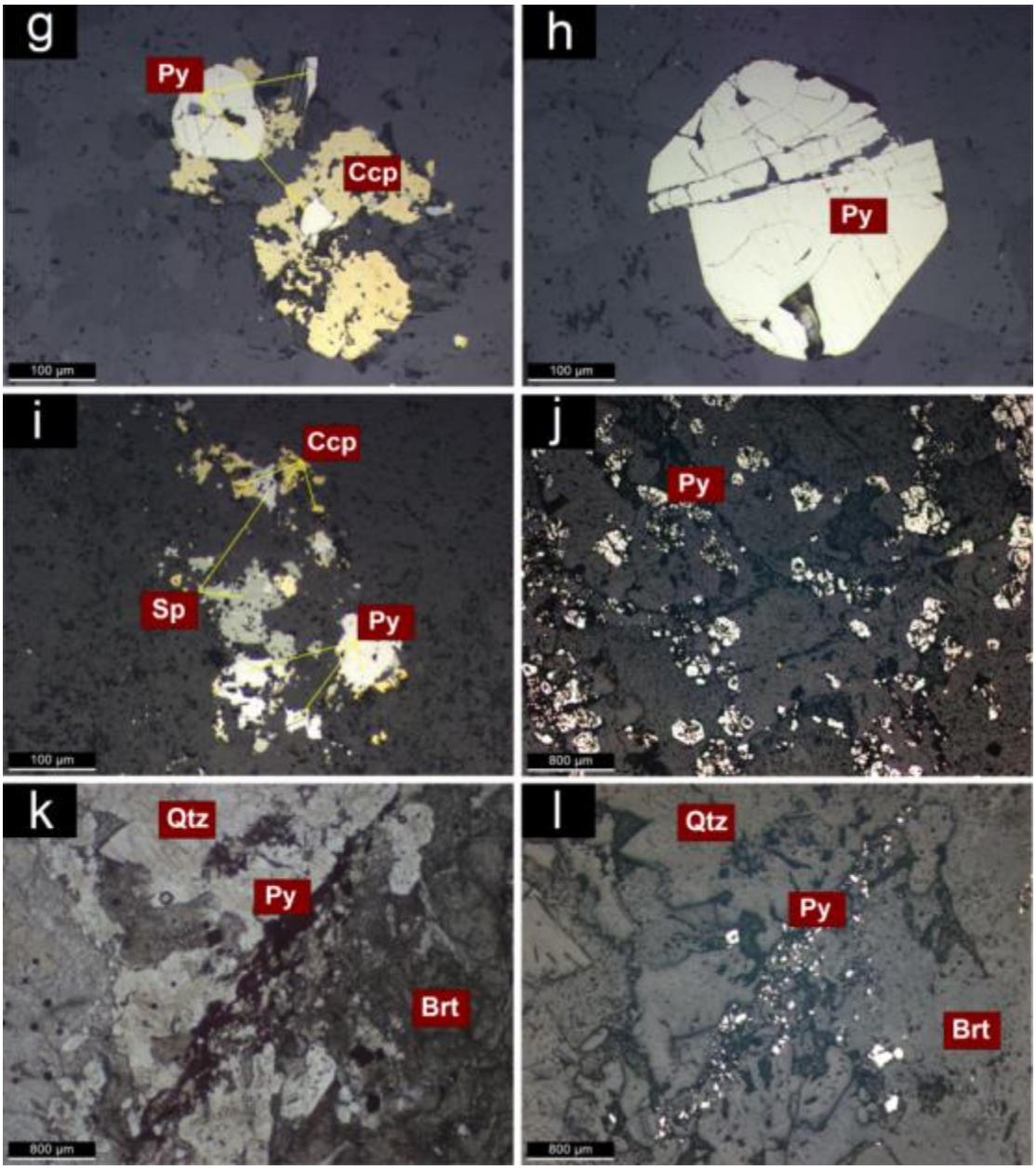

Figure 4.30 - **Longtougou (orogenic) Au deposit – ore vein (mineralisation)**
This plate displays the different types of mineralisation styles within the Longtougou orogenic Au deposit. **(g)** 15LT_A – PPL (reflected), earlier formed chalcopyrite grains are overprinted by later stage pyrite. The chalcopyrite has been largely attacked, while the pyrite (although it does not demonstrate well-formed cubic habit) appears to be less corroded. Note the minor sphalerite inclusion in the larger (100 µm) pyrite grain; **(h)** 15LT_A – PPL (reflected), sub-rounded pyrite grain with major fracture separating the top third from the main crystal. Note, the fracture appears to be infilled a grey mineral (sphalerite?); **(i)** 15LT_A – PPL (reflected), dispersed and dismembered mineralisation (chalcopyrite, sphalerite and pyrite) within a baryte matrix; **(j)** 15LT_A – PPL (reflected), interspersed pyrite that demonstrates attack largely within the middle of the grains. Cubic habit of some grains has been preserved, however most grains are subhedral; **(k)** 15LT_A – PPL, & **(l)** 15LT_A – PPL (reflected), mineralisation occurs most prominently on the contact, or boundary between baryte and quartz veins; this feature may be the result of fluids passing through two units (i.e. baryte and siliceous siltstone units)

4.8 LIUJIAXIA (orogenic) Au DEPOSIT

4.8.1 Classification

In hand specimen this unit represents a fine-grained siltstone grading to a shale (Figure 4.32a). Lenses of baryte are also apparent in the hand sample, identifiable by white coloration as opposed to the grey colour which dominants the unit. No mineralisation is observable. Polished thin section and XRD analysis indicate a mineral assemblage incorporating major minerals: quartz (50%), baryte (35%); accessory minerals: calcite, dolomite, ankerite (total accessory minerals 12%); and secondary minerals: hematite, pyrite, chalcopyrite, sericite, gold (3%).

In thin section quartz is more abundant than baryte, consistent with hand specimen observations. As such the quartz may represent the original sedimentary unit before having undergone episodes of deformation. Similar to the previously described Longtougou (orogenic) Au deposit, mineralisation in thin section is very small (1 – 3 μm) and difficult to identify. The Liujiaxiam (orogenic) Au deposit is part of a much larger sedimentary package consisting of conglomerates and dolomites (Figure 4.31a). Herein, this unit will be described as siltstone.

Figure 4.31- Liujiaxia (orogenic) Au deposit field work photographs

a) Representative sample of the larger sedimentary package (in this instance conglomerate sequence) with which the Liujiaxiam (orogenic) Au deposit is hosted
b) The Qinlng Orogenic Belt (QOB) provides the perfect setting for orogenic gold deposits with structural controls combined with typically steeply dipping and plunging strata

4.8.2 Minerals

Quartz SiO_2

Quartz is more prevalent over baryte in thin section. Some regions within the sample preserve sedimentary features; thus Figure 4.32b represents a domain with graded beds (a possible turbidite sequence). There is a sharp basal contact followed by coarse-grained quartz gradually grading into fine-grained quartz at the top of the photomicrograph. Abundant quartz veinlets also occur throughout the sequence (Figure 4.32f). One of the most notable features observed under thin section is the orogenic gold model on a microscale; whereby quartz is orientated along the fold-axis, commonly followed by baryte (Figure 4.32c & d).

Baryte $BaSO_4$

Baryte occurs in a much similar fashion to that observed at the previous Longtougou (orogenic) Au deposit; the mineral occurs as earthy aggregates distinguishable from calcite by its dark brown colour (Figure 4.32e).

4.8.3 Paragenesis:

As previously mentioned, the Liujiaxia (orogenic) Au deposit is part of a much larger sedimentary package consisting of conglomerates and dolomites. This unit overall represents quartz-rich mature sediments. Within the adjacent conglomerate unit no volcanic clasts were observed. Although much more investigation would be required to confirm, on these observations alone (assuming that the siltstone unit has uniformly consistent mature quartz-rich sediments, and the conglomerate unit contains little to no volcanic clasts) the setting of the sedimentary package could be that of an intra-cratonic fore-land basin, or possibly a back-arc basin.

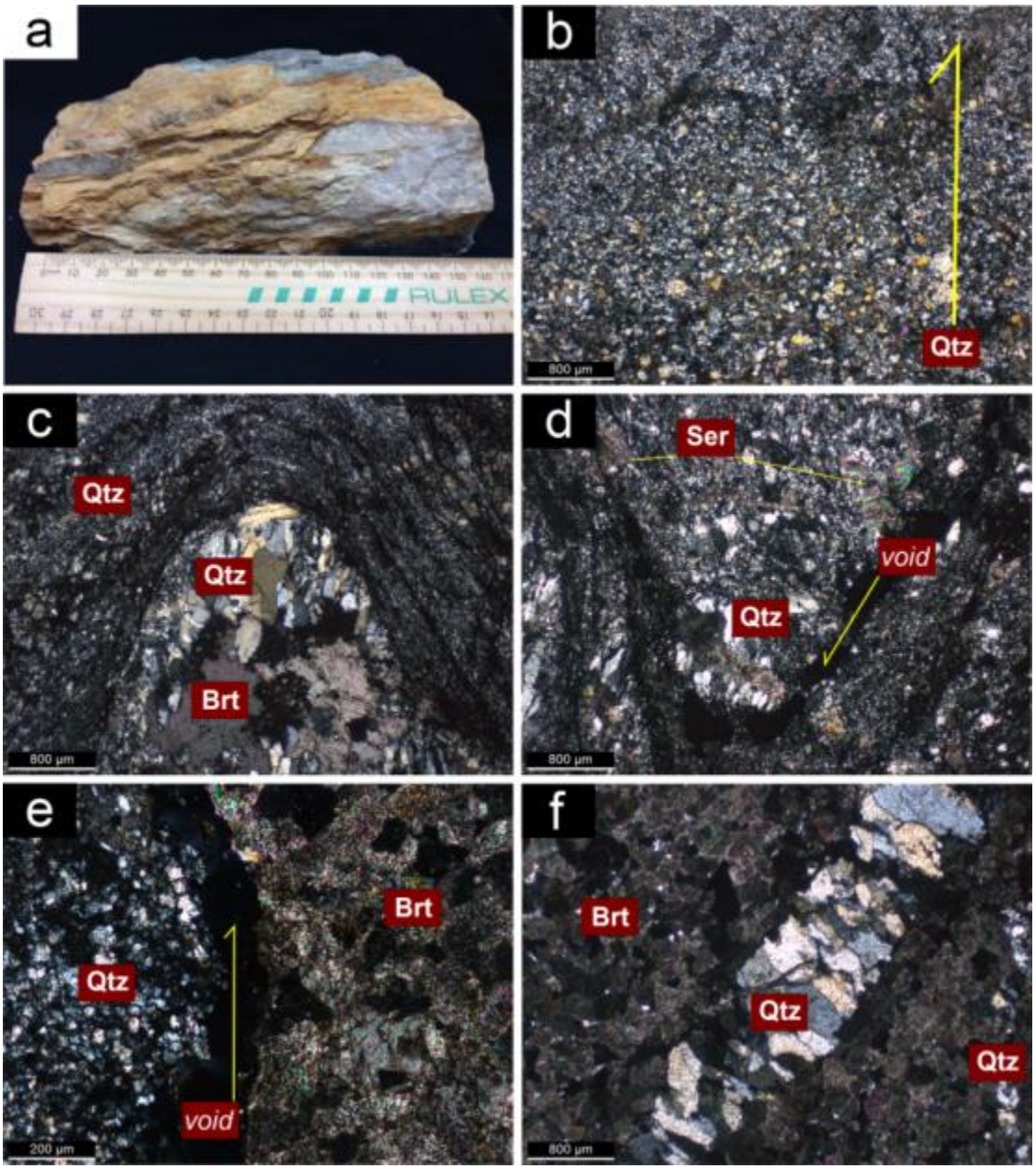

Figure 4.32 – **Liujiaxia (orogenic) Au deposit – Siltstone**
(a) 15LJ_B, fine-grained baryte, note: this is a vein rather than a host rock sample; **(b)** 15LJ_B – XPL, the abundant quartz in this sample may be representative of the original sedimentary rock (i.e. siltstone). This photomicrograph demonstrates a region within the thin section that represents graded beds (potentially a turbidite sequence). A fining upwards sequence is demonstrated by a yellow arrow; **(c)** 15LJ_B – XPL, & **(d)** 15LJ_B – XPL, the Liujiaxia orogenic Au deposit occurs in the apex of an anticline. This is also featured under thin section, where folds are observed with coarse-grained quartz aggregates (300 – 500 µm) occurring in the fold axis. This photomicrograph demonstrates an orogenic gold model on a microscale; **(e)** 15LJ_B – XPL, contact between quartz and baryte with void space in between indicated by a yellow arrow; **(f)** 15LJ_B – XPL, quartz often occurs as veinlets, rather than dispersed grains throughout the sample similar to the previous gold deposit

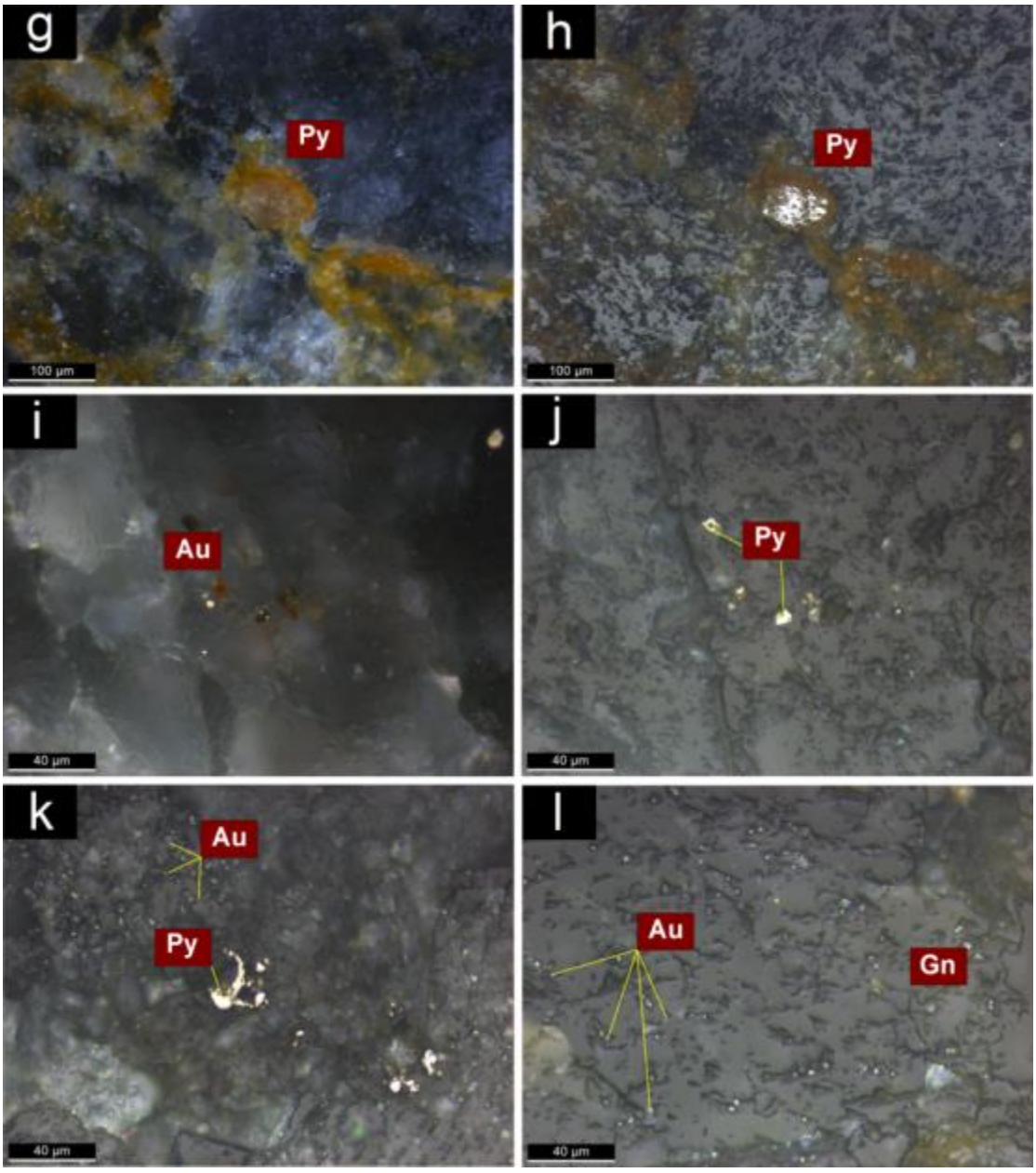

Figure 4.33 - **Liujiaxia (orogenic) Au deposit – Siltstone (mineralisation)**
This plate displays the different mineralisation styles within the Liujiaxia orogenic Au deposit. **(g)** 15LJ_B – XPL (reflected), & **(h)** 15LJ_B – PPL (reflected), Fe oxide is observed precipitating proximal to the pyrite grain. Fine grained gold is observed in the matrix as small granules; **(i)** 15LJ_B – XPL (reflected), & **(j)** 15LJ_B – PPL (reflected), hematite is found occurring marginal to granular gold in a bartye matrix, with a proximal quartz vein to the left of the gold grains; **(k)** 15LJ_B – XPL (reflected), where gold is observed it is in association with pyrite; **(l)** 15LJ_B – PPL (reflected), gold occurs as intergrowths within a quartz matrix. The gold grains are very small occurring as 1-3 µm blebs

4.9 DAMOGOU Zn-CaF_2 DEPOSIT

4.9.1 Classification

In hand specimen, this unit presents largely as purple fluorite hosting massive sphalerite with minor galena, chalcopyrite, and pyrite (Figure 4.34a & Figure 4.36a). Most of the samples also have easily distinguishable bornite. Polished thin section, SEM-EDS and XRD analysis indicate a mineral assemblage incorporating major mineral: fluorite (70%); minor mineral: quartz (10%); and secondary minerals: sphalerite, chalcopyrite, galena and pyrite (mineralisation accounting for up to 20% of this unit).

In thin section the unit represents a rock that has largely undergone hydrothermal alteration and replacement to such an extent that the original rock type cannot be ascertained. The deposit occurs in a contact zone between alkali volcanic rocks (trachyte) and limestone, with the deposit itself having been allocated an age between Lower Permian – Upper Triassic. Field work indicated that along with hydrothermal alteration, supergene enrichment was a process prevalent in the Damogou Zn-CaF_2 deposit (Figure 4.34b). Herein, this unit will be described as a hydrothermal sphalerite vein (or 'ore-vein' in the photomicrograph plates).

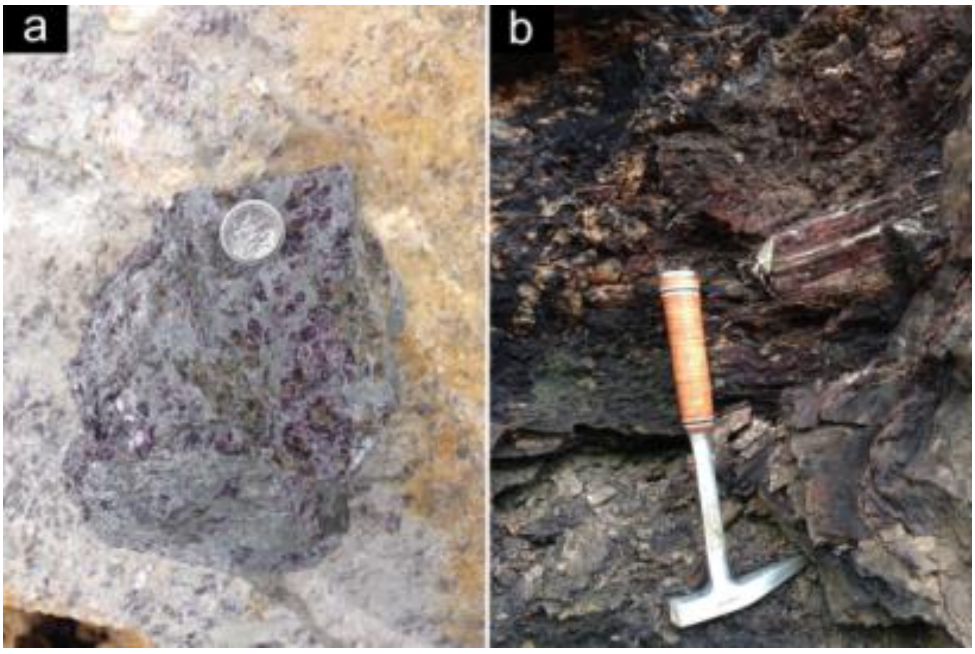

Figure 4.34 – Damogou Zn-CaF_2 deposit field work photographs

a) Representative sample of the fluorite hosting hydrothermal sphalerite vein
b) Supergene enrichment profile

4.9.1 Minerals

Fluorite CaF_2

Fluorite constitutes the majority of the mineral assemblage (~70%) of the Damogou Zn-CaF_2 deposit, and appears to be a host for zinc mineralisation having hydrothermally replaced the original rock-type. Seeing as the deposit is constrained by volcanic rocks and limestone it can be assumed that these were the host. It is more likely that the limestone would have been the original rock-type, having undergone massive alteration and mineralisation as opposed to the alkali volcanics. The fluorite grains are cream-purple in thin section, with three distinct directions of perfect cleavage. The halide group member demonstrates a particularly low refractive index (characteristic low relief), with isotropic characterisation (Figure 4.36f) making it easy to distinguish between other minerals observed under thin section of the Damogou Zn-CaF_2 deposit samples.

Sphalerite ZnS

Sphalerite, second to fluorite, makes up a significant proportion of the mineralogical assembly (Figure 4.37). It occurs as resinous, transparent grains, with the majority of the sphalerite demonstrating opaque mass aggregates. The mineral has a brown-yellow colour, which can be linked, to the iron content; yellow sphalerite indicates only small fractions of iron being incorporated into the crystal lattice, indicating a low-temperature formation, whereas black sphalerite (e.g. Broken Hill sphalerite) is indicative of increased amounts of iron being taken up into the mineral requiring high-temperature formation conditions (Fleet 2006).

Chalcopyrite $CuFeS_2$

Chalcopyrite makes for an important part of the sulphide assemblage and is observed most commonly in association with sphalerite rather than grains located throughout the fluorite matrix of the unit. In most instances the chalcopyrite occurs as bleb-like inclusions within sphalerite. Chalcopyrite has also been observed as overgrowths around the earlier stage sphalerite (Figure 4.37).

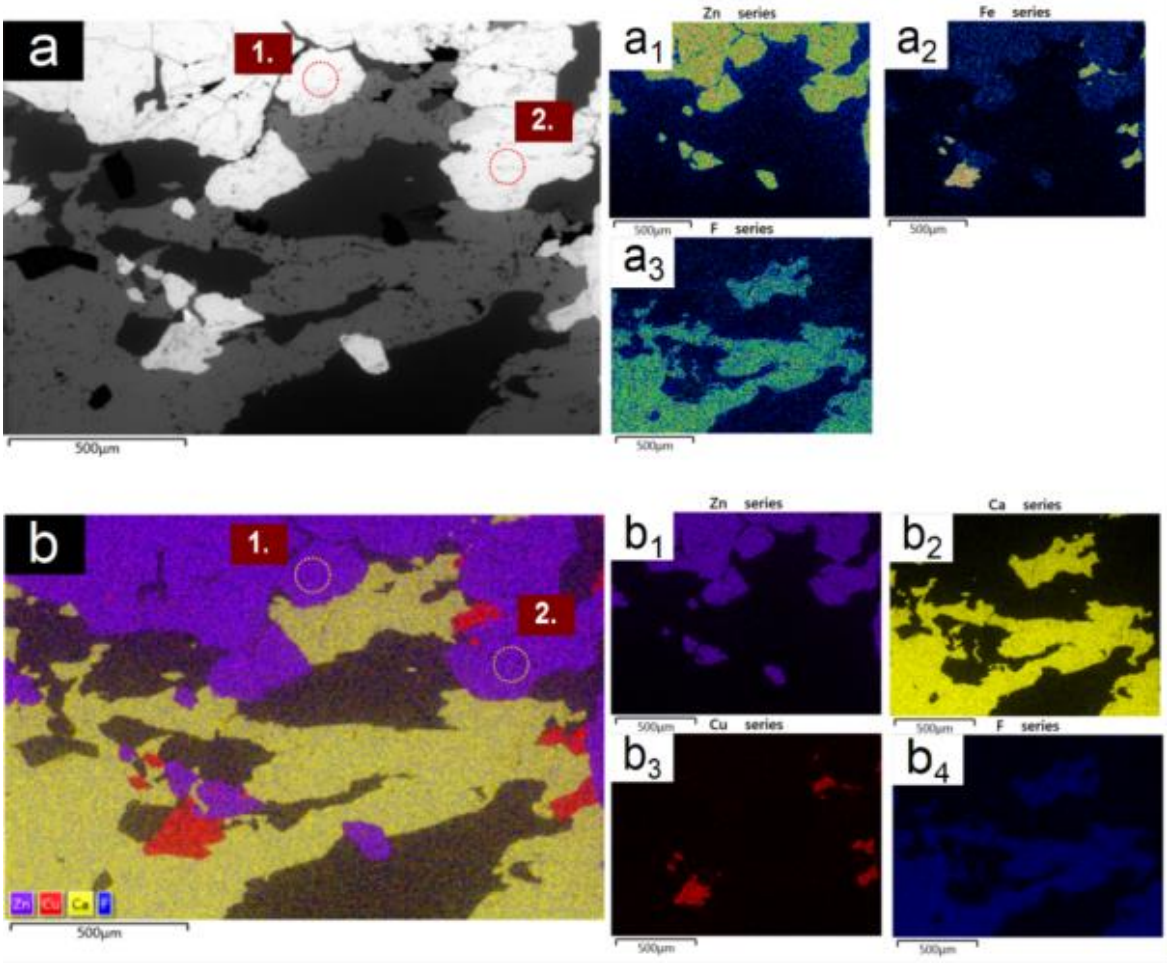

Figure 4.35 - SEM-EDS results of Damogou Zn-CaF_2 sample 15DG_A

a) Electron image taken of thin section 15DG_A

a_1 – a_3) Discrete colour maps displaying the occurrence of Zn, Fe and F within sample 15DG_A

b) Layered image of thin section 15DG_A

b_1) – b_4) Raster maps displaying the occurrence of Zn, Ca, Cu and F within sample 15DG_A. As expected, the F-raster and the Ca-raster plot over the same areas within the region of interest indicative of fluorite (CaF_2)

Refer to Appendix D for further analyses for of Damogou Zn-CaF_2 sample 15DG_A, including elemental graphs for the spectrum points of analysis, identified by numerical maroon boxes

4.9.3 Paragenesis

Fluorite is known to occur as a late-stage accessory mineral in granites and greisens however, applicable to the Damogou Zn-CaF_2 deposit, the mineral is also found occurring as a product of hydrothermal mineralisation in limestones (Deer *et al.* 2013, Ying *et al.* 2015). Seeing as the orebody is constrained by Triassic volcanic rocks (tracyte) and limestone, this latter scenario is the best fit. The main assemblage, as indicated by thin section, SEM-EDS and XRD analysis is a sphalerite + chalcopyrite + galena + pyrite, associated with a fluorite + quartz gangue assemblage. In the Damogou Zn-CaF_2 deposit, sphalerite is not pure ZnS (which presents are colourless), rather impurities with the mineral (commonly Fe) produces the yellow-brown colouration. Other sphalerite varieties can be attributed to impurities in the form of manganese, copper and cadmium being incorporated into the crystal lattice (Barton and Toulmin 1966). There is a texture commonly observed throughout the Damogou Zn-CaF_2 deposit whereby there is an intergrowth of oriented and unorientated inclusions of chalcopyrite in sphalerite, otherwise termed 'chalcopyrite disease'. Misra (2001) summarises three main processes which could attribute to the intimate formation of chalcopyrite in association with sphalerite; i) high temperatures acting on a sphalerite-chalcopyrite solid solution resulting in the exsolution of chalcopyrite; ii) simultaneous precipitation of both sphalerite and chalcopyrite; and iii) interaction of Cu-bearing hydrothermal fluids resulting in subsequent replacement of sphalerite. The third process would best suit the setting of the Damogou Zn-CaF_2 deposit. Misra (2001) notes that the replacement theory would be the best explanation for chalcopyrite disease on account of experiments conducted to simulate hydrothermal conditions where iron-bearing sphalerite was reacted with copper-bearing chloride fluids, which in turn produced chalcopyrite disease. Furthering on this, investigations into the stability fields of the Cu-Fe-Zn-S system, particularly regarding the solubility of copper in sphalerite, have demonstrated limited chance for precipitation between 300 - 700°C. The sphalerite observed within the Damogou Zn-CaF_2 deposit is low temperature (indicted by brown-yellow colour), supporting a hydrothermal regime.

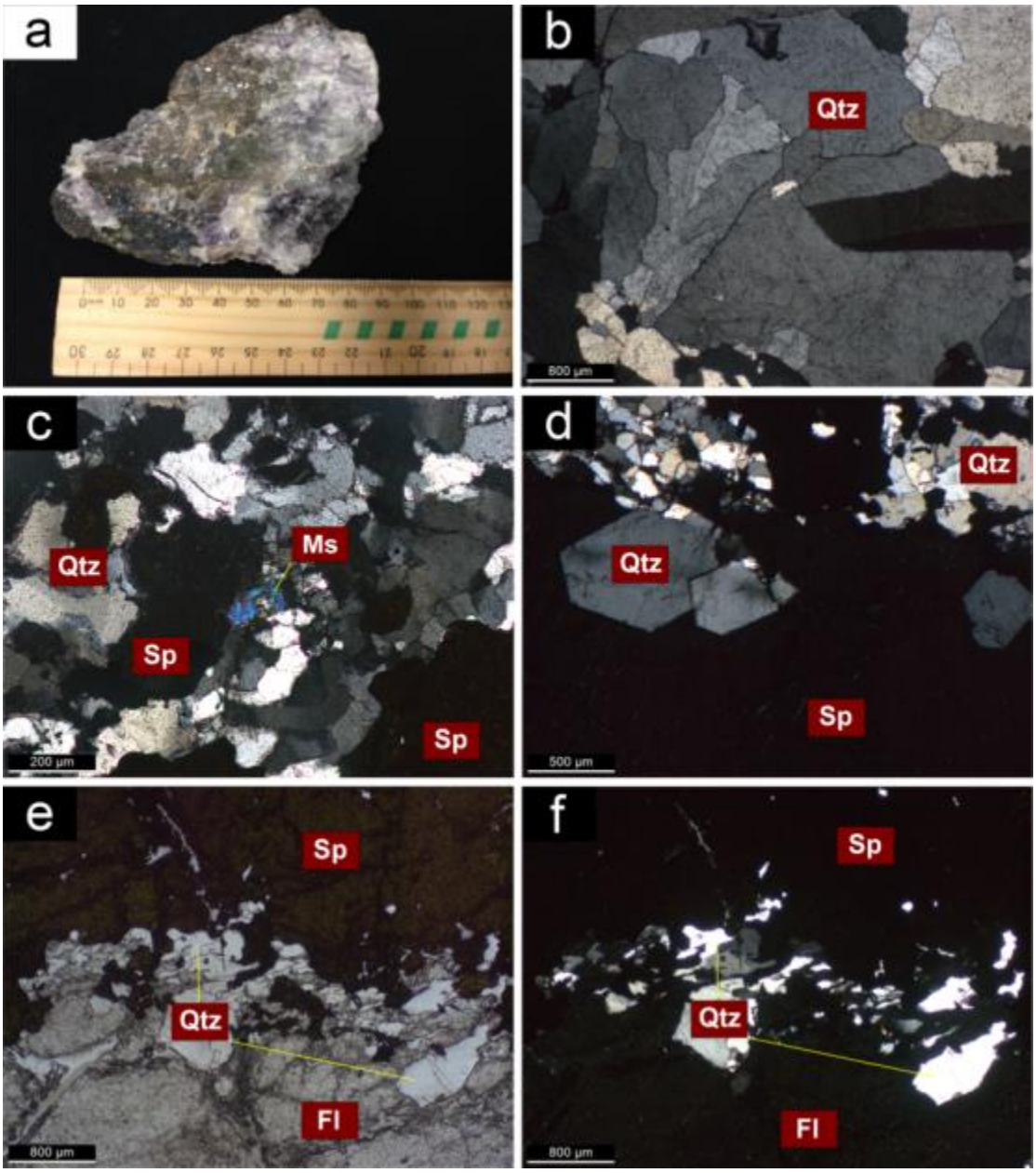

Figure 4.36 - **Damogou Zn-CaF_2 deposit – Ore vein**
(a) 15DG_A, fluorite hosting zinc-ore. Note: this is a vein rather than a host rock sample**; (b)** 15DG_A – XPL, this photomicrograph exemplifies typical quartz grains, which occur as aggregates throughout the fluorite groundmass; **(c)** 15DG_A – XPL, muscovite alongside sphalerite in a larger quartz matrix; **(d)** 15DG_A – XPL, fine-grained quartz vein with large (400-700 µm), well-developed (euhedral) quartz phenocrysts, bordering sphalerite (black); **(e)** 15DG_A – PPL, sphalerite is easily distinguishable under PPL where it presents dark brown-yellow coloration; **(f)** 15DG_A – XPL, quartz vein transecting through massive sphalerite

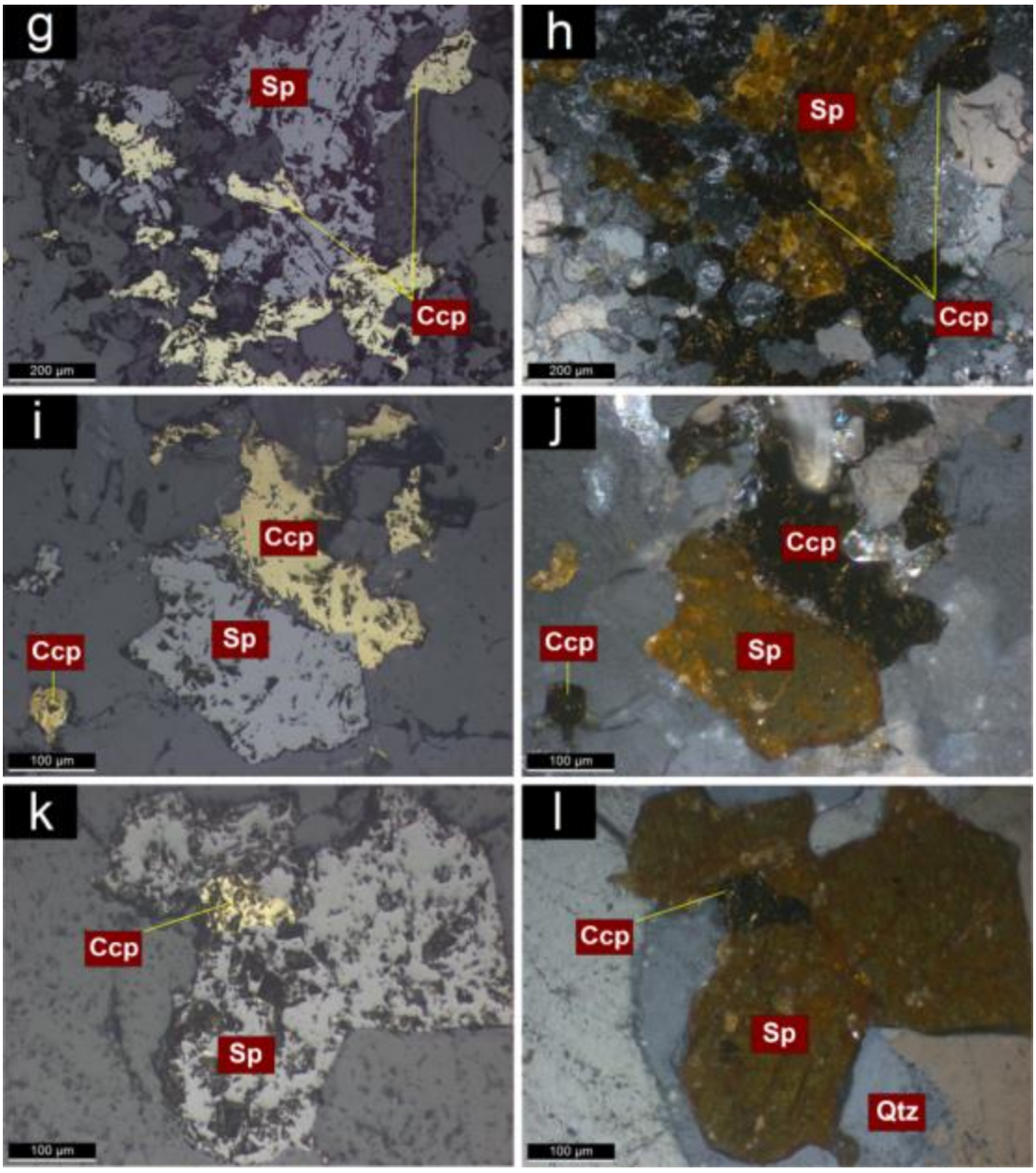

Figure 4.37 - **Damogou Zn-CaF_2 deposit – Ore vein (mineralisation)**
This plate displays the common association of sphalerite and chalcopyrite. Sphalerite, being the important ore mineral for the Damogou Zn-CaF_2 deposit; the mineral presents in a brown-yellow colour, which can be linked, to the Fe content. The above photomicrographs exemplify chalcopyrite disease in sphalerite, assumed to be a result of the replacement of sphalerite by the interaction with Cu-bearing hydrothermal solutions. **(g)** 15DG_A – PPL (reflected), & **(h)** 15DG_A – XPL (reflected), chalcopyrite occurring as large growths within sphalerite; **(i)** 15DG_A – PPL (reflected), & **(j)** 15DG_A – XPL (reflected), chalcopyrite replacing a once whole sphalerite grain, maintaining much of the original grain shape; **(k)** 15DG_A – PPL (reflected), & **(l)** 15DG_A – XPL (reflected), bleb of chalcopyrite (100 µm) within a larger sphalerite mass

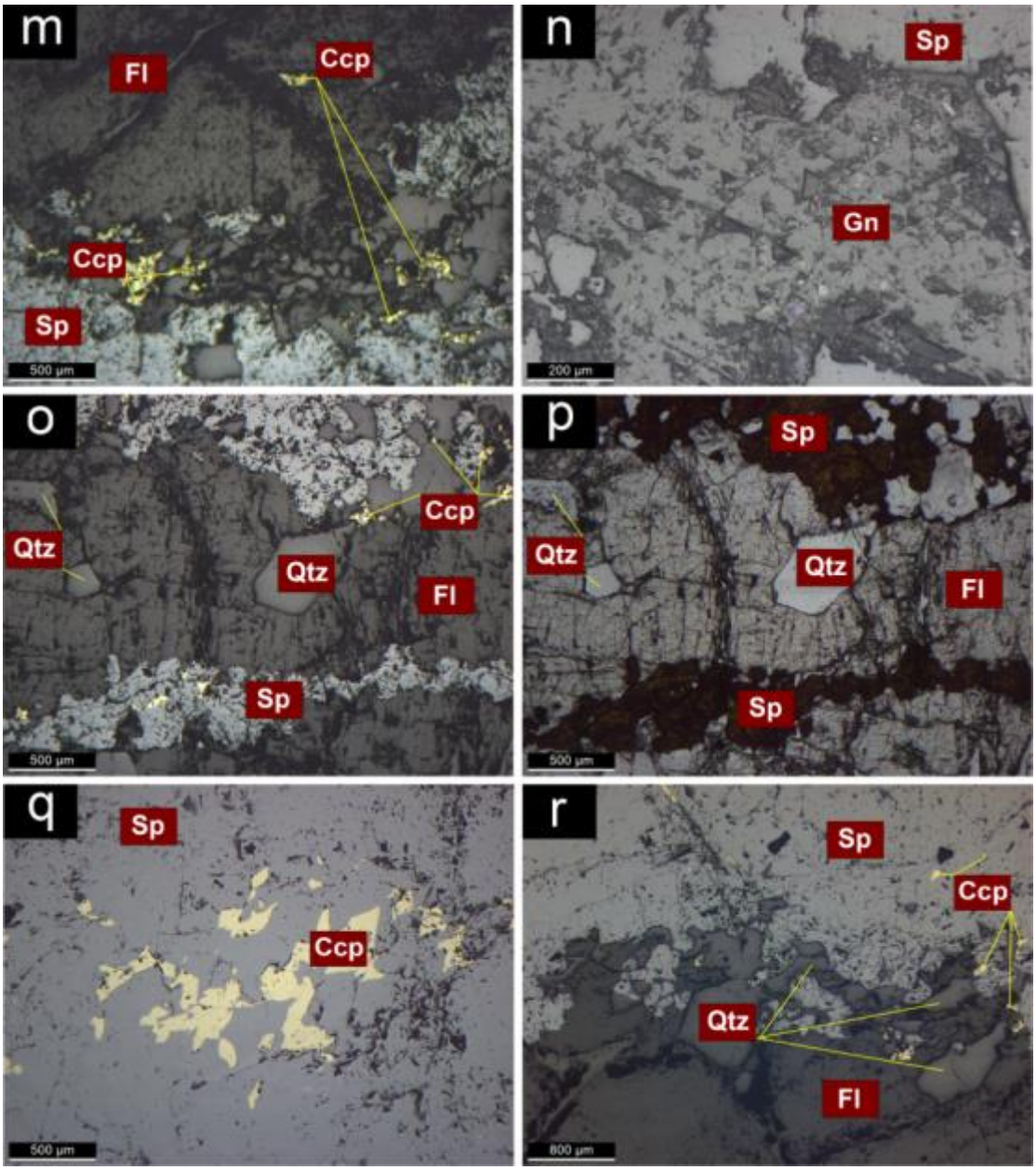

Figure 4.38 - **Damogou Zn-CaF_2 deposit – Ore vein (mineralisation)**
(m) 15DG_A – PPL (reflected), chalcopyrite is not restricted to only occurring as 'disease' within the sphalerite. This photomicrograph demonstrates chalcopyrite occurring within fluorite also; **(n)** 15DG_A – XPL (reflected), galena is a mineral found commonly occurring with sphalerite. Note the characteristics triangular pits of the galena compared with sphalerite; **(o)** 15DG_A – PPL (reflected), & **(p)** 15DG_A – PPL, sphalerite occurs as dispersed grains and as observed in this instance as veins; **(q)** 15DG_A – PPL (reflected), chalcopyrite disease occurring within sphalerite; **(r)** 15DG_A – PPL (reflected), this photomicrograph further demonstrates that chalcopyrite occurs over all mineral assemblages within the Damogou Zn-CaF_2 deposit

5.1 INTRODUCTION

Whole rock geochemistry is used to classify and constrain the geotectonic setting of plutonic rocks (Gill 2011). The prime focus will be on the Nantai Mo-(Cu) deposit, with less attention paid to the Miaoya REE deposit, the Longtougou and Liujiaxia orogenic Au deposits and the Damogou Zn-CaF_2 deposit. Geochemical data was acquired by X-ray fluorescence (XRF) and inductively coupled plasma mass spectrometry (ICP-MS), and is interpreted with the assistance of discrimination diagrams widely used in the literature. The theory of plate tectonics and the recognition that allochthonous terranes sometimes travel many thousands of kilometres before being amalgamated onto the margins of continental nuclei, brought with it the need to determine the tectonic affinity of igneous rocks caught up in complexly deformed orogens for which the origins were unknown. It became recognisable that geochemical signatures of igneous rocks could be linked to particular geotectonic settings, as well as identifying geological processes, such as the partial melting, fractional crystallisation, liquid immiscibility and contamination responsible for the diversity of compositions within igneous suites (Pearce *et al*. 1984; Figure 5.1). The geochemical 'fingerprinting' of modern environments provides a tool to recognise the geodynamic setting from geochemistry alone, when the structural and paleaogeographic context of these rocks has been destroyed (Rollinson 1993).

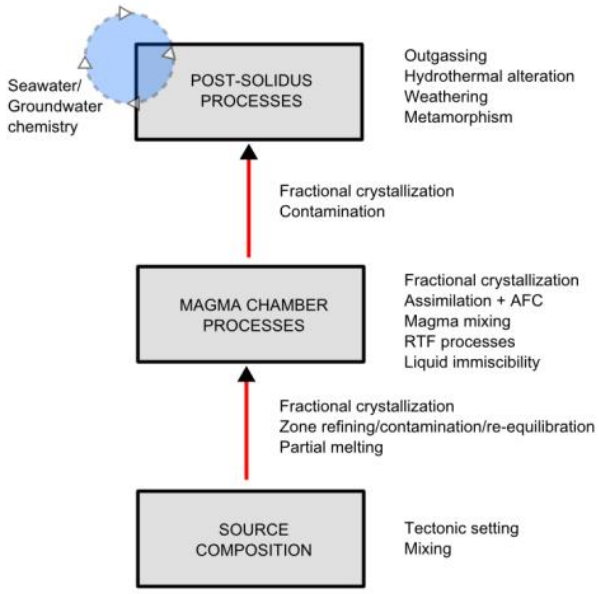

Figure 5.1 - Flow diagram showing the principal processes that controls the chemical composition of igneous rocks. Adapted from Rollinson (1993)

5.2 METHODS

Principles of X-ray Fluorescence

The XRF method relies on the interaction between X-rays and the targeted material, specifically the behaviour of atoms when they are exposed to radiation (Shackley 2010, Margui and Grieken 2013). When geological materials are exposed to radiation exhibiting both high-energy and short wavelengths the sample, on excitement, becomes ionised. Inner electrons become unstable and, if the X-ray beam is sufficient, knock the electron from its orbital surrounding the nucleus within an atom of the geological material. The resultant atom is unstable due to the change in configuration of the orbital, that being the creation of a vacancy. In order to restore equilibrium within the atom, one of the electrons from the outer orbits falls into the newly created space. Excess energy is emitted in the form of a fluorescent X-ray, as the higher energy electron has repositioned into a lower energy orbit. Herein explains the usefulness of XRF; the characteristic difference in energy from the expelled and replaced electrons can be used to identify the element atom in which the process is taking place. In other words, the energy of the emitted fluorescent X-ray is directly linked to the specific element being analysed (Margui and Grieken 2013).

Seventeen samples were first crushed for 10 – 15 seconds into a fine powder at the University of Wollongong (UOW) using a TEMA chromium steel ring mill. The mill was rinsed with quartz between each sample in order to avoid cross-contamination between samples. An aliquot of powder was sent for whole-rock geochemistry at ALS Ltd. Minerals Division, Brisbane where the remaining process of XRF was completed by laboratory technicians. For trace element analysis, pressed pellets were prepared through combining 5 g of each crushed sample with a binder of PolyVinyl Acetate (PVA) before being transferred to aluminium moulds pressed at 2500 psi. The moulds were subsequently heated for 24 hours in an oven at 65°C after which were analysed for trace elements. Those samples identified as having > 400 ppm copper and >1000 ppm sulphur required oxidation prior to fusing for major element analysis; the oxidation process required the addition of 5 ml of $LiNO_3$ to the samples then allowing them to dry overnight in an oven at 65°C. After the completion of this, the samples were then heated to 100°C for one hour, then increased by 50°C every 20 minutes until reaching 600°C, at which the samples were then allowed to gradually cool.

With regard to major element analysis, a metaborate flux was added to high silica (>65 wt.% SiO_2) samples and a 12:22 tetraborate to metaborate flux was added to mafic (45 – 65 wt.% SiO_2) samples. The mixtures were then placed in platinum crucibles and, over the duration of one hour, were heated from 600°C to 970°C and then making a glass disc from the fused material. Loss on ignition (LOI) was determined through measuring the difference between the initial and subsequent weights after the heating of 1 g of each sample at 1050°C for two hours. Ametek Materials Analysis Division Inc. software was utilised for spectral investigation and subsequent identification. The software maintains accuracy through calibrating against various natural and synthetic materials.

With regard to rare-earth element (REE) analysis, powdered samples were first fused in a furnace after being mixed into a lithium tetraborate or lithium metaborate flux. After cooling, dissolution of the glass was by the addition of nitric, hydrofluoric and hydrochloric acids. The subsequent solution was then adequately prepared to undergo analysis using inductively coupled plasma mass spectrometry (ICP-MS).

Rock classification and geotectonic discrimination diagrams and plots were created using a combination of GCDkit (Janoušek *et al.* 2006) and Microsoft Excel.

Analytical Procedures

ALS Code	Description	Instrument
ME-OG62	Ore Grade Elements - Four Acid	ICP-AES
Cu-OG62	Ore Grade Cu -Four Acid	ICP-AES
Zn-OG62	Ore Grade Zn - Four Acid	ICP-AES
Au-AA25	Ore Grade Au 30g FA AA Finish	AAS
ME-XRF26	Whole Rock By Fusion/XRF	XRF
ME-GRA05	H2O/LOI by TGA furnace	TGA
ME-MS61r	48 element four acid ICP-MS + REEs	ICP-MS

Table 5.1 - ALS analytical procedures, with description and instrument used for the determination of major, trace and rare-earth elements (REE), along with ore-grade separation techniques utilised in this investigation for Au, Cu and Zn

5.3 NANTAI Mo-(Cu) DEPOSIT

Earth's continental crust is dominated by igneous rocks that are broadly granitic in composition. Granitoid rocks form in an array of different geotectonic settings, ranging from orogenic and collisional (e.g. Andes and Himalaya complexes) to within-plate anorogenic regions, volcanic arc settings and even as small volumes in mid-ocean ridges (Gill 2010). Granitic rocks are host to important metalliferous mineral deposits, with volatile and heat transfer into the batholith roof working as a driving force for hydrothermal mineralisation (Ridley 2013).

The major element concentrations of the representative aplite dykes from the Nantai Mo-(Cu) deposit are shown in Table 5.2. The Nantai aplite (n = 5) yield the following wt. % (where μ = population mean): SiO_2 = 74.92 to 80.66% (μ 77.57%); Al_2O_3 = 9.49 to 13.32% (μ 12.0%); Fe_2O_3 = 0.15 to 0.38 % (μ = 0.26%); MgO = 0.07 – 0.44% (μ 0.23%); CaO = 0.15 – 0.83% (μ 0.38%); Na_2O = 0.17 – 3.80% (μ 2.02%); and K_2O = 5.59 – 7.96% (μ 6.56%). Those oxides (i.e. TiO_2, MnO, BaO, Cr_2O_3, SO_3 and SrO) not included in the description occur below specified detection limits (i.e. <0.5 %).

5.3.1 Plutonic rock classification

According to the total-alkalis versus silica (TAS) diagram of Cox *et al.* (1979) adapted by Wilson (1989) and further modified for intrusive igneous rocks by Middlemost (1985) the chemical classification and nomenclature of the dykes of the Nanatai Mo-(Cu) deposit indicates that they are of granitic affinity (Figure 5.2). This is consistent with petrographic analysis whereby the aplite samples have a corresponding quartzo-feldspathic composition. This is supported in Figure 5.3, which displays a ternary *QAP plot showing the relative modal proportions of quartz (Q), alkali feldspar (A) and plagioclase (P), defining the IUGS fields for granitic rocks, after Le Maitre (2002). In order to plot the mode of the aplite rock in the ternary QAP plot, the proportions of quartz, alkali feldspar and plagioclase were normalised and scaled to produce a sum of 100% (exclusive of other minerals present in the rock). The petrographic distinction between alkali feldspar and plagioclase in plutonic rocks is as follows: alkali feldspar = albite, anorthoclase, microcline, orthoclase and sanidine; plagioclase: anorthite, bytownite, labradorite, andesine, oligoclase (further more: IUGS defines 'plagioclase' as feldspar with >5 % An and 'alkali feldspar' as having <5 % An).

*QAP ternary plot: the diagram is designed for model mineral content (e.g. what is actually there). Norms for granitic rocks are not quite accurate. This is because the norms cast the Fe-Mg as largely anhydrous phases, whereas in granites Fe-Mg are associated with K in biotite. This means the normative QAP overestimates the alkali feldspar content.

Nantai Mo-(Cu) deposit											
Affinity	Aplite	Aplite	Aplite	Aplite	Aplite	Q.V	D.M	Q.V	Lamp	Lamp	Lamp
Sample	15NT_01	15NT_02	15NT_03	15NT_A	15NT_B	15NT_C	15NT_D	15NT_E	15NT_J	15NT_K	15NT_L
Age (Ma)	150	150	150	150	150	?	?	?	?	?	?
Lat. (N)	33°27'42"	33°27'42"	33°27'42"	33°27'42"	33°27'42"	33°27'42"	33°27'42"	33°27'42"	33°27'42"	33°27'42"	33°27'42"
Long. (E)	109°58'54"	109°58'54"	109°58'54"	109°58'54"	109°58'54"	109°58'54"	109°58'54"	109°58'54"	109°58'54"	109°58'54"	109°58'54"
Major elements (wt.%)											
SiO_2	78.6	76.91	74.92	80.66	76.74	96.08	37.06	83.68	65.14	47.87	48.72
TiO_2	0.06	0.06	0.06	0.04	0.05	0.01	0.02	0.04	0.56	1.22	1.2
Al_2O_3	11.85	13.1	13.32	9.49	12.26	0.15	0.16	8.03	11.14	15.02	14.68
$^{*}Fe_2O_3$	0.15	0.17	0.38	0.27	0.32	0.28	1.03	0.64	4.37	9.21	9.13
MnO	0.01	0.01	0.01	<0.01	0.01	0.02	0.22	<0.01	0.3	0.11	0.13
MgO	0.07	0.07	0.32	0.11	0.44	0.61	18.7	0.28	4.88	7.97	7.79
CaO	0.39	0.28	0.83	0.15	0.26	1.04	28.9	0.04	4.85	4.69	6.33
K_2O	5.62	5.59	6.1	7.96	7.53	0.05	0.04	6.3	5.4	4.38	2.88
SO_3	0.25	0.17	0.57	0.68	0.6	0.41	0.67	0.44	0.27	0.36	0.42
LOI	0.41	0.38	1.3	0.98	1.44	0.88	13.13	0.41	0.97	6.07	5.36
Total	**97.41**	**96.74**	**97.81**	**100.34**	**99.65**	**99.53**	**99.93**	**99.86**	**97.88**	**96.9**	**96.64**
Trace elements (ppm)											
Li	1.8	1.3	5.7	2.3	10.7	17.5	2.7	11	42.2	80.3	56.7
Be	4.85	4.5	3.61	1.02	2.27	0.22	0.46	1.59	2.89	1.34	1.34
P	50	50	50	40	50	20	750	20	3010	3220	2970
Sc	4	4.9	4.8	2.3	4.6	0.3	0.3	2	12.9	17.7	17.1
V	2	2	2	4	3	4	3	3	33	170	159
Cr	1	1	1	156	81	114	19	115	85	223	228
Mn	58	69	99	26	52	202	1570	15	2250	852	925
Co	0.2	0.2	0.5	1.2	1.7	1.1	6.5	1.6	8.9	29.4	28.2
Ni	0.2	0.3	0.3	4.8	3.9	4.3	2.8	3.8	39.9	119.5	118.5
Cu	10.3	14.3	19	15.5	5.3	1.5	472	24.9	76.6	33.2	30.3
Zn	110	59	22	50	106	10	128	49	117	100	114
Ga	18.35	21.2	22.2	18.45	21	0.76	0.96	15	17.4	19.75	17.75
Ge	0.18	0.21	0.22	0.13	0.18	0.13	0.15	0.21	0.29	0.27	0.26
As	0.9	0.3	7.3	7.6	6.2	0.8	14.1	772	3.2	1.6	1
Se	1	1	1	1	1	1	1	1	2	1	1
Rb	290	297	333	240	395	6.6	9	340	365	255	121.5
Sr	39.5	39.7	74.5	44.4	45.2	5.7	94.5	46.3	153.5	438	944
Y	18.2	22.8	27.2	11.4	16.1	0.2	0.7	9.3	67.4	17.8	17.5
Zr	40.7	49.3	51.1	31.6	44.2	3.3	2.1	28.1	29.2	165	153.5
Nb	79.1	96.6	97.1	66.3	92.3	4.8	0.6	57.8	17.5	17.3	15.7

Nantai Mo-(Cu) deposit											
Affinity	Aplite	Aplite	Aplite	Aplite	Aplite	Q.V	D.M	Q.V	Lamp	Lamp	Lamp
Sample	15NT_01	15NT_02	15NT_03	15NT_A	15NT_B	15NT_C	15NT_D	15NT_E	15NT_J	15NT_K	15NT_L
Age (Ma)	150	150	150	150	150	?	?	?	?	?	?
Lat. (N)	33°27'42"	33°27'42"	33°27'42"	33°27'42"	33°27'42"	33°27'42"	33°27'42"	33°27'42"	33°27'42"	33°27'42"	33°27'42"
Long. (E)	109°58'54"	109°58'54"	109°58'54"	109°58'54"	109°58'54"	109°58'54"	109°58'54"	109°58'54"	109°58'54"	109°58'54"	109°58'54"
Trace elements (ppm) contin.											
Mo	3.35	1.02	10.45	3660	2040	2520	83	973	30.3	2.27	1.26
Ag	0.15	0.1	0.01	0.33	0.06	0.14	0.77	2.53	0.59	0.14	0.1
Cd	0.18	0.16	0.18	0.34	0.23	0.02	0.46	0.11	0.37	0.09	0.13
Sn	2.5	3.4	4.5	3.2	3.6	0.5	6.4	2.9	9.7	1.3	1.1
Sb	0.3	0.38	1.33	1.75	3.43	0.44	0.82	3.73	0.74	0.55	0.63
Ba	350	320	370	410	430	10	10	710	3150	1930	3570
La	7.8	9	9.5	4.4	8.3	<0.5	0.8	3.6	52.6	45.6	45.3
Ce	16.9	19.85	20.9	10.2	17.65	0.59	2.17	8.21	106	90.3	88.5
Pr	2.14	2.52	2.56	1.27	2.11	0.05	0.18	0.99	13.2	10	10.05
Nd	8.6	10	10.3	5.1	8.1	0.2	0.7	3.9	52.8	38.4	38
Sm	2.33	2.76	3.04	1.56	2.17	0.06	0.11	1.03	9.51	5.61	5.58
Gd	2.51	3.03	3.4	1.48	2.15	<0.05	0.11	1.12	9.97	4.46	4.5
Tb	0.44	0.54	0.63	0.28	0.39	<0.01	0.01	0.21	1.5	0.59	0.59
Dy	2.82	3.41	4.03	1.79	2.54	<0.05	0.1	1.36	9.45	3.21	3.21
Ho	0.54	0.65	0.75	0.35	0.48	0.01	0.02	0.27	1.96	0.6	0.6
Er	1.51	1.86	2.23	1.03	1.42	<0.03	0.05	0.81	5.61	1.6	1.63
Yb	1.54	1.84	2.25	1.1	1.4	<0.03	0.04	0.87	4.35	1.37	1.44
Hf	2.3	2.7	2.9	1.9	2.5	<0.1	<0.1	1.6	0.9	4	3.9
W	11.3	6	9.2	10.4	9.6	18	103	20.3	79.7	2.5	0.9
Pb	14.6	13	23.1	22.8	26.6	2.6	25.5	188	27.2	14.2	20.3
Bi	0.32	0.1	0.12	2.24	0.36	1.79	29.1	8.33	0.78	0.11	0.07
Th	18.4	21.8	21.3	14.3	19	<0.2	<0.2	12.5	11.3	7.8	8.1
U	7.4	9.1	13.8	14.8	15.8	1.1	0.3	3.1	0.7	1.3	1.4

Table 5.2 - Whole-rock geochemical data for the Nantai Mo-(Cu) deposit. Oxides (<0.01) and elements (<0.05) below detection limits were omitted (P_2O_5, SrO, BaO and Te). $^{*}FeO_{total}$ expressed as Fe_2O_3. Q.V = quartz vein, D.M = dolomitic marble, Lamp = lamprophyre

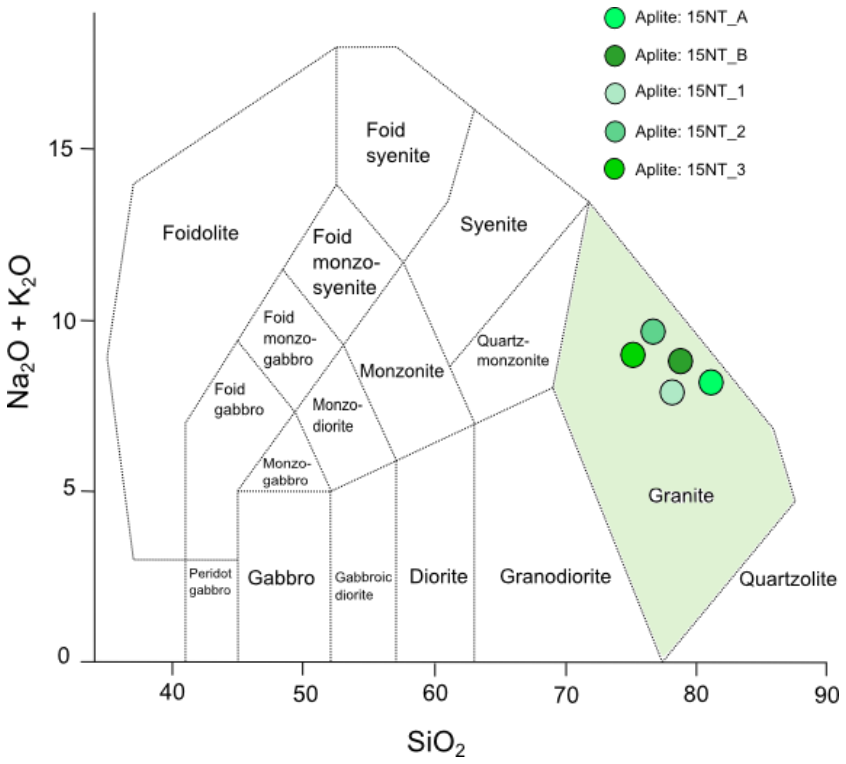

Figure 5.2 - TAS diagram for the classification of plutonic rocks (Middlemost 1985); aplite samples of the Nanatai Mo-(Cu) deposit are plotted

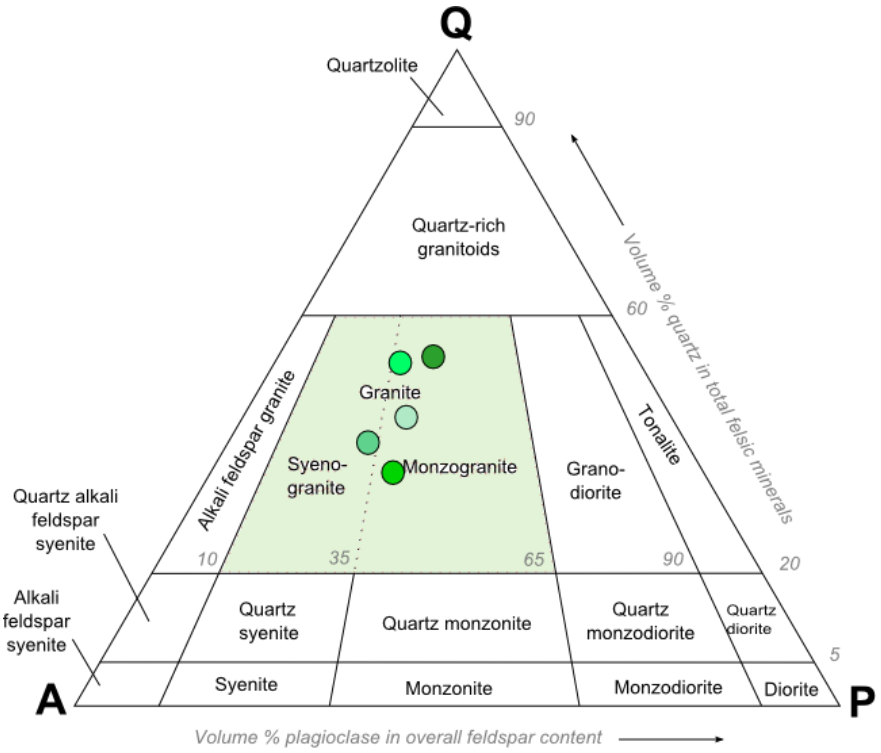

Figure 5.3 - Ternary QAF diagram for the classification of plutonic rocks defined by the IUGS showing the relative proportions of quartz (Q), alkali feldspar (A) and plagioclase (P) of the aplite samples of the Nanatai porphyry-skarn Mo-(Cu) deposit (Le Maitre 2002)

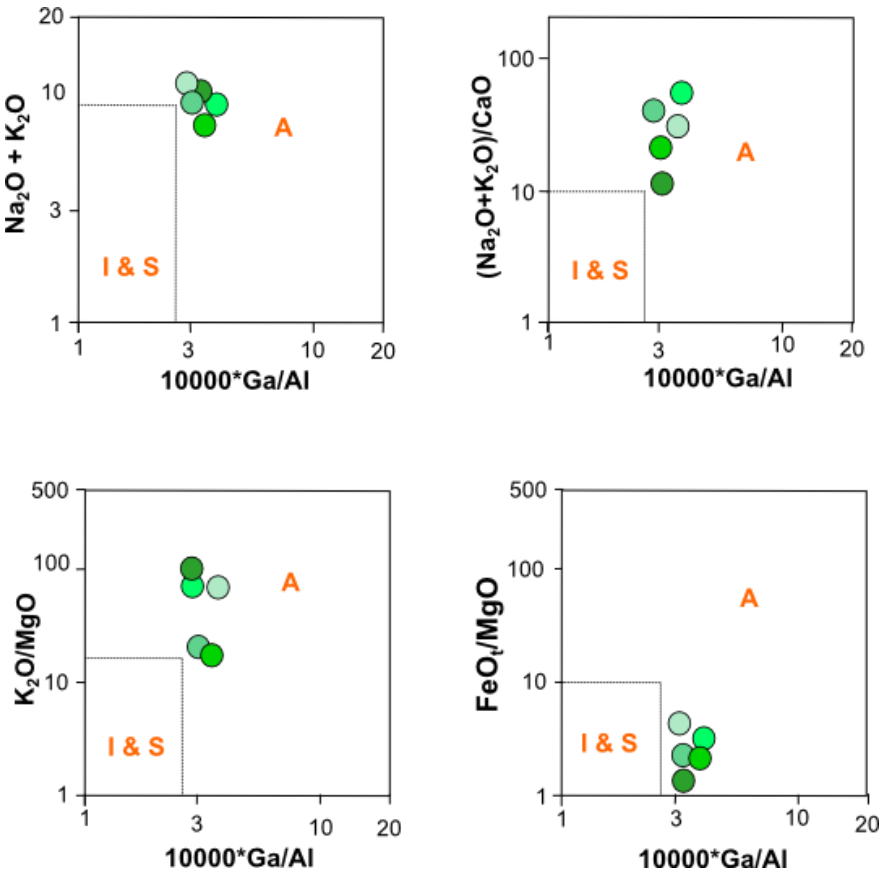

Figure 5.4 - Discrimination diagrams (Whalen *et al.* 1987) to determine I- & S- or A-type granites based on the following plots:

$Na_2O + K_2O$ vs. 10000*Ga/Al
$(Na_2O + K_2O)/CaO$ vs. 10000*Ga/Al
K_2O/MgO vs. 10000*Ga/Al
$^{*}FeO_t/MgO$ vs. 10000*Ga/Al

These diagrams are utilised to assist in further classifying the aplite samples of the Nanatai porphyry-skarn Mo-(Cu) deposit (Whalen *et al.* 1987). $^{*}FeO_t$ is representative of the total amount of Fe_2O_3 and FeO

With regards to Figure 5.4 for this investigation major element oxides, rather than trace elements were chosen to demonstrate whether the aplite samples of the Nanatai Mo-(Cu) deposit were I- & S- or A-type. Whalen *et al.* (1987) produced other plots (e.g. Zr vs. 10000*Ga/Al; Nb vs. 10000*Ga/Al; Ce vs. 10000*Ga/Al; Y vs. 10000*Ga/Al; Zn vs. 10000*Ga/Al), which may be used in conjunction with the major oxide plots if the results are not definitive. This was not required in this investigation. The aplite samples plot within the A-type granite field in all four diagrams.

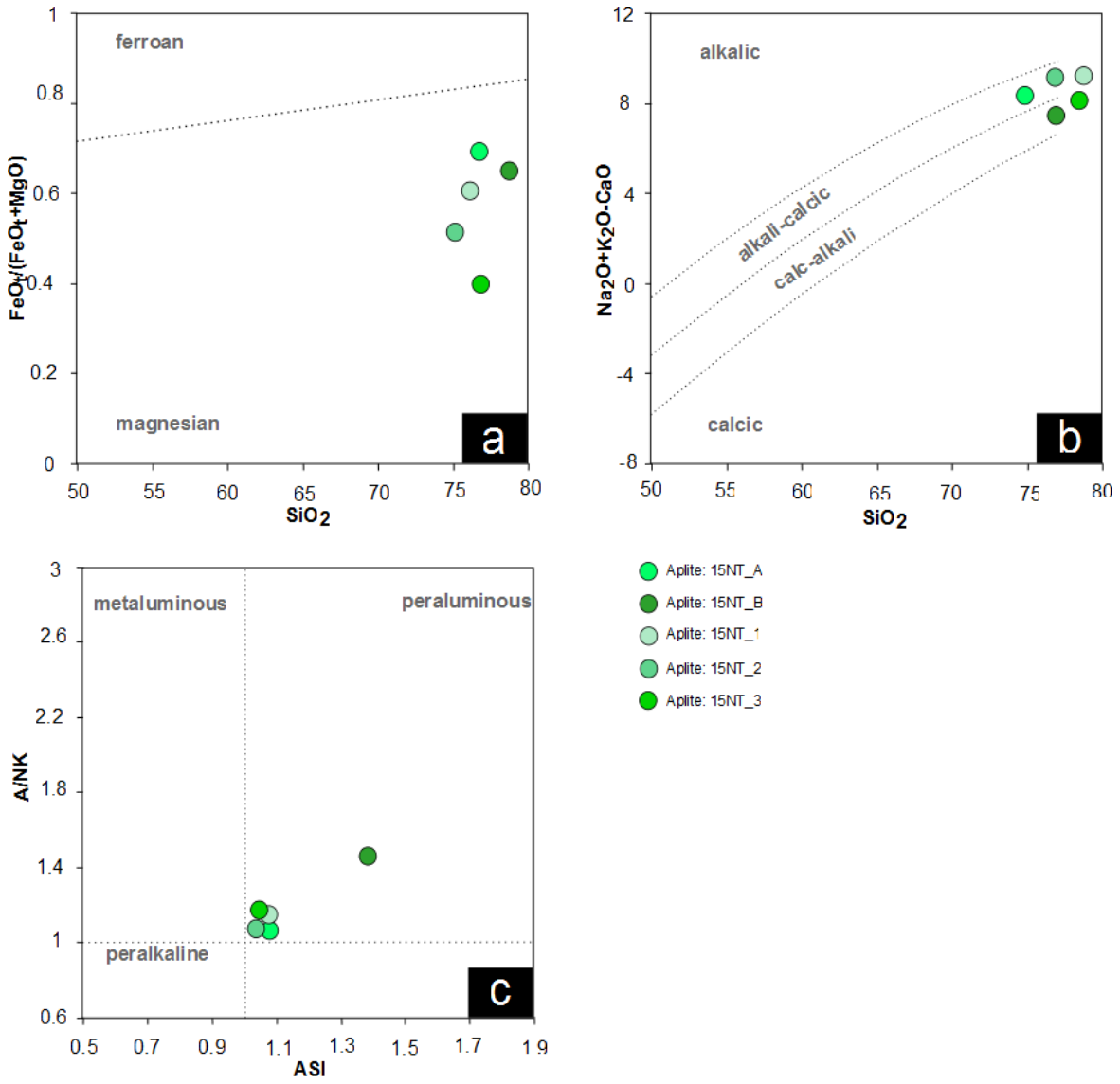

Figure 5.5 - Geochemical classification for granitic rocks (Frost *et al.* 2001) based on three variables:

a. Fe-number
b. Modified alkali-lime index or MALI
c. Aluminium saturation index or ASI

Frost *et al.* (2001) proposed a geochemical classification for granitic rocks fundamentally reliant on three variables: Fe-number (FeO_{total}/ FeO_{total} + MgO), the modified alkali-lime index or MALI ($Na_2O + K_2O – CaO$) and the aluminium saturation index or ASI [Al/(Ca - 1.67P + Na + K). With reference to Figure 5.5:

a. This diagram utilises the Fe-number to differentiate ferroan (iron enriched) and magnesian (iron depleted) granitoids. All the Nantai aplite samples plot within the magnesian field. This is consistent with the setting of the deposit which sees the larger Nantai batholith as a whole was intruded into dolomite (magnesian-rich carbonate). Fluids circulating on intrusion of the granitic material into dolomite could account for the enrichment of magnesium within the system
b. This diagram utilises the MALI variable that differentiates granitoids on the transition between alkalic and calcic end-members. The Nantai aplite samples plot in the transition zone in the fields alkali-calcic and calc-alkali
c. This diagram utilises the ASI variable which differentiates granitoids on the basis of aluminium saturation. The field definitions are as follows:

Peraluminous: $(Al_2O_3)_{mol} > (Na_2O)_{mol} + (K_2O)_{mol} + (CaO)_{mol}$
Peralkaline: $(Al_2O_3)_{mol} < (Na_2O)_{mol} + (K_2O)_{mol}$
Metaluminous: $(Al_2O_3)_{mol} > (Na_2O)_{mol} + (K_2O)_{mol}$

In accordance with Table 5.3, the aplite dykes of the Nantai deposit are magnesian, transiting from calc-alkali to alkali-calcic, with a peraluminous signature. With regard to findings made by Frost *et al.* (2001) this classifies the Nantai aplite as either granodiorite (plutons occurring in the main portion of Cordilleran batholiths) or high-K granite (plutons associated with delamination of overthickened crust).

Fe-no. or Fe*:	MAGNESIAN							
MALI:	calcic		calc-alkalic		alkali–calcic		alkalic	
ASI:	metaluminous	peraluminous	metaluminous	peraluminous	metaluminous	peraluminous	metaluminous	peralkaline
Rock types	diorite, quartz diorite	tonalite	diorite, monzodiorite,	**granodiorite**	monzonite, syenite	**high K-granite**	monzonite, syenite, granite	alkali fsp. syenite, alkali fsp. granite
Occurrences	plutons on the outboard portions of Cordilleran batholiths	plutons in island arcs	plutons in the main portion of Cordilleran batholiths		plutons inboard from Cordilleran batholiths,	plutons associated with delamination of overthickened crust	plutons inboard from Cordilleran batholiths	
Examples	La Posta pluton (Walawender *et al.* 1990)	Cornucopia stock (Johnson *et al.* 1997)	Tuolumne suite (Bateman & Chappell 1979)	N. Idaho batholith (Hyndman 1984)	Ben Nevis (Haslam 1968)	portions of the Vosges granites (Altherr *et al.* 2000)	Yamato Mtns (Zhao *et al.* 1995)	Shonkin Sag (Nash & Wilkinson 1970)

Fe-no. or Fe*:	FERROAN							
MALI:	calcic		calc-alkalic		alkali–calcic		alkalic	
ASI:	metaluminous	peraluminous	metaluminous	peraluminous	metaluminous	peraluminous	metaluminous	peralkaline
Rock types	none known	none known	granite	two-mica granite	ferrodiorite, syenite, granite	two-mica granite	anorthosite, ferrodiorite, monzonite, granite	alkaji gabbro, syenite, alkali granite
Occurrences	-	-	some A-type plutons, some granophyres in mafic plutons	some A-type plutons	A-type granites, granophyres associated with mafic dikes and plutons		within-plate plutons, plutons in cores of alkalic volcanoes	
Examples	-	-	Bunger Hills (Sheraton *et al.* 1992)	some Lachlan A-type granites (King *et al.* 1997)	Sherman batholith (Frost *et al.* 1989)	St. Vrain, Silver Plume (Anderson & Thomas 1985)	Bjerkreim–Sokndal (Duchesne & Wilmart 1997)	Na series of Pikes Peak (Smith *et al.* 1999)

Table 5.3 - A geochemical classification scheme for granitoids, adapted from Frost *et al.* (2001)

5.3.2 Plutonic rock geotectonic classification

The classification scheme of Pearce *et al.* (1984) was to discriminate granites of different settings by using trace element geochemical data for Rb, Y, Yb, Nb and Ta. With the exception of post-orogenic and supra-subduction zone ocean ridge granites*, Pearce *et al.* (1984) was able to classify granites into four geotectonic settings including i) syn-collisional granites (syn-COL), ii) within-plate granites (WPG), iii) volcanic-arc granites (VAG), and iv) ocean-ridge granites (ORG). The Nantai aplite samples plot as WPG, in accordance with Figure 5.6 and Figure 5.7. *Post-orogenic granites plot in all fields aside from ORG, and supra-subduction zone granites plot in the VAG field (because they are one in the same) (Rollinson 1993).

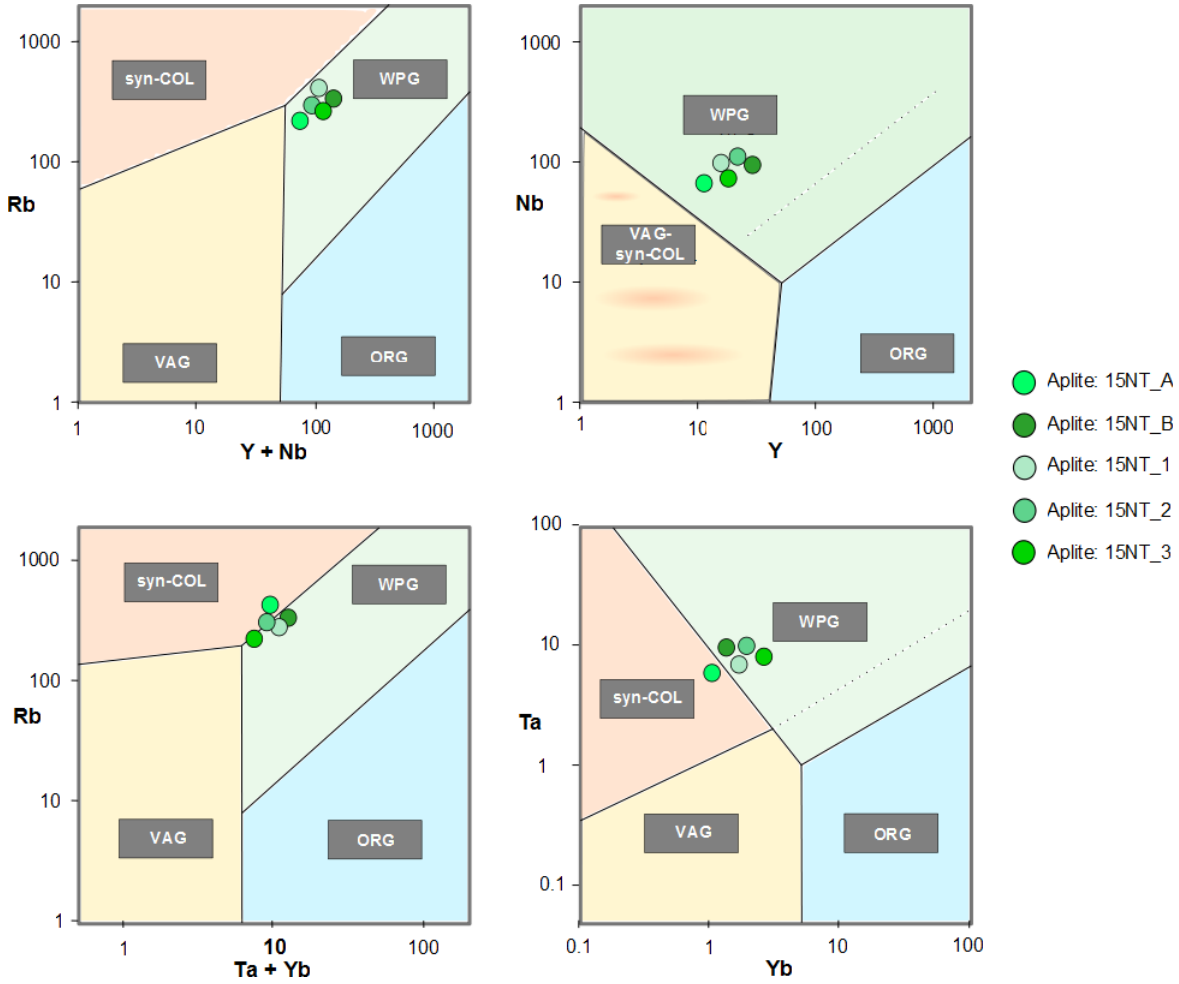

Figure 5.6 - Granite discrimination diagrams utilising Rb, Y, Yb, Nb and Ta (all measurements in ppm) to identify the geotectonic setting i.e. syn-COL, WPG, VAG or ORG (Pearce *et al.* 1984). A note about these classification diagrams; they are for liquid (melt compositions). Samples with 'accumulations' of early crystallised phases will be translated out of their correct position. For example a sample with accumulated biotite will be enriched in Rb

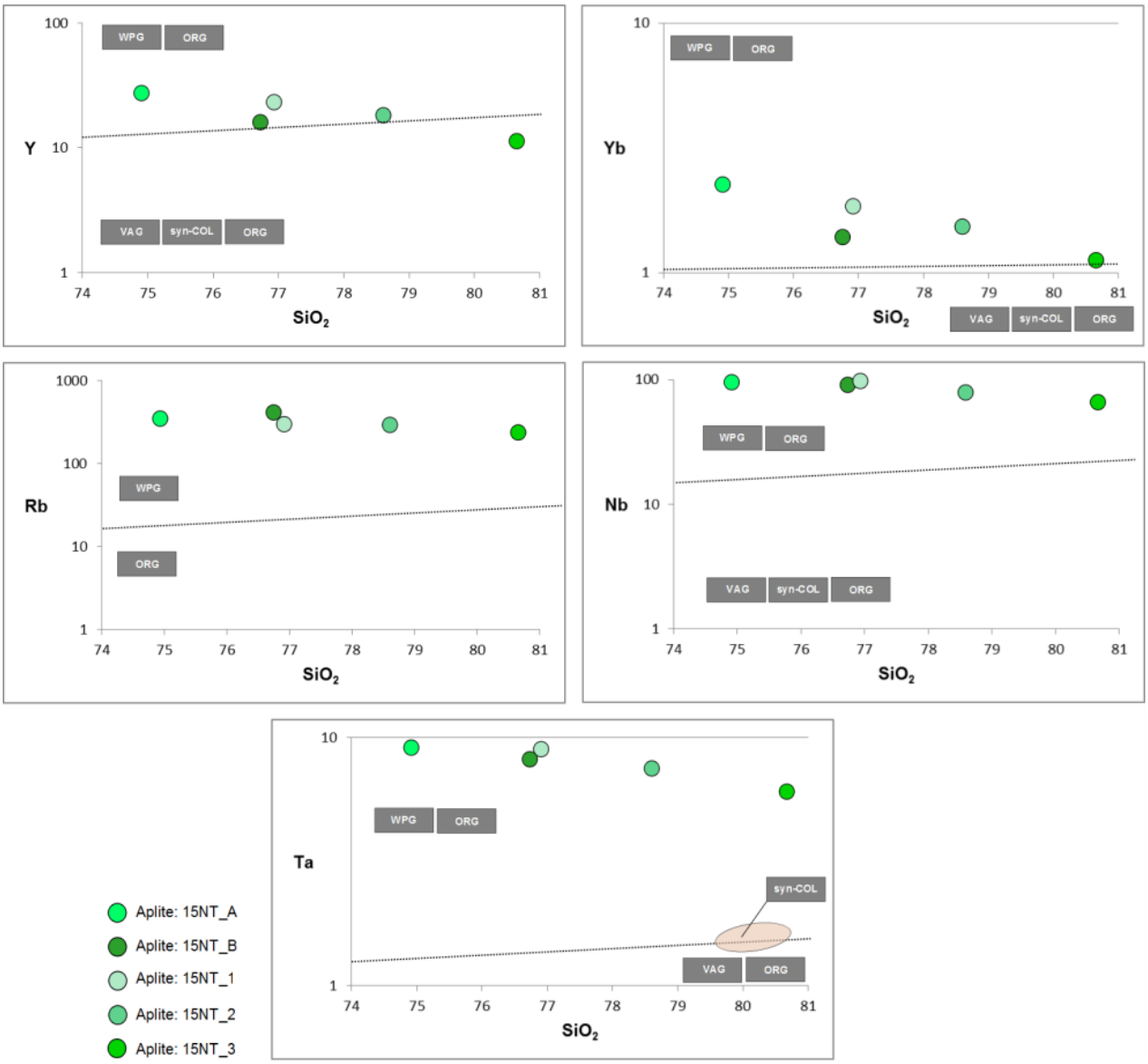

Figure 5.7 - SiO_2 (wt.%) variation diagrams ('Harker plots') for geotectonic discrimination trace elements including Y, Yb, Rb, Nb and Ta (ppm). The geotectonic boundaries in the plots, i.e. syn-collisional granites (syn-COL), within-plate granites (WPG), volcanic-arc granites (VAG) and ocean-ridge granites (ORG) are consistent with those outlined by Pearce *et al.* (1984)

5.3.3 REE Geochemistry

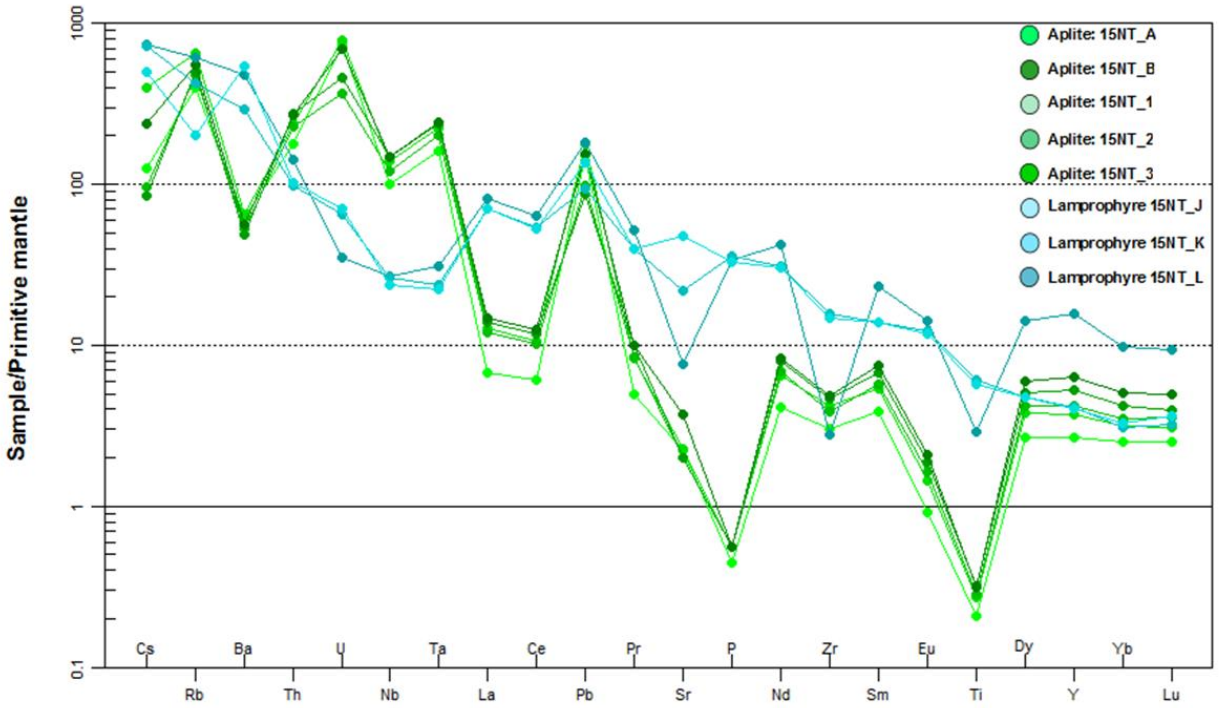

Figure 5.8 - Trace-element abundances of the Nantai aplite and lamprophyre samples normalised to the primitive mantle. Normalisation values are from McDonough and Sun (1995)

Spider diagrams are an extension of the normalised REE technique used for trace elements; normalised multi-element diagrams use a broad spectrum of elements which are grouped in accordance with incompatibility with respect to the mantle mineralogy. Spider diagrams prove to be an effective way of representing the whole composition of multiple samples on a single diagram while allowing for comparison to be made between elements of different mobility and compatibility. For the aplite (green) samples of the Nantai Mo-(Cu) deposit the multi-element diagram has been normalised for primitive mantle (McDonough and Sun 1995); the diagram also features three lamprophyre (blue) samples taken from the Nantai Mo-(Cu) deposit (Figure 5.8).

With regard to the aplite samples there is a big negative Ti anomaly, and a positive Nb anomaly. These results are inconsistent with a geotectonic setting typified by arc/suprasubduction where the diagnostic geochemical signature is a negative anomaly in both Ti and Nb. Furthermore, the big negative Ti anomaly and overall low Fe suggest the fractionation of phases such as titanomagnetite and ilmenite. Definite negative Eu and Sr anomalies indicate plagioclase fractionation and/or plagioclase being left as a residual phase. A negative P anomaly (or low P abundance) is indicative of apatite existing as a fractionated phase. High Nb (and Ta) anomalies are normally due to high rutile (TiO_2) content; however the trace element diagram indicates that Ti is depleted. There are also high concentrations of Th and U; however there is a slight negative Zr anomaly. The Nb, Th and U have been incorporated into an unidentified mineral phase(s). Overall, within the Nantai aplite samples, there is enrichment of light REE (e.g. La, Ce) versus heavy REE (e.g. Yb, Lu). This indicates overall melting of fractionated enriched materials (e.g. MORB is more or less flat).

With regard to the lamprophyre samples, there are high abundances of enriched LREE; this indicates smaller degrees of partial melting from an enriched mantle source. Scatter for some of the other elements may be due to sample heterogeneity in terms of phenocryst/xenocryst abundance, between lamprophyre (1) – unfoliated, fine- to medium-grained, and lamprophyre (2) – foliated, fine-grained (Chapter 4: Petrography).

5.3.4 Comments

There are particularly high levels of U and Th in the Nantai aplite samples (Figure 5.9). Enriched levels of these trace elements indicate 'hot' granites relative to upper continental crust. This further supplements the findings in the trace element geotectonic discrimination diagrams (Figure 5.6.and Figure 5.7), as hot granites are indicative of WPG; this can further lead to two options i.e. an extensional/rifting setting or orogenic collapse. This will be further explored in Chapter 6: Tectonometallogenic Evolution.

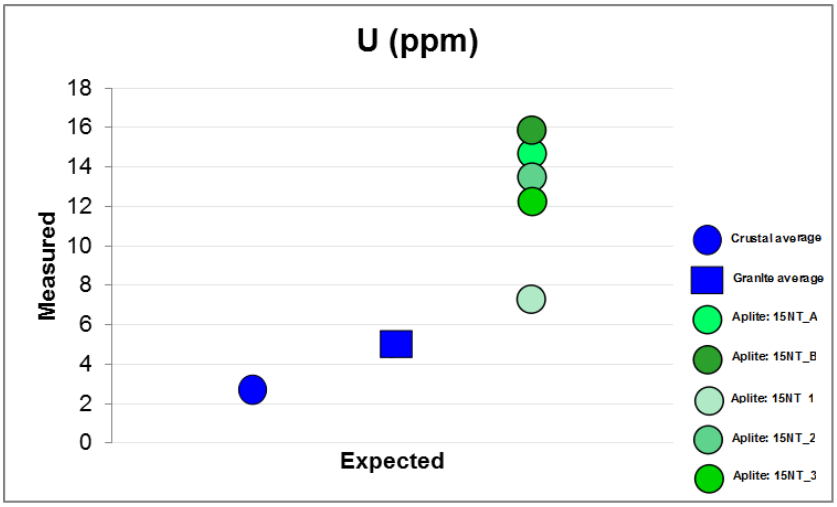

U (ppm)		
Crustal average		2.7
Granite average		4.8
Nantai abundances	*Sample*	
	15NT_A	14.8
	15NT_B	15.8
	15NT_1	7.4
	15NT_2	9.1
	15NT_3	13.8

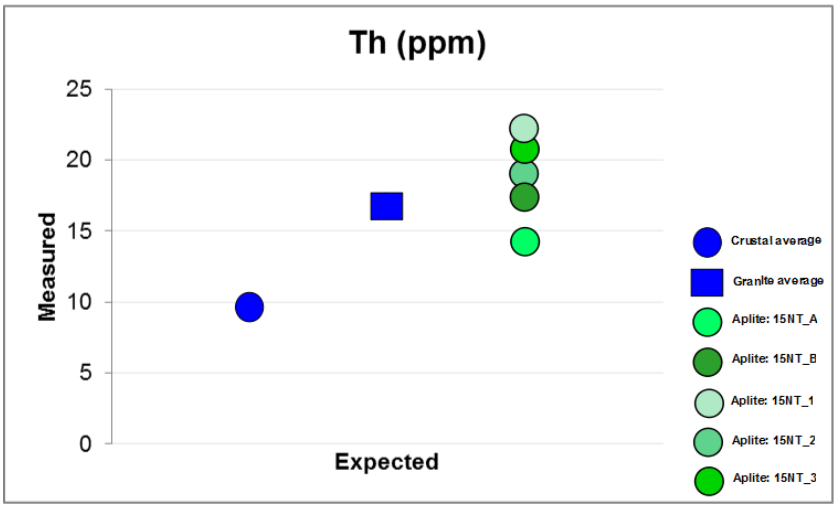

Th (ppm)		
Crustal average		9.6
Granite average		17
Nantai abundances	*Sample*	
	15NT_A	14.3
	15NT_B	19
	15NT_1	18.4
	15NT_2	21.8
	15NT_3	21.3

Figure 5.9 - Graphs of ICP-MS measurements of the Nantai Mo-(Cu) deposit aplite samples against expected crustal and granite averages, values consistent with Heier and Carter (1963) and Taylor (1964). All measurements for uranium (U) and thorium (Th) are taken in ppm. The levels of both U and Th are elevated, indicating that the aplite dykes of the Nantai Mo-(Cu) deposit are 'hot' granites, relative to upper continental crust

As would be assumed from a porphyry-skarn Mo-(Cu) deposit there are significant levels of both Mo and Cu (ppm). What is notable is that mineralisation occurs in all the sampled units within the deposit, rather than being restricted to only the aplite samples. This is consistent with the observations made in Chapter 4: Petrography, where mineralisation was described in thin section for not only the aplite and lamprophyre samples, but also in the marl and dolomitic marble samples.

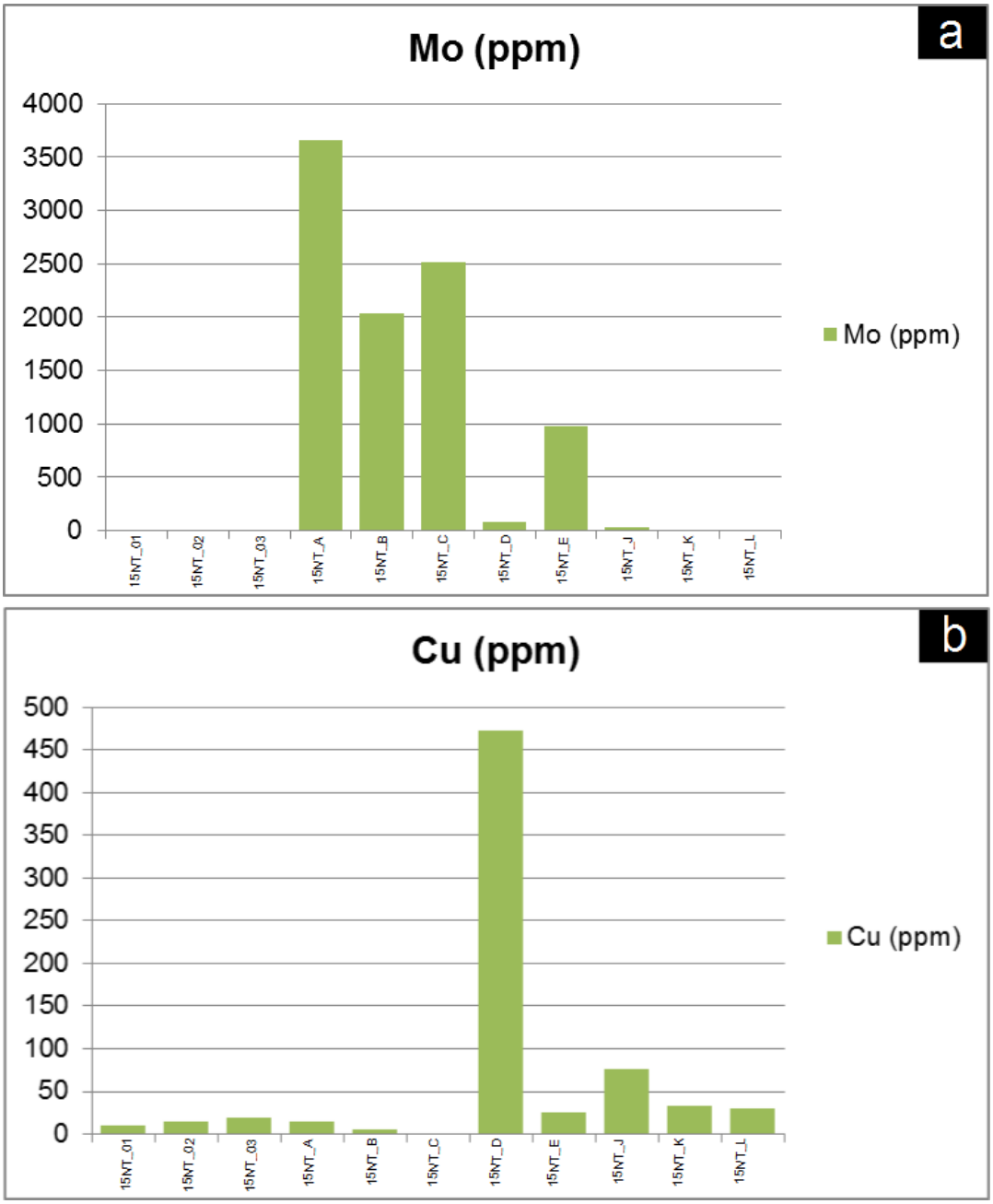

Figure 5.10 - Mo (ppm) and Cu (ppm) abundances for the samples of the Nantai Mo-(Cu) deposit

5.4 MIAOYA REE DEPOSIT

Carbonatite samples contain variable compositions of SiO_2 (<14 wt.%), FeO_{total} (<10 wt.%), MgO (<5 wt.%) and alkalis, CO_2 was not determined in analysis, but most of the loss on ignition (LOI) for these samples (Table 5.5) will be CO_2 not H_2O. They are characterised by enrichment in Sr and LREE (i.e. La, Ce, Pr, Nd, Sm, Eu). There is also significant enrichment of U in some samples (i.e. 15MY_F, 15MY_G, 15MY_H and 15MY_I). However over the entire dataset the U abundances vary significantly. There are also variable levels of Cs and Rb amongst the samples while demonstrating negative anomalies in primitive mantle normalised patterns for Ta, Pb, Pr, P, Zr and Ti (Figure 5.11). Calcite carbonatites have been studied over a variety of settings worldwide, and have typical negative signatures in Pb, Zr and Hf; the Miaoya carbonatites are consistent with these previous investigations (Nelson *et al.* 1988, Wooley and Kempe 1989). The chondrite-normalised REE patterns of the carbonatites samples from the Miaoya REE deposit display a steep negative slope (high La/Yb), and a negative Ce anomaly. The negative Ce anomaly may relate to the redox environment of the system. Previous investigations of the Miaoya carbonatites have demonstrated different chondrite-normalised REE profiles; Xu *et al.* (2010) produced findings that showed a smooth chondrite-normalisaed REE pattern of the carbonatites, with a lack of any obvious Ce or Eu anomalies, whereas Xu *et al.* (2015) produced a steep negative slope, consistent with the findings of this investigation. Carbonatites exhibit significant variations in HFSE, i.e. Ti, Nb, Ta, Zr and Hf (Chakhmouradian 2006). The Zr/Hf ratio is variable amongst the samples at Miaoya, as is the Nb/Ta ratio; differences however are not recognised in the order of magnitude, as found by Xu *et al.* (2015).

	Element ratios				*References*
	Nb/Ta	Zr/Hf	Zr/Nb	Zr/Ta	
Primitive mantle	18	37	16	284	McDonough and Sun (1995)
Carbonatites*	35	60	0.8	29	Chakhmouradian (2006)
Miaoya carbonatites	90	50	1.4	125	This study (2015)
	231	27	0.2	48	
	117	16	0.4	52	
	12	96	0.4	5	
	476	16	0.0	6	
	20	68	1.4	27	
	39	47	0.1	4	

Table 5.4 - Element ratios comparing primitive mantle, average carbonatites and the Miaoya carbonatites. *These values are an accumulation of data for carbonatites sources from 119 locations around the world, in attempt to better define the average HFSE abundances

Miaoya REE deposit							
Affinity	Carbonatite	Carbonatite	Carbonatite	Carbonatite	Carbonatite	Carbonatite	Carbonatite
Sample	15MY_A	15MY_B	15MY_C	15MY_F	15MY_G	15MY_H	15MY_I
Age (Ma)	234	234	234	234	234	234	234
Lat. (N)	32°49'48"	32°49'48"	32°49'48"	32°49'48"	32°49'48"	32°49'48"	32°49'48"
Long. (E)	109°53'37"	109°53'37"	109°53'37"	109°53'37"	109°53'37"	109°53'37"	109°53'37"
Major elements (wt.%)							
SiO_2	2.96	2.28	2.12	13.25	2.24	9.38	8.86
TiO_2	0.02	0.04	0.01	0.13	0.1	0.52	0.84
Al_2O_3	0.43	0.07	0.01	5.13	0.55	3.03	3.59
$^{*}Fe_2O_3$	1.41	2.02	0.75	2.59	1.86	9.12	6.26
MnO	0.6	0.68	0.63	0.67	0.54	0.51	0.49
MgO	0.09	0.28	0.13	0.82	0.14	1.29	1.74
CaO	52.3	52.4	53.4	40	51.9	38.9	40.6
K_2O	0.24	0.03	0.01	3.05	0.36	1.21	1.88
SO_3	1.52	1.03	0.04	0.77	1.86	1.53	2.11
SrO	0.36	0.42	0.87	0.22	0.23	1.16	0.99
LOI	40.88	40.88	42.54	31.92	37.37	30.3	28.31
Total	**100.81**	**100.13**	**100.51**	**98.55**	**97.15**	**96.95**	**95.67**
Trace elements (ppm)							
Li	0.2	0.2	0.2	8.5	0.2	9.2	14.3
P	1550	1020	70	4520	>10000	8390	>10000
Sc	0.3	0.4	0.4	0.6	2.6	0.8	0.5
V	18	18	8	58	57	397	109
Cr	9	8	8	7	5	7	29
Mn	4310	4610	4380	4900	3630	3480	3290
Co	0.6	3.4	0.3	2.3	4.8	3.7	6.9
Ni	1.4	0.5	0.2	1.9	5.2	0.2	2.8
Cu	2.7	1.6	0.7	1.1	4.1	23.7	8.8
Zn	103	117	16	123	12	172	208
Ga	3.24	3.31	2.6	10.5	6.73	12.85	14.35
Ge	0.48	0.55	0.49	0.56	0.83	0.53	0.69
As	0.5	0.2	0.2	0.2	2.8	0.2	0.6
Se	2	3	3	3	4	2	3
Rb	2.8	0.8	0.3	56.8	5.5	30.6	47.1
Sr	3380	3740	7890	2090	2080	>10000	8800
Y	91.5	116	118	112	147.5	86	110.5
Zr	10	5.3	3.1	28.8	3.2	190	28.1
Nb	7.2	25.4	7	72.3	268	136	309

Miaoya REE deposit							
Affinity	Carbonatite	Carbonatite	Carbonatite	Carbonatite	Carbonatite	Carbonatite	Carbonatite
Sample	15MY_A	15MY_B	15MY_C	15MY_F	15MY_G	15MY_H	15MY_I
Age (Ma)	234	234	234	234	234	234	234
Lat. (N)	32°49'48"	32°49'48"	32°49'48"	32°49'48"	32°49'48"	32°49'48"	32°49'48"
Long. (E)	109°53'37"	109°53'37"	109°53'37"	109°53'37"	109°53'37"	109°53'37"	109°53'37"
Trace elements (ppm) contin.							
Mo	3.84	15	5.86	11.85	4.91	1.07	30.1
Ag	0.08	0.16	0.07	0.25	1.08	0.39	0.76
Cd	0.49	0.55	0.47	0.52	0.32	0.44	0.52
Sn	0.2	0.2	0.2	0.4	1.2	0.9	0.4
Sb	0.24	0.26	0.19	0.22	0.54	0.33	0.3
Te	0.05	0.08	0.05	0.06	0.15	0.06	0.13
Ba	170	100	210	1030	170	650	840
La	351	434	368	420	640	361	460
Ce	500	550	521	531	560	600	510
Pr	72.5	88.2	73.6	81.8	145.5	77.8	110
Nd	241	284	248	263	485	262	372
Sm	31.3	37.5	34.2	32.6	60.5	33.1	45.4
Gd	24.2	31.3	30.5	25.1	43.9	25.2	32.9
Tb	3.14	4.15	4.13	3.3	5.9	3.17	4.1
Dy	16.45	21.6	21.5	18.05	31	16.2	21
Ho	3.09	3.78	3.8	3.37	5.39	2.85	3.61
Er	8.4	9.85	9.99	9.08	13.5	7.06	8.89
Yb	7.14	8.23	8.15	7.61	9.97	4.87	5.92
Hf	0.2	0.2	0.2	0.3	0.2	2.8	0.6
W	0.5	1.2	0.4	2.8	1.1	3.1	2.5
Pb	16.3	27.1	20.5	32.3	28.2	9.4	40.5
Bi	0.03	0.13	0.02	0.04	0.06	0.01	0.08
Th	3.4	29.2	17.5	18.8	30.1	11.1	17.9
U	1.2	0.6	0.1	5.5	130	19.1	123

Table 5.5 - Whole-rock geochemical data for the Miaoya REE deposit. Oxides (<0.01) and elements (<0.05) below detection limits were omitted (P_2O_5, BaO and Be). $^{*}FeO_{total}$ expressed as Fe_2O_3. LOI will be mostly CO_2

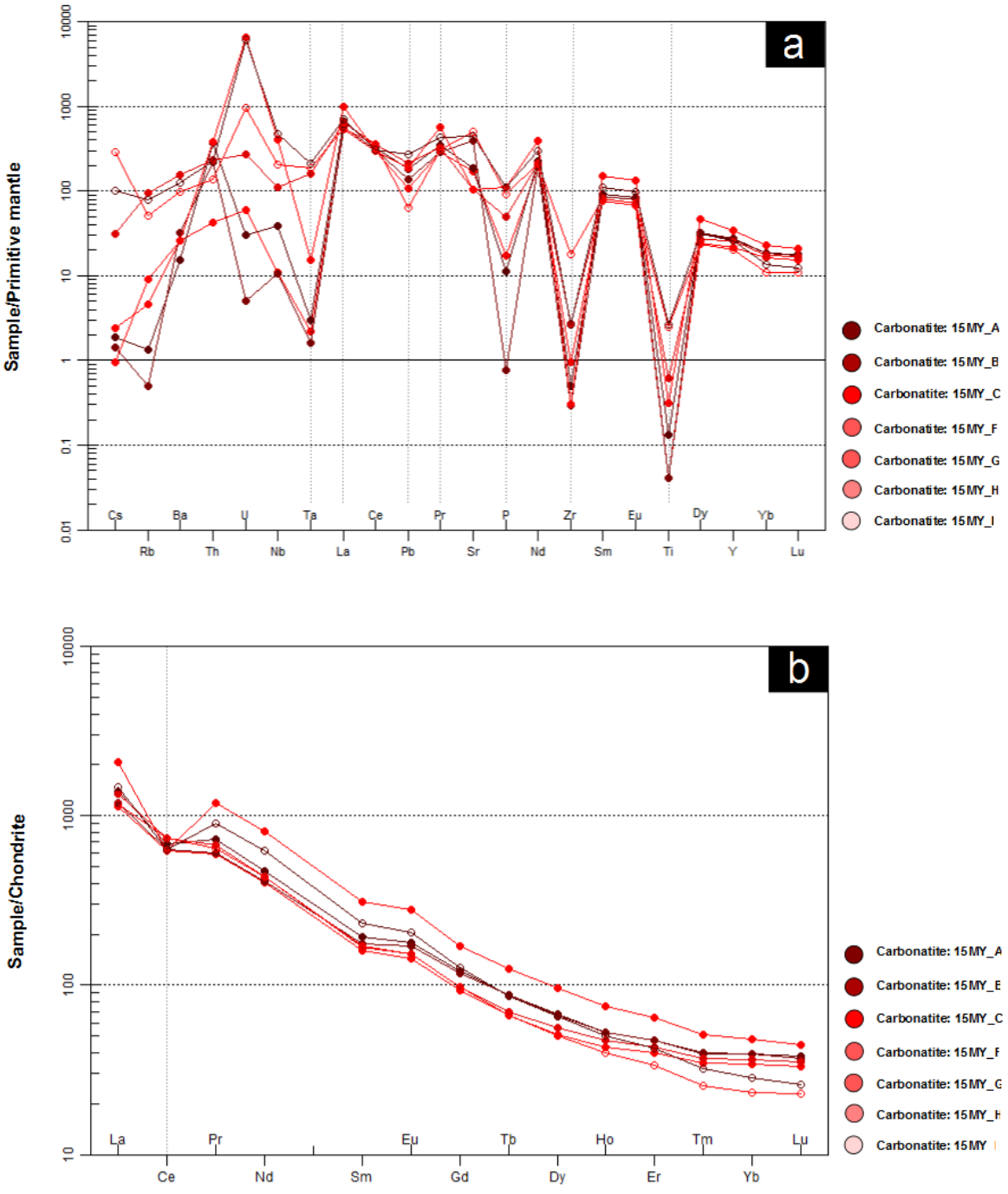

Figure 5.11 - The Miaoya REE deposit trace-element diagrams

a. Trace-element abundances of the Miaoya carbonatites normalised to the primitive mantle. Normalisation values are from McDonough and Sun (1995)
b. REE abundances normalised to chondrite for the Miaoya carbonatites. Normalisation values are from Boynton (1984)

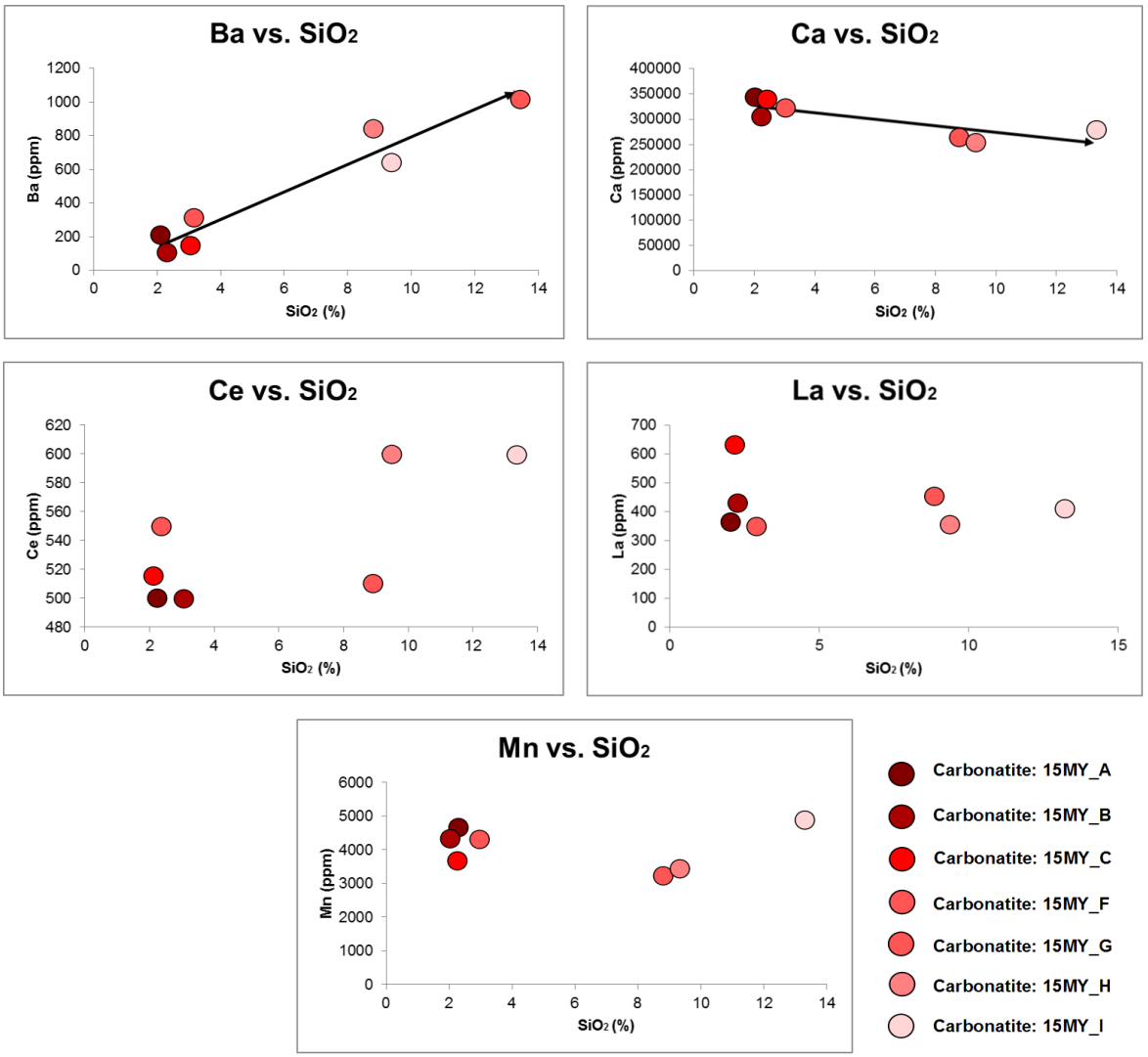

Miaoya REE Deposit (ppm)						
Sample	Rock type	Ba	Ca	Ce	La	Mn
15MY_A	Carbonatite	170	323000	500	351	4310
15MY_B	Carbonatite	100	326000	550	434	4610
15MY_C	Carbonatite	210	336000	515	368	4380
15MY_F	Carbonatite	1030	273000	600	420	4900
15MY_G	Carbonatite	170	319000	500	640	3630
15MY_H	Carbonatite	650	258000	600	361	3480
15MY_I	Carbonatite	840	269000	510	460	3290

Figure 5.12 – Harker diagrams demonstrating fractionation trends for those elements (i.e. Ba, Ca, Ce, La and Mn) demonstrating the highest abundances in the carbonatites of the Miaoya REE deposit in accordance with XRF and ICP-MS data. The attached table features the values of the elements (ppm). Increasing fractionation is inferred to relate to decreasing silica (SiO_2) rather than increasing as is the norm, seeing as the majority of the silica has been used up in the early stages of fractionation, leaving a carbonate-rich melt

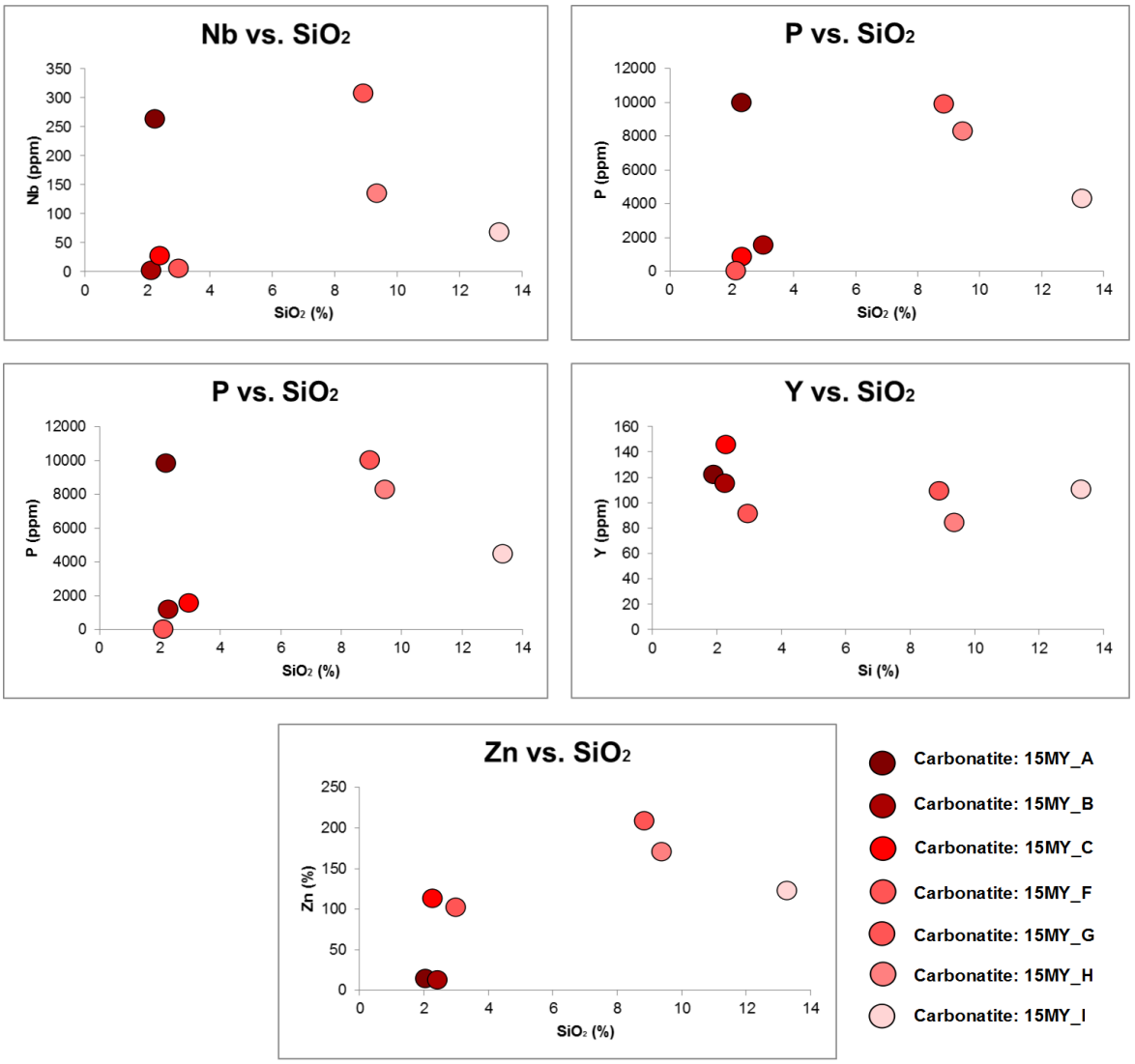

Miaoya REE Deposit (ppm)						
Sample	Rock type	Nb	P	Sr	Y	Zn
15MY_A	Carbonatite	7	1550	3380	92	103
15MY_B	Carbonatite	25	1020	3740	116	117
15MY_C	Carbonatite	7	70	7890	118	16
15MY_F	Carbonatite	72	4520	2090	112	123
15MY_G	Carbonatite	268	10000	2080	148	12
15MY_H	Carbonatite	136	8390	10000	86	172
15MY_I	Carbonatite	309	10000	8800	111	208

Figure 5.13 - Harker diagrams demonstrating fractionation trends for those elements (i.e. Ba, Ca, Ce, La and Mn) demonstrating the highest abundances in the carbonatites of the Miaoya REE deposit in accordance with XRF and ICP-MS data. The attached table features the values of the elements (ppm)

5.4.1 Comments

Carbonatites exhibit extreme variability with regards to their mineral assemblage and even vast differences in the relative abundances of elements within different mineral suites (Chakhmouradian 2006). However, what can be easily demonstrated is the abundance of CaO over MgO, indicating a calcite-rich original carbonatitic melt (Figure 5.14). For example the absolute abundances of high-field strength elements (HFSE) can vary by multiple orders of magnitude within the same carbonatitic unit (Viladkar and Wimmenauer 1986). Carbonatites were only recognised as being igneous in origin from the 1950-60s (Tuttle and Gittins 1966). Since then research into these rocks has progressed rapidly (Lee and Wyllie 1988, Bell and Tilton 2001, Grassi *et al.* 2012). Obviously melting a limestone versus a dolomite will give melts of different composition; due to the complexity and diversity of these carbonate-rich igneous rocks even at the deposit scale makes for complicated identification of the original carbonatitic magma geochemistry. The previous diagrams (Figure 5.12 and Figure 5.13) were selected to highlight those elements that have produced the highest whole-rock abundances (ppm) in the Miaoya carbonatites, i.e. Ba, Ca, Ce, La, Mn, Nb, P, Sr, Y and Zn. Calcite was chosen to illustrate the remarkably high abundances, compared to the other elements also high in abundance. In order to truly examine the evolution of REE mineralisation at Miaoya the whole-rock geochemical budget needs to be partitioned into mineral suites, rather than conducting analyses on abundances extending over entire assemblages. This investigation is limited to whole-rock geochemical analyses of the Miaoya REE-bearing carbonatites rather than an exploration into the mineralogical assembly and individual geochemical results for the different minerals within the unit (e.g. electron-microprobe and laser-ablation microprobe ICP-MS analysis). As such, the following geochemical interpretation will be supplemented by previous workings to allow for a more robust examination into the results acquired through XRF and ICP-MS methods of this investigation.

The Miaoya intrusive complex is a combination of primary syenites with associated carbonatites occurring as secondary stocks. There have been proven economic resources of both REE and Nb at the Miaoya deposit; as such, the evolution of REE mineralisation and tectonic setting are incredibly important. It could be assumed that the initial carbonatitic magma was rich in REE, best proven by the variations of REE distribution and abundances throughout the carbonatitic samples. With regard to

fractionation trends, the mineral suites within the carbonatitic melt underwent multistage fractional crystallisation, which saw precipitation of primary phosphates (i.e. fluoroapatite and monazite) followed by the REE-poor calcite, post-dated by REE-fluorocarbonates (i.e. bastnäsite, ancylite and synchysite). On crystallisation of the relatively poor REE-bearing calcite (following phosphate precipitation) it could be assumed that residual melt was enriched in REE, leading to late-stage precipitation of fluorocarbonates, which may have been able to more readily take REE's into the minerals on crystallisation. With reference to Figure 5.11 the overall carbonatites are not very REE-enriched.

With regard to tectonic evolution, predating the emplacement of the carbonatites was the closure of the Mianlue Ocean during the Early to Middle Triassic as a result of oceanic crust subduction (Dong and Santosh 2015). Preceding emplacement in the south of the Qinling Orogenic Belt (QOB), the REE-rich carbonate melt responsible for the Miaoya REE deposit may have combined with recycled previously subducted Mianlue oceanic crust material before transitioning through the crust and being emplaced in its current location followed by transition into a postorogenic regime, whereby deposit evolution is controlled by processes such as metasomatism, regional deformation, hydrothermal alteration etc. (Xu *et al.* 2015).

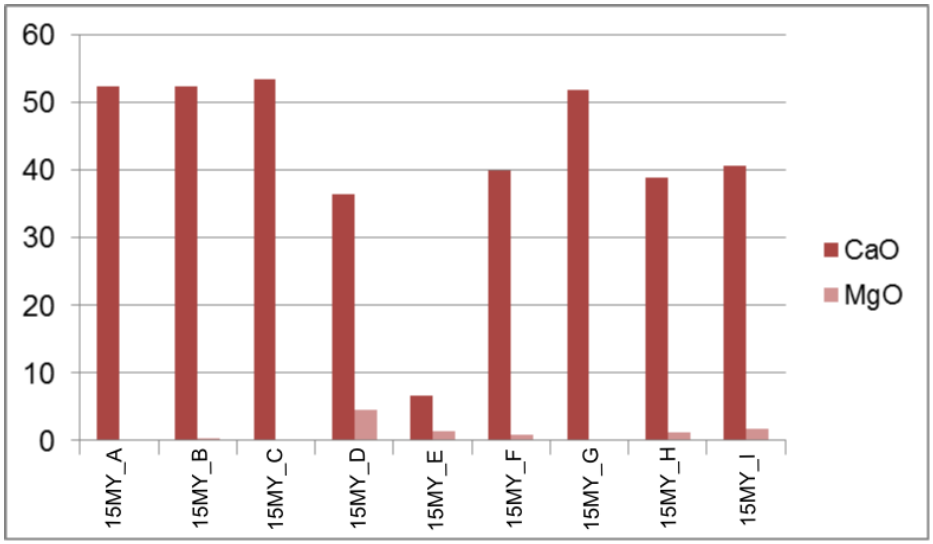

Figure 5.14 - This graph compares the difference between CaO and MgO throughout the carbonatite samples of the Miaoya REE deposit. Across all samples CaO dominates over MgO indicating a calcite-rich carbonatite as opposed to a dolomite-rich carbonatitic original melt

5.5 OROGENIC GOLD DEPOSITS

LONGTOUGOU (orogenic) Au DEPOSIT

LIUJIAXIA (orogenic) Au DEPOSIT

Five samples from the Longtongou deposit and one from the Liujiaxia deposit were analysed for whole-rock geochemistry (Table 5.6). The results of both of these orogenic gold deposits will be discussed together. With regard to major element analyses the results from the samples of the Longtougou deposit all demonstrate significant loss on ignition (LOI) values, whereby heating of the specimen has led to the release of volatiles (e.g. water, carbon dioxide), and a resultant decrease in mass. Samples 15LT_A, 15LT_B, 15LT_C and 15LT_D have all produced significant results in SiO_2 (>20 wt.%) and minor amounts of Fe_2O_3 (where $^{*}FeO_{total}$ expressed as Fe_2O_3), suggesting a silica-rich presumably quartz ore-vein. Sample 15LT_E has significant amounts of CaO (>50 wt.%) suggesting a carbonate rather than a silica-rich rock type (Figure 5.15). With regard to the major elements analysed of the Liujiaxia deposit (n = 1; 15LJ_B), the major component is SiO_2, making up for >90 wt.%) of the sample with CaO representing 3 wt.%. Loss on ignition is significantly less compared to the samples analysed from the Longtougou deposit. The large proportion of SiO_2 in sample 15LT_B of Liujiaxia is consistent with petrographic findings (Chapter 4: Petrography) that describes the unit as a siltstone with quartz-rich mature sediments.

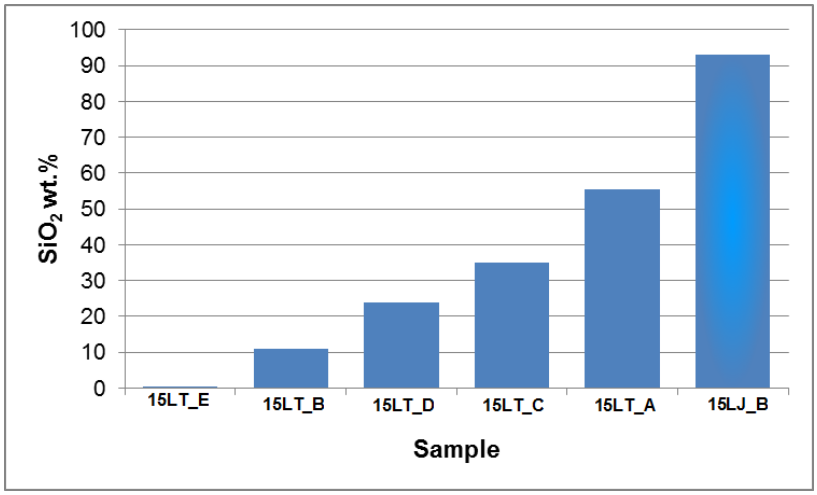

Figure 5.15 - Comparison of SiO_2 wt.% between samples of the Longtongou (15LT_A, 15LT_B, 15LT_C and 15LT_D) and Liujiaxia (15LJ_B) orogenic gold deposits

There are other elemental abundances aside from the aforementioned major element values that have produced elevated amounts; for the Longtougou deposit these include P, Cr, Mn, Zn, Cu, As and Sr. All the samples (i.e.15LT_A, 15LT_B, 15LT_C and 15LT_D) aside from sample 15LT_E have appreciable amounts in these trace elements. Sample 15LT_E has elevated amounts in Ba suggesting that the specimen may be a carbonate-rich section with considerable amounts of baryte throughout it. The sample from the Liujiaxia deposit (15LJ_B) contains appreciable amounts of Cr and Mn, however on comparison of the abundances detected from the Longtougou these amounts are much less.

Figure 5.16 demonstrates that the highest amount that gold was detected within these two deposits was in sample 15LT_C (29.3 ppm), followed by 15LT_D (19.55 ppm), 15LT_A (11.75 ppm), 15LT_B (1.77 ppm), 15LT_ E (0.03 ppm) and 15LJ_B (0.03 ppm).

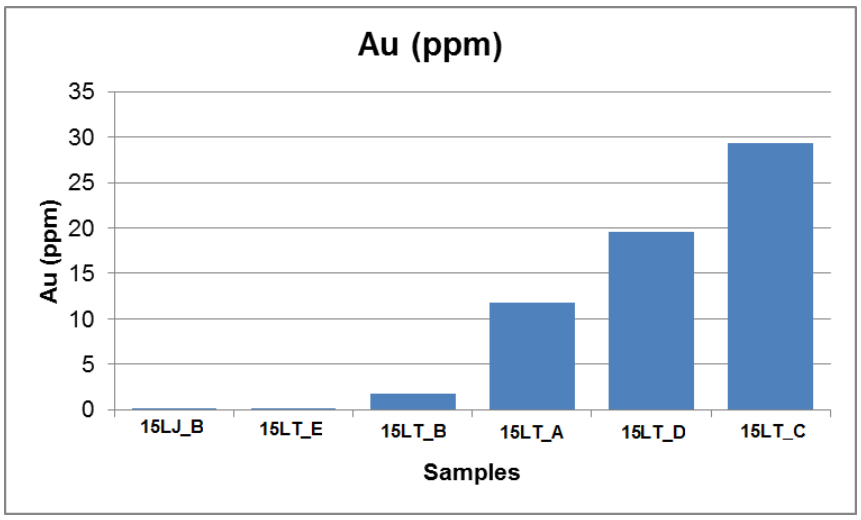

Figure 5.16 - Gold mineralisation detected in samples from the Longtongou and Liujiaxia orogenic Au deposits

Longtougou and Liujiaxia (orogenic) Au deposits						
Affinity	Ore-vein	Ore-vein	Ore-vein	Ore-vein	Ore-vein	Siltstone
Sample	15LT_A	15LT_B	15LT_C	15LT_D	15LT_E	15LJ_B
Age (Ma)	?	?	?	?	?	?
Lat. (N)	33°27’42”	33°27’42”	33°27’42”	33°27’42”	33°27’42”	33°25’39”
Long. (E)	109°58’54”	109°58’54”	109°58’54”	109°58’54”	109°58’54”	109°65’24”
Major elements (wt.%)						
SiO_2	55.45	21.1	35.08	23.96	0.01	93.03
TiO_2	0.03	0.01	0.05	0.04	0.01	0.01
Al_2O_3	0.39	0.49	0.47	0.41	0.01	0.32
$^{*}Fe_2O_3$	10.78	10.82	17.69	16.31	2.12	0.26
MnO	0.12	0.21	0.16	0.12	0.05	0.01
MgO	3.84	10	5.23	5.41	1.24	0.42
CaO	8.71	23.5	12.2	12.95	53.4	3.02
K_2O	0.06	0.07	0.06	0.08	0.01	0.05
BaO	2.69	6.43	3.51	7.9	0.28	0.01
SO_3	11.1	7.11	21.5	22.4	0.28	0.01
SrO	0.1	0.17	0.14	0.19	0.05	0.01
LOI	10.4	21.59	10.7	16.25	43.32	2.81
Total	**103.67**	**101.5**	**106.79**	**106.02**	**100.78**	**99.96**
Trace elements (ppm)						
Li	4.9	2.2	4.5	2.9	0.3	1.6
Be	0.28	0.78	0.35	0.48	0.54	0.05
P	170	190	300	200	10	20
Sc	0.9	2.1	1.4	1.5	0.2	0.3
V	11	29	14	19	6	4
Cr	111	33	58	35	9	88
Mn	848	1520	1060	968	326	55
Co	5.6	8.4	11.9	13.3	0.4	0.7
Ni	15.3	17.3	23.7	20.9	0.2	4.1
Cu	939	515	693	1750	3.6	1.7
Zn	65	189	86	154	84	26
Ga	0.51	0.65	0.55	0.55	0.11	0.7
Ge	0.15	0.14	0.18	0.18	0.07	0.13
As	107.5	67.3	131	234	0.2	25
Se	4	5	7	10	1	1
Rb	2.5	2.6	1.9	2.5	0.1	1.4
Sr	620	1155	674	528	445	13.3
Y	7.7	18.6	10	11.8	8.9	3.8
Zr	3.5	8.2	4.4	5.1	8.9	2.1
Nb	1.6	0.4	1.9	1.7	0.4	0.4

Longtougou and Liujiaxia (orogenic) Au deposits						
Affinity	Ore-vein	Ore-vein	Ore-vein	Ore-vein	Ore-vein	Siltstone
Sample	15LT_A	15LT_B	15LT_C	15LT_D	15LT_E	15LJ_B
Age (Ma)	?	?	?	?	?	?
Lat. (N)	33°27'42"	33°27'42"	33°27'42"	33°27'42"	33°27'42"	33°25'39"
Long. (E)	109°58'54"	109°58'54"	109°58'54"	109°58'54"	109°58'54"	109°65'24"
Trace elements (ppm) contin.						
Mo	1.57	0.83	1.01	0.82	0.22	1.33
Ag	0.84	0.58	1.9	4.58	0.04	0.03
Cd	0.19	0.67	0.35	0.73	0.59	0.02
Sn	0.2	<0.2	0.2	0.2	<0.2	0.2
Sb	27.2	94.1	17.9	150.5	0.41	0.96
Te	0.34	0.62	1.15	1.6	<0.05	0.39
Ba	40	100	20	20	2410	20
La	1.7	5.7	1.9	1.4	2.3	0.5
Ce	4.06	9.99	5.97	5.03	4.45	1.14
Pr	0.62	1.16	0.95	0.84	0.65	0.14
Nd	2.9	4.8	4.4	4.1	3.2	0.6
Sm	0.77	1.36	1.12	1.05	1.04	0.16
Gd	1.16	2.62	1.58	1.71	1.58	0.3
Tb	0.21	0.51	0.28	0.32	0.23	0.05
Dy	1.35	3.4	1.78	2.2	1.33	0.39
Ho	0.27	0.68	0.35	0.45	0.24	0.08
Er	0.75	1.87	0.96	1.19	0.62	0.22
Yb	0.56	1.42	0.73	0.89	0.47	0.18
Hf	0.1	0.1	0.1	0.1	0.1	0.1
W	13.8	1.6	17	13.6	1.7	0.7
Pb	18.4	408	36.8	159	47.9	0.5
Bi	0.17	0.97	0.36	1.25	<0.01	0.01
Th	0.9	2.5	1.6	1.6	0.4	0.5
U	0.3	0.7	0.3	0.4	0.5	1.6
Ore-grade elements (ppm)						
Au	11.75	1.77	29.3	19.55	0.03	0.03

Table 5.6 - Whole rock geochemical data for the Longtougou and Liujiaxia (orogenic) Au deposits. Oxides (<0.01) and elements (<0.05) below detection limits were omitted (P_2O_5 and In). *FeO_{total} expressed as Fe_2O_3. The broader literature accounts for the orogenic Au deposits within the QOB (particularly the western segment) being hosted in Devonian to Carboniferous marine derived clastic and carbonate sequences, however no ages for the subsequent mineralisation have been derived (Chen *et al*. 2015)

5.6 DAMOGOU Zn-CaF_2 DEPOSIT

One sample was analysed for whole-rock geochemistry from the Damogou Zn-CaF_2 deposit (Table 5.7). All the samples collected from this deposit (n = 3) were representative of ore body material, rather than the host rock. Ore material was targeted rather than the host rock in order to better define the primary components accounting for mineralisation to supplement the results and paragenesis discussed in Chapter 4: Petrography. There are some important geochemical results worthy of highlighting; for example with regard to the major element oxides, or major elements (wt.%) the total amount accounts for just over 46% of the entire whole-rock geochemical budget. This is largely because Zn was not analysed as a major element (i.e. ZnO). This anomaly is a result of the larger majority of the sample being mineralised (Zn 34.4%; Cu 1.5%), rather than being representative of the original host-rock. With the host-rock being originally limestones, what is present now however, is ore material; hydrothermally mineralised limestone (would expected LOI >>0.18). Other than mineralisation, another major constituent is fluorite; a limitation to whole-rock geochemistry is that abundances of F were not calculated; therefore the content can be loosely applied to the CaO amount in the sample (however this is not an adequate representation). There are other elemental abundances aside from those associated with mineralisation that demonstrate elevated amounts. For example in Figure 5.17, Cd, Pb, Mn, Sn and Sr all demonstrate appreciably amounts within the Damogou Zn-CaF_2 sample. Another notable feature is Ag which accounts for 11 ppm.

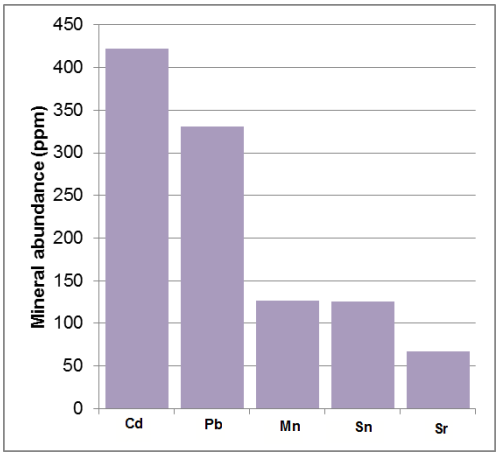

Figure 5.17 - Elevated amounts of Cd, Pb, Mn, Sn and Sr for sample 15DG_A of the Damogou Zn-CaF_2 deposit

Damogou Zn-CaF_2 Deposit			
Affinity	Ore-vein		
Sample	15DG_A		
Age (Ma)	?		
Lat. (N)	32°14’51”		
Long. (E)	109°30’17”		
Major elements (wt.%)		Trace elements (ppm) contin.	
SiO_2	21.52	**Mo**	0.96
TiO_2	0.01	**Ag**	10.65
Al_2O_3	0.01	**Cd**	422
$^{*}Fe_2O_3$	4.39	**In**	27.7
MnO	0.02	**Sn**	126
MgO	0.11	**Sb**	0.97
CaO	17.95	**Te**	0.05
K_2O	0.01	**Ba**	10
BaO	0.01	**La**	0.5
Cr_2O_3	0.02	**Ce**	0.8
SO_3	2.02	**Pr**	0.12
SrO	0.08	**Nd**	0.6
LOI	0.18	**Sm**	0.12
Total	**46.33**	**Gd**	0.3
		Tb	0.08
Trace elements (ppm)		**Dy**	0.7
Li	0.4	**Ho**	0.15
Be	0.06	**Er**	0.35
P	10	**Yb**	0.13
Sc	0.1	**Hf**	0.1
V	1	**W**	0.3
Cr	39	**Pb**	331
Mn	127	**Bi**	0.24
Co	24.6	**Th**	0.2
Ni	1.5	**U**	0.1
Cu	>10000		
Zn	>10000	Ore-grade elements (%)	
Ga	6.9	**Cu**	1.455
Ge	0.26	**Zn**	34.4
As	2.4		
Se	25		
Rb	0.4		
Sr	67		
Y	23		
Zr	0.5		
Nb	0.5		

Oxides (<0.01) and elements (<0.05) below detection limits were omitted (Na_2O, P_2O_5, Cs, Eu, Tm, Lu, Ta, Re and Tl). $^{*}FeO_{total}$ expressed as Fe_2O_3

Table 5.7 - Whole rock geochemical data for the Damogou Zn-CaF_2 Deposit

CHAPTER SIX – TECTONOMETALLOGENIC EVOLUTION

6.1 DISCUSSION

Overall, central China has undergone an extremely mobile tectonic history, with multiple stages of mantle-crustal metasomatism and enrichment (Kynicky *et al.*2012). The Qinling Orogenic Belt (QOB) represents a composite orogen that has witnessed multiple episodes of accretion and collision between discrete continental blocks, namely the North China Block and South China Block (NCB and SCB). These multiple orogenic events have resulted in abundant mineralisation (Dong and Santosh 2015, Dong *et al.* 2015). What follows is a tectonic reconstruction of the QOB from its earliest subduction and accretion events during the Neoproterozoic, followed by continental consolidation and more recent intracontinental orogenic processes including compression, thrusting, collapse and depression. The specific deposits investigated throughout this study will be incorporated, and used to represent the different mineralisation systems/episodes within the broader Qinling Orogen. The following description of the tectonometallogenic evolution of the QOB is supplemented with i) a diagram demonstrating the distribution of different mineral deposits (Figure 6.1); ii) a time-space diagram referencing the tectonic, intrusive and metallogenic events (Figure 6.2) and; iii) a tectonic model depicting the evolution of the orogen (Figure 6.3).

The QOB is a construction attributed to the collision between the NCB and the SCB. This model of amalgamation is generally accepted by the broader literature (Bader *et al.* 2013a, Bader *et al.* 2013b, Li *et al.*2015). However, there has been contention into i) the timing of collision, and ii) the positions of sutures within this collisional belt for many decades, with no consensus yet reached. The timing of collision between the NCB and the SCB has been proposed as Early Paleozoic (Mattauer *et al.* 1985), Devonian (Zhang *et al.* 1997), and Late Triassic (Sengör *et al.*1985); whereas other authors propose multi-stage subduction and accretion between these two continental blocks, thereby contrasting single-stage amalgamation models (Wu and Zheng 2013, Dong and Santosh 2015, Dong *et al.* 2015). With regard to the position of collisional sutures there are three main schools of thought – from north to south, firstly it is believed that the main collisional zone can be represented by the Erlangping ophiolitic mélange (Ratschbacher *et al.* 2006, Wang *et al.* 2001a). Secondly, it is believed that the Shangdan Suture represents the main collisional

zone with the Erlangping ophiolitic mélange being indicative of a back-arc basin (Dong *et al.* 2011a; Dong *et al.* 2011b; Dong *et al.* 2012b). Thirdly, it is believed that the Mianlue Suture could be representative of the dominant collisional suture zone (Zhang *et al.* 2001). In accordance with recent compilations, it is inferred that the second school of thought is most likely, with the major boundary between the NCB and SCB represented by the modern Shangdan Suture with accompanying Erlangping back-arc basin. This will be elaborated on in Section 6.1.3.

6.1.1 North Qinling Microcontinent

The North Qinling Belt (NQB), or as it is commonly referred to in its earliest form the North Qinling Terrane, plays an important role in establishing the beginnings of the tectonic interaction between the NCB and the SCB. There have been three main proposals as to the tectonic affinity of the NQB; i) it was thought that it may be representative of the southern part of the NCB (S-NCB) having been split by the spreading of either the Proterozoic Kuanping back-arc basin (Dong *et al.* 2008a), or the Paleozoic Erlangping back-arc basin (Dong *et al.* 2011a; Dong *et al.* 2011b), ii) it was believed that components of the NQB were derived from the NCB and SCB, these being the upper lithostratigraphic units and crystalline basement, respectively, and iii) it has been proposed that the NQB is representative of an independent microcontinent having intervened between the NCB and the SCB. The first and second proposals for the tectonic affinity of the NQB seem unlikely seeing as the tectonic units of the QOB, i.e. S-NCB, NQB, SQB and N-SCB demonstrate differing Nd model ages and Pb isotopic compositions (Zhang *et al.* 1996a), and varied deformation and metamorphic events (e.g. the Archean-Paleoproterozoic basement complex of the NCB is characterised by resultant metamorphism during the Lüliang tectonic event 1.8 – 1.6 Ga, whereas the oldest basement rocks of the NQB underwent their first metamorphic overprint at 1.0 Ga; Dong *et al.* 2015). Furthermore, differing paleogeographic locations of the NCB and the SCB during the Precambrian suggests that the NQB is unlikely to be composed of components attributed by the aforementioned continental blocks. Taking these suggestions into considerations, it is assumed that the NQB was a distinctly independent continental terrane; with terrane being described as a fault bounded package of rocks of regional extent characterised by a geological history that differs from its neighbouring tectonic units (Howell 1995).

6.1.2 The Kuanping Ocean

The Kuanping Suture, located directly south of the S-NCB is believed to represent the remnants of a Meso-Neoproterozoic Ocean (herein, the Kuanping Ocean; Dong and Santosh 2015). The ophiolite unit (commonly referred to as an ophiolitic mélange) can be divided into two distinct types, based on their geochemical affinities; i) N-MORB (1445 ± 60 Ma; LA-ICP-MA zircon U-Pb; Dong *et al.* 2014) and, ii) E-MORB and OIB. At the time of writing there was no known age specifically for the second type (i.e. E-MORB and OIB) within the ophiolite unit, however whole-rock Sm-Nd isochronology of the ophiolite produced an age range from 1.2 – 0.94 Ga (Zhang *et al.* 1994). Inference has been made, suggesting that the Kuanping Suture (specifically the ophiolitic unit) is representative of both oceanic crust and ocean island basalt (OIB) that occurred between the NCB and the NQB (at this stage the North Qinling Terrane). Furthering on this evidence, it is suggested that the Kuanping Ocean existed during 1.45 – 0.95 Ga (Dong and Santosh 2015). Detrital zircons were extracted from the overlying metasedimentary unit, within the Kuanping Suture; detrital zircon geochronology works on the premise that the youngest grains extracted are indicative of the oldest possible depositional age, with deposition potentially being younger than this. The zircon grains produced an age range of 610 – 500 Ma, with geochemical signatures corresponding to the S-NCB and NQB, thereby assuming that these were contributing sources – potentially accretionary wedge material attributable to the closure of the Erlangping back-arc basin during the Paleozoic (Dong *et al.* 2014). The oceanic crust of the Kuanping Ocean underwent southward subduction from the NCB underneath the NQB, initiating the first of four subduction/accretionary episodes leading to the eventual consolidation of the QOB during the Early Jurassic (Dong *et al.* 2014; Dong and Santosh 2015; Dong *et al.* 2015). This subduction event is also marked by a large number of granitoid intrusives in the NQB (Wang *et al.* 2013).

6.1.3 The Shangdan Ocean

As previously mentioned, there has been contention into both the timing of collision and the positions of sutures within the QOB. Recent investigations have suggested that the main boundary between the NCB and SCB is represented by the Shangdan Suture zone with the Erlangping suture zone, specifically the ophiolitic mélange unit, representing the subduction related back-arc basin (Dong *et al.* 2011a; Dong *et al.*

2011b). The existence of the Shangdan Ocean is postulated between 600 – 420 Ma. Subduction of the oceanic crust northward under the NQB is believed to have begun during the existence of this long-lived ocean at 534 Ma, with final closure followed by accretion at 420 Ma. This subduction event is also marked by a large number of granitoid intrusives in the NQB (Wang *et al.* 2013). The Erlangping unit, located between the S-NCB and the Qinling Group (within the NQB) is inferred to have existed as a back-arc basin between 550 – 508 Ma. The closure of this basin (southward subduction) and subsequent collision of the S-NCB and the NQB has been constrained to 508 – 450 Ma, and 450 Ma, respectively (Dong and Santosh 2015). The subduction of this back-arc basin has also resulted in abundant and voluminous granitoid intrusives within the NQB (Wang *et al.* 2013).

6.1.4 The Mianlue Ocean

The Mianlue Suture located between the SQB and the N-SCB is representative of the subduction/accretion event marking the final amalgamation of all the units of the broader QOB into a final intracontinental orogenic belt. The Mianlue Suture has been largely overprinted by the late-stage Mianlue-Bashan-Xiangguang-fault (Late Jurassic to Early Cretaceous). The ophiolitic complex within the Mianlue Suture, before being superimposed has been suggested to represent remnants of oceanic crust of the Paleo-Tethyan Ocean (Lai *et al.* 2004a). The initial spreading of the Mianlue Ocean marks a rift, dividing the N-SCB and SQB believed to have started 440 Ma. Following maturity of the ocean, subduction northward underneath the SQB started in 250 Ma. Continued subduction and eventual consumption of the Mianlue Ocean led to the final stage collision between the N-SCB and SQB between 220 – 210 Ma (Dong and Santosh 2015; Dong *et al.* 2015). This subduction event is also marked by a large number of granitoid intrusives in the SQB (Wang *et al.* 2013).

6.1.5 Metallogenesis related to tectonics

The QOB represents abundant types of mineral systems over an array of different geodynamic settings. Synthesizing the tectonic evolution of collisional orogens has proven to be an important tool for the identification of architectural controls, and what these imply regarding ore genesis. As previously outlined, the QOB is an amalgamation based on multiple episodes of subduction/accretion and subsequent collision. As previously stated (Chapter 2: Mineralisation Systems), this investigation aims to illustrate the diversity of mineralisation types within this orogenic system.

Within the context of this study, the S-NCB has proven to be the most significant tectonic unit, with regard to the abundance of mineralisation and the different deposit types; this unit contains the majority of the porphyry Mo deposits of the QOB making for the largest molybdenum producer/province in the world. With regard to the Nantai porphyry-skarn Mo-(Cu) deposit, the aplite samples (151 ± 4 Ma and 148 ± 3 Ma SHRIMP zircon U-Pb; this study) demonstrated particularly high levels of U and Th. Enriched levels of these trace elements indicate 'hot' granites relative to upper continental crust. These hot granites are indicative of WPG; this can further lead to two options i.e. an extensional/rifting setting or orogenic collapse. Following the outline of the tectonic evolution of the region supplemented with a comparison to other temporally and spatially associated porphyry Mo deposits (i.e. the Nannihu, Shangfanggou and Shibaogou porphyry Mo deposits; Chapter 3: Geochronology), it can be inferred that mineralisation can be accounted for by post-collisional extension of the orogen. The formation of these porphyry Mo deposits is also coeval with the large-scale Mesozoic tectono-magmatic intrusives within the QOB (Gao *et al.* 2015). A new type of porphyry Mo deposit has been proposed for the Donggou porphyry Mo deposit of the S-NCB, one that is typified by formation in a continental collisional orogeny in response to post collisional extension. This new classification scheme could extend to encompass other porphyry Mo deposits within the QOB such as the Nantai porphyry-skarn Mo-(Cu) deposit. The multi-stage granitoid influx has been a vital component to mineralisation within the QOB; northward shallow subduction (5 - 10°) of the Mianlue Ocean underneath the SQB could produce intrusives up to 300 km away. Using this theory, the Mesozoic granites (e.g. Nantai pluton) could be accounted from oceanic slab melt, and rise of the granitic plutons through the crust, appearing majorly in the S-NCB over the NQB. The Nantai aplite demonstrated

a peraluminous geochemical signature, which may be attributed to the partial melting of sedimentary oceanic crust while also typifying as an A-type granite.

Another prominent feature within the S-NCB and extending into the SQB is the abundant amount of gold deposits, specifically Carlin-type/like and orogenic gold. The tectonic evolution of the eastern Asian continent has been dominated by the multi-stage interaction between a number of Precambrian microcontinents which along many suture zones has deformed sedimentary basins, and accreted island arcs; as such orogenic gold deposits are a common occurrence throughout the QOB manifesting in geological structures (such as anticlines) occurring as a direct result of the tectonic deformation and subsequent evolution of the region. Both the Longtougou (orogenic) Au and the Liujiaxia (orogenic) Au orebodies are representative of deposits formed due to an actively evolving orogenic belt, hosted in regionally metamorphosed Devonian strata. Although these orogenic gold deposits are hosted in Devonian sedimentary packages, broader literature places mineralisation having occurred during the Early Cretaceous (Mao *et al.* 2002). Although not hosted in, the gold deposits are spatially and temporally associated with the Mesozoic granitoids (158 – 100 Ma), which may have had some influence on the generation of fluids with dissolved gold. Some authors (e.g. Zhou *et al.* 2014) have proposed that many of the gold deposits could have been formed during the final stages of Triassic amalgamation and suturing between the NCB and SCB, however these younger deposits have been classified as generally less productive. Goldfarb and Gardoll (2011) suggested that the gold deposits of the QOB may have been part of a much larger circum-Pacific gold province; this theory is based on the Tanlu fault system located between the QOB and the adjacent Dabie orogenic belt in the east. The Tanlu fault is representative of a 500km displacement event, which saw both orogens thrust northward during the Late Jurassic to Early Cretaceous.

Some investigations (e.g. Xu et al. 2014) describe carbonatites within the QOB (particularly those with associated mineralisation) as mantle-derived. At the time of writing no known reports were made considering an alternative situation, possibly involving a skarn-type setting, which sees the partial melting of carbonate-rich rocks. This investigation, based on petrographic and geochemical analysis of the carbonatite rocks of the Miaoya REE deposit suggests they may have formed via the interaction of highly fractionated, alkalic silica-poor magmas which may have interacted with the abundant

limestone country rocks to produce the carbonatite magmas and associated REE mineralisation. With regard to the tectonic evolution of the QOB, REE-carbonatite deposits (e.g. Miaoya REE deposit) have been accounted for by the transition from a compressional tectonic regime, to one that is dominated by extension. Furthermore, REE-bearing carbonatites have been used as 'tectonic indicators' to further constrain the collision between the tectonic units of the QOB. There may be discrepancies using carbonatites and their associated mineralisation epochs as tectonic consolidators when their genesis (i.e. mantle-derived or melt produced as a product of dolostone fluxing) has not been adequately confirmed.

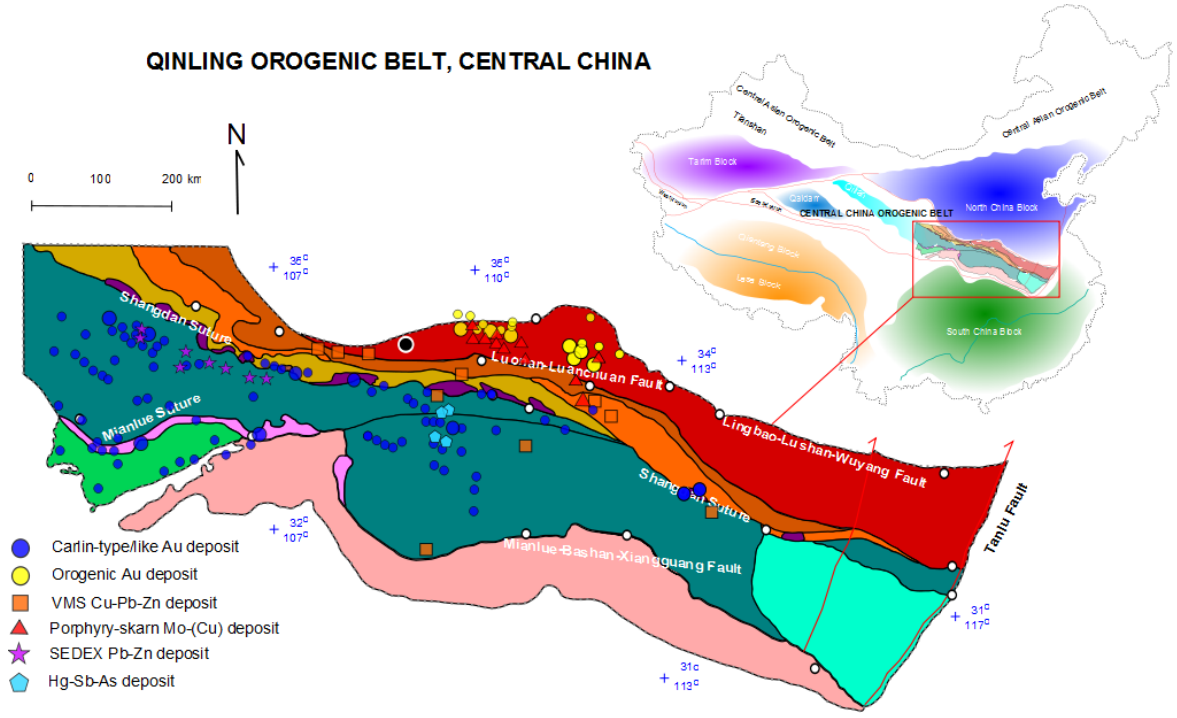

Figure 6.1 - Figure 6.1: Distribution of the mineral deposits (i.e. Carlin-type/like Au deposits, orogenic Au deposits, VMS Cu-Pb-Zn deposits, porphyry-skarn Mo-(Cu) deposits, SEDEX Pb-Zn deposit, and Hg-Sb-As deposits) within the Qinling Orogenic Belt, central China. Compiled after Yao *et al.* (2002); Zhu *et al.* (2008a); Zhu *et al.* (2008b); Wang *et al.* (2013); Chen and Santosh (2014); Li *et al.* (2014); Dong and Santosh 2015; Dong *et al.* (2015)

Figure 6.2 – (figure on following page) Time-space diagram describing the tectonic, granitoid intrusive and mineralisation evolution of the QOB from the Precambrian to the Cenozoic . Compiled after Yao *et al.* (2002); Zhu *et al.* (2008a); Zhu *et al.* (2008b); Chen and Santosh (2014); Wang *et al.* (2013); Li *et al.* (2014); Dong and Santosh 2015; Dong *et al.* (2015)

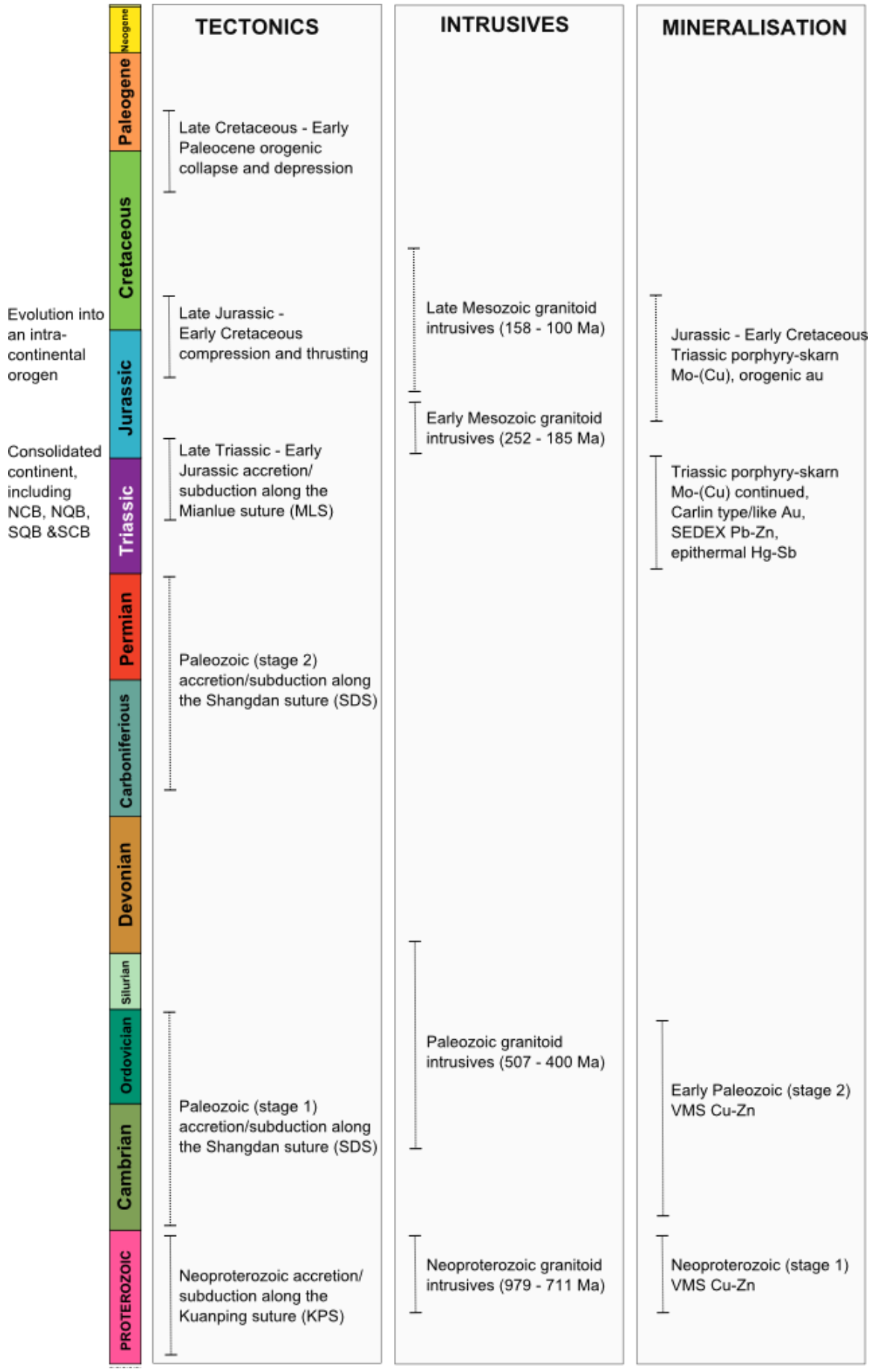
TECTONICS
INTRUSIVES
MINERALISATION
Neogene
Paleogene
Cretaceous
Jurassic
Triassic
Permian
Carboniferious
Devonian
Silurian
Ordovician
Cambrian
PROTEROZOIC
Evolution into an intra-continental orogen
Consolidated continent, including NCB, NQB, SQB &SCB
Late Cretaceous - Early Paleocene orogenic collapse and depression
Late Jurassic - Early Cretaceous compression and thrusting
Late Triassic - Early Jurassic accretion/ subduction along the Mianlue suture (MLS)
Paleozoic (stage 2) accretion/subduction along the Shangdan suture (SDS)
Paleozoic (stage 1) accretion/subduction along the Shangdan suture (SDS)
Neoproterozoic accretion/ subduction along the Kuanping suture (KPS)
Late Mesozoic granitoid intrusives (158 - 100 Ma)
Early Mesozoic granitoid intrusives (252 - 185 Ma)
Paleozoic granitoid intrusives (507 - 400 Ma)
Neoproterozoic granitoid intrusives (979 - 711 Ma)
Jurassic - Early Cretaceous Triassic porphyry-skarn Mo-(Cu), orogenic au
Triassic porphyry-skarn Mo-(Cu) continued, Carlin type/like Au, SEDEX Pb-Zn, epithermal Hg-Sb
Early Paleozoic (stage 2) VMS Cu-Zn
Neoproterozoic (stage 1) VMS Cu-Zn

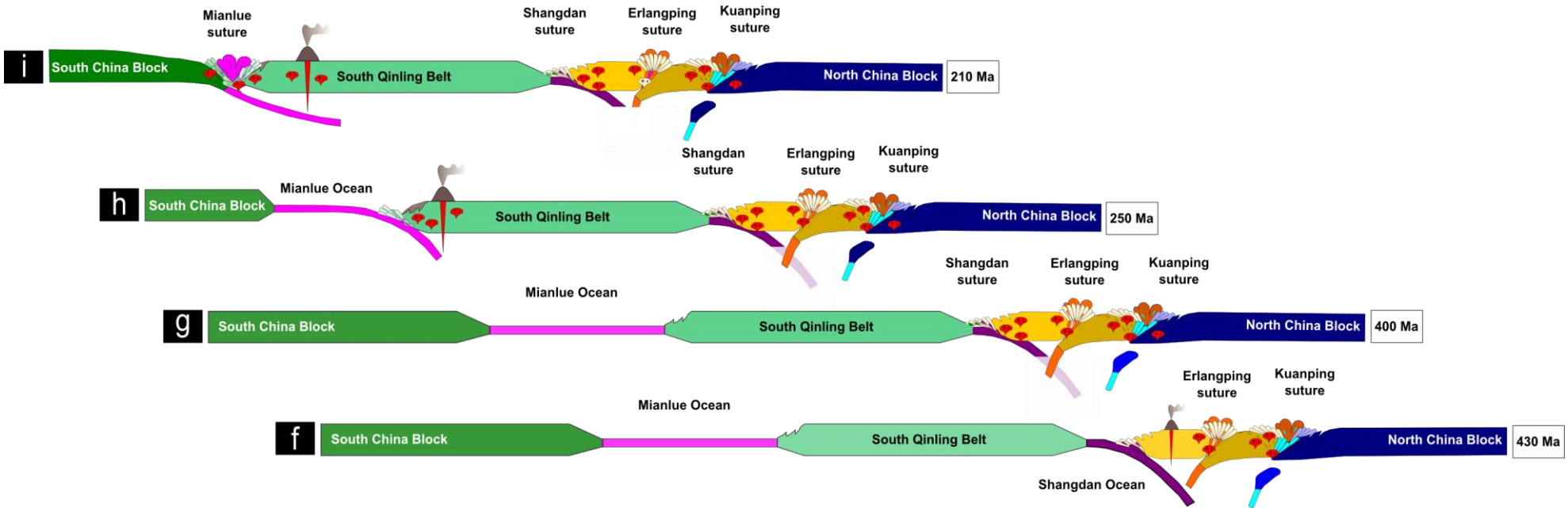
i
South China Block
Mianlue suture
South Qinling Belt
Shangdan suture
Erlangping suture
Kuanping suture
North China Block
210 Ma
h
South China Block
Mianlue Ocean
South Qinling Belt
Shangdan suture
Erlangping suture
Kuanping suture
North China Block
250 Ma
g
South China Block
Mianlue Ocean
South Qinling Belt
Shangdan suture
Erlangping suture
Kuanping suture
North China Block
400 Ma
f
South China Block
Mianlue Ocean
South Qinling Belt
Erlangping suture
Kuanping suture
Shangdan Ocean
North China Block
430 Ma

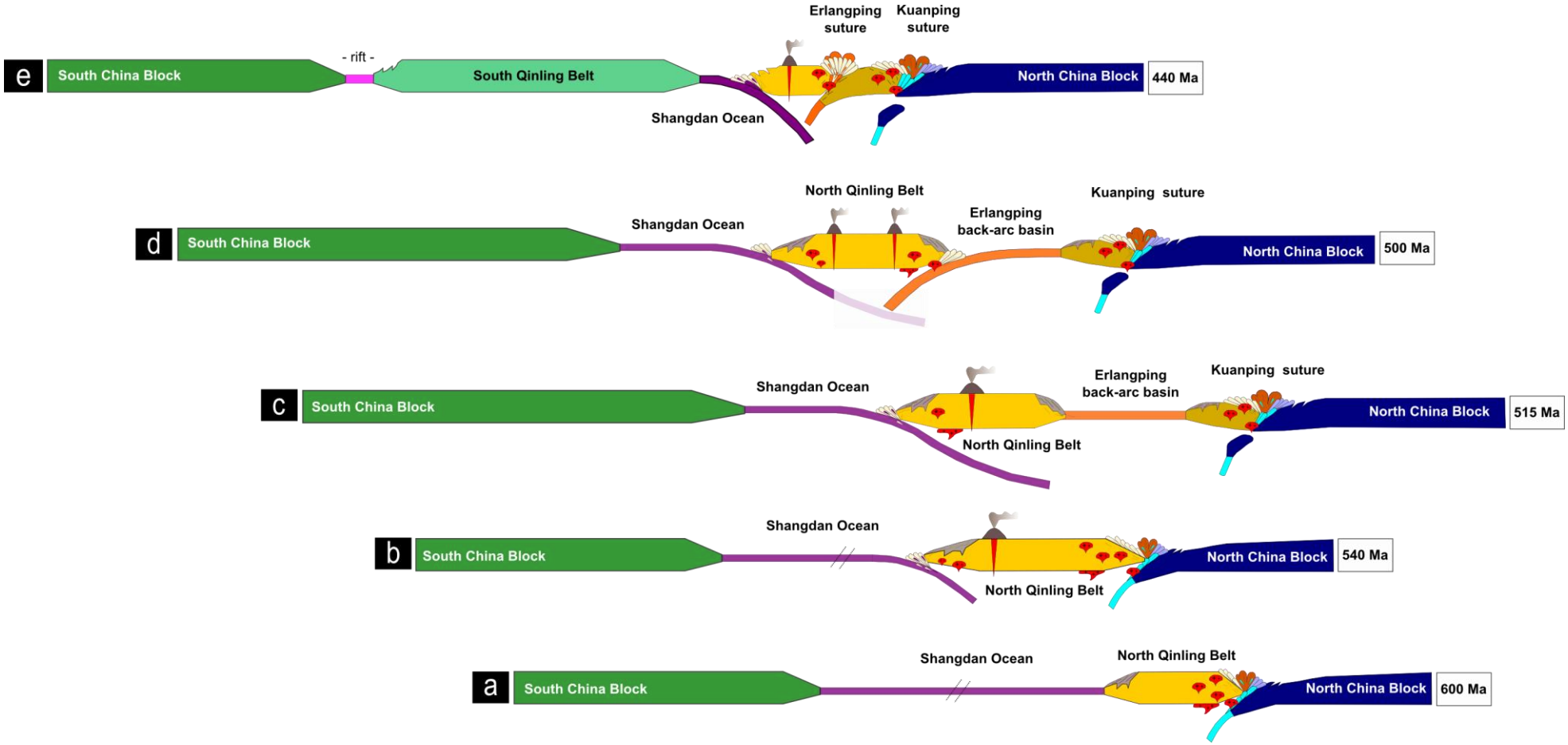

Figure 6.3 - Tectonic model (a – i) displaying the tectonic evolution of the Qinling Orogenic Belt, central China from the Neoproterozoic (600 Ma) to the Late Triassic (210 Ma). No scale, see text for explanation. Complied after Yao *et al.* (2002); Zhu *et al.* (2008a); Zhu *et al.* (2008b); Wang *et al.* (2013); Chen and Santosh (2014); Li *et al.* (2014); Dong and Santosh 2015; Dong *et al.* (2015)

CHAPTER SEVEN – CONCLUSION AND RECOMMENDATIONS

7.1 CONCLUSION

A detailed examination into the geochronological, petrographic, geochemical and tectonometallogenesis of the QOB has resulted in the following major findings:

1. The tectonic evolution of the QOB involving from north to south, the S-NCB, NQB, SQB and N-SCB is attributed to the multi-stage subduction/accretion and collision of these tectonic units
2. The Kuanping Suture is attributed to the southward subduction of the Kuanping Ocean underneath the NQB during the Neoproterozoic, the Shangdan Suture is attributed to the northward subduction of the Shangdan Ocean underneath the NQB during the early Paleozoic, the Erlangping Suture is attributed to the southward subduction of the Erlangping back-arc basin underneath the NQB during the late Paleozoic, and the Mianlue Suture is attributed to the northward subduction of the Mianlue Ocean underneath the SQB during the Triassic
3. The Nantai porphyry-skarn Mo-(Cu) deposit is representative of the vast suite of porphyry Mo deposits located in the S-NCB, which have been directly influenced by a post-collisional extension regime and subsequent influx of two-stage Mesozoic granitoid intrusive events
4. The orogenic gold deposits (e.g. Longtougou and Liujiaxia) located in the S-NCB to the SQB are spatially and temporally associated with the Mesozoic granitoids (158 – 100 Ma), which may have had some influence on the generation of fluids with dissolved gold and subsequent precipitation
5. The Miaoya REE deposit and associated carbonatites may not represent a mantle-derived magma. As such, those models constraining tectonic events based on influence from the mantle may need to incorporate a skarn-type setting
6. Multi-stage (Neoproterozoic, Paleozoic, early Mesozoic, and late Mesozoic) granitoid influx has been a vital component to mineralisation within the QOB
7. Although there are several metallogenic epochs throughout the geological evolution of the QOB and the adjacent areas including the NCB and the SCB, that have contributed significantly to the metallognesis of the composite orogen (including Archean BIF type iron ore deposits, Proterozoic SEDEX type Pb-Zn and Cu deposits), the most pervasive, voluminous and abundant is the large-scale mineralisation event (porphyry Mo deposits, orogenic gold deposits) having occurred during the Mesozoic

7.2 RECOMMENDATIONS

In addition to the preliminary investigations provided in this project, there is still further work that could be carried out to better define and describe the various mineralisation styles within the QOB. With regard to the Nantai Mo-(Cu) deposit an investigation of inclusions within the aplite igneous zircons could assist in better defining a petrogenetic model for the evolution of the melt/s and their relationship with the mineralisation. REE analysis of the zircons could provide information on oxidation of the melt and if they show evidence of magma first boiling as they crystallised.

Mineralisation systems and the models used to describe them are important for greenfield exploration and have been applied widely to porphyry, skarn, orogenic gold and Carlin-type/like gold deposits. Much less studies have been developed for carbonatitic complexes hosting REE, exemplified by the Miaoya REE deposit. Thus an obvious direction of research to deliver better controls on REE mineralisation and deposit forming processes. At a deposit scale, the mineral phases and distribution of REE in the Miaoya REE deposit could be better established and defined with an in-depth study using techniques such as electron-microprobe and laser-ablation microprobe ICP-MS analysis guided by petrographic studies. A key issue to resolve in these studies are i) is the carbonatite mantle-derived or is it a product of dolostone fluxing from late magmatic fluids derived out of the spatially associated syenite, and ii) were the REE always carried by the carbonatite melt or were they transferred from the syenites late in its crystallisation.

With regard to the orogenic gold deposits (Longtougou and Liujiaxia), as with any orogenic mineralisation system, whether it be gold or another precious metal, structural controls are the defining factor for the accumulation and in turn formation of a deposit (assuming that the fluid source is from metamorphic devolatilisation reactions). As such detailed structural geological mapping is a necessity for greenfield investigation of these two orogenic gold deposits.

With regard to the Damogou Zn-CaF_2 deposit, as with the orogenic gold deposits no structural mapping was available at the time of writing. This needs to be the first step to establish the relative timing of geological units, emplacement or intrusion events, and mineralisation of the system. There is no known age for the emplacement of this deposit; therefore it is recommended that there should be geochronology on the host rocks and mineralised samples. Furthermore, seeing as sphalerite is an abundant mineral at this deposit,

it would be of interest to investigate the geothermometric and geobarometic conditions under which sphalerite developed; this could provide further detail, and better constrain the subsequent mineralisation of the system.

There has been contention into the tectonic evolution of the QOB for many decades and still continues in the broader literature (Dong *et al.* 2014, Dong and Santosh 2015, Dong *et al.* 2015). An orogenic belt having formed under multiple episodes of accretion, collision and deformation since its early beginnings provides geologists with a canvas to paint, one which draws on a broad timescale of events. The only recommendation that this study can provide, out of respect for those who have dedicated their life's work to studying this complex orogenic belt, is to continue with the development of tectonic models that challenge current theories, provide reconstructions incorporating new data and observations published in international journals rather than confined to Chinese language journals that restricts access to the broader community, and continue with robust scientific methods to continue to better define and describe the tectonometallogenic evolution of the Qinling Orogenic Belt, central China.

REFERENCES

Allègre, C. J. (2008). "Isotope Geology." Cambridge: Cambridge University Press.

Aoki, H., Syono, Y., and Hemley, R. J. (2000). Physics meets mineralogy: condensed matter physics in the geosciences. London, Cambridge University Press.

Audétat, A. (2010). "Source and Evolution of Molybdenum in the Porphyry Mo(–Nb) Deposit at Cave Peak, Texas." Journal of Petrology **51**(8): 1739-1760.

Bader, T., L. Ratschbacher, L. Franz, Z. Yang, M. Hofmann, U. Linnemann and H. Yuan (2013b). "The heart of China revisited, I. Proterozoic tectonics of the Qin mountains in the core of supercontinent Rodinia." Tectonics **32**(3): 661-687.

Bader, T., L. Franz, L. Ratschbacher, C. de Capitani, A. A. G. Webb, Z. Yang, J. A. Pfänder, M. Hofmann and U. Linnemann (2013b). "The heart of China revisited: II Early Paleozoic (ultra)high-pressure and (ultra)high-temperature metamorphic Qinling orogenic collage." Tectonics **32**(4): 922-947.

Bao, Z., Wang, T. Zhao, C. Li and X. Gao (2014). "Petrogenesis of the Mesozoic granites and Mo mineralization of the Luanchuan ore field in the East Qinling Mo mineralization belt, Central China." Ore Geology Reviews **57**: 132-153.

Barton, P. B. and P. Toulmin (1966). "Phase relations involving sphalerite in the Fe-Zn-S system." Economic Geology **61**: 815 - 849.

Bea, F. (1996). "Residence of REE, Y, Th and U in granites and crustal protoliths; Implications for the chemistry of crustal melts." Journal of Petrology **37**: 521 - 552.

Bell, K. and G. R. Tilton (2001). "Nd, Pb, and Sr isotopic compositions of east African carbonatites: evidence for mantle mixing and plume inhomogeneity." Journal of Petrology **42**: 1927 - 1945.

Bierlein, F. P., D. I. Groves, R. J. Goldfarb and B. Dube (2006). "Lithospheric controls on the formation of giant orogenic gold deposits."Mineralium Deposita **40**: 874 - 886.

Black, L. P., S. L. Kamo, C. M. Allen, D. W. Davis, J. N. Aleinikoff, J. W. Valley, R. Mundil, I. H. Campbell, R. J. Korsch, I. S. Williams and C. Foudoulis (2004). "Improved $^{206}Pb/^{238}U$ microprobe geochronology by the monitoring of a trace-element-related matrix effect; SHRIMP, ID–TIMS, ELA–ICP–MS and oxygen isotope documentation for a series of zircon standards." Chemical Geology **205** (1-2): 115-140.

Blount, C. W. (1977). "Barite soluabilities and thermodynamic quantities." American Mineralologist **62**: 942 - 957.

Blundy, J. and B. Wood (2003). "Partitioning of trace elements between crystals and melts." Earth and Planetary Science Letters **210**: 383 - 397.

Boggs, S. and D. H. Krinsley (2006). "Application of cathodoluminescene imaging to the study of sedimentary rocks." Cambridge : Cambridge University Press.

Bowles, J. F. W., R. A. Howie, D. J. Vaughan and J. Zussman (2011). Rock-forming Minerals. Non-silicates: Oxides, Hydroxides and Sulphides. London, Geological Society of London.

Boynton, W. V. (1984). "Geochemistry of the rare earth elements: meterorite studies. In: Henderson, P. (eds), Rare earth element geochemistry." Elsevier: 63 - 114.

Chakhmouradian, A. R. (2006). "High-field strength elements in carbonatitic rocks: Geochemistry, crystal chemistry and significant for constraining the sources of carbonatites." Chemical Geology **235**: 138 - 160.

Chakhmouradian, A. R. and F. Wall (2012). "Rare Earth Elements: Minerals, Mines, Magnets (and More)." Elements **8**(5): 333-340.

Chakhmouradian, A. R. and A. N. Zaitsev (2012). "Rare Earth Minerlisation in Igneous Rocks: Sources and Processes." Elements **8**(5): 347 - 353.

Chen, L., X. H. Li, J. W. Li, A. H. Hofstra, Y. Liu and A. E. Koenig (2015). "Extreme variation of sulfur isotopic compositions in pyrite from the Qiuling sediment-hosted gold deposit, West Qinling orogen, central China: an in situ SIMS study with implications for the source of sulfur."Mineralium Deposita **50**(6): 643-656.

Chen, Y.-J. and M. Santosh (2014). "Triassic tectonics and mineral systems in the Qinling Orogen, central China." Geological Journal **49**(4-5): 338-358.

Claypool, G. E., W. T. Holser, I. R. Kalpan, H. Sakai and I. Zak (1980). "The age curves of sulfur and oxygen isotopes in marine sulfate and their mutual interpretation." Chemical Geology **28**: 199 - 260.

Clemens, J. D. (1995). "Phlogopite stability in the silica-staurated portion of the system: new data and a reappraisal of phase relations to 1.5GPa." American Mineralologist **80**: 982 - 997.

Cody, R. M. (2005). "Geochemical connections to primitive metabolism." Elements **1**: 135 - 137.

Compston, W., I. Williams and C. Meyer (1984). "U-Pb geochronology of zircons from lunar Breccia 73217 using a sensitive high mass-resolution ion microprobe." Journal of Geophysical Research **32**: 433 - 436.

Corfu, F., J. M. Hanchar, P. Hoskin and P. Kinny (2003). "Atlas of zircon textures. In Hanchar, J. & Hoskin, P. (eds.)." Reviews in Mineralogy and Geochemistry **53**: 469 - 500.

Cox, Bell and Pankhurst (1979). The interpretation of igneous rocks London, George, Allen and Unwin.

Davis, D., I. Williams and T. Krogh (2003). "Historical development of zircon geochronology. In Hanchar, J. & Hoskin, P. (eds.)." Reviews in Mineralogy and Geochemistry **53**: 145 - 181
.

Deer, W. A., R. A. Howie and J. Zussman (2013). An Introduction to the Rock-forming Minerals. Third Edition. London, Mineralogical Society

Diwu, C., Y. Sun, L. Liu, C. Zhang and H. Wang (2010). "The disintegration of Kuanping Group in North Qinling orogenic belts and neo-proterozoic N-MORB', Acta Petrologica Sinica." Acta Petrologica Sinica **26**: 2025 - 2038.

Dong, Y., X. Liu, F. Neubauer, G. Zhang, N. Tao, Y. Zhang, X. Zhang and W. Li (2013). "Timing of Paleozoic amalgamation between the North China and South China Blocks; evidence from detrital zircon U-Pb ages." Tectonophysics **586**: 173 - 191.

Dong, Y., X. Liu, M. Santosh, Q. Chen, X. Zhang, W. Li, D. F. He and G. Zhang (2012). "Neoproterozoic accretionary tectonics along the northwestern margin of the Yangtze Block, China: contraints from zircon U-Pb gechronology and geochemistry." Precambrian Research **196 - 197**: 247 - 274.

Dong, Y. and M. Santosh (2015). "Tectonic architecture and multiple orogeny of the Qinling Orogenic Belt, China " Gondwana Research
Article in Press http://dx.doi.org/10.1016/j.gr.2015.06.009.

Dong, Y., G. Zhang, S. Lai, D. Zhou and B. Zhu (1999a). "An ophiolitic tectonic melange first discovered in Huashan area, south margin of Qinling Orogenic Belt, and its tectonic implications." Science in China Series D: Earth Sciences **42**(3): 292-302.

Dong, Y., G. Zhang, S. Lai, D. Zhou and B. Zhu (1999b). "An ophiolitic tectonic melange first discovered in Huashan area, south margin of the Qinling Orogenic Belt, and its tectonic implications" Science China **42**: 292 - 302.

Dong, Y., G. Zhang, C. Hauzenberger, F. Neubauer, Z. Yang and X. Liu (2011a). "Palaeozoic tectonics and evolutionary history of the Qinling orogen: Evidence from geochemistry and geochronology of ophiolite and related volcanic rocks." Lithos **122**(1-2): 39-56.

Dong, Y., G. Zhang, F. Neubauer, X. Liu, J. Genser and C. Hauzenberger (2011b). "Tectonic evolution of the Qinling orogen, China: Review and synthesis." Journal of Asian Earth Sciences **41**(3): 213-237.

Dong, Y., X. Zhang, X. Liu, W. Li, Q. Chen, G. Zhang, H. Zhang, Z. Yang, S. Sun and F. Zhang (2015). "Propagation tectonics and multiple accretionary processes of the Qinling Orogen." Journal of Asian Earth Sciences **104**: 84-98.

Dong, Y. P., Z. Yang, X. M. Liu, X. N. Zhang, D. F. He, W. Li, F. F. Zhang, S. S. Sun, H. F. Zhang and G. W. Zhang (2014). "Neoproterozoic amalgamation of the Northern Qinling terrain to the North China Craton: constraints from geochemistry of the Kuanping ophiolite."Precambrian Research **255**: 77 - 95.

Dong, Y. P., X. F. Zha, M. Q. Fu and Q. Zhang (2008). "The structure of the Dabashan fold thrust belt, southern Qinling, China " Geochemical Bulletin of China **27**: 1493 - 1508.

Dong, Y. P., G. W. Zhang, X. Zhao, A. P. Yao and X. M. Liu (2004). "Geochemistry of the subduction-related magmatic rocks in the Dahong Mountains, northern Hubei Province: constraint on the existence and subduction of the eastern Mianlue oceanic basin." Science China **47**: 366 - 377.

Downes, P. M., P. Blevin, D. B. Forster, J. Whitehouse and R. Barnes (2010). "An integrated scheme for the classification of Mineral Systems" http://www.dpi.nsw.gov.au/__data/assets/pdf_file/0015/230631/Mineral_System_Poster.pdf.

Dubessy, J., M.-C. Caumon and F. Rull (2012). Raman spectroscopy applied to earth sciences and cultural heritage, The Mineralogical Society of Great Britain and Ireland.

Dunham, K. C. (1990). "Geology of the Northern Pennine orefield " Memoir of the Geological Survey of Great Britian

Einaudi, M. (1982). Description of skarns associated with porphyry copper plutons: southwestern North America. (eds), Advances in Geology of the Porphyry Copper Deposits: southwestern North America Tucson, U.S. , University of Arizona Press

Finch, R. J. and J. M. Hanchar (2003). "Structure and chemistry of zircon and zircon-group minerals. In Hanchar, J. & Hoskin, P. (eds.)."Reviews in Mineralogy and Geochemistry **53**: 1 - 27.

Fleet, M. E. (2006). "Phase equilibria at high temperatures (eds) Sulfide Mineralogy and Geochemistry." Mineralogical Society of America and Geochemical Society **61**: 365 - 419.

Frost, B. R., C. G. Barnes, G. C. Collins, W. J. Arculus, D. J. Ellis and C. D. Frost (2001). "A geochemical classification for granitic rocks " Journal of Petrology **42**: 2033 - 2048.

Gebre-Marium, M., S. G. Hagemann and D. I. Groves (1995). "A classification scheme for epigenetic Archean lode-gold deposits."Mineralium Deposita **30**: 408 - 410.

Gill, R. (2010). Igenous rocks and processes: a practical guide. London, Wiley-Blackwell.

Goldfarb, R. J. and D. I. Groves (2015). "Orogenic gold: common or evolving fluid and metal sources throughout time." Lithos **233**: 2 - 26.

Goldfarb, R. J., D. I. Groves and S. Gardoll (2001). "Orogenic gold and geological time: A global synthesis." Ore Geology Reviews **18**: 1 - 75.

Goldstein, J., D. E. Newbury, P. Echlin, D. C. Joy, A. D. Romig Jr, C. E. Lyman, C. Fiori and E. Lifshin (2012). Scanning electron microscopy and X-ray microanalysis: a text for biologists, materials scientists, and geologists, Springer Science & Business Media.

Grassi, D., M. W. Schmidt and D. Gunther (2012). "Element partitioning during the carbonated pelite melting at 8, 13 and 22 GPa and the sediment signature in the EM mantle components." Earth and Planetary Science Letters **327 - 328**: 84 - 96.

Groves, D. I. (1993). "The crustal continuum model for late-Archean lode gold deposits of the Yilgarn block, Western Australia " Mineralium Deposita **28**: 366 - 374.

Groves, D. I., M. Gebre-Marium, S. G. Hagemann and F. Robert (1998). "Orogenic gold deposits: A proposed classification in the context of their crustal distribution and relationship to other gold deposit types." Ore Geology Reviews **13**: 7 - 27.

Groves, D. I. and M. Santosh (2015). "The giant Jiaodong gold province: the key to a unified model for orogenic gold deposits?" Geoscience Frontiers **Article in Press**.

Guidotti, C. V. (1984). Micas in metamorphic rocks (eds) Micas. Washington, D.C.

Hagemann, S. G. and K. F. Cassidy (2000). "Archean orogenic gold deposits In: Hagermann, S.G. & Brown, P.E. (eds). Gold in 2000." Reviews in Economic Geology **13**: 9 - 68.

Haggerty, S. E. (1991). "Oxide mineralogy of the upper mantle. (eds) Oxide Minerals: Petrologic and Magnetic Significance." Reviews in Mineralogy, Mineralological Society of America **25**: 355 - 416.

Harrison, R. J. and A. Putnis (1996). "Magnetic properties of the magnetite-spinel solid solution: Curie temperatures, magnetic susceptibilities and cation ordering." American Mineralologist **81**: 375 - 384.

Hatch, G. P. (2012). "Dynamics in the Global Market for Rare Earths." Elements **8**(5): 341-346.

Hawkesworth, C. J. and A. I. S. Kemp (2006). "Using hafnium and oxygen isotopes in zircons to unravel the record of crustal evolution "Chemical Geology **226**: 144 - 162.

He, Y., G. Zhao, M. Sun and X. Xia (2009). "SHRIMP and LA-ICP-MS zircon geochronology of the Xiong'er volcanic rocks: implications for the Paleo-Mesoproterozoic evolution of the southern margine of the North China Craton." Precambrian Research **168**: 213 - 222.

Heier, K. S. and J. L. Carter (1963). Uranium, thorium and potassium contents in basic rocks. Processings of the International Symposium on the Natural Radiation Environment. New York, University of Chicago Press

Hoskin, P. and U. Schaltegger (2003). "The composition of zircon and igneous and metamorphic petrogenesis. In Hanchar, J. & Hoskin, P. (eds.)." Reviews in Mineralogy and Geochemistry **53**(27 - 62).

Howell, D. G. (1995). Principles of terrane analysis: new applications for global tectonics, Springer Science & Business Media.

Ireland, T. and I. Williams (2003). "Considerations into zircon geochronology by SIMS. In: Hanchar J.M and Hoskin P.W.O (eds.)." Reviews in Mineralogy and Geochemistry **53**: 215 - 241.

Janoušek, V., C. M. Farrow and V. Erban (2006). "Interpretation of whole-rock geochemical data in igneous geochemistry: introducing
Geochemical Data Toolkit (GCDkit)." Journal of Petrology **27**: 1255 - 1259.

Jenner, G. A. and D. H. Green (1983). "Equilibria in the Mg-rich part of the pyroxene quadrilateral." Mineralogical Magazine **47**: 153 - 160.

Ke, C. H., X. X. Wang, Y. Yang, Q. J. Qi, Z. P. Fa, F. Gao and X. Y. Wang (2012). "Rock-forming and ore-forming ages of the Nantai Mo polymetallic deposit in North Qinling Mountains and its zircon Hf isotope composition." Geology in China **39**(6).

Kempe, U., T. Grunder, L. Nasdala and D. Wolf (2000). "Relevance of cathodoluminescence for the interpretation of U–Pb zircon ages, with an example of an application to a study of zircons from the Saxonian Granulite Complex, Germany. In Pagel, M., Barbin, V., Blanc, P., Ohnenstetter, D. (eds)." Cathodoluminescence in Geosciences: 415 - 455.

Kynicky, J., M. P. Smith and C. Xu (2012). "Diversity of rare earth deposits: the key example of China." Elements **8**(5): 361 - 367.

Lai, S. C. (2004). "Geochemistry and regional distribution of ophiolites and associated volcanics in the Mianlue suture, Qinling-Dabie Mountains. " Science China **47**: 289 - 299.

Larkin, P. (2011). Infrared and Raman spectroscopy; principles and spectral interpretation, Elsevier.

Le Maitre, R. W. (2002). Igneous rocks - a classification and glossary of terms. Recommendations of the IUGS subcommission on the Systematics of Igenous Rocks. Cambridge, Cambridge Univeristy Press.

Lee, W. J. and P. J. Wyllie (1988). "Petrogenesis of carbonatite magmas from mantle to crust." Journal of Petrology **39**: 495 - 517.

Lentz, D. R. (1999). "Carbonatite genesis: A reexamination of the role of intrusion-related pneumatolytic skarn processes in limestone melting." Geology **27**(4): 335-338.

Li, N., Y.-J. Chen, M. Santosh and F. Pirajno (2015a). "Compositional polarity of Triassic granitoids in the Qinling Orogen, China: Implication for termination of the northernmost paleo-Tethys." Gondwana Research **27**(1): 244-257.

Li, S. (1980). "Geochemical features and petrogenesis of Miaoya carbonatites " Geochimica et Cosmochimica Acta **4**: 345 - 355.

Li, X., X. Mo, X. Huang, G. Dong, X. Yu, M. Luo and Y. Liu (2015b). "U–Pb zircon geochronology, geochemical and Sr–Nd–Hf isotopic compositions of the Early Indosinian Tongren Pluton in West Qinling: Petrogenesis and geodynamic implications." Journal of Asian Earth Sciences **97**: 38-50.

Lin, Z. W., Y. Qin, Z. J. Zhou, S. W. Yue, Q. T. Zeng and L. X. Wang (2013). "Zircon U-Pb dating and geochemistry of the volcanic rocks at Huachanggou area, Mianlue suture, South Qinling." Acta Petrologica Sinica **29**: 83 - 94.

Liu, J., C. Liu, E. J. M. Carranza, Y. Li, Z. Mao, J. Wang, Y. Wang, J. Zhang, D. Zhai, H. Zhang, L. Shan, L. Zhu and R. Lu (2015). "Geological characteristics and ore-forming process of the gold deposits in the western Qinling region, China." Journal of Asian Earth Sciences **103**: 40-69.

Liu, S., Y. Wan, H. Sun, A. P. Nutman, H. Xie, C. Dong, M. Ma, D. Liu and B. Jahn (2013). "Paleo- to Eoarchean crustal evolution in eastern Hebei, North China Craton: new evidence from SHRIMP U–Pb dating and in-situ Hf isotopic study of detrital zircons from paragneisses."Journal of Asian Earth Sciences **78**: 4-17.

Ludwig, K. (2008). "User's manual for Isoplot 3.70: A Geochronological Toolkit for Microsoft Excel." Berkeley Geochronological Center(Special Publication Number 4).

MacKenzie, W. S. and C. Guilford (1980). Atlas of rock forming minerals London, Longman Group Limited.

Mao, J., F. Pirajno and N. Cook (2011). "Mesozoic metallogeny in East China and corresponding geodynamic settings — An introduction to the special issue." Ore Geology Reviews **43**(1): 1-7.

Mao, J., Y. Wang, Z. Zhang, J. Yu and B. Niu (2003). "Geodynamic settings of Mesozoic large-scale mineralization in North China and adjacent areas." Science in China Series D: Earth Sciences **46**(8): 838-851.

Mao, J. W., Y. M. Qiu, R. J. Goldfarb, Z. C. Zhang, S. Garwin and F. S. Ren (2002). "Geology, distribution, and classification of gold deposits in the western Qinling belt, central China." Mineralium Deposita **37**(3-4): 352-377.

Margui, E. and R. V. Grieken (2013). X-Ray Fluorescence Spectrometry and Related Techniques: An Introduction. New York, Momentum Press

Marsh, B. (2006). "Dynamics of magmatic systems " Elements **2**: 287 - 292.

Mattauer, M., P. Matte, J. Malavieille, P. Tapponnier, H. Maluski, X. Z. Qin, L. Y. Lun and T. Y. Qin (1985). "Tectonics of the Qinling Belt: build-up and evolution of eastern Asia." Nature **317** (6037): 496-500.

Matthews, A. (1976). "Magnetite formation by the reduction of hematite with iron under hydrothermal conditions " American Mineralologist **61**: 927 - 932.

McDonough, W. F. and S.-S. Sun (1995). "The composition of the Earth." Chemical geology **120**(3): 223-253.

Meinert, L. D. (1992). "Skarns and skarn deposits " Geoscience Canada **19**: 145 - 162.

Middlemost, E. A. K. (1985). Magmas and magmatic rocks. London, Longman.

Miller, C. F., S. M. McDowell and R. W. Mapes (2003). "Hot and cold granites? Implications of zircon saturation temperatures and preservation of inheritance." Geology **31**(6): 529-532.

Misra, K. (2012). Understanding mineral deposits, Springer Science & Business Media.

Mitchell, R. H. (2005). "Carbonatites and carbonatites and carbonatites." Canadian Mineralogist **43**: 2049 - 2068.

Nelson, D. R., A. R. Chivas, B. W. Chappell and M. T. McCulloch (1988). "Geochemical and isotopic systematics in carbonatites and implications for the evolution of ocean-island sources " Geochimica et Cosmochimica Acta **52**: 1 - 17.

Nutman, A. P., V. C. Bennett, C. R. Friend, F. Jenner, Y. Wan and D. Liu (2009). "Episodic Eoarchaean crustal accretion (3.87 to 3.66 Ga) in West Greenland (Itsaq Gneiss Complex) and in northeastern China: review and synthesis."

Pagel, M., V. Barbin, P. Blanc and D. e. Ohnenstetter (2000). "Cathodoluminescence in Geosciences." Springer-Verlag Berlin Heidelberg.

Paktunc, A. D. and N. K. Dave (2002). "Formation of secondary pyrite and carbonate minerals in the lower Williams Lake tailings basin, Elliot Lake, Ontario, Canada." American Mineralologist **87**: 593 - 602.

Pearce, J. A., N. B. W. Harris and A. G. Tindle (1984). "Trace element discrimination diagrams for the tectonic interpretation of granitic rocks " Journal of Petrology **25**: 956 - 983.

Pirajno, F. (2012). The Geology and Tectonic Settings of China's Mineral Deposits. Dordrecht, Springer.

Poller, U. (2000). "A combination of single zircon dating by TIMS and cathodoluminescence investigations of the same grain: the CLC method – U-Pb geochronology for metamorphic rocks. In Pagel, M., Barbin, V., Blanc, P., Ohnenstetter, D. (eds)." Cathodoluminescence in Geosciences 401 - 414.

Putnis, A. and J. D. C. McConnell (1976). "The transformation behaviour of metal-enriched chalcopyrite." Contributions to Mineralogy and Petrology **58**: 127 - 136.

Ratschbacher, L., L. Franz, E. Enkelmann, R. Jonckeere, A. Poerschke, B. R. Hacker, S. Dong and Y. Q. Zhang (2006). "Sino-Korean–Yangtze suture, Huwan detachment, and Paleozoic–Tertiary exhumation of (ultra)high-pressure rocks in Tongbai–Xinxian–Dabie." Geological Society of America, Special Publication **403**: 45 - 75.

Ridley, J. (2013). Ore deposit geology. London, Cambridge University Press.

Robb, L. (2007). Introduction to ore-forming processes Malden, USA, Blackwell Publishing

Rollinson, H. (1993). Using geochemical data: evaluation, presentation, interpretation Essex, England Longman Group UK Ltd.

Rubatto, D. and D. Gebauer (2000). "Use of cathodoluminescence for U–Pb zircon dating by ion microprobe: some examples from the western Alps. In Pagel, M., Barbin, V., Blanc, P., Ohnenstetter D. (eds) " Cathodoluminescence in Geosciences: 373 - 400.

Schoene, B. (2014). "U-Th-Pb Geochronology. (eds.) In: Holland, H. and Turekian, K. The Crust, Treatise on Geochemistry (2nd Edition)."Earth Systems and Environmental Science **4**: 341 - 378.

Schoene, B., D. J. Condon and L. M. N. McLean (2013). "Precision and Accuracy in Geochronology" Elements (One Hundred Years of Geochronology) **9**: (19 - 24).
Scotese, C. R. (2004). "A Continental Drift Flipbook." The Journal of Geology **112**(6): 729-741.

Sengor, A. (1985). "East Asian tectonic collage." Nature **318**(6041): 16-17.

Shackley, S. M. (2010). An Introduction to X-Ray Fluorescence (XRF) Analysis in Archaeology, Springer.

Shi, Y., J.-H. Yu and M. Santosh (2013). "Tectonic evolution of the Qinling orogenic belt, Central China: New evidence from geochemical, zircon U–Pb geochronology and Hf isotopes." Precambrian Research **231**: 19-60.

Sillitoe, R. H. (2010). "Porphyry Copper Systems." Economic Geology **105**(1): 3-41.
Stebbins, J. F., J. B. Murdoch, I. S. E. Carmichael and A. Pines (1986). "Defects and short-range order in nepheline group minerals." Physics and Chemistry **13**: 371 - 381.

Stern, R. A., S. Bodorkos, S. L. Kamo, A. H. Hickman and F. Corfu (2009). "Measurement of SIMS Instrumental Mass Fractionation of Pb Isotopes During Zircon Dating." Geostandards and Geoanalytical Research **3**: 145 - 168.

Sun, Y., X. Lu, S. Han, Z. G. and S. Yang (1996). "Composition and formation of Paleozoic Erlangping ophiolitic slab, North Qinling: evidence from geology and geochemistry " Science in China, Institute of Geology, Chinese Academy of Geosciences, Beijing **39**: 50 - 59.

Tait, K. T., E. Sokolova, F. C. Hawthorne and A. P. Khomyokov (2003). "The crystal chemistry of nepheline " The Canadian Mineralogist **41**: 61 - 70.

Takeda, H. and M. Ross (1995). "Mica polymorphism: Identification and origin." American Mineralologist **80**: 715 - 724.

Tang, L., M. Santosh and Y. Dong (2015). "Tectonic evolution of a complex orogenic system: Evidence from the northern Qinling belt, Central China " Journal of Asian Earth Sciences **Article in Press** http://dx.doi.org/10.1016/j.jseaes.2015.03.033.

Taylor, S. R. (1964). "Abundance of chemical elements in the continental crust: a new table " Geochimica et Cosmochimica Acta **28**: 1273 - 1285.

Tera, F. and G. J. Wasserburg (1972). "U-Th-Pb systematics in three Apollo 14 basalts and the problem of initial Pb in lunar rocks." Earth and Planetary Science Letters **14**: 281 - 304.

Tuttle, O. F. and J. Gittins (1966). Carbonatites New York, Wiley.

Vaughan, D. J. (2006). "Sulfide Mineralogy and Geochemistry " Reviews in Mineralogy and Geochemistry, Mineralogical Society of America and Geochemical Society **61**: 714.

Viladkar, S. G. and W. Wimmenauer (1986). "Mineralogy and geochemistry of the Newania carbonatite-fenite complex, Rajasthan, India."Neues Jahrb. Mineral. Abh **156**: 1- 21.

Wang, H. L., S. Zhang and G. He (2005). "China and Mongolia." Encyclopedia Of Geology, Five Volume Set: 345-358.

Wang, X., T. Wang and C. Zhang (2013). "Neoproterozoic, Paleozoic, and Mesozoic granitoid magmatism in the Qinling Orogen, China: Constraints on orogenic process." Journal of Asian Earth Sciences **72**: 129-151.

Watson, E. B. (1979). "Zircon saturation in felsic liquids: experimental results and applications to trace element geochemistry."Contributions to Mineralogy and Petrology **70**(4): 407-419.

Watson, E. B. and M. Harrison (1983). "Zircon saturation effects revisited: temperature and composition effects in a variety of crustal magma types." Earth and Planetary Science Letters **64**: 295 - 304.

Wetherill, G. W. (1965). "Discordant uranium-lead ages." Transactions of the American Geophysical Union **37**: 320 - 326.

Whalen, J., K. L. Currie and B. W. Chappell (1987). "A-type granites: geochemical characteristics, discrimination and petrogenesis "Contributions to Mineralogy and Petrology **95**: 407 - 419.

Whitney, D. L. and B. W. Evans (2010). "Abbreviations for names of rock-forming minerals" American Mineralogist **95**: 185 - 187.

Williams, I. S. (1998). "U-Th-Pb Geochronology by Ion Microprobe. *In:* McKibben, M.A., Shanks III, W.C. & Ridley, W.I (eds.)." Applications of microanalytical techniques to understanding mineralizing processes, Reviews in Economic Geology.

Wilson, M. (1989). Igneous petrogenesis. London, Unwin Hyman.

Winkler, H. G. F. (1974). Petrogenesis of Metamorphic Rocks New York, Springer-Verlag.

Wooley, A. R. and D. R. C. Kempe (1989). Carbonatites: nomenclature, average chemical compositions, and element distribution. In: Bell, K. (eds), Carbonatites: genesis and evolution. London, Unwin Hyman.

Wu, Y.-B. and Y.-F. Zheng (2013). "Tectonic evolution of a composite collision orogen: An overview on the Qinling–Tongbai–Hong'an–Dabie–Sulu orogenic belt in central China." Gondwana Research **23**(4): 1402-1428.

Wyllie, P. J. and O. F. Tuttle (1960). "The system CaO-CO_2-H2O and the origin of carbonatites." Journal of Petrology **1**: 1 - 46.

Xiaoyong, L., P. Zhu, T. M. Kusky, Y. Gu, S. Peng, Y. Yuan and J. Fu (2015). "Has the Yangtze craton lost its root? A comparison between the North China and Yangtze cratons" Tectonophysics **655**: 1 - 14.

Xie, Y., Y. Li, Z. Hou, D. R. Cooke, L. Danyushevsky, S. C. Dominy and Y. Shuping (2015). "A model for carbonatite hosted REE mineralisation — the Mianning–Dechang REE belt, Western Sichuan Province, China." Ore Geology Reviews **70**: 595-612.

Xu, C., A. R. Chakhmouradian, R. N. Taylor, J. Kynicky, W. B. Li, W. L. Song and I. R. Fletcher (2014). "Origin of carbonatites in the South Qinling orogen: Implications for crustal recycling and timing of collision between the South and North China Blocks." Geochimica Et Cosmochimica Acta **143**: 189-206.

Xu, C., J. Kynicky, A. R. Chakhmouradian, I. H. Campbell and C. M. Allen (2010a). "Trace-element modeling of the magmatic evolution of rare-earth rich carbonatite from the Miaoya deposit, Central China." Lithos **118**: 145 - 155.

Xu, C., J. Kynicky, A. R. Chakhmouradian, L. Qi and W. Song (2010b). "A unique Mo deposit associated with carbonatites in the Qinling orogenic belt, central China." Lithos **118**(1–2): 50-60.

Xu, C., J. Kynicky, A. R. Chakhmouradian, L. Xianhua and S. Wenlei (2015). "A case example of the importance of multi-analytical approach in deciphering carbonatite petrogenesis in South Qinling orogen: Miaoya rare-metal deposit, central China." Lithos **227**: 107 - 121.

Yang, K. F., H. R. Fan, M. Santosh, F. F. Hu and K. Y. Wang (2011). "Mesoproterozoic carbonatitic magmatism in the Bayan Obo deposit, Inner Mongolia, North China: Constraints for the mechanism of super accumulation of rare earth elements." Ore Geology Reviews **40**(1): 122-131.

Yang, L.-Q., J. Deng, K.-F. Qiu, X.-Z. Ji, M. Santosh, K.-R. Song, Y.-H. Song, J.-Z. Geng, C. Zhang and B. Hua (2015a). "Magma mixing and crust–mantle interaction in the Triassic monzogranites of Bikou Terrane, central China: Constraints from petrology, geochemistry, and zircon U–Pb–Hf isotopic systematics." Journal of Asian Earth Sciences **98**: 320-341.

Yang, S. J., D. L. Chen, X. K. Gong and J. Zhao (2015b). "The geochemistry, geochronology and its geological implications of leucosomes in the basic volcanics of the Erlangping Group in the eastern segment of the North Qinling " Acta Petrologica Sinica **31**: 2009 - 2022.

Ying, L. C., Y. S. Zhu, T. H. Shi, S. C. Yu and Z. R. Hong (2015). "Fluid origin of fluorite-rich carbonate-hosted Pb–Zn mineralization of the Himalayan–Zagros collisional orogenic system: A case study of the Mohailaheng deposit, Tibetan Plateau, China." Ore Geology Reviews **70**: 546 - 561.

Zhang, G. W., Q. R. Meng and S. C. Lai (1995). "Structure and tectonics of the Qinling Orogenic belt." Science China **25**: 994 - 1003.

Zhang, G. W., Z. P. Yu, Y. P. Dong and A. P. Yao (2000). "On Precambrian framework and evolution of the Qinling belt." Acta Petrologica Sinica **16**: 11 - 21.

Zhang, G. W., B. R. Zhang, X. C. Yuan and Q. H. Xiao (2001). "Qinling Orogenic Belt and Continental Dynamics." Science Press, Beijing: 1 - 855.

Zhang, Z., L. Sanzhong, C. Huahua, I. D. Somerville and S. Zhao (2015). "Origin of the North Qinling Microcontinent and Proterozoic geotectonic evolution of the Kuanping Ocean, Central China." Precambrian Research **266**: 179 - 193.

Zhang, Z. Q., D. Y. Liu and G. M. Fu (1994). Isotopic geochronology of metamorphic strata in the North Qinling. Beijing, Geological Publishing House.

Zhang, Z. Q. and Q. Zhang (1995). "Geochemistry of metamorphosed Late Proterozoic Kuanping ophiolite in the Northern Qinling, China."Acta Petrologica Sinica **11**: 165 - 177.

Zhao, X., Z. Yang, Y. Zheng, Y. Liu, S. Tian and Q. Fu (2015). "Geology and genesis of the post-collisional porphyry–skarn deposit at Bangpu, Tibet." Ore Geology Reviews **70**: 486-509.

Zhu, L., G. Zhang, B. Guo and B. Li (2008a). "U–Pb (LA-ICP-MS) zircon dating for the large Jinduicheng porphyry Mo deposit in the East Qinling, China, and its metallogenetic geodynamical setting." Acta Geologica Sinica **82**(2): 204-220.

Zhu, L., G. Zhang, B. Li and B. Guo (2008b). "Main geological events, genetic types of metallic deposits and their geodynamical setting in the Qinling orogenic belt." Bulletin of Mineralogy, Petrology and Geochemistry **27**(4): 384-390.

APPENDIX A - FIELD NOTES

DEPOSIT 1

NANTAI Mo-(Cu) DEPOSIT

Location:	33°27’42” N, 109°58’54” E
Host units:	granite and dolomitic marble
Age:	~150 Ma
Date accessed:	14/05/2015
Field notes:	

Located in the north Qinling Orogenic Belt (QOB), south of the township of Shangluo sits the Nantai Mo-(Cu) porphyry-skarn deposit. Molybdenite mineralisation is observed within and around the granitic (aplite) body. The granite age has been dated as Triassic (~150 Ma), with subsequent mineralisation assumed to have been generated soon after. The source of the metallogenic material is inferred to be the same as that of the granitic material. Notably, mineralisation observed in the field occurs as veinlet disseminations within the exposed granite. Distal to the porphyry-skarn body occurs a phase dominated by mixed sulphide oxide type facies, jasperoidal silica and fine-grained pyrite. The porphyry-skarn body can be described as magnesium- rather than calcite-rich. The aplite dykes, composed of mainly granitic constituents (i.e. QAF constituents) is extremely fine-grained. The fine-grained nature of this intrusive body in indicative of rapid heat loss; heat is generally lost to that of the surrounding country-rock with volatiles being rapidly released lending to fine-grained solidification of the rock.

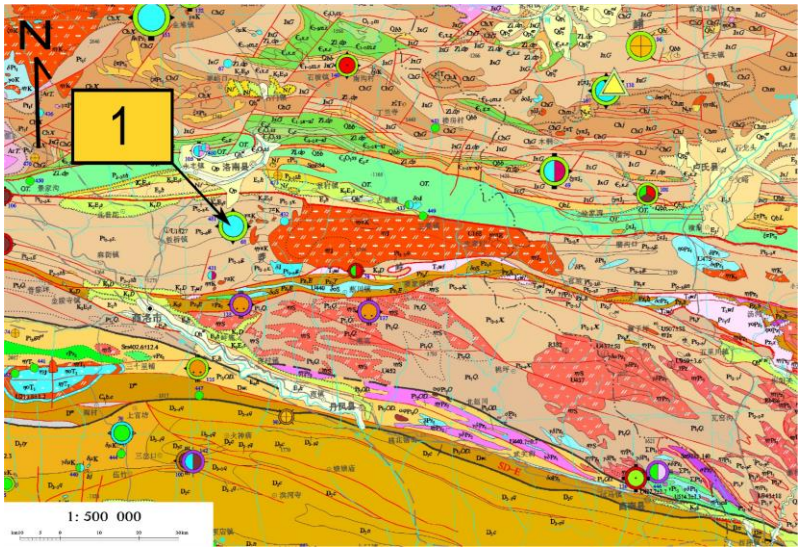

DEPOSIT 2

LIUJIAXIA OROGENIC Au DEPOSIT

Location:	33°25’39” N, 109°65’24” E
Host units:	conglomerates and dolomites
Age:	Devonian to Carboniferous
Date accessed:	16/05/2015
Field notes:	

Located in the north Qinling Orogenic Belt (QOB), between cities Shanglou and Shangyang sits the Liujiaxia Au Deposit. The orebody is currently being mined with an average grade of ~ 6g/T and the highest grades being ~13g/T. Similar to the aforementioned Longtougou orogenic gold deposit, the gold is trapped inside the pyrite with neither being observable. The Au is part of a much larger sedimentary package, consisting of conglomerates and dolomites. The conglomerate unit is assumed to be fore-arc basin derived, as no volcanic clasts were observed while in the field; rather chert and sedimentary clasts were identified. Flame structures were identified in the dolomite whereby upward-pointing finer-grained sediment ‘tongues’ protrude into coarser sediment; the higher-density sand sinks into the lower-density underlying unit, for example a shale.

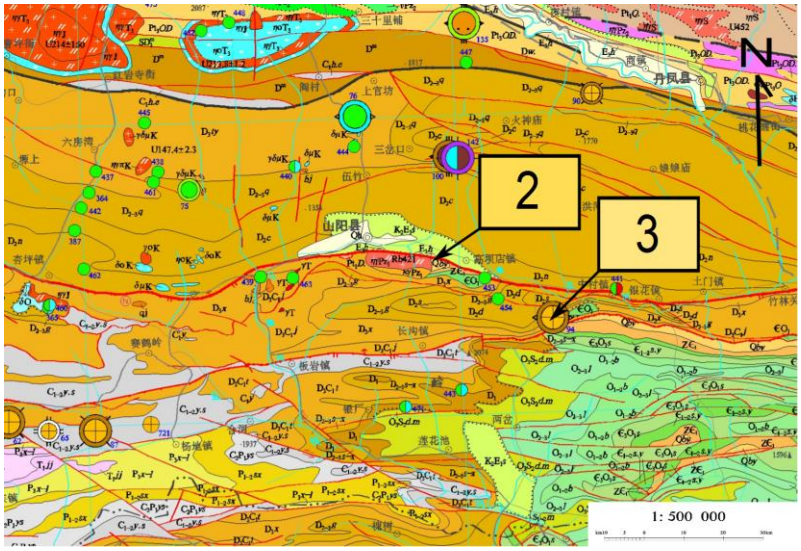

DEPOSIT 3

LOUGTOUGOU OROGENIC Au DEPOSIT

Location:	33°27’42” N, 109°58’54” E
Host units:	dolomites, siltstones and conglomerates
Age:	Devonian to Carboniferous
Date accessed:	17/05/2015
Field notes:	

Located in the Qinling Orogenic Belt (QOB) between the cities of Shanyang and Shiyan sits the Longtougou Au Deposit. The orebody lies within an Early to Late Devonian sedimentary package including dolomites, siltstones and conglomerates. The mineralisation occurs in the middle of an anticline, which leads to suggest the deposit type is orogenic rather than Carlin-type. There is also no presence of limestone, which further infers it is unlikely the system is Carlin-type. The Longtougou Au Deposit is confined to the shear fracture on the wing of an anticline (strike-slip fault derived), with veinlets distributing from this structure. The major alteration phases observed in the field include barition, pyritisation and silicification. As with both the Liujiaxia Au Deposit the Au is inside pyrite with neither being observable in hand specimen.

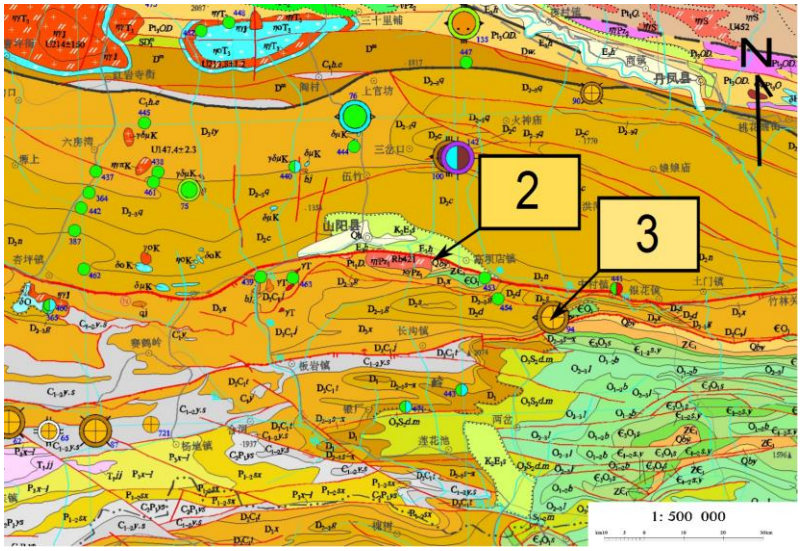

DEPOSIT 4

MIAOYA REE DEPOSIT

Location:	32°49’48” N, 109°53’37” E
Host units:	carbonatites and syenites
Age:	~234 Ma
Date accessed:	21/05/2015
Field notes:	

Located in the southern margin of the Qinling Orogenic Belt (QOB) proximal to Miaoya village, the Miaoya REE deposit is emplaced in relatively low-grade metavolcanic rocks (originally rift or hotspot derived; alkali-rich magmas with low degrees of partial melting). The deposit was first discovered in the early 1960’s, having been explored in the early 1970’s and again in the 1980’s. Rare Earth Elements (REE) and incompatible minerals occur in carbonatite and possibly in associated syenites. Field relationships indicate that the (~Permian) carbonatites intrude into the Archean – Mesoproterozoic metavolcanic rocks. The intrusive event could be related to an earlier collision (for example the continental collisional event between the North China Block and the South China Block), with subsequent relaxation allowing for carbonatite intrusives to occur. Voluminous Triassic granites flood the QOB having occurred after the previously mentioned continental collisional event; the carbonatite intrusive event is inferred to have taken place after the Triassic granites, that being ~ Late Permian following the collision.

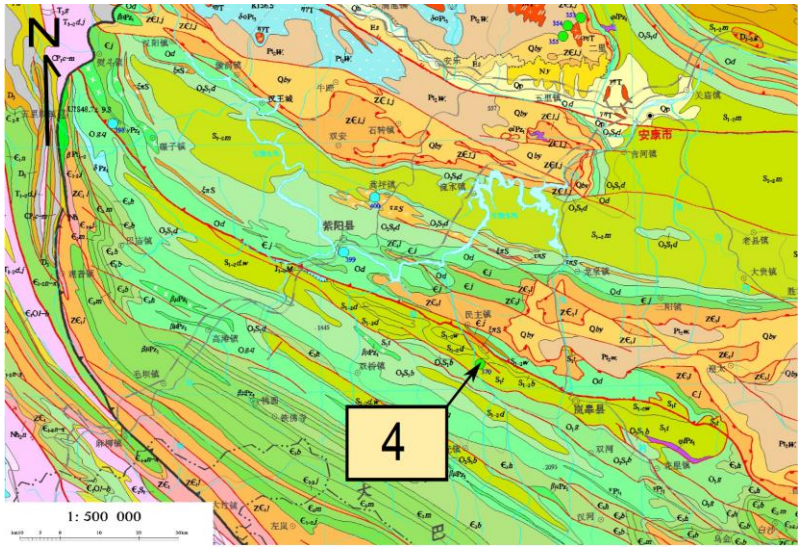

DEPOSIT 5

DAMOGOU Zn-CaF_2 DEPOSIT

Location:	32°14’51” N, 109°30’17” E
Host units:	trachyte and limestone
Age:	Unknown
Date accessed:	22/05/2015
Field notes:	

Located in the contact zone between the south Qinling Orogenic Belt (QOB) and the north Dabashan Orogenic Collage (DOC) proximal to Ankang city is the Damogou zinc-fluorite (Zn-CaF_2) deposit. The deposit is constrained by Triassic alkali volcanics (namely trachyte) and limestone. The Zn and CaF_2 mineralisation is controlled by the locally named F7 fault structure. Multiple orebodies (K1, K2, K3, K4, K5, K6, KH7 and K8) have been identified from this deposit in what has been described as vein-type in geometric construction. Field work was undertaken at the K1 orebody (Damogou Zn ore deposit), which has a Zn grade range of 2.36 – 19.20%, with an average of 10.57%. The associated CaF_2 has a grade range of 0.00 – 31.00%. The K1 orebody is located in the northern part of the mining area around the Damogou area.

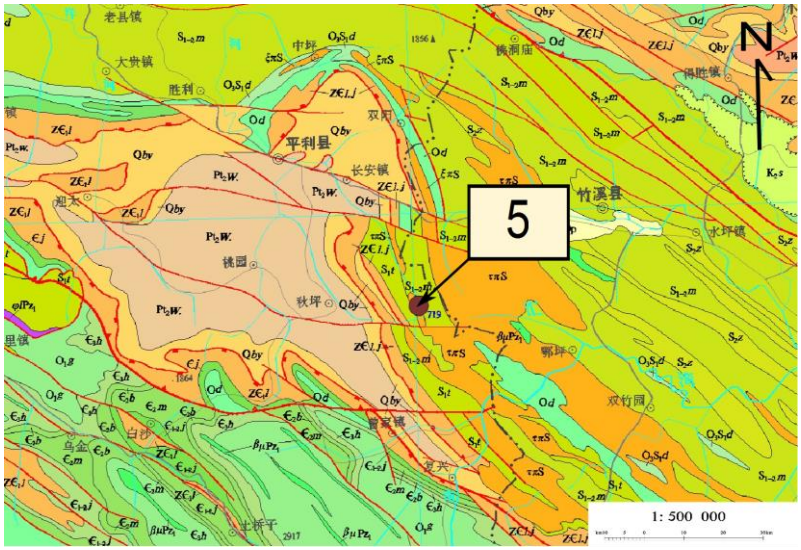

西 秦 岭 地 质 矿 产 图

（铜、铅、锌、金、银、钼）

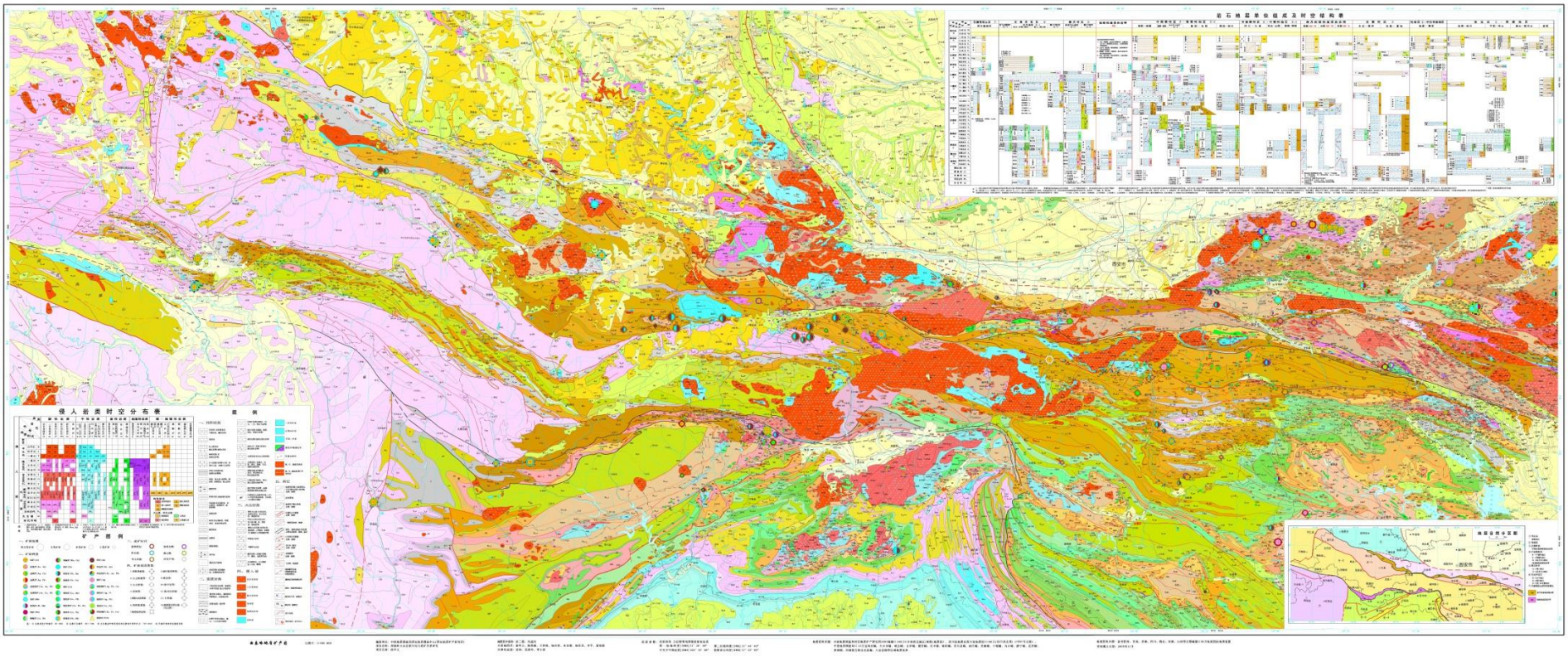

This detailed geological map of the Qinling Orogenic Belt, Central China is courtesy of the Institute of Geology and Geophysics, Chinese Academy of Science (IGGCAS)

APPENDIX B - SAMPLE LIST

Deposit	Sample ID	Polished thin section	RAMAN	XRD	XRF	LA-ICP-MS	CL-imaging	SHRIMP U-Pb	Description
1. NANTAI Mo-(Cu) DEPOSIT	15NT_01	✓		✓	✓	✓	✓	✓	Mineralised aplite Mo-(Cu)
	15NT_02	✓		✓	✓	✓			Mineralised aplite Mo-(Cu)
	15NT_03	✓		✓	✓	✓	✓	✓	Mineralised aplite Mo-(Cu)
	15NT_A	✓		✓	✓	✓			Mineralised aplite Mo-(Cu)
	15NT_B	✓		✓	✓	✓			Mineralised aplite Mo-(Cu)
	15NT_C	✓		✓	✓	✓			Mineralised aplite Mo-(Cu)
	15NT_D	✓		✓	✓	✓			Dolomite
	15NT_E	✓		✓	✓	✓			Weathered granite (Mo)
	15NT_F	✓							Marble (trace magnetite)
	15NT_G	✓		✓		✓			Massive Mo Ore
	15NT_H	✓							Interbedded quartz + greenstone
	15NT_I	✓							Marl
	15NT_J	✓		✓	✓	✓			Lamprophyre
	15NT_K	✓		✓	✓	✓			Lamprophyre
	15NT_L	✓		✓	✓	✓			Lamprophyre
2. MIAOYA REE DEPOSIT	15MY_A	✓	✓	✓	✓	✓			Mineralised carbonatite REE
	15MY_B	✓	✓	✓	✓	✓			Mineralised carbonatite REE
	15MY_C	✓		✓	✓	✓			Mineralised carbonatite REE
	15MY_D	✓		✓	✓	✓			Mineralised carbonatite REE
	15MY_E	✓		✓	✓	✓			Mineralised carbonatite REE
	15MY_F	✓		✓	✓	✓			Mineralised carbonatite REE
	15MY_G	✓		✓	✓	✓			Mineralised carbonatite REE
	15MY_H	✓		✓	✓	✓			Mineralised carbonatite REE
	15MY_I	✓		✓	✓	✓			Mineralised carbonatite REE
3. LIUJIAXIA (orogenic) Au DEPOSIT	15LJ_A								Dog-toothed calcite
	15LJ_B	✓		✓	✓	✓			Siltstone
4. LONGTOUGOU (orogenic) Au DEPOSIT	15LT_A	✓		✓	✓	✓			Marl
	15LT_B			✓	✓	✓			Marl
	15LT_C			✓	✓	✓			Marl
	15LT_D			✓	✓	✓			Marl
	15LT_E	✓		✓	✓	✓			Mineralised barite-vein
5. DAMOGOU Zn-CaF_2 DEPOSIT	15DG_A	✓		✓	✓	✓			Mineralised fluorite-vein
	15DG_B								Mineralised fluorite-vein
	15DG_C								Mineralised fluorite-vein

APPENDIX C - ZIRCON CHARACTERISTICS

(W41) 15NT_01

(W41) 15NT_03

15NT-01

[1.1]

Shape:	Euhedral
Prismatic faces:	Well-preserved prismatic faces
Size:	150 μm in length
Elongation ratio:	4:1
Preservation state:	Complete grain free of fracturing and fragmentation
Zonation and colouring:	Well-developed bands of contrasting bright and dark oscillatory zones. Within this individual grain there are strong variations in the development of zoned domains, where one large central bright zone (core complex) is succeeded by much finer oscillatory-zoned bands with a large, dark band (particularly thick around grain terminations) marking the final stage of development

15NT-01

[2.1]

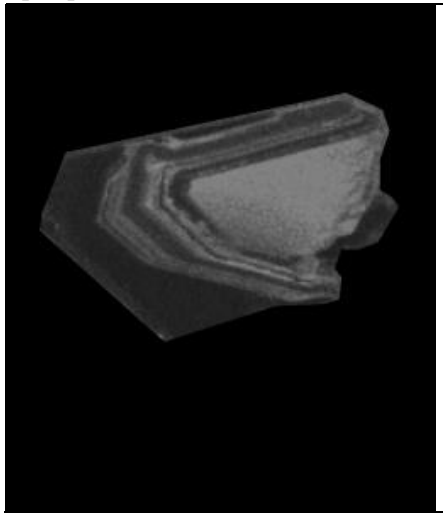

Shape:	Subhedral to euhedral
Prismatic faces:	Well-preserved prismatic faces
Size:	125 μm in length (approximately 200 μm in length had the grain been preserved)
Elongation ratio:	3:1
Preservation state :	Incomplete grain, approximately one third of the length of the grain has been broken off through the core and other oscillatory zones
Zonation and colouring:	Well-developed bands of contrasting bright and dark oscillatory bands. As with [1.1], there is strong variation between zones varying between bright, dark and some grey bands. The one visible grain termination (the other has been destroyed and as such is not present) is marked by a large, dark band defining the final stage of grain development

15NT-01

[3.1]

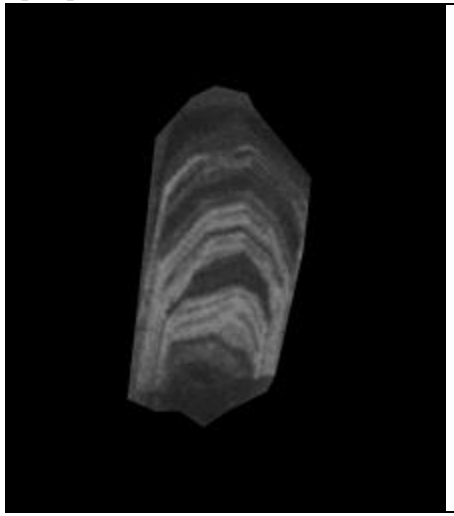

Shape:	Euhedral
Prismatic faces:	Well-preserved prismatic faces
Size:	100 μm in length (~150 μm in length had the grain been preserved)
Elongation ratio:	2:1
Preservation state:	Incomplete grain, approximately one third of the length of the grain has been broken
Zonation and colouring:	Well-developed bands of contrasting bright and dark oscillatory zones, with variations demonstrating intermediate grey as well as bright and dark bands. There is slight truncation between some of the zones indicating a degree of complex, rather than simple banding texture. The core of the grain is indistinguishable due to one of the grain terminations (inclusive of the core) being destroyed

15NT-01

[4.1]

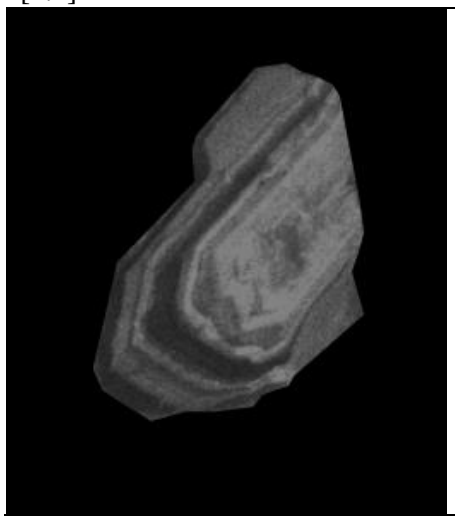

Shape:	Subhedral to euhedral
Prismatic faces:	Well-preserved prismatic faces
Size:	140 μm in length (approximately 200 μm in length had the grain been preserved)
Elongation ratio:	3:1
Preservation state:	Incomplete grain, approximately a quarter of the length of the grain has been broken off
Zonation and colouring:	Truncated growth banding is apparent surrounding the (bright) core complex of this grain, followed by relatively thin grey and dark oscillatory banding that defines the rest of the zircon. Although the grain is not wholly preserved the shape can still be classified as subhedral to euhedral

15NT-01

[5.1]

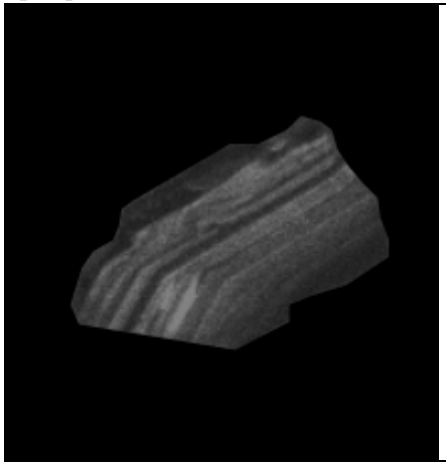

Shape:	Subhedral to euhedral
Prismatic faces:	Prismatic faces are difficult to define, due to little preservation of the grain
Size:	100 μm in length (approximately 200 μm in length had the grain been preserved)
Elongation ratio:	~3:1
Preservation state:	Incomplete grain, approximately three quarters of the grain has been broken off
Zonation and colouring:	Of what is preserved of this grain, there are well-developed bands of contrasting bright and dark oscillatory zones. The core has not been preserved, and as such its luminescence factor cannot be commented on. The size and shape have been estimated with reference to the remainder of the zircon grain

15NT-01

[6.1]

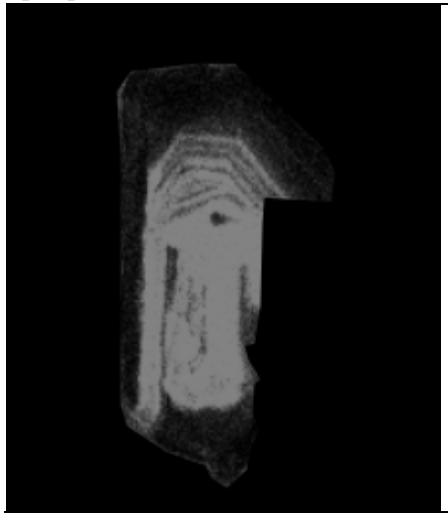

Shape:	Subhedral to euhedral
Prismatic faces:	Well-preserved prismatic faces. Note: the apparent ‘cut-out’ section of the grain is due to Cl image extraction
Size:	120 μm in length
Elongation ratio:	2:1
Preservation state:	Complete grain free of fracturing and fragmentation
Zonation and colouring:	The CL image of this grain has produced what appears to be a very bright core, with surrounding bright to grey bands. There is some truncation in the immediate bands following the crystallisation of the core. These bands (after the apparent truncation texture) demonstrate oscillatory zonation. The grain terminations exemplify dark (assumedly high uranium containing) thick band/s

15NT-01

[7.1]

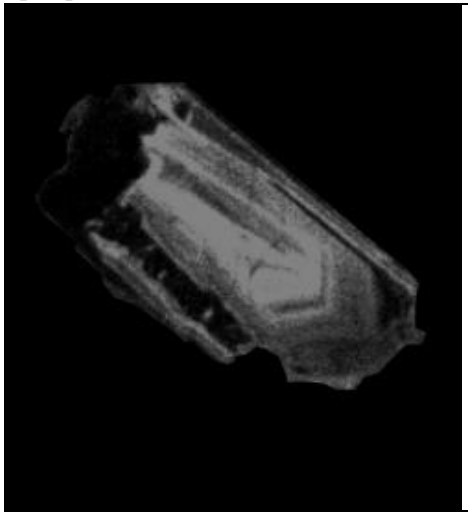

Shape:	Subhedral to euhedral
Prismatic faces:	Poorly preserved prismatic faces
Size:	125 μm in length
Elongation ratio:	2:1
Preservation state:	Complete grain with apparent fracturing/cracking from the core radiating towards the longest dimensions
Zonation and colouring:	This grain demonstrates one large central bright zone (core), which is succeeded by poorly developed grey bands (poorly developed comparative to previous grains [1.1] – [6.1]). Dark seams indicate altered fractures disrupting what may have been regular domainal texture within the grain

15NT-01

[8.1]

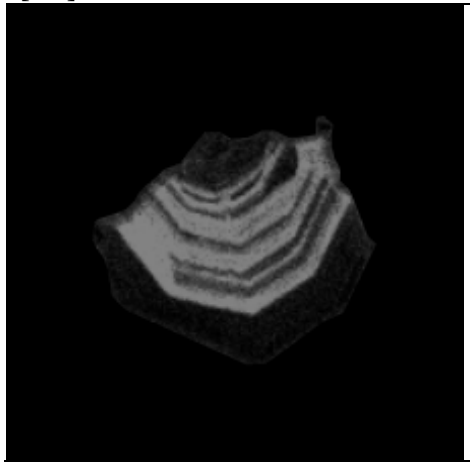

Shape:	Euhedral
Prismatic faces:	Well-preserved prismatic faces (evident from the remainder of the grain)
Size:	50 μm in length (approximately 150 - 200 μm in length had the grain been wholly preserved)
Elongation ratio:	~3:1
Preservation state:	Incomplete grain, approximately three quarters of the grain has been broken off
Zonation and colouring:	Well-developed bands of contrasting bright and dark oscillatory zones. Within this individual grain there are strong variations in the development of zoned domains, with clear definition between individual bands. The preserved grain termination is marked by a large, dark band marking the final stage of development

15NT-01

[9.1]

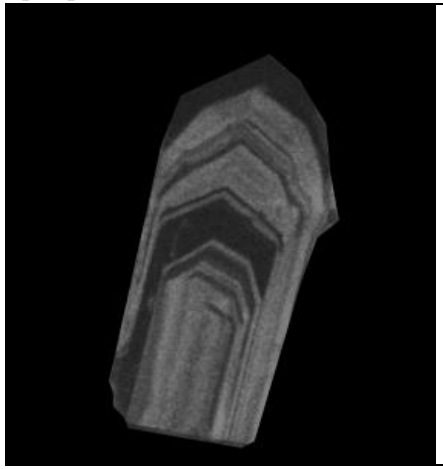

Shape:	Euhedral
Prismatic faces:	Well-preserved prismatic faces
Size:	150 μm in length (200 μm in length had the grain been preserved)
Elongation ratio:	4:1
Preservation state:	Incomplete grain, approximately one quarter of the grain has been broken off
Zonation and colouring:	Well-developed bands of contrasting bright and dark oscillatory zones. Within this individual grain there are relatively large variations in the width of the bands, with some displaying very thin (<1 μm) widths, with other bands having larger domains (~5 μm) directed towards the grain termination (only one preserved)

15NT-01

[10.1]

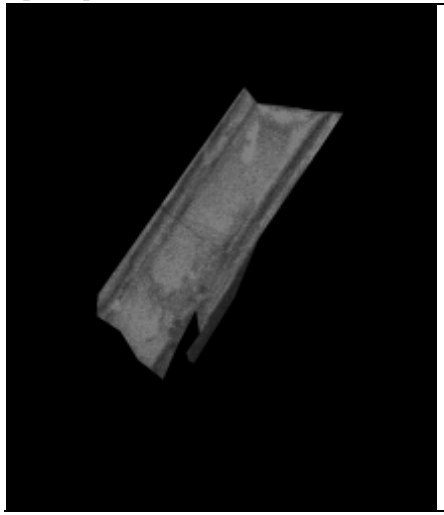

Shape:	Subhedral to anhedral
Prismatic faces:	Poorly preserved prismatic faces
Size:	120 μm in length (200 μm in length had the grain been preserved)
Elongation ratio:	~3:1
Preservation state:	Grain is poorly preserved; CL image displays a crack that passes through the width of the zircon. The two grain terminations have also been destroyed
Zonation and colouring:	This grain demonstrates only apparent simple zonation. What is left of the grain appears to be the central domain, or the core complex. The true development of the grain, and its assumed subsequent bands cannot be commented on other than it could be inferred that the grain would have displayed similar characteristics and development to those grains already identified

15NT-01

[11.1]

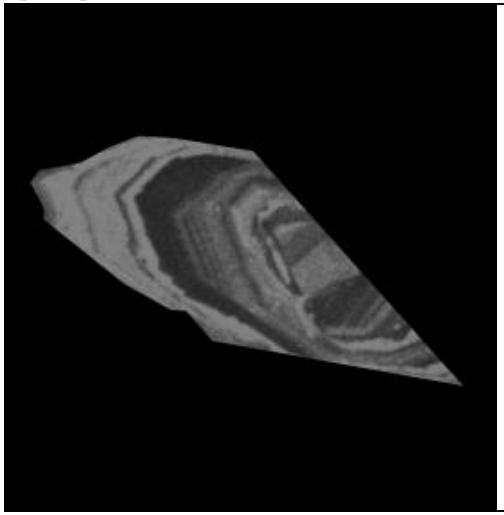

Shape:	Subhedral
Prismatic faces:	Well-preserved prismatic faces. Note: the apparent ‘cut-out’ section of the grain is due to Cl image extraction
Size:	200 μm in length
Elongation ratio:	4:1
Preservation state:	Complete grain free of fracturing and fragmentation
Zonation and colouring:	Truncated zonation, with some zones difficult to distinguish. Bands range from dark to bright, inclusive of intermittent gray bands also. Recrystallization could account for the appearance of the core being disturbed of this grain

15NT-01

[12.1]

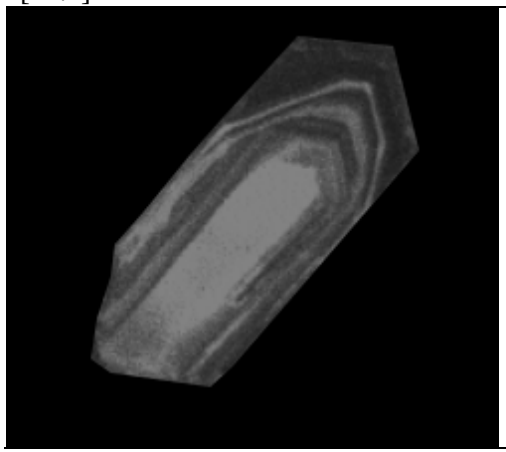

Shape:	Eubhedral
Prismatic faces:	Well-preserved prismatic faces
Size:	120 μm in length
Elongation ratio:	2:1
Preservation state:	Complete grain free of fracturing and fragmentation
Zonation and colouring:	Well-defined oscillatory zonation is apparent in this grain; successions of primarily bright and gray bands account for the majority of the zircon with one late stage dark band forming around one of the grain terminations

15NT-01

[13.1]

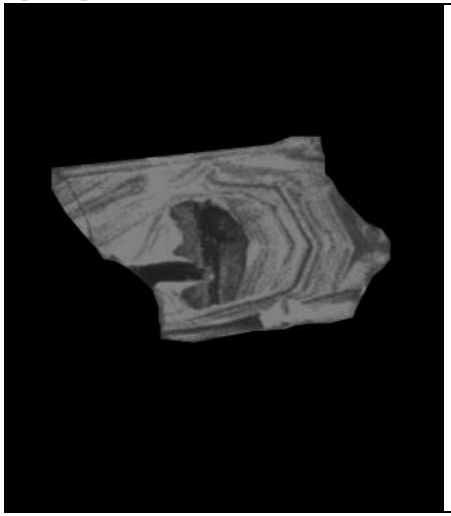

Shape:	Subhedral
Prismatic faces:	Well-preserved prismatic faces
Size:	125 μm in length (200 μm in length had the grain been preserved)
Elongation ratio:	3:1
Preservation state:	Incomplete grain, approximately one third of the grain has been broken off
Zonation and colouring:	The core of the grain is particularly dark, with oscillating bands of bright and grey colouring. The bright bands tend to be thicker than the grey banding. Truncated zonation, with some zones difficult to distinguish. Bands range from dark to bright, inclusive of intermittent grey bands also. Recrystallization could account for the appearance of the core being disturbed of this grain

15NT-01

[14.1]

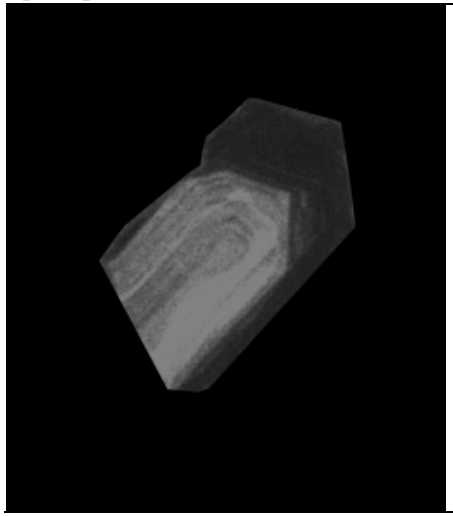

Shape:	Euhedral
Prismatic faces:	Well-preserved prismatic faces
Size:	100 μm in length (150 μm in length had the grain been preserved)
Elongation ratio:	3:1
Preservation state:	Incomplete grain, approximately one third of the grain has been broken off
Zonation and colouring:	Within this grain the core is difficult to distinguish. The inner bands surrounding the non-observed core are very bright, and also difficult to differentiate. The outer bands are incredibly dark in comparison, accounting for late stage crystallization derived from a uranium-rich melt

15NT-01

[15.1]

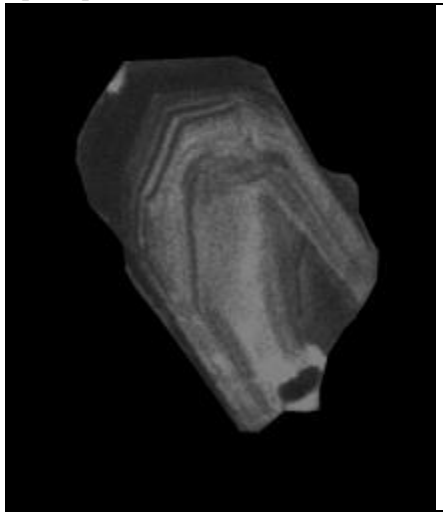

Shape:	Euhedral
Prismatic faces:	Well-preserved prismatic faces
Size:	100 μm in length (150 μm in length had the grain not been broken)
Elongation ratio:	3:1
Preservation state:	Incomplete grain, approximately one quarter has been broken off
Zonation and colouring:	Unlike many of the other grains, the core or central domain of this zircon is distinctly dark. There is evidence of recrystallization, apparent in the dark bleb-like formation at base to the left of the core. There is also complex growth zoning with possible local intermediate resorption in the zircon grain from anatectic granite from the Nantai deposit

15NT-01

[16.1]

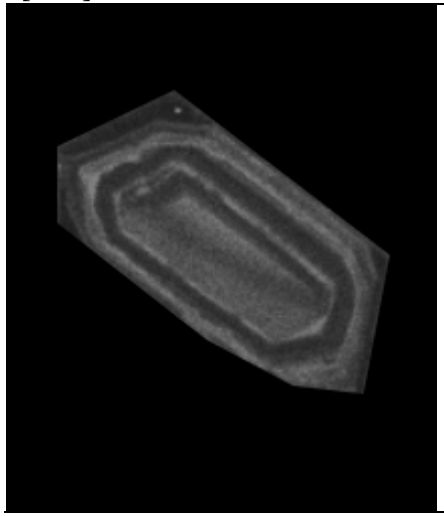

Shape:	Euhedral
Prismatic faces:	Well-preserved prismatic faces
Size:	100 μm in length
Elongation ratio:	2:1
Preservation state:	Complete grain free of fracturing and fragmentation
Zonation and colouring:	Well-developed bands of contrasting bright and dark oscillatory zones. Within this individual grain there are strong variations in the development of zoned domains, combined with a well-preserved euhedral shape

15NT-03

[1.1]

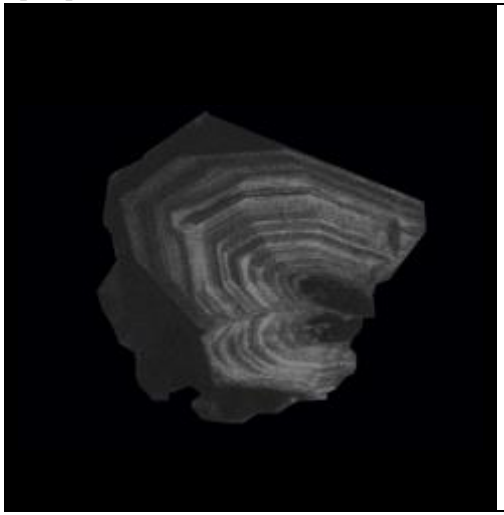

Shape:	Subhedral to anhedral
Prismatic faces:	Well-preserved prismatic faces
Size:	125 μm in length (approximately 160 μm in length had the grain not been preserved)
Elongation ratio:	3:1
Preservation state:	Incomplete grain, approximately one quarter has been broken off
Zonation and colouring:	Well-developed bands of contrasting bright and dark oscillatory zones occur successively after the dark core. The grain appears to have been cracked from outer rims inwards towards the core, displaying what is similar to a smaller, duplicate grain coupled with the 'parent' zircon

15NT-01

[2.1]

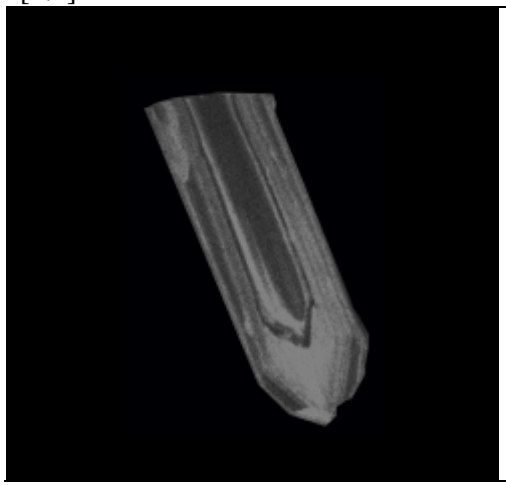

Shape:	Euhedral
Prismatic faces:	Well-preserved prismatic faces
Size:	150 μm in length (approximately 180 μm in length had the grain not been preserved)
Elongation ratio:	5:1
Preservation state:	Incomplete grain, approximately a quarter of the length of the grain has been broken off
Zonation and colouring:	Well-developed bands of contrasting bright and dark oscillatory zones, with a dark central domain or core complex. This grain is needle-shaped and acicular in habit; the elongation ratio of this grain is reflective of the rapid crystallisation velocity

15NT-03

[3.1]

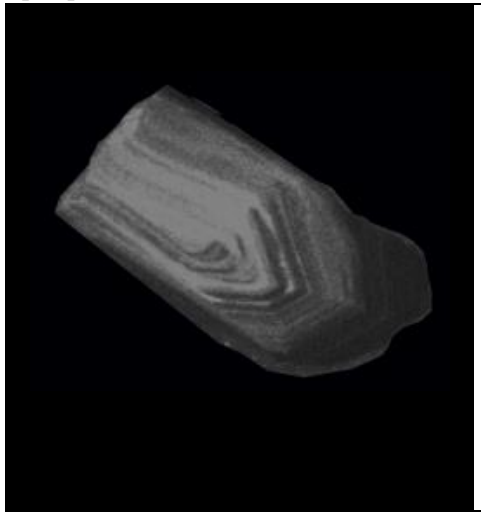

Shape:	Euhedral
Prismatic faces:	Well-preserved prismatic faces
Size:	150 μm in length
Elongation ratio:	5:1
Preservation state:	Complete grain free of fracturing and fragmentation
Zonation and colouring:	Well-developed bands of contrasting bright and dark oscillatory zones, simple growth zoning. Within this individual grain there are strong variations in the development of zoned domains, where one large central bright zone is succeeded by much finer oscillatory-zoned bands with a large, dark band (particularly thick around grain terminations) marking the final stage of development of the crystal

15NT-01

[4.1]

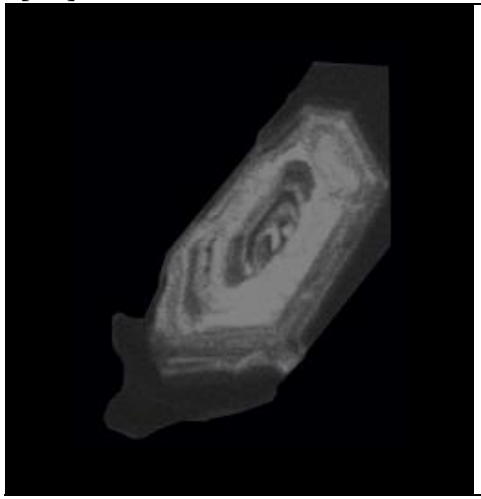

Shape:	Subhedral
Prismatic faces:	Well-preserved prismatic faces. Note: the apparent 'cut-out' section of the grain is due to Cl image extraction
Size:	150 μm in length
Elongation ratio:	3:1
Preservation state:	Complete grain free of fracturing and fragmentation
Zonation and colouring:	Well-developed bands of contrasting bright and dark oscillatory zones. The inner bands surrounding the core are very bright; the outer bands are incredibly dark in comparison, accounting for late stage crystallization derived from a uranium-rich melt

15NT-03

[5.1]

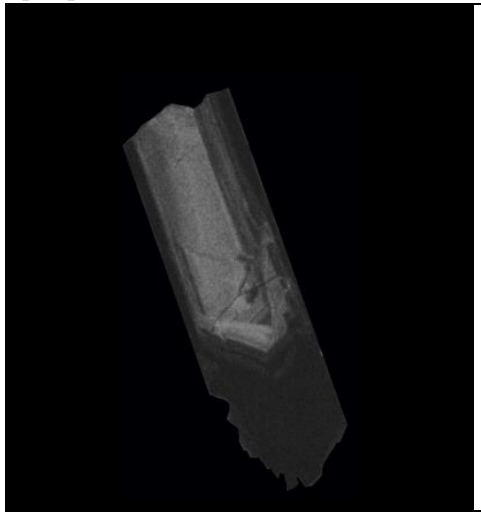

Shape:	Euhedral
Prismatic faces:	Well-preserved prismatic faces
Size:	250 μm in length (approximately 300 μm in length had the grain been preserved
Elongation ratio:	5:1
Preservation state:	Incomplete grain, approximately a quarter of the length of the grain has been broken off through the core and other oscillatory zones. There are also fractures throughout the grain
Zonation and colouring:	Well-developed bands of contrasting bright and dark oscillatory zones. Within this individual grain there are strong variations in the development of zoned domains, where one large central bright zone is succeeded by large dark bands developed through to the one preserved grain termination. There is evidence of some truncation growth surrounding core

15NT-01

[6.1]

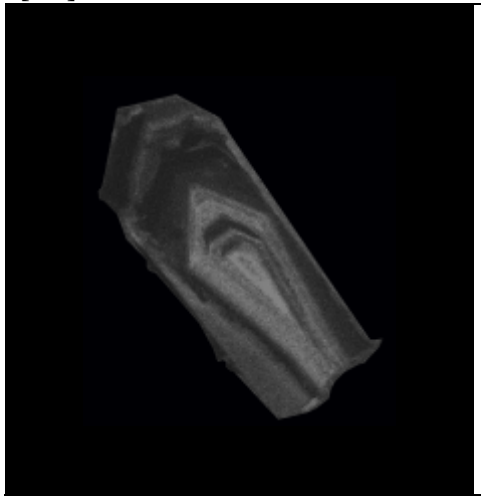

Shape:	Euhedral
Prismatic faces:	Well-preserved prismatic faces
Size:	180 μm in length (approximately 200 μm in length had the grain not been broken).
Elongation ratio:	3:1
Preservation state:	Incomplete grain, approximately a third of the length of the grain has been broken off
Zonation and colouring:	Well-developed bands of contrasting bright and dark oscillatory zones succeeding a bright core. The brightest bands occur in the middle of the grain, and progressively get darker towards the outer rim of the zircon

15NT-03

[7.1]

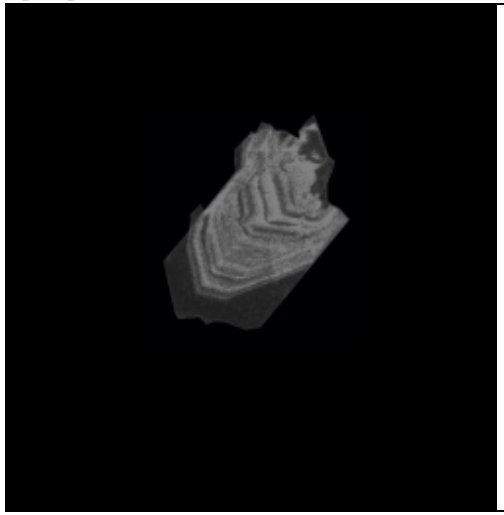

Shape:	Euhedral
Prismatic faces:	Well-preserved prismatic faces
Size:	100 μm in length (approximately 200 μm in length had the grain not been broken)
Elongation ratio:	3:1
Preservation state:	Incomplete grain, half of the length of the grain has been broken off through the core and other oscillatory zones
Zonation and colouring:	Well-developed bands of contrasting bright and dark oscillatory zones. From what is preserved of the grain, it seems the core is dark which is surrounded by thin bright and dark bands with one final dark band marking the one preserved grain termination exemplifying the final stage of development

15NT-01

[8.1]

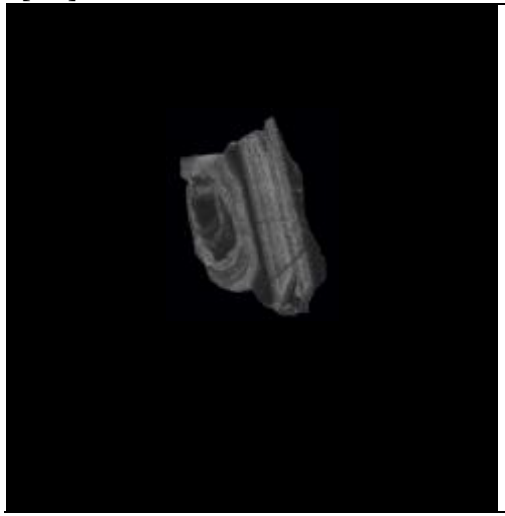

Shape:	Subhedral to euhedral
Prismatic faces:	Preservation state of the faces is difficult to define, as a significant proportion of the grain has been dismembered. Some fractures present through the oscillatory zones of the zircon
Size:	100 μm in length (approximately 200 - 250 μm in length had the grain not been broken)
Elongation ratio:	~4:1
Preservation state:	Incomplete grain, three quarters of the grain has been broken off
Zonation and colouring:	Well-developed bands of contrasting bright and dark oscillatory zones, from what can be gathered from the remaining proportion of the grain. The dark core is surrounded by thin bright, dark and grey bands

15NT-03

[9.1]

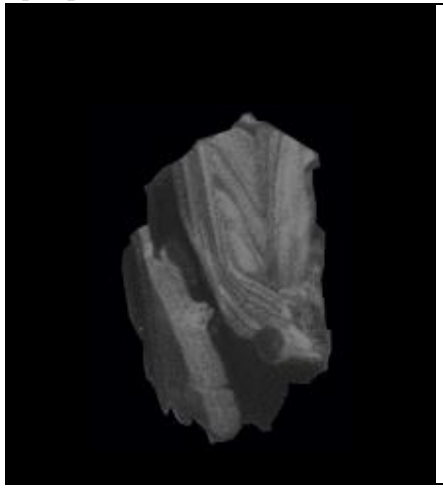

Shape:	Subhedral
Prismatic faces:	Preservation state of the faces is difficult to define, as a significant proportion of the grain has been dismembered
Size:	180 μm in length (approximately 250 μm in length had the grain not been broken)
Elongation ratio:	4:1
Preservation state:	Incomplete grain, approximately a third of the length of the grain has been broken off through the core and other oscillatory zones
Zonation and colouring:	Truncated zonation is a prominent texture of the grain, with some zones difficult to distinguish. Bands range from dark to bright, inclusive of intermittent grey bands also.

15NT-01

[10.1]

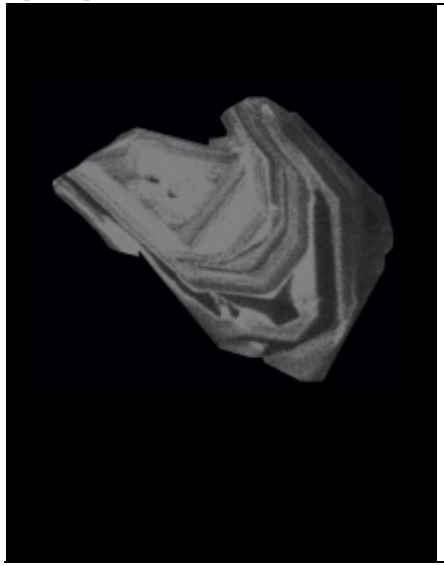

Shape:	Subhedral
Prismatic faces:	Preservation state of the faces is difficult to define, as a significant proportion of the grain has been dismembered
Size:	160 μm in length (approximately 220 μm in length had the grain not been broken).
Elongation ratio:	3:1
Preservation state:	Incomplete grain, approximately a third of the length of the grain has been broken off through the core and other oscillatory zones
Zonation and colouring:	The core of the grain is particularly bright. Truncated zonation radiates from the central domain of the grain, with some zones difficult to distinguish. Bands range from dark to bright, inclusive of intermittent grey bands also. Recrystallization could account for the appearance of the core being disturbed of this grain

15NT-03

[11.1]

Shape:	Subhedral
Prismatic faces:	Well-preserved prismatic faces
Size:	110 μm in length
Elongation ratio:	3:1
Preservation state:	Complete grain free of fracturing and fragmentation
Zonation and colouring:	Well-developed bands of contrasting bright and dark oscillatory zones. Within this individual grain there are strong variations in the development of zoned domains, accounting for the bands being easily distinguishable

15NT-01

[12.1]

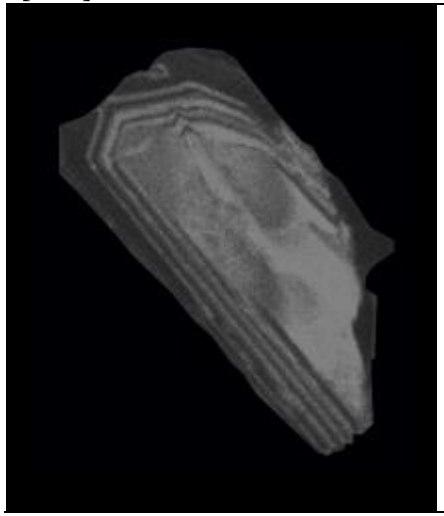

Shape:	Subhedral to euhedral
Prismatic faces:	Well-preserved prismatic faces
Size:	200 μm in length (approximately 250 μm in length had the grain not been broken).
Elongation ratio:	4:1
Preservation state:	Incomplete grain, approximately a fifth of the length of the grain has been broken off through the core and other oscillatory zones
Zonation and colouring:	This grain contains what appears to be a large central domain or core complex. Within the core there are variations in luminescence, which could account for interference with the system and possible recrystallization

15NT-03

[13.1]

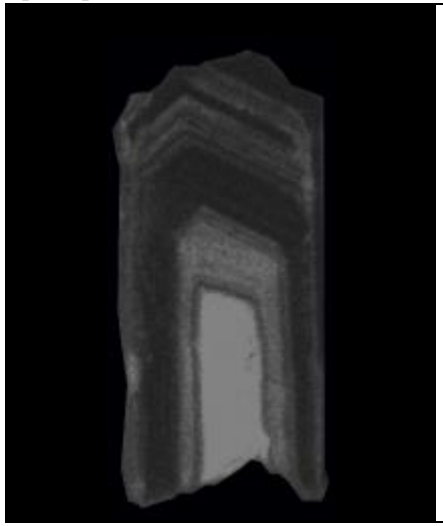

Shape:	Euhedral
Prismatic faces:	Well-preserved prismatic faces
Size:	150 μm in length (approximately 180 μm in length had the grain not been broken).
Elongation ratio:	4:1
Preservation state:	Incomplete grain, approximately a quarter of the length of the grain has been broken off through the core and other oscillatory zones
Zonation and colouring:	Well-developed bands of contrasting bright and dark oscillatory zones. Within this individual grain there are strong variations in the development of zoned domains, where one large central bright zone, or core complex is succeeded by much finer (darker) oscillatory-zoned bands

15NT-01

[14.1]

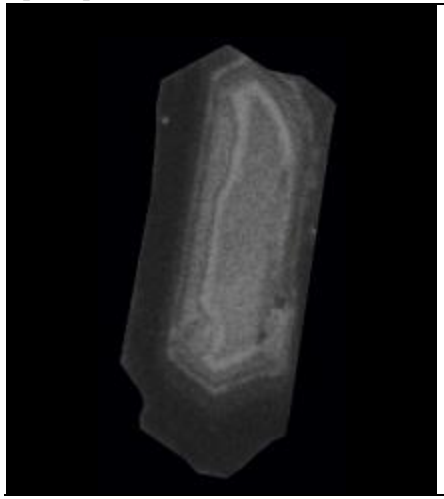

Shape:	Subhedral
Prismatic faces:	Well-preserved prismatic faces
Size:	130 μm in length (approximately 200 μm in length had the grain not been broken)
Elongation ratio:	3:1
Preservation state:	Incomplete grain, with one of the zircon terminations broken away
Zonation and colouring:	Well-developed bands of contrasting bright and dark oscillatory zones. Within this individual grain there are strong variations in the development of zoned domains, this is best demonstrated by one large dark band (particularly thick around preserved grain termination) marking the final stage of development of the crystal

15NT-03

[15.1]

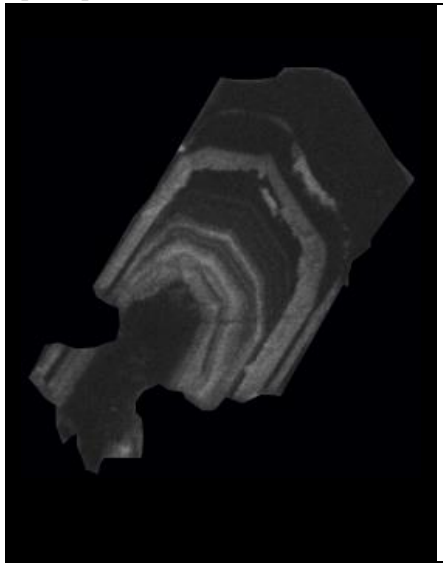

Shape:	Euhedral
Prismatic faces:	Well-preserved prismatic faces. Note: the apparent ‘cut-out’ section of the grain is due to Cl image extraction
Size:	180 μm in length (approximately 200 μm in length had the grain not been broken)
Elongation ratio:	4:1
Preservation state:	Incomplete grain, approximately a quarter of the length of the grain has been broken off through the core and other oscillatory zones. Rare cracks present
Zonation and colouring:	Well-developed bands of contrasting bright and dark oscillatory zones. Within this individual grain the central domain or core complex is dark; this is succeeded by oscillating bands of bright, dark and grey zones. One large, dark band (particularly thick around grain termination) marks the final stage of development of the crystal

15NT-01

[16.1]

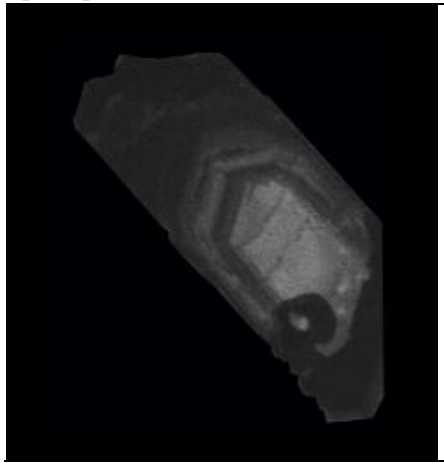

Shape:	Euhedral
Prismatic faces:	Well-preserved prismatic faces. Note: the apparent ‘cut-out’ section of the grain is due to Cl image extraction
Size:	230 μm in length (approximately 250 μm in length had the grain not been broken).
Elongation ratio:	4:1
Preservation state:	Complete grain. Rare fracturing present
Zonation and colouring:	Fairly well-developed oscillating bands of bright and dark luminescence. The core complex of this grain represents the brightest domain. An interesting feature of this zircon is the ‘bleb-like inclusion located at the base of the core. All zones succeeding the central domain are darker

APPENDIX D - SEM-EDS RESULTS

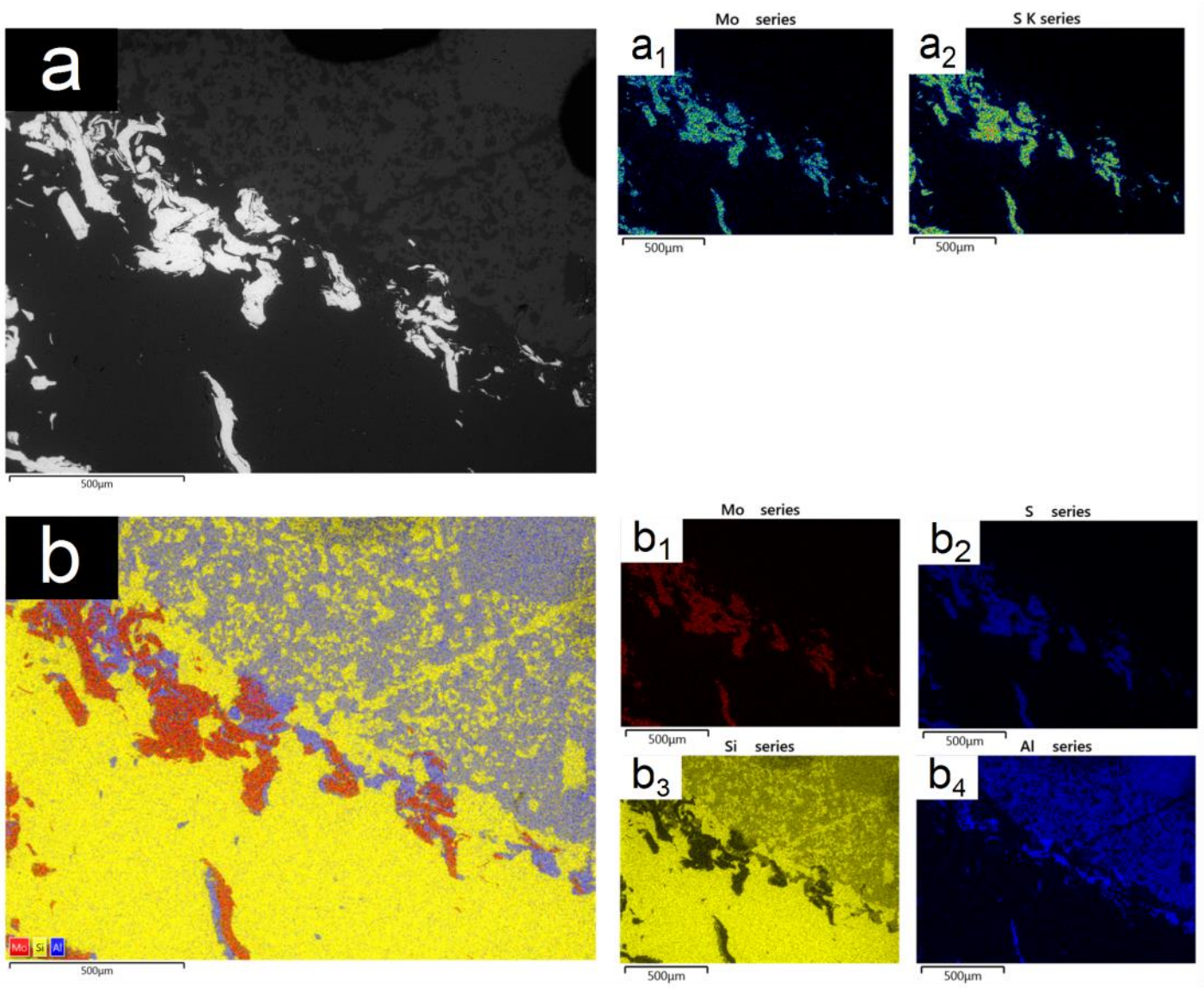

Figure 1: SEM-EDS results of Nantai Mo-(Cu) deposit sample 15NT_A

a) Electron image taken of thin section 15NT_A

a_1 & a_2) Discrete color maps displaying the occurrence of Mo and S within sample 15NT_A

b) Layered image of thin section 15NT_A

b_1) – b_4) Raster maps displaying the occurrence of Mo, S, Si, and Al within sample 15NT_A. As expected, the Mo-raster and the S-raster plot over the same areas within the region of interest indicative of molybdenite (MoS_2)

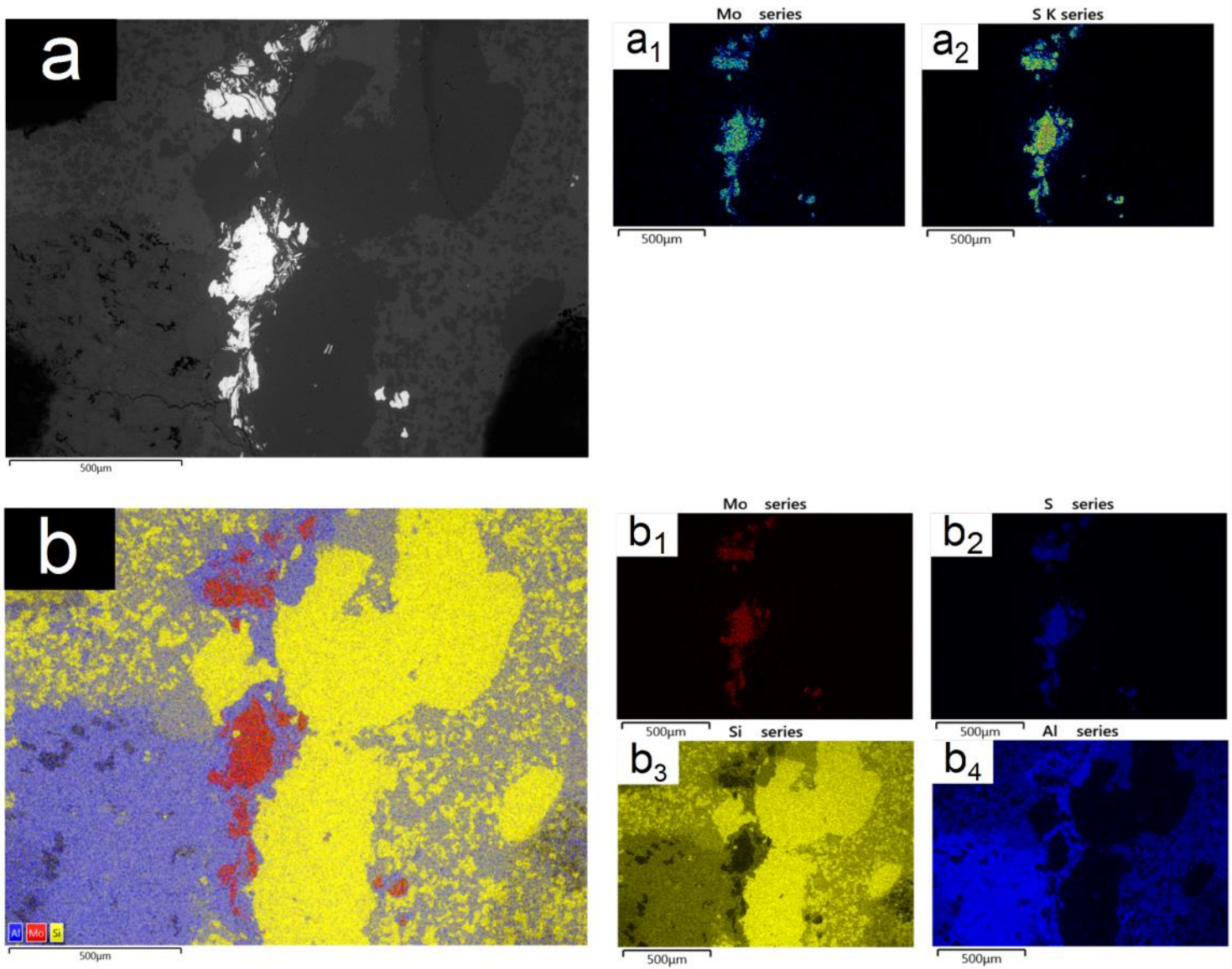

Figure 2: SEM-EDS results of Nantai Mo-(Cu) deposit sample 15NT_A

a) Electron image taken of thin section 15NT_A

a_1 & a_2) Discrete color maps displaying the occurrence of Mo and S within sample 15NT_A

b) Layered image of thin section 15NT_A

b_1) – b_4) Raster maps displaying the occurrence of Mo, S, Si, and Al within sample 15NT_A. As expected, the Mo-raster and the S-raster plot over the same areas within the region of interest indicative of molybdenite (MoS_2)

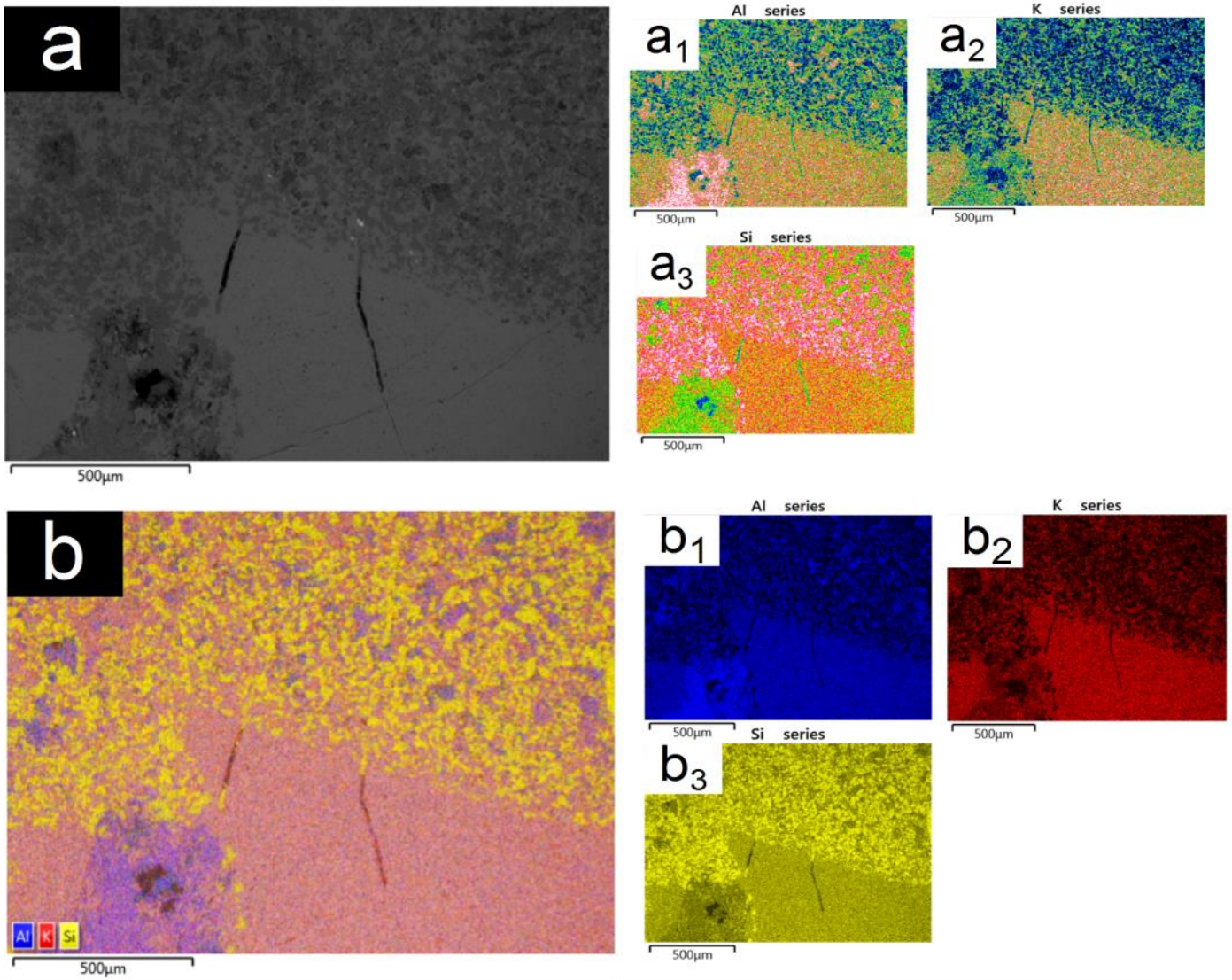

Figure 3: SEM-EDS results of Nantai Mo-(Cu) deposit sample 15NT_A

a) Electron image taken of thin section 15NT_A

a_1 – a_3) Discrete color maps displaying the occurrence of Al, K and Si within sample 15NT_A

b) Layered image of thin section 15NT_A

b_1) – b_3) Raster maps displaying the occurrence of Al, K and Si within sample 15NT_A

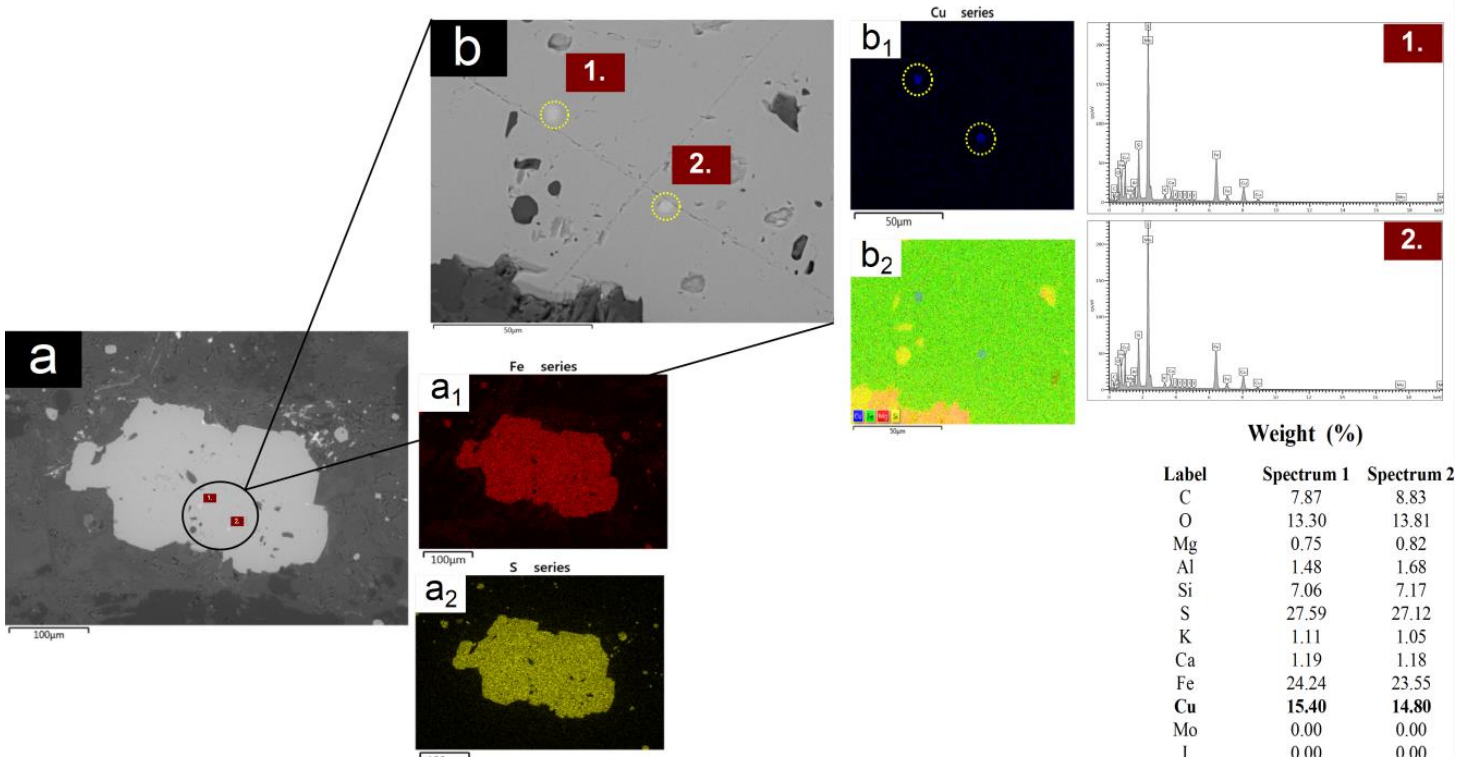

Label	Spectrum 1	Spectrum 2
C	7.87	8.83
O	13.30	13.81
Mg	0.75	0.82
Al	1.48	1.68
Si	7.06	7.17
S	27.59	27.12
K	1.11	1.05
Ca	1.19	1.18
Fe	24.24	23.55
Cu	**15.40**	**14.80**
Mo	0.00	0.00
I	0.00	0.00

Figure 4: SEM-EDS results of Nantai Mo-(Cu) deposit (lamprophyres) sample 15NT_J

a) Electron image taken of thin section 15NT_J

$a_1 – a_2$) Raster maps displaying the occurrence of Fe and S within sample 15NT_J. As expected, the Fe-raster and the S-raster plot over the same areas within the region of interest indicative of pyrite (FeS_2)

b) Increased magnification of electron image a) taken of thin section 15NT_J

b_1) Raster map displaying the occurrence of Cu blebs (chalcopyrite) within the greater pyrite mass
b_2) Layered image of thin section 15NT_J

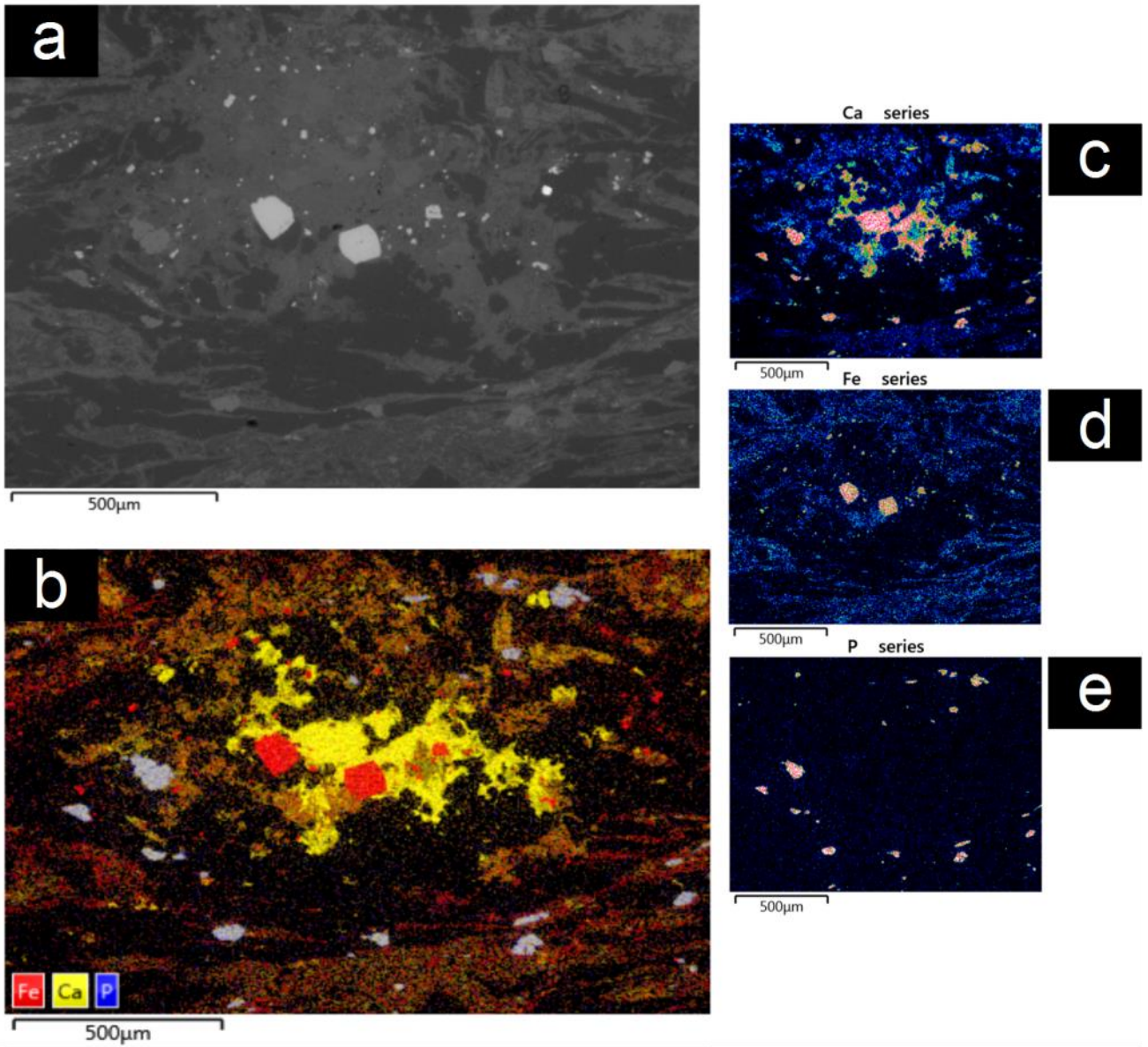

Figure 5: SEM-EDS results of Nantai Mo-(Cu) deposit (lamprophyres) sample 15NT_J

a) Electron image
b) Layered image
c) Discrete colour image displaying the occurrence of Ca
d) Discrete colour image displaying the occurrence of Fe
e) Discrete colour image displaying the occurrence of P

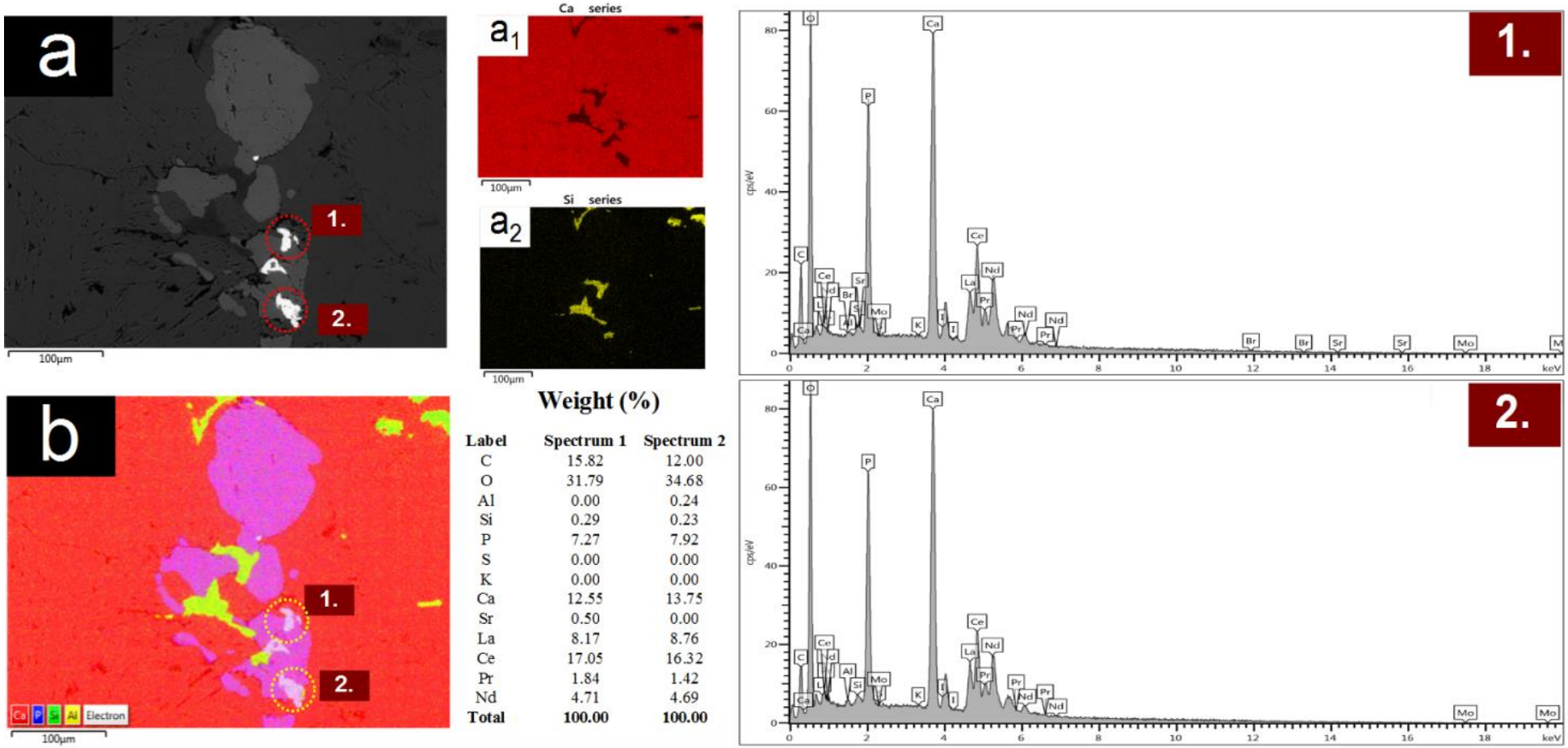

Label	Spectrum 1	Spectrum 2
C	15.82	12.00
O	31.79	34.68
Al	0.00	0.24
Si	0.29	0.23
P	7.27	7.92
S	0.00	0.00
K	0.00	0.00
Ca	12.55	13.75
Sr	0.50	0.00
La	8.17	8.76
Ce	17.05	16.32
Pr	1.84	1.42
Nd	4.71	4.69
Total	**100.00**	**100.00**

Figure 6: SEM-EDS results of Miaoya REE Deposit sample 15MY_A

a) Electron image taken of thin section 15MY_A
   a_1 & a_2) Raster maps displaying the occurrence of Ca and Si within 15MY_A
b) Layered image of thin section 15MY_A

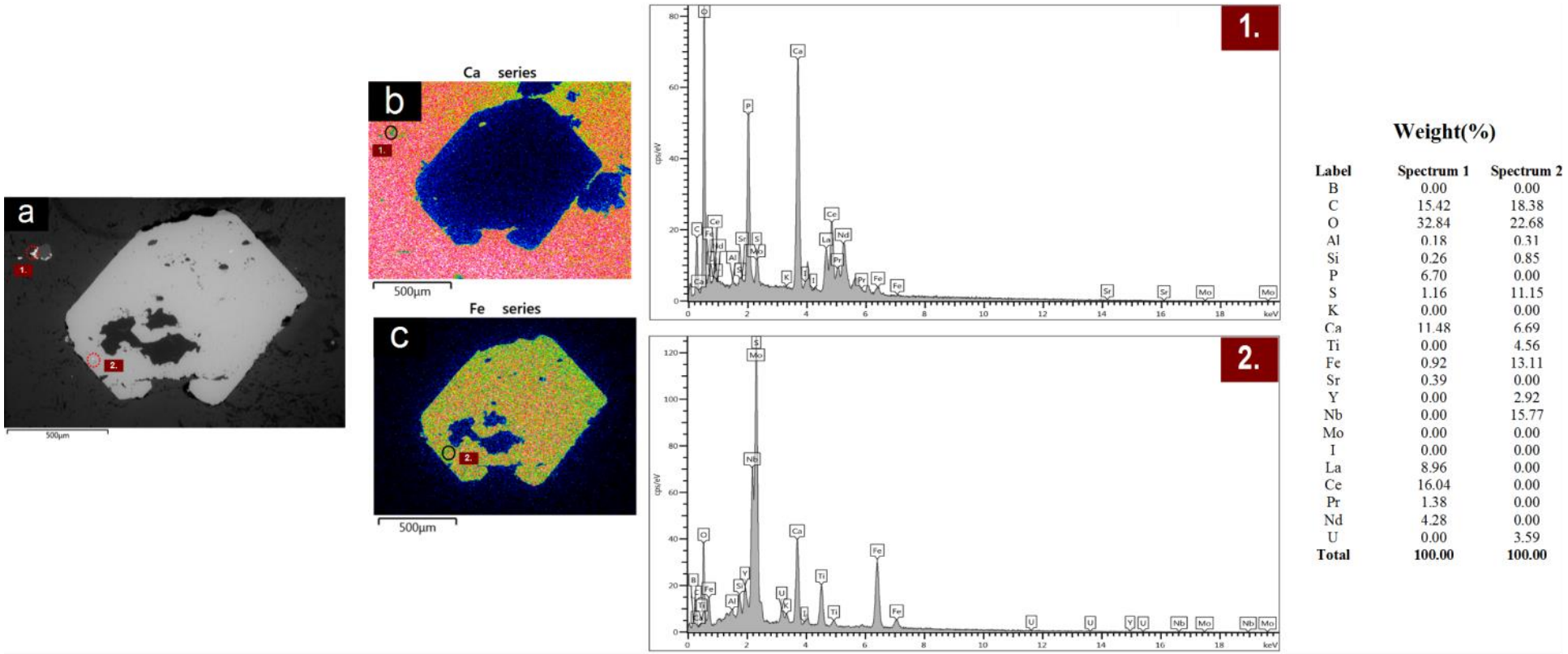

Weight(%)

Label	Spectrum 1	Spectrum 2
B	0.00	0.00
C	15.42	18.38
O	32.84	22.68
Al	0.18	0.31
Si	0.26	0.85
P	6.70	0.00
S	1.16	11.15
K	0.00	0.00
Ca	11.48	6.69
Ti	0.00	4.56
Fe	0.92	13.11
Sr	0.39	0.00
Y	0.00	2.92
Nb	0.00	15.77
Mo	0.00	0.00
I	0.00	0.00
La	8.96	0.00
Ce	16.04	0.00
Pr	1.38	0.00
Nd	4.28	0.00
U	0.00	3.59
Total	**100.00**	**100.00**

Figure 7: SEM-EDS results of Miaoya REE Deposit sample 15MY_A

a) Electron image taken of thin section 15MY_A
b) Discrete colour image displaying the occurrence of Ca
c) Discrete colour image displaying the occurrence of Fe

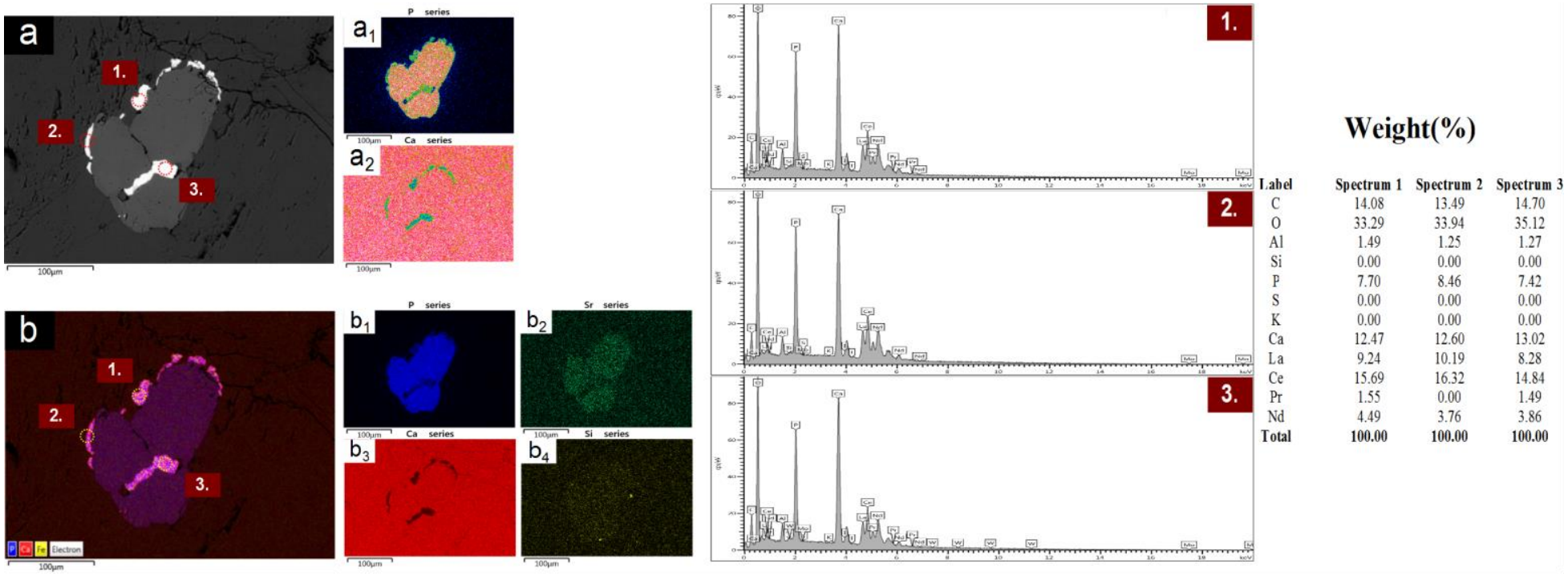

Weight(%)

Label	Spectrum 1	Spectrum 2	Spectrum 3
C	14.08	13.49	14.70
O	33.29	33.94	35.12
Al	1.49	1.25	1.27
Si	0.00	0.00	0.00
P	7.70	8.46	7.42
S	0.00	0.00	0.00
K	0.00	0.00	0.00
Ca	12.47	12.60	13.02
La	9.24	10.19	8.28
Ce	15.69	16.32	14.84
Pr	1.55	0.00	1.49
Nd	4.49	3.76	3.86
Total	**100.00**	**100.00**	**100.00**

Figure 8: SEM-EDS results of M Miaoya REE Deposit sample 15MY_A

a) Electron image taken of thin section 15MY_A

a_1 & a_2) Discrete color maps displaying the occurrence of P and Ca within sample 15MY_A

b) Layered image of thin section 15MY_A

b_1) – b_4) Raster maps displaying the occurrence of P, Sr, Ca and Si within sample 15MY_A

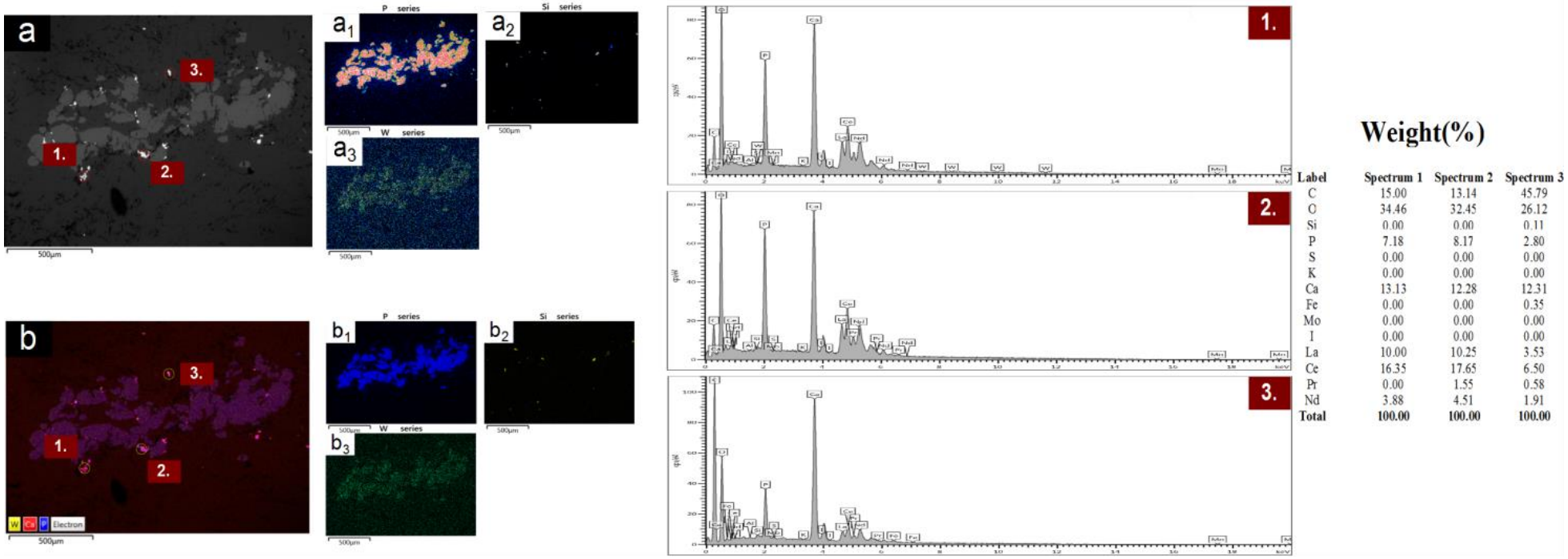

Figure 9: SEM-EDS results of Miaoya REE Deposit sample 15MY_A

a) Electron image taken of thin section 15MY_A

a_1 – a_3) Discrete color maps displaying the occurrence of P, Si and W within sample 15MY_A

b) Layered image of thin section 15MY_A

b_1) – b_4) Raster maps displaying the occurrence of P, Si and W within sample 15MY_A

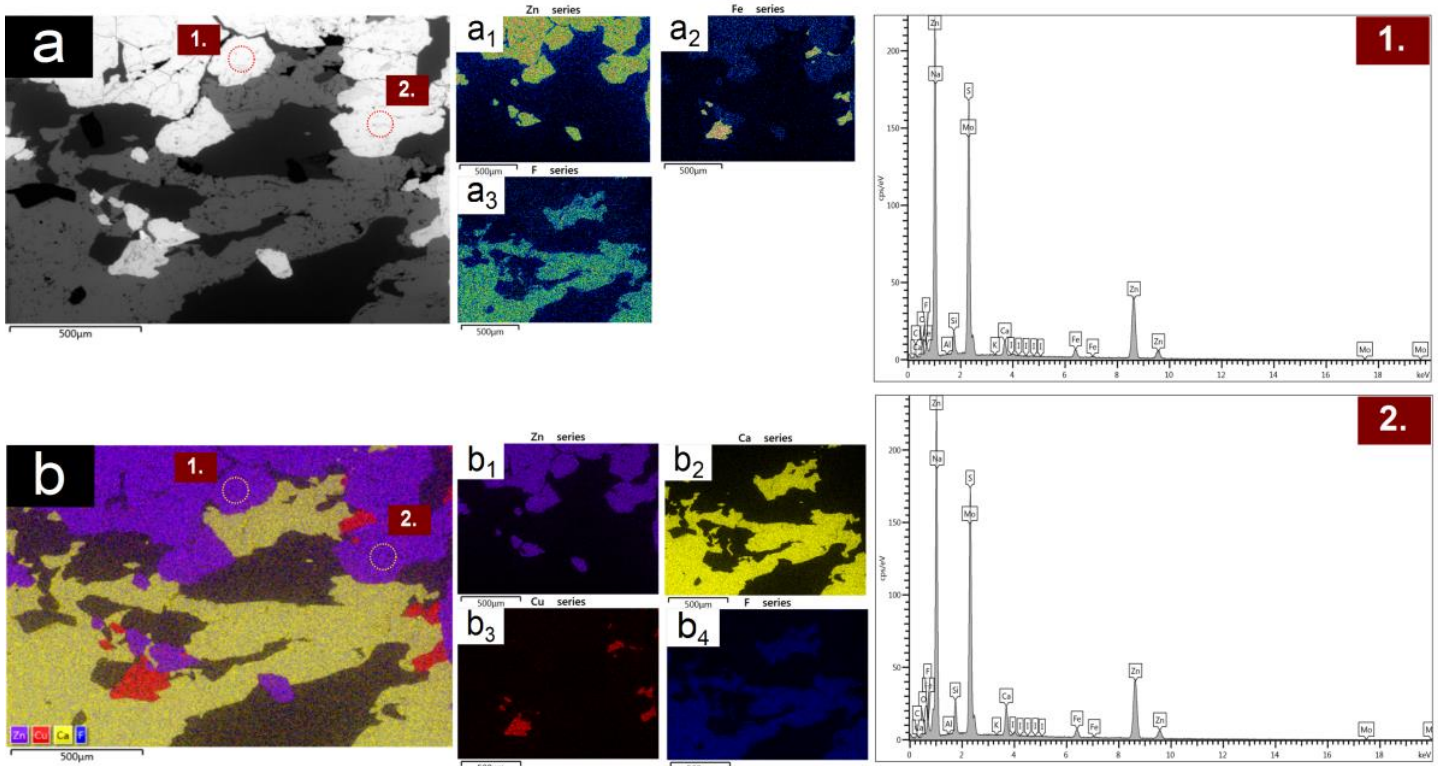

Weight (%)

Label	Spectrum 1	Spectrum 2
C	19.16	11.77
O	3.62	4.61
F	0.90	1.82
Na	3.24	3.69
Al	0.00	0.00
Si	2.03	3.33
S	21.87	22.55
K	0.00	0.00
Ca	1.81	3.74
Fe	2.29	2.51
Zn	45.10	45.99
Mo	0.00	0.00
Total	**100.00**	**100.00**

Figure 10: SEM-EDS results of Damogou Zn-CaF_2 sample 15DG_A

a) Electron image taken of thin section 15DG_A

a_1 – a_3) Discrete color maps displaying the occurrence of Zn, Fe and F within sample 15DG_A

b) Layered image of thin section 15DG_A

b_1) – b_4) Raster maps displaying the occurrence of Zn, Ca, Cu and F within sample 15DG_A. As expected, the F-raster and the Ca-raster plot over the same areas within the region of interest indicative of fluorite (CaF_2)

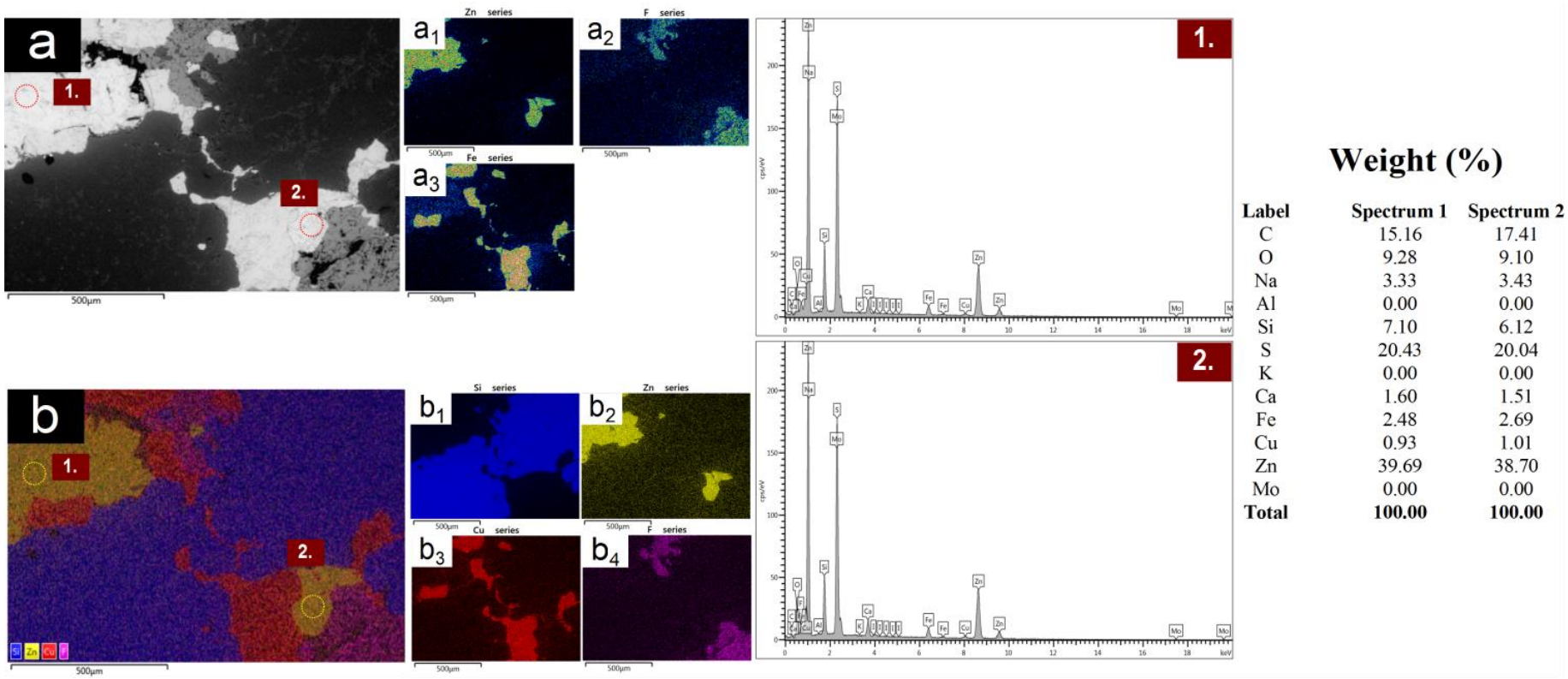

Figure 11: SEM-EDS results of Damogou Zn-CaF_2 sample 15DG_A
a) Electron image taken of thin section 15DG_A

a_1 – a_3) Discrete color maps displaying the occurrence of Zn, F and Fe within sample 15DG_A

b) Layered image of thin section 15DG_A

b_1) – b_4) Raster maps displaying the occurrence of Zn, Ca, Cu and F within sample 15DG_A. As expected, the F-raster and the Ca-raster plot over the same areas within the region of interest indicative of fluorite (CaF_2)

APPENDIX E - XRD RESULTS

Deposit	1	1	1	1	1	1	1	1	1	1	1	2	2	2	2	2	2	2	2	2	3	4	5
Sample	15NT_A	15NT_B	15NT_C	15NT_1	14NT_2	15NT_3	15NT_D	15NT_I	15NT_J	15NT_K	15NT_L	15MY_A	15MY_B	15MY_C	15MY_D	15MY_E	15MY_F	15MY_G	15MY_H	15MY_I	15LT_A	15LJ_B	15DG_A
Chi^2	6.4	5.3	7.3	8.6	4.3	5.1	6.2	7.4	4.6	4.5	5.9	8.6	5.7	5.1	5.3	8.4	7.6	4.4	7.6	5.6	8.1	15.6	5.2
Primary lithology	Aplite	Aplite	Aplite	Aplite	Aplite	Aplite	Dolomite	Marl	Lamp	Lamp	Lamp	Sövite	Sövite	Sövite	Sövite	Sövite	Sövite	Sövite	Sövite	Sövite	Vein	Siltstone	Vein
Quartz																							
Fluorite																							
Sphalerite																							
Chalcopyrite																							
Galena																							
Pyrite																							
Baryte																							
Hematite																							
Sericite (musc)																							
Calcite																							
Tremolite																							
Nepheline																							
Biotite																							
Apatite																							
Serpentine																							
Fayalite																							
Molybdenite																							
Dolomite																							
Fosterite																							
Talc																							
Actinolite																							
Magnetite																							
Ankerite																							
Phlogopite																							
Rutile																							
Albite																							
Anorthite																							
Bytownite																							
Anorthoclase																							
Microcline																							
Sanidine																							

Major > 30%
Accessory > 10%
Secondary 2 - 10%
Trace

1) NANTAI Mo-(Cu) DEPOSIT
2) MIAOYA REE DEPOSIT
3) LIUJIAXIA (orogenic) Au DEPOSIT
4) LONGTOUGOU (orogenic) Au DEPOSIT
5) DAMOGOU Zn-CaF_2 DEPOSIT